

STRUCTURAL EVOLUTION AND ELECTRICAL CONDUCTIVITY  
OF SINTERED URANIUM DIOXIDE

By

STEPHEN MARK GEHL

A DISSERTATION PRESENTED TO THE GRADUATE COUNCIL OF  
THE UNIVERSITY OF FLORIDA  
IN PARTIAL FULFILLMENT OF THE REQUIREMENTS FOR THE  
DEGREE OF DOCTOR OF PHILOSOPHY

UNIVERSITY OF FLORIDA

1977

~~FM 9-9 7-8. 0385~~

UNIVERSITY OF FLORIDA



3 1262 08552 4188

Dedicated to  
my wife, Patsy,  
and  
my parents, Mr. and Mrs. Frank H. Gehl

## ACKNOWLEDGEMENTS

The author wishes to acknowledge the encouragement and helpful discussions in the course of this research provided by the chairman of his supervisory committee, Dr. R. T. DeHoff, and by Dr. F. N. Rhines. Thanks are due also to Drs. E. D. Verink, Jr. and C. P. Luehr for serving on the committee.

The assistance of Drs. P. F. Johnson and L. L. Hench with the electrical measurements and their interpretation is gratefully acknowledged. In addition, Dr. Johnson's assistance in the art of "dissertationeering" was invaluable.

The encouragement and forbearance of L. A. Neimark, L. R. Kelman, Dr. R. W. Weeks, and Dr. B. R. T. Frost of the Materials Science Division of Argonne National Laboratory are also appreciated.

The financial support of the U. S. Atomic Energy Commission and the National Institutes of Health is gratefully acknowledged.

## TABLE OF CONTENTS

	Page
ACKNOWLEDGEMENTS . . . . .	iii
ABSTRACT . . . . .	vii
INTRODUCTION . . . . .	1
CHAPTER I. REVIEW OF LITERATURE . . . . .	6
The Methods and Results of Quantitative Stereology . . . . .	6
Notation . . . . .	7
The Counting Measurements . . . . .	7
Total Curvature . . . . .	12
Contiguity . . . . .	14
The Microstructural State and the Path of Microstructural Change . . . . .	16
Shape Parameters . . . . .	20
Sintering . . . . .	23
Sintering Mechanisms . . . . .	23
Geometric Changes during Sintering . . . . .	25
Sintering of $UO_2$ . . . . .	31
The Electrical Properties of Heterogeneous Structures . . . . .	32
Experimental Studies of the Electrical Properties of Heterogeneous Systems . . . . .	39
The Electrical Properties of Porous Materials . . . . .	42
The Electrical Properties of $UO_2$ . . . . .	45

TABLE OF CONTENTS - continued

	Page
CHAPTER II. EXPERIMENTAL PROCEDURE . . . . .	50
Material Characterization . . . . .	50
Sample Preparation . . . . .	57
Conventional Sintering . . . . .	57
Hot Pressing . . . . .	58
Quantitative Metallography . . . . .	60
Electrical Measurements . . . . .	62
CHAPTER III. THE METRIC PROPERTIES OF SINTERED AND HOT PRESSED $UO_2$ . . . . .	68
The Path of Microstructural Change . . . . .	68
Cold Compaction . . . . .	82
Conventional Sintering . . . . .	87
Hot Pressing . . . . .	108
Contiguity . . . . .	129
The Variation of Grain Contiguity during Sintering and Hot Pressing . . . . .	129
Contiguity and Pore-solid Surface Area . . . . .	131
Contiguity and Triple-line Length . . . . .	136
Grain-face Contiguity . . . . .	140
Shape . . . . .	146
The Pore-solid Interface . . . . .	146
Grain Shape . . . . .	148

TABLE OF CONTENTS - continued

	Page
CHAPTER IV. THE ELECTRICAL PROPERTIES OF SINTERED URANIUM DIOXIDE . . . . .	163
Electrical Conductivity under "Dry" Conditions . . . . .	164
Electrical Conductivity and Dielectric Properties under Humid Conditions . . . . .	172
CHAPTER V. DISCUSSION . . . . .	173
The Path of Microstructural Change . . . . .	173
The Effect of Compaction Pressure . . . . .	173
Additional Relationships . . . . .	182
Extensions of the Path of Microstructural Change to Other Systems . . . . .	184
Relationships between Electrical Conductivity and the Quantitative Stereology Parameters . . . . .	188
CHAPTER VI. SUMMARY AND CONCLUSIONS . . . . .	192
CHAPTER VII. SUGGESTIONS FOR FUTURE RESEARCH . . . . .	195
APPENDIX A. THE GROSS TANGENT COUNT . . . . .	198
APPENDIX B. THE AREA INFLECTION POINT COUNT . . . . .	212
APPENDIX C. NOTES ON THE GRAIN CONTIGUITY AND THE GRAIN FACE CONTIGUITY . . . . .	222
APPENDIX D. ELECTRICAL MEASUREMENTS FOR SPECIMENS WITH WATER VAPOR ADSORBED . . . . .	226
LIST OF REFERENCES . . . . .	238
BIOGRAPHICAL SKETCH . . . . .	246

Abstract of Dissertation Presented to the Graduate Council  
of the University of Florida in Partial Fulfillment of the Requirements  
for the Degree of Doctor of Philosophy

STRUCTURAL EVOLUTION AND ELECTRICAL CONDUCTIVITY  
OF SINTERED URANIUM DIOXIDE

By

Stephen Mark Gehl

December 1977

Chairman: R. T. DeHoff  
Major Department: Materials Science and Engineering

The simple counting measurements of quantitative stereology were used to determine the sequences of microstructural states attained during conventional sintering and hot pressing of uranium dioxide powders. Each such sequence, called a path of microstructural change, was evaluated by measuring, for a series of specimens, the pore volume fraction; the area, total curvature, and gross tangent count of the pore-solid interface; the grain-boundary area; and the lengths of the triple lines formed by the intersection of the grain boundaries with each other, and with the pore-solid interface. The paths of microstructural change were found to be functions of the scale of the system, the compaction pressure used prior to conventional sintering, and the applied pressure during hot pressing. Quantitative relationships were developed between pore volume fraction, pore-solid surface area, grain-boundary area, and the lengths of both kinds of triple lines. These relationships, with appropriate values for the empirical constants, were valid for all fabrication conditions explored. The grain contiguity parameter was found to provide a useful index of the extent to which the

grain structure had developed during sintering and hot pressing. An additional parameter, the grain-face contiguity, was defined in this study and was linearly related, by a factor of  $\sim 0.6$ , to the grain contiguity. This relationship, which was valid for both conventional sintering and hot pressing, was found to be an indication that the grain boundaries preferentially intersected the pore-solid interface, and avoided intersections with other grain boundaries.

The areal density of inflection points formed by the intersection of a sectioning plane with a saddle surface was demonstrated to be proportional to the integral of the asymptotic line curvature. The area inflection point count was evaluated for a series of hot-pressed specimens and was found to decrease by a factor of  $\sim 50$  as pore volume fraction decreased from 0.24 to 0.08.

The gross tangent count was demonstrated to be upper bound for the total absolute curvature. For saddle surface, the gross tangent count was found to be approximately equal to the integral of the root mean square local curvature over the domain of surface area.

Electrical conductivity measurements were performed on a series of conventionally sintered specimens. The results of these experiments were compared with the quantitative stereology measurements to determine the effect of microstructure on electrical conductivity. In the early stages of sintering electrical conductivity was found to be strongly correlated with grain-boundary area and grain contiguity, an indication that the bulk electrical conductivity is controlled by the grain contacts, which are the minimum cross-section area through which current passes. In the latter stages of sintering, the minimum cross-section area is no longer controlled by the grain contact area.

## INTRODUCTION

All materials, whether by design or accident, contain heterogeneities in structure. These heterogeneities range from vacant lattice sites and dislocations in high-purity single crystals to large slag entrapments in metal castings. The external surface is a heterogeneity which is present in all real materials. It is not surprising, therefore, that there is much interest in the physical properties of heterogeneous systems. The important class of heterogeneity which is the subject of this dissertation is the microstructure, i.e., the arrangement of volumes and interfaces that define the distribution of the crystalline and amorphous constituents of a system. It is usual to restrict the term microstructure to features too small to be resolved with unaided vision; this convention will be followed here.

Several strategies have been used to explore relations between structure and properties. These methods may be summarized as follows:

In one type of investigation the heterogeneous system is represented by a model simple enough to allow a priori calculation of its physical properties. An important example of this approach is the Maxwell-Wagner-Sillars (MWS) theory of heterogeneous dielectrics,<sup>1-3</sup> which begins with Maxwell's field equations, and predicts the dielectric properties of a medium in which the electric field is perturbed

by a small amount of a disperse second phase with dielectric constant different from the matrix. The major limitation of this approach is the requirement of mathematical tractability. If the set of equations generated is to be solvable, simplifying assumptions about the geometry of the heterogeneous system must be made. For the MWS theory, the second phase is assumed to consist of a small volume fraction of isolated ellipsoidal particles with an electrical conductivity higher than the matrix. The danger lies in applying such a theoretical model to systems in which the model's assumptions are not valid.

In other studies the variation of physical properties with fabrication conditions is explored. Since the processing variables control the microstructure, which in turn determines the physical properties, this type of investigation is actually one step removed from a direct study of the relations between microstructure and properties. While the use of this indirect method is no longer prevalent, some examples can be found in the recent literature.<sup>4-5</sup>

A third group consists of studies in which structural characterization is performed, for which a wide variation exists in the effort expended toward this end. In some cases, a somewhat limited set of structural parameters is determined, such as grain size or volume fraction of a second phase. In other studies, a more detailed structural investigation is undertaken: the physical properties of heterogeneous structures have been related to mean phase intercept,<sup>6</sup> contiguity,<sup>7</sup> genus,<sup>8</sup> and "shape parameters,"<sup>9</sup> in addition to volume fraction and grain size.<sup>10-14</sup> The development of an empirical relation, the form of which may be suggested by theoretical considerations, is the goal of studies of this type.

Such an empirical equation will express the physical property of interest as a function of some set of structural parameters,  $P = \{P_1, P_2, \dots, P_N\}$ . If the relation is general, the physical property will depend only on the set  $P$ , and will be independent of all other structural parameters. The difficulty in the development of general relations lies in the determination of the set  $P$ . When the makeup of  $P$  is uncertain, the extension of empirical relations to new material or structure types must be done with caution.

In this study, the problem of generating relations between a structure and its properties was attacked in the following way. After all of the accessible parameters of quantitative stereology were determined, an attempt was made to define, on one or several of these parameters, a function whose variation from sample to sample would parallel the behavior of some physical property measured for the same samples. A long list of stereological properties was measured to increase the probability of finding a precise relation, with a simple mathematical form, between the structure and its physical properties. To enable a large number of samples to be characterized, those parameters which require time-consuming serial sectioning techniques were not determined. While it was recognized that the topological properties of number and genus, which can only be measured by serial sectioning methods, often directly determine the physical properties of a heterogeneous system, the necessity of testing a proposed relation against a large number of widely differing structures was judged to be of primary importance. The experimental methods actually used in this study provided a critical test of the ability of the more easily obtained stereological properties to predict the physical properties of a heterogeneous structure.

The physical properties selected for measurement were the room temperature electrical conductivity and dielectric constant of sintered uranium dioxide. The electrical properties were chosen because there is much interest in the electrical behavior of heterogeneous systems, and because the electrical properties can be calculated for some simple structures but not in the general case. Sintered structures were examined because of their complexity, and because sintering is a common fabrication method for many ceramic articles. The electrical behavior of sintered uranium dioxide is of special interest to the nuclear industry because the present-day laboratory simulation of reactor conditions utilizes the principle of direct electrical heating of  $UO_2$  fuel rods.<sup>15</sup>

In addition to the development of relationships between the microstructure and the electrical properties of  $UO_2$ , the structural characterization studies performed in the course of this research led to several advances. A new metric property, the total curvature of the asymptotic lines on saddle surface, was discovered and methods for its measurement were developed. A new contiguity parameter, the grain face contiguity, was defined. For sintering, this parameter was found to be simply related to an earlier measure of contiguity.<sup>16</sup>

In this dissertation, three major topics are discussed. These are quantitative structure analysis, sintering, and the electrical behavior of heterogeneous structures. In Chapter I the literature on these topics is reviewed separately. In the results section, Chapter III, and the discussion section, Chapter V, the analysis of structure is

grouped with the sintering study, since quantitative structure analysis was the primary tool used to investigate the sintering process. Results of the electrical measurements and correlations with the stereological data are presented in Chapter IV. A description of the experimental procedure is contained in Chapter II.

CHAPTER I  
REVIEW OF LITERATURE

The Methods and Results of  
Quantitative Stereology

As used by Underwood,<sup>17</sup> stereology includes "not only the quantitative study and characterization of any spatial structure, but also its qualitative interpretation." Stereology may be differentiated from other structure-measuring techniques such as gas-adsorption surface area determination, in which no direct image of the structure is formed.

The basic tools of stereology are a set of counting measurements, which are performed on a section or series of sections through the structure. These measurements yield information about the number, size, distribution, shape, and extent of features in the three-dimensional structure, when appropriate assumptions about the uniformity of the structure and the orientation of features with respect to the sectioning plane are made.

In this section, the counting measurements used in the present study, and the relations between these measurements and the metric properties of a three-dimensional structure, are reviewed. Special attention is given to surface curvature and to measures of contiguity, since these parameters were determined for many samples in the course of the experimental work on which this dissertation is based. The concept of the path of microstructural change is reviewed.

## Notation

The notation used in the dissertation for expressing stereology parameters is derived from the system proposed by Underwood.<sup>17</sup> Most of the parameters are written as upper case letters and are identified in Table I-1. The terms usually have obvious meanings, such as "T" for tangent, "S" for surface area, and "N" for number. The upper-case subscripts "P," "L," "A," and "V" indicate the basis for normalization of the major term, e.g., number of points, unit line length, unit area, and unit volume, respectively. The superscripts  $\alpha$ , for the crystalline phase, and P, for the pore phase indicate the volumes that meet to form the specific feature. For example,  $\alpha\alpha$  indicates the grain boundaries between  $\alpha$  crystals,  $\alpha P$  the interfaces between the crystalline and pore phase,  $\alpha\alpha\alpha$  the lines formed by the juncture of three  $\alpha$  grains, and  $\alpha\alpha P$  the lines formed by the juncture of two  $\alpha$  grains with the pore phase.

## The Counting Measurements

The counting measurements used in this study are the systematic point count, the line intercept count, the area feature count, and the area tangent count.

In the point count, a regular grid of points is placed at random on the structure. The fraction of the total number of points falling in the phase of interest, for a sufficiently large number of grid placements, is called the point fraction  $P_p$ . The average point fraction has been shown<sup>18</sup> to be an unbiased estimator of the volume fraction of a phase,

$$P_p = V_v. \quad (1-1)$$

Table I-1

## Notation Used for the Quantitative Stereology Parameters

## I. Root Symbols (indicate the measured quantity).

A - area

C - contiguity

D - caliper diameter

G - genus

H - mean surface curvature

I - inflection point

K - Gaussian curvature

L - length

M - total surface curvature

N - number

P - point

Q - total curvature of lineal features

S - surface area

T - tangent

V - volume

W - total torsion of lineal features

## II. Subscripts (indicate the normalization base).

A - per unit area

L - per unit length

P - per point

V - per unit volume

g - per gram

Table I-1 - continued

III. Superscripts (indicate the feature being measured by specifying the bounding phase or phases).

- $\alpha$  - the solid, i.e., crystalline, phase
- P - the pore phase
- $\alpha\alpha$  - the boundaries between  $\alpha$  grains
- $\alpha P$  - the pore-solid interface
- $\alpha\alpha\alpha$  - triple lines at the juncture of 3  $\alpha$  grains
- $\alpha\alpha P$  - triple lines at the juncture of 2  $\alpha$  grains with the  $\alpha P$  interface
- $\alpha\alpha\alpha\alpha$  - quadruple points at the juncture of 4  $\alpha$  grains
- $\alpha\alpha\alpha P$  - quadruple points at the juncture of 3  $\alpha$  grains with the  $\alpha P$  interface

The line intercept count consists of placing a test line on the section, and counting the number of intersections of the line with traces of interface in the three-dimensional structure. The average value of the line intercept count,  $P_L$ , is related to the surface area of the interface producing the trace by<sup>19</sup>

$$P_L = \frac{1}{2} S_V \quad (1-2)$$

where  $S_V$  is the interfacial area in unit volume.

The area feature count is simply the determination of the number, per unit area, of some feature on the sectioning plane. The feature may be a point representing the intersection of a linear feature with the sectioning plane. For this case, it can be shown<sup>19</sup> that

$$P_A = \frac{1}{2} L_V \quad (1-3)$$

where  $P_A$  is the number of points per unit area of sectioning plane and  $L_V$  is the length of line in unit volume.

When the feature on the section has some spatial extension, for example a particle outline, the net number of particles per unit area is related to the total curvature of particle boundary per unit volume by<sup>20,21</sup>

$$N_{Anet} = \frac{1}{2\pi} M_V \quad (1-4)$$

where  $M_V$  is the total curvature in unit volume and  $N_{Anet}$  is the number of features in unit area summed so that a particle outline with  $n$  internal holes ( $n \geq 0$ ) contributes  $1-n$  to the total number.

An alternate method for the determination of total curvature is the area tangent count.<sup>22</sup> This measurement consists of sweeping the section with a test line and counting the number of times the test line makes a tangent with an arc element of particle outline. The net number of tangents is obtained by choosing the volume on one side of the interface as the reference phase: tangents formed with elements of arc which are convex with respect to the reference phase are counted as positive; tangents with concave elements of arc are counted as negative. The net number of tangents per unit area, summed in this way, is related to the total curvature by<sup>20</sup>

$$T_{\text{Anet}} = \frac{1}{\pi} M_V \cdot \quad (1-5)$$

The use of the area feature count to determine the length per unit volume of lineal features has already been mentioned. When the lineal features are grain edges, they contribute to the total curvature of interfaces in the structure. The grain edge curvature is given by<sup>23</sup>

$$M_{\text{Vedge}} = \frac{\bar{\theta}}{2} L_V, \quad (1-6)$$

where  $\bar{\theta}$  is the average dihedral angle between the surfaces that meet to form the edge.

An additional feature which may be present on polished sections is an inflection point in the trace of an interface. At inflection points the curvature of the trace changes sign. The number of inflection points per unit area,  $I_A$ , is proportional to the integral of the curvature of asymptotic lines over the domain of saddle surface in unit volume,

$$I_A = \frac{1}{2} \iint_S \kappa_{\text{as}}^{\pm} dS_V^{\pm} \quad (1-7)$$

where  $k_{as}$  is the curvature of the asymptotic lines, and the superscript  $\pm$  indicates saddle surface. This relation was discovered as a part of this research, and is included in this summary of the counting measurements for completeness. A derivation of the relationship is presented in Appendix B.

### Total Curvature

Of the metric properties which can be obtained from the counting measurements, the volume of a phase, the area of phase or grain boundary, and the length of lineal feature in a unit volume of structure, are all easily visualized concepts whose intuitive meaning correspond closely to the geometric definitions. Total curvature is a somewhat more abstract concept. The local mean curvature of a surface is defined by

$$H = \frac{1}{2} \left[ \frac{1}{R_1} + \frac{1}{R_2} \right] \quad (1-8)$$

where  $R_1$  and  $R_2$  are the principle normal curvatures at a point on the surface. To illustrate this definition, note that the tip of a needle has a higher curvature than a pencil point, which in turn has a higher curvature than the tip of a crayon. Note also that  $H$  is a local property, e.g., the radii of curvature are not the same on the shank of a needle as at the point. The total curvature of a surface is simply the integral of  $H$  over the surface, or

$$M = \iint_S H(u,v) \, dudv \quad , \quad (1-9a)$$

where  $u$  and  $v$  are a set of coordinates on the surface. The total curvature in unit volume is usually written

$$M_V = \iint_S H dS_V \quad , \quad (1-9b)$$

where  $dS = dudv$ , and the subscript  $V$  is added to balance the units.

If the mean curvature is high at a point on the surface, the pressure differential across the interface is also high since<sup>24</sup>

$$\Delta P = 2\gamma H \quad (1-10)$$

where  $\gamma$  is the surface energy. Thus, high curvatures are often associated with large driving forces for microstructural change. Unfortunately, the curvature parameter accessible by quantitative stereology measurements,  $M_V$ , is the result of an algebraic summation of the local values of mean curvature. This means that positive and negative values of  $H$  will cancel when integrated to give  $M_V$ . Therefore, in many cases  $M_V$  will not report the existence of highly curved surface elements.

The total curvature parameter can also give a misleading picture of the curvature of interfaces in single-phase grain structures. Since all interfaces except the external surface are shared by two grains, the curvature of every element of surface of one grain is exactly cancelled by a contribution of equal magnitude but opposite sign from the adjacent grain. Thus, while the grain surfaces can be, and almost always are, curved, their contribution to  $M_V$  is identically zero. (For single-phase grain structures the only nonzero contribution to  $M_V$  is the grain edge curvature.)

Thus,  $M_V$  is seen to provide somewhat limited information about the curvature of interfaces in a structure. In order to overcome these limitations, alternate methods of measuring curvature have been sought. One of these, proposed by Johnson,<sup>25</sup> consists of performing a tangent count only in selected areas of the structure. For the sintered structures considered, Johnson counts tangents only near interparticle necks, since these are the regions whose curvature is assumed to determine the

driving force for densification. The subjective nature of this selective measurement technique make its results sensitive to the biases of the individual operator, and thus Johnson's method<sup>25</sup> does not lie within the framework of the quantitative techniques used in this research.

Another method for reporting surface curvature is the gross tangent count.<sup>26</sup> If a section through a structure is found to have large numbers of both positive and negative tangents, the net tangent count may be very small, but the structure is quite different from one in which a small number of tangents, all of one sign, are counted. The gross tangent count,

$$T_{Ag} = T_A^+ + T_A^- \quad (1-11)$$

can be used to differentiate two such structures. The gross tangent count also may be applied to single phase grain structures and to surfaces which are not closed. In general, large values of  $T_{Ag}$  will be associated with structures with a large amount of highly curved interface. A more precise interpretation of the gross tangent count was formulated in the course of this research. These results are summarized in Appendix A.

### Contiguity

The contiguity of a phase is a concept first formulated by Gurland,<sup>16</sup> who was interested in reporting the results of quantitative stereological measurements in a manner which might explain observed physical properties such as the electrical conductivity of two-phase

alloys or the fracture behavior of systems containing both brittle and ductile constituents. Gurland's contiguity parameter, which will be called the grain contiguity, is defined by<sup>16</sup>

$$C^\alpha = \frac{2S_V^{\alpha\alpha}}{2S_V^{\alpha\alpha} + S_V^{\alpha P}} \quad (1-12)$$

for a two-phase system.

The phase whose contiguity is determined, the  $\alpha$  phase, must consist of a number of particles which form a definite interface when placed in contact. For most systems, this requirement means that the phase is crystalline. Gurland's definition was extended to multiple-phase systems by Dorfler.<sup>27</sup> The two-phase definition will be used in the present discussion.

The definition of contiguity may be combined with the definitions of mean grain intercept,  $\bar{\lambda}^g$ , and mean phase intercept,  $\bar{\lambda}^\alpha$ , to yield<sup>28,29</sup>

$$C^\alpha = 1 - \frac{\bar{\lambda}^g}{\bar{\lambda}^\alpha} . \quad (1-13)$$

Other contiguity parameters, such as the lengths of the several types of triple lines and the total perimeter length of grain contacts, have been proposed,<sup>30</sup> but these are largely dependent on the scale of the system and on the shape of particles, and thus do not directly indicate the contiguity of a phase. Ratios of surface areas similar to the grain contiguity  $C^\alpha$  have also been used,<sup>30</sup> but these are not independent of the contiguity parameter.

The determination of contiguity parameters for sintered structures is a relatively new concept.<sup>31</sup> The crystalline phase in a sintering is always continuous, but its contiguity varies from a value of zero for an unfired compact (if the initial particles are monocrystalline) to one for a fully dense body.

A new parameter, similar in form to the grain contiguity but consisting of ratios of triple line lengths, was devised to analyze some of the stereological data generated in this research. This parameter, called the grain face contiguity, is discussed in Chapter III and in Appendix C.

#### The Microstructural State and the Path of Microstructural Change

The methods of quantitative stereology yield a large amount of information about a structure. Some method of organizing these data is useful for describing the results of studies of the stereological parameters. The method used in this dissertation describes individual structures in terms of their "quantitative microstructural state," and the evolution of microstructure by the "path of microstructural change."

The quantitative microstructural state. Each microstructural feature may be characterized by determining its associated stereological properties. These properties may be divided into two broad classes: metric properties, which are sensitive to the size and shape of the features, and the topological properties of number and genus, which are independent of the scale of the features and are unchanged by bending and stretching operations. A determination of the quantitative microstructural state consists of measuring all of these stereological properties, listed in Table I-2. However, at least at the present stage of

Table I-2  
Stereological Properties of Two-phase Sintered Structures

Feature	Dimension	Metric Properties	Topological Properties
$\alpha$ grains	3		$\alpha$ $N_V$
porosity	3	$V_V^P$	$N_V^P$
$\alpha\alpha$ surfaces	2	$S_V^{\alpha\alpha}$ , $\pi T_{Ag}^{\alpha\alpha}$	$N_V^{\alpha\alpha}$
$\alpha P$ surfaces	2	$S_V^{\alpha P}$ , $M_V^{\alpha P}$ , $\pi T_{Ag}^{\alpha P}$	$N_V^{\alpha P}$ , $G_V^{\alpha P}$
$\alpha\alpha\alpha$ triple lines	1	$L_V^{\alpha\alpha\alpha}$ $Q_V^{\alpha\alpha\alpha}$ , $W_V^{\alpha\alpha\alpha}$	$N_V^{\alpha\alpha\alpha}$
$\alpha\alpha P$ triple lines	1	$L_V^{\alpha\alpha P}$ $Q_V^{\alpha\alpha P}$ , $W_V^{\alpha\alpha P}$	$N_V^{\alpha\alpha P}$
$\alpha\alpha\alpha\alpha$ quadruple points	0	-	$N_V^{\alpha\alpha\alpha\alpha}$
$\alpha\alpha\alpha P$ quadruple points	0	-	$N_V^{\alpha\alpha\alpha P}$

advancement, all of the topological properties and some of the metric properties of an opaque material can only be determined by reconstructing the spatial structure by means of a laborious serial sectioning procedure. Only those properties which can be determined by measurements on a single polished plane section were determined in this investigation. These properties are enclosed in a box in Table I-2.

The path of microstructural change. The quantitative microstructural state of a specimen may be regarded as a point in an  $n$ -dimensional Euclidean space, where  $n$  is the total number of stereological properties which may be defined for the structure. If the structure is altered by a physical or chemical process, the point moves through  $n$ -space and traces out a curve. This curve describes the sequence of microstructural states through which the system passes during the process and is called the path of microstructural change.<sup>32</sup> Since a complete description of the quantitative microstructural state is almost never available, the path of microstructural change is usually observed as a projection onto a lower-dimensional space, whose coordinate axes are the properties actually determined. Figure 1-1 provides an example of the path in three dimensions for a simple sintering experiment. In practice, the path of microstructural change is usually presented as a series of  $k-1$  planar projections, where  $k$  is the number of stereological properties determined.

Most of the graphical presentations of the path of microstructural change in this dissertation have pore volume fraction as the abscissa. Pore volume fraction has several advantages as an independent variable with which to describe the sintering process: 1) volume fraction is

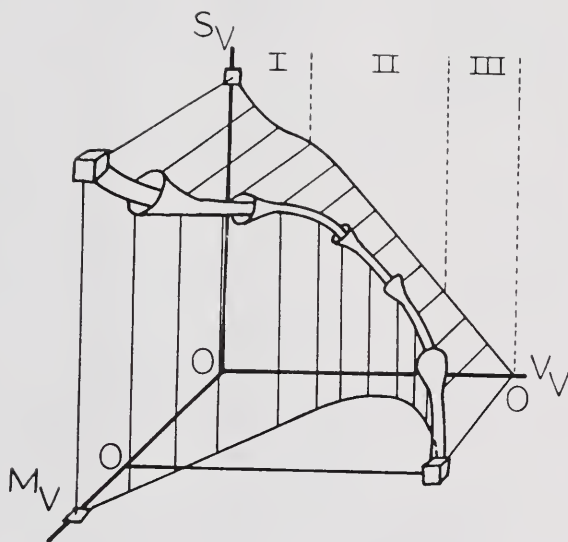


Figure 1-1. Three-dimensional representation of the path of microstructural change for a simple sintering experiment.

commonly used to measure the degree to which a compact has sintered into a coherent entity, and 2) volume fraction decreases monotonically but not linearly with time. Use of  $V_V^P$  as the independent variable has the effect of expanding the time scale at short times, when the structural changes are occurring most rapidly, and compressing the scale at long times.

### Shape Parameters

The problem of specifying the shape of features in complex structures has received attention in the fields of mathematics, biology, and materials science.<sup>17,33-37</sup> The wide range of shapes present in materials systems has been reviewed by Smith,<sup>37</sup> who also summarized the physical processes (and combinations of processes) that produce the various classes of shapes.

A complete specification of shape might consist of a description of the relative numbers, positions and equations of the points, curves, and surfaces that form the structure. Two broad classes of shape, topological and geometric, are represented in such a specification. Topological shape is a description of the number of each type of feature, the genres of the surfaces in the structure, and the connectivities of the lineal networks. Several experimental determinations of one or more aspects of the topological shape of materials systems are represented in the literature.<sup>38-42</sup> Most of these studies employed serial sectioning techniques.

Geometric shape is the description of the positions and equations of the curves and surfaces of a structure. Experimental studies usually attempt to quantitatively characterize the average geometric shape of a structure in terms of a "shape parameter," sometimes called a "form factor." The shape parameter should satisfy the requirement being sensitive to the shape but independent of the scale of structural features. This requirement means that a shape parameter is a dimensionless quantity. Underwood<sup>17</sup> has compiled a list of twelve parameters that have been proposed for the evaluation of shape. Fischmeister<sup>43</sup> has pointed out that of the parameters on Underwood's list, four pertain only to oriented structures, four contain quantities that can only be evaluated by serial sectioning, and one is not a dimensionless quantity. Fischmeister also showed that the remaining three parameters are all closely related and may be written as simple products and ratios of the counting measurements  $P_p$ ,  $P_L$ , and  $N_A$ .

The shape parameters that require serial sectioning analysis for their determination are calculated from the average dimensions, surface areas, and volumes of the particles or grains in the structure. For example, one of Underwood's expressions is

$$f_1 = \frac{\bar{V}^{1/3}}{\bar{S}^{1/2}} \quad (1-14)$$

where  $\bar{V}$  and  $\bar{S}$  are the average particle volume and surface area respectively.<sup>17</sup>

One of the parameters that can be calculated from counting measurements on a single plane section was first proposed by DeHoff<sup>44</sup> for structures consisting of isolated particles of constant size and shape and was later extended by Rhines, DeHoff, and Kronsbein<sup>45</sup> to sintered structures. For the latter case, this parameter may be written

$$\overline{H}^{\alpha P} \overline{\lambda}^P = \frac{4V_V^P M_V^{\alpha P}}{(S_V^{\alpha P})^2} \quad (1-15)$$

where  $\overline{H}^{\alpha P} = M_V^{\alpha P} / S_V^{\alpha P}$  is the average mean curvature of the pore-solid interface, and  $\overline{\lambda}^P = 4V_V^P / S_V^{\alpha P}$  is the mean pore intercept.

It is difficult to ascribe a physical meaning to a given value of  $\overline{H}^{\alpha P} \overline{\lambda}^P$  in the general case. However, several observations may be made for particulate structures: First,  $\overline{H} \overline{\lambda}$  approaches one for prolate ellipsoids or rod-shaped cylinders and zero for oblate ellipsoids and plate-shaped cylinders. Second, even for particles of the same class (e.g., ellipsoids or cylinders), a single value of the shape parameter may be shared by particles with two different aspect ratios.<sup>44</sup> Third,  $\overline{H} \overline{\lambda}$  depends on the details of the particle size distribution, even if all particles have the same shape. Generally  $\overline{H} \overline{\lambda}$  increases as the dispersion of the size distribution increases.

A geometric shape parameter applicable to single-phase grain structures was proposed by DeHoff and determined for recrystallized aluminum structures by Craig.<sup>40</sup> This parameter is  $L_V^{\alpha\alpha} / (S_V^{\alpha\alpha})^2$ . Several additional shape parameters, similar in form to the preceding expression but appropriate to two-phase sintered structures, are developed in Chapter 3.

## Sintering

The voluminous nature of the literature on sintering attests to the controversies which the subject has engendered. These controversies are often kindled by the fact that various researchers in the field ascribe different meanings to the term "sintering." A simple definition which includes all of the various kinds of sintering is that provided by Rhines,<sup>46</sup> who defined sintering as "that process by which particles bond themselves into coherent bodies, usually, although not necessarily, under the influence of pressure and elevated temperature." This definition identifies geometrical change as the factor common to all types of sintering. An investigation of sintering in a particular system might consist of a description of the geometrical changes which take place and the identification of the atomic mechanisms which produce the observed changes. For a variety of reasons, studies of sintering mechanisms and studies of microstructural change are usually performed separately, so that a survey of sintering literature may be naturally divided into two parts. Since the research done for this dissertation was intended to be a geometric study, more emphasis will be placed on other geometric studies. A brief review of the mechanistic studies will be presented first.

### Sintering Mechanisms

Early investigators proposed that sintering was due to partial melting of the powders caused by high pressure or friction at contact points during pressing,<sup>47,48</sup> the lower melting point of small particles,<sup>49</sup> or recrystallization and phase changes.<sup>50</sup>

The nature of the sintered bond was explored by Sauerwald.<sup>51-54</sup> He proposed that atomic orbitals extended outward as temperature increased until atoms, which were initially separated, formed a bond. These new bonds increased the effective area of contact and thus the strength of the compact. Other workers established Sauerwald's hypothesis that the bonds which joined particles (or massive bodies) at contact points are the same as the interatomic bonding forces in a single crystal.<sup>55,56</sup>

Surface-tension forces, which were known to smooth the crevices in a rough surface,<sup>57</sup> were identified as the driving force for sintering by Jones<sup>56</sup> and Balke.<sup>58</sup> These surface-tension effects were observed to occur in short times at high temperatures. Since plastic flow and diffusion are promoted by high temperature, these two processes became popular candidates for the role of the mechanism of sintering. As other modes of material transport were identified, the list of possible sintering mechanisms grew to include volume diffusion, boundary diffusion, surface diffusion, evaporation-condensation, plastic flow, and viscous flow. Shaler and Wulff<sup>59</sup> argued that mechanisms could be differentiated on the basis of their ability to produce densification. Today, it is generally agreed that surface diffusion and evaporation-condensation processes can produce only a surface-smoothing effect, while the others listed above have the potential of producing densification.

Kuczynski<sup>60</sup> provided a simple set of rules for determining which mechanism is active in a particular sintering experiment. In his method, the growth of interparticle necks was observed for geometrically simple systems. The time dependence of neck radius was used to determine the mode of material transport. The appeal of this approach may be

demonstrated by the enthusiasm with which other workers attempted to apply Kuczynski's rules to sintering in a wide variety of systems.<sup>61-64</sup> The main drawback to this type of mechanism-determining study is the assumption that a three-dimensional network of particles may be adequately represented by a simple model consisting of a sphere on a plate,<sup>60,61</sup> twisted wires,<sup>65</sup> or spools of wires.<sup>62</sup> Because of the limitations of the geometrical models, experimentally observed densification rates on real sintered structures seldom agree with the model's predictions. In order to resolve these discrepancies, more recent sintering models have included the possibility of the simultaneous action of several mechanisms,<sup>66</sup> or of a change in the predominant mechanism as sintering occurs.<sup>67</sup>

#### Geometric Changes during Sintering

This discussion will be restricted to the sintering of systems consisting of one solid phase and the vapor phase.

The microstructural evolution which takes place during sintering has been described by Rhines<sup>68</sup> as a combination of four distinct and somewhat independent processes: densification, surface rounding, isolation of pores, and coarsening of the pore structure. All of these have the potential for reducing surface area.

Densification is the most easily observed process, since density measurements do not rely on microscopy techniques. It is not surprising, therefore, that density was the first geometric parameter to be carefully monitored for the various steps in a powder metallurgy process (by Wollaston<sup>69</sup> in 1829). During sintering, densification occurs by a reduction in the average center-to-center distance of neighboring

particles, and not by a decrease in the number of particle centers.<sup>68</sup> Density, or equivalently volume fraction of either solid or pore phase, is a convenient parameter for following the progress of a sintering experiment, and for comparison of the paths of microstructural change during sintering of different materials, and of different powder types and sizes. The variations of the other geometrical parameters at a constant volume fraction of porosity will be used for many comparisons of microstructures in this dissertation.

Surface rounding processes were observed by Desch<sup>57</sup> in 1923. In his experiments, small pieces of gold were melted and allowed to solidify in the shape of droplets. The initial freezing of the outer layer produced a thin solid skin, which then wrinkled to accommodate the shrinkage that occurred as the interior of the droplet froze. When the solid droplet was reheated below the melting point, the wrinkled surface was smoothed out until it had the same appearance as the surface of a liquid drop. Two geometric parameters underwent change in the experiment just described: the surface area of the system and gradients in surface curvature were both reduced. The concurrent reduction of surface area and curvature gradients is a characteristic of surface-tension-driven processes.\*

---

\*Changes in surface area and curvature gradients are not necessarily tied together for all geometric processes. For example, an initially flat sheet of paper may be crumpled to introduce curvature and curvature gradients, with no change in surface area.

The most striking change which a powder mass undergoes during sintering is the conversion of the initially multiply connected pore phase into a number of isolated, nearly spherical pores. The isolation of pores is accomplished by breaking the connections which join the pore phase. If all of the connections or channels leading to a particular region of porosity are severed, an isolated pore is produced. Rhines has shown<sup>68</sup> that the closing off of a channel usually reduces the genus of the pore-solid interface by one. Thus, the channel-closing and pore-isolation process may be followed by measuring the topological properties of a system as it sinters. Methods for the measurement of topological properties have been reported by Kronsbein et al.<sup>41</sup> Aigeltinger<sup>42</sup> measured the topological properties of sintered copper, and showed that most of the channel closure events occurred in a narrow volume fraction range, from 0.25 to 0.15.

Three sequential stages of the sintering process have been defined<sup>68</sup> in terms of the changes in topological state which the system experiences. These stages are:

First stage - Growth of interparticle welds; genus is constant or increases slightly as new contacts form.

Second stage - Genus decreases from initial value to zero; isolation of pores.

Third stage - Genus constant at zero; pore volume continues to decrease.

The final geometric process, coarsening of the pore structure, was first observed by Rhines et al.<sup>70</sup> Coarsening is a redistribution process in which the larger pores grow at the expense of the smaller ones. Densification continues to occur, however, so that coarsening of the porosity in sintered structures is characterized by an increase in

average pore size, and a decrease in pore volume fraction. In the work of Rhines et al.,<sup>70</sup> coarsening of isolated pores was observed during the latter stages of the sintering of copper powders. Coarsening of multiply connected pore phases has also been reported for the "inhibition sintering" of antimony powder,<sup>71</sup> and for sintering of compacted copper<sup>71</sup> and uranium dioxide<sup>72</sup> powders.

As a result of the action of the four geometric processes, the microstructural parameters vary with the volume fraction of porosity in a characteristic way for sintering. The variation of the topological properties, genus and number, has already been discussed.

The decrease in surface area which is observed in second stage sintering is a combined result of the densification, channel closure, and surface rounding processes.<sup>68</sup> As densification occurs, the length to diameter ratio of channels increases until a tubular channel becomes unstable.<sup>68</sup> As the unstable channel pinches shut, regions of high curvature are momentarily produced at the collapsed end of the channel. The curvature gradients thus produced are smoothed out and the surface area reduced by the action of the surface rounding processes.

DeHoff et al.<sup>71</sup> found that a straight line which extrapolated to the origin described the relationship between pore-solid surface area and volume fraction of porosity for second stage sintering of uncompact powders. The linear relationship was taken to indicate that a balance existed between surface rounding and densification processes. Support for this hypothesis was obtained from experiments in which powders were compacted prior to sintering. The additional surface area (per unit volume) produced by precompaction led to a dominance of surface rounding over densification processes. Surface area versus volume

fraction plots for compacted powders were curved lines lying above, and approaching asymptotically, the straight line characteristic of loose-stack (uncompacted) sintering. Schematic surface area versus volume fraction curves for different sintering conditions are shown in Figure 1-2. For uncompacted powders, the mean pore intercept ( $\bar{\lambda}^P = 4V_V^P/S_V^{\alpha P}$ ) is a constant; for compacted powders,  $\bar{\lambda}^P$  continually increases during sintering.

While direct measurements of curvature gradients have never been made, the variation of total curvature during sintering has been reported by Rhines et al.<sup>45</sup> and Rhines and Gregg.<sup>73</sup> For uncompacted spherical powders,  $M_V^{\alpha P}$  was found to be greater than zero during first stage sintering, pass through zero and go through a minimum during second stage, and approach zero during third stage sintering. Tuohig<sup>72</sup> reported total curvature values for pressed and sintered  $UO_2$  powders, but made no attempt to determine the effect of compaction pressure on the total curvature versus volume fraction relationships. One of the goals of this research was a study of the total curvature of compacted powder systems.

In addition to changes in the geometry of the pore network and the pore-solid interface, the grain structure is also subject to rearrangement during sintering. Since the grain structure usually depends on the geometry of the pore structure, it is convenient to discuss the evolution of grain structure in terms of the parallel development of the porosity as the system passes through the three stages of sintering. For the moment, assume that the unsintered powder consists of single grain particles. During the first stage of sintering, grain edges of the type  $\alpha\alpha P$  are generated by the formation of weld necks between the

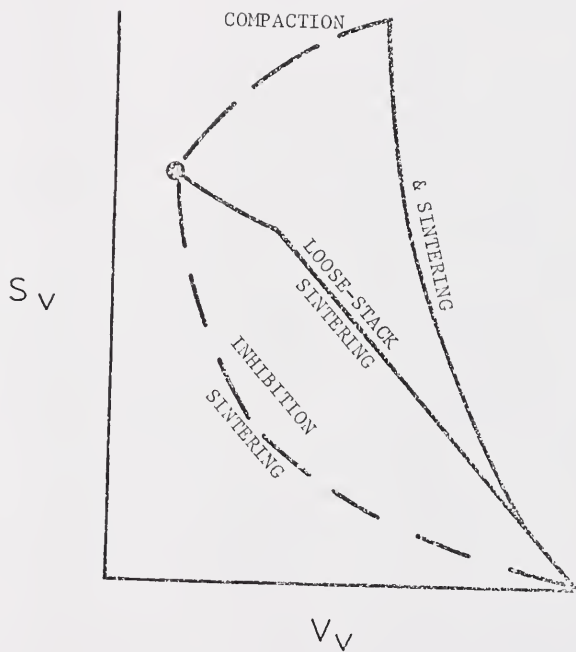


Figure 1-2. The effect of fabrication variables on the path of pore-solid surface area change.

individual particles. Each area of interface is bounded by an  $\alpha\alpha P$  triple line. As neck growth proceeds, the area of  $\alpha\alpha$  interface and the length of  $\alpha\alpha P$  line increases. The channel closure events which predominate in second stage sintering will usually result in the joining of three  $\alpha\alpha$  surfaces to form an  $\alpha\alpha\alpha$  triple line.

During the third stage of sintering, several distinct geometrical changes have been observed. In some studies,<sup>74-76</sup> the grain boundaries break away from the pores and coarsen at a much faster rate than the coarsening of the porosity. Both uniform grain growth<sup>42</sup> and exaggerated grain growth,<sup>75</sup> which resembles secondary recrystallization in fully dense material, have been reported. In other systems, usually oxide ceramics with additions of aliovalent cations as "sintering aids," grain growth does not occur<sup>77</sup> in third stage sintering. This stability of the grain structure has been attributed to the segregation of the impurities to the grain boundaries, which impedes boundary motion.<sup>78</sup>

### Sintering of $UO_2$

While  $UO_2$  has many characteristics in common with other sinterable powders, certain of its properties distinguish its sintering behavior from that of other materials.

The multiple oxidation states of  $UO_2$  lead to the existence of at least four stable oxides.<sup>79</sup> The composition  $UO_2$ , which corresponds to the stable oxide of lowest valence, crystallizes in the cubic fluorite structure. The cubic structure is thought to be stable for O/U ratios ranging from 2.00 to 2.25.<sup>79</sup> The stoichiometry of " $UO_2$ " affects the physical properties and the sintering behavior. For example, Williams et al.<sup>80</sup> sintered material with O/U ratios ranging from 2.00 to 2.18 and

found a large increase in densification rate as O/U was increased from 2.00 to 2.02. Further increase in O/U ratios produced little increase in rate, however. Williams et al.<sup>80</sup> attributed the observed behavior to increased cation mobility caused by a larger number of lattice defects. Stoichiometry may affect the path of microstructural change for sintering of  $UO_2$ , but no investigation of a possible effect is known to the author.

The response of a powder to mechanical stress also influences the sintering behavior. At ambient temperatures,  $UO_2$  is very nearly a perfect elastic solid.<sup>81</sup> Thus, cold compaction will not plastically deform the individual particles. At temperatures above about 1300°C,  $UO_2$  becomes capable of plastic flow,<sup>82</sup> so that at usual sintering temperatures, or during hot pressing, plastic flow may be an active densification mechanism.

Other properties which may affect the sintering of  $UO_2$  are its high vapor pressure ( $10^{-4}$  Torr at 1700°C),<sup>83</sup> which promotes surface rounding processes by the vapor transport mechanism, and the tendency of  $UO_2$  powder to agglomeration and aggregation,<sup>83</sup> which may cause defects in either pressed or fired material.

#### The Electrical Properties of Heterogeneous Structures

Consider a unit cube of a homogeneous, isotropic substance with electrical contacts attached to two opposite faces. If a potential is applied across the electrodes, current will flow. By measuring this current, the electrical conductivity can be calculated. If a small volume of material is removed from the interior of the cube and is

replaced by an equal volume of a substance with a different electrical conductivity, the effective conductivity of the unit cube will be altered. If the second substance has a higher conductivity than the first, the conductivity will be increased. If successively larger amounts of the second material are added, a larger increase in the conductivity of the mixture will be observed. This type of reasoning leads to the intuitive notion that the conductivity of a heterogeneous system is a monotonic function of the conductivities and volume fractions of the phases which make up the structure. That this notion is misleading is demonstrated in Figure 1-3. Assume that the two phases present are phase A, a substance with a small but finite conductivity, and phase B, a high conductivity material. The two structures shown have equal volumes of B, but the structure with the continuous path of high conductivity material between the electrodes clearly has the higher effective conductivity. This demonstration suggests that the conductivity of heterogeneous systems is a complicated function of the distribution of phases in a structure. Still, it is possible, at least in principle, to calculate the conductivity of an arbitrary heterogeneous system in terms of the conductivities and the spatial distributions of the phases that make up the structure. The result is obtained by simultaneous solution of the Laplace steady-state heat-flow equation,<sup>84</sup> and the Gauss electric field equation.<sup>85</sup> Because the mathematical methods are entirely analogous, the same treatments can be used to obtain the electrical conductivity, static dielectric constant, magnetic permeability, thermal conductivity, and diffusion coefficient of heterogeneous systems.

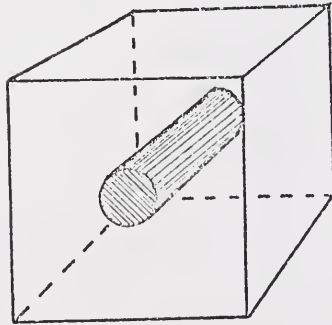
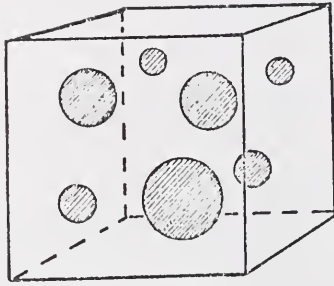


Figure 1-3. Unit cubes of heterogeneous structures showing (a) particles dispersed in a matrix, and (b) a single particle extending the length of the cube.

If an alternating electric field is applied to a heterogeneous structure, dielectric relaxation may occur. When the observed dispersions are due to polarization of the internal interfaces, the relaxation times may be calculated if the spatial distribution of the interfaces is known.

The methods outlined above lead to mathematical forms which, for the general case, require complete information about the spatial distribution of phases in the structure. Even if this information is available, the mathematical expressions soon become intractable. As a result, theories of the electrical properties of heterogeneous structures employ approximate methods. These theories may be conveniently divided into two broad classes: (1) those theories in which a specific geometric model of the structure is assumed, and (2) theories in which no model is assumed. Examples of the first class far outnumber the second and will be reviewed first.

The initial analysis of the dielectric constant of a heterogeneous structure was done by Maxwell<sup>1</sup> in 1873. He obtained an expression for the dielectric constant of a system consisting of  $n$  parallel slabs of material, each with a different dielectric constant. A two-phase layered dielectric is a special case of Maxwell's model. In 1892 Lord Rayleigh<sup>86</sup> extended Maxwell's analysis to additional two-phase geometries. He presented solutions for the dielectric constant of systems of spheres on a cubic lattice and of parallel arrays of cylinders at right angles to the field direction. These solutions included the effect of electrostatic interaction between second phase particles. Wagner<sup>2</sup> neglected electrostatic interaction and obtained the dielectric constant of a random array of spheres. The assumption of no electrostatic

interaction is valid if the interparticle distance is large compared to particle radius. In 1925, Fricke<sup>87</sup> attacked the problem of electrostatic interaction by adding to the original field a value obtained by averaging the effect of all the charges on suspended particles over the sample volume. With this technique, Fricke calculated the conductivity of suspensions of ellipsoids of revolution or spheroids.<sup>87</sup> These solutions were extremely cumbersome but gave good agreement with experimental measurements on several systems. Fricke's experimental results will be discussed in the next section. Sillars<sup>3</sup> also examined suspensions of spheroids. He followed the same method as Wagner, i.e., assumed a dilute suspension, and made the further assumption that the suspending medium was a perfect dielectric (conductivity = 0). Sillars' equations treat the dielectric relaxation problem as well as the static case, but are valid only for low volume fractions of the dispersed phase.

Bruggeman<sup>88</sup> offered another approach to the problem of large volume fractions. He differentiated an approximate solution for the conductivity of suspensions of spheres and assumed that the resulting differential equation was valid for all volume fractions. By an iterative integration process, he was able to calculate the dielectric constant over the full volume fraction range. In another publication, Bruggeman presented formulae for the dielectric constant of single phase polycrystals in which the single crystal properties are anisotropic.<sup>89</sup>

Nearly thirty years after his initial publications, Fricke<sup>90</sup> extended his average field approach to suspensions of triaxial ellipsoids. This publication is noteworthy for several reasons. First, with the exception of multiply connected structures, triaxial ellipsoids may

be used to model most structures in real materials. Second, Fricke gives complete calculations of static dielectric constants and relaxation times for the full volume fraction range and for parallel or random orientation of the ellipsoids. Thus the solutions for a broad range of practical problems is compiled in one source. Third, the dielectric dispersion equations predict three relaxation times for randomly oriented ellipsoids. This result suggests that more complex geometries will have very complicated relaxation behavior.

Recently, interest in the microstructure of fiber-reinforced composite materials has led to the use of electrical resistivity measurements as a means of characterizing the composites. Several investigators<sup>91-93</sup> have used an electrical analog technique in which the composite is modeled as a group of resistors. Various series and parallel combinations of the resistors are used to simulate fiber branching, nonparallel fibers and fiber termination. In most of these models,<sup>91,92</sup> the assumption is made that no field perturbations occur when second phase particles are embedded in a matrix with a different electrical conductivity. This simplifying assumption makes the electrical analog models much less rigorous than any of the solutions derived from the Maxwell equations. Recently, Watson et al.<sup>93</sup> partially overcame this objection by using Rayleigh's cylinder equation to calculate the resistance of some of the circuit elements in their model.

The results of these geometrical modeling studies indicate that the electrical properties of heterogeneous structures depend on the amount of second phase and on particle shape but not on particle size or details of particle size distribution, as long as shape is independent of size and the particles are small compared to the specimen size. The

best agreement with experimental results is obtained with the more complicated formulae, e.g., those of Fricke.<sup>90</sup> The simpler mathematical expressions, such as those of Wagner,<sup>2</sup> are only valid for a restricted set of geometries. None of the models treat the case of multiply connected structures.

The limitations of the geometrical models have led several workers to devise solutions for the electrical properties (of heterogeneous mixtures) in which no model is assumed. The results of such studies should thus apply to a wide range of structures.

Brown,<sup>94</sup> for example, calculated the dielectric constant of a two-phase system by writing the polarization vectors as a power series in the dielectric constants of the two phases, and throwing away higher order terms. Herring<sup>95</sup> used a similar Fourier series expansion technique and applied it to several electrical properties. He restricted his analysis to small fluctuations in the electrical properties, but found that the formulae often gave useful approximations for large fluctuations. For a porous structure, however, in which the conductivity of one phase is zero, Herring's equation predicts a linear relation between conductivity and volume fraction, and negative conductivities at high pore volumes.

Hashin and Shtrikman<sup>96</sup> used a variational method to obtain upper and lower bounds for the magnetic permeability of multiphase materials. They found that the bounds gave a good estimate of the effective permeability only for relatively small permeability variations between the phases.

The results of the theories of the electrical properties of heterogeneous systems can be summarized as follows:

1. Dispersed phase systems may be effectively described by any one of several geometrical model solutions based on the Maxwell Field Equations.
2. Other approximate methods may be used for any system geometry if the spatial variations in electrical properties are small enough.
3. All solutions depend on the details of the spatial distribution of the several phases.
4. No solution exists for a general structure, containing multiply connected and dispersed elements, if large property fluctuations are present.

The sintered structures studied in this research had multiply connected pore and solid phases, and a connected grain boundary network. Fluctuations in electrical conductivity were discontinuous and large. For a system this complicated, direct experimental observation is the only means of correlating microstructure with electrical properties.

#### Experimental Studies of the Electrical Properties of Heterogeneous Systems

The development of theoretical treatments of the electrical properties of heterogeneous structures was accompanied by a number of experimental studies designed to test the validity of the various theories. Millikan,<sup>97</sup> for example, found that Rayleigh's cubical array equation<sup>86</sup> accurately described the dielectric constant of random dispersions of water in benzol-chloroform. Similar experiments were performed by Sillars<sup>3</sup> on emulsions of water in paraffin and by Dryden and Meakins<sup>98</sup> on emulsions of water in lanolin.

The use of electrical measurements as a probe with which to measure structure was first proposed by Fricke<sup>87</sup> in 1924. The utility of this technique was demonstrated in subsequent publications. Fricke and Morse used conductivity measurements to determine the relative volumes in butterfat-milk mixtures<sup>99</sup> and capacity measurements to estimate the membrane thickness of the red blood cell.<sup>100</sup> Fricke's 1925 value of  $33 \text{ \AA}$  is remarkably close to recent values determined by electron microscopy.<sup>101</sup> Other examples of structural determinations by means of electrical measurements may be found in the literature of the biological sciences, and have been reviewed by Cole.<sup>102</sup>

Electrical measurements have also been used to determine structure in the materials field. In metals, resistivity measurements have been used to estimate dislocation density by Blewitt *et al.*<sup>103</sup> and Clarebrough *et al.*,<sup>104</sup> and to monitor the recovery of lattice defects in cold worked metals by Sharp *et al.*<sup>105</sup>

Several studies of the structures produced by varying heat treatments of glass have used dielectric measurements to detect the presence of heterogeneous structures. Owen<sup>106</sup> interpreted the loss behavior of  $\text{CaO-B}_2\text{O}_3\text{-Al}_2\text{O}_3$  glasses as an effect of a Maxwell-Wagner dispersion. Charles<sup>107</sup> examined a series of lithia-silica glasses and concluded that the observed dielectric loss behavior was an effect of the heterogeneous (two-phase) nature of the liquid from which the glass was generated. Charles corroborated the dielectric behavior with replica electron micrographs. Kinser and Hench<sup>108</sup> examined the effect of thermal history on structure, also in the lithia-silica system. In contrast to Charles, they observed no loss peaks in quenched material, but noted relaxation effects after heat treatment at  $500^\circ\text{C}$ . The loss peaks, ascribed to the

presence of a metastable crystalline lithium metasilicate phase, disappeared after prolonged heat treatment as the metasilicate dissolved and was replaced by the equilibrium disilicate phase. Replica and thin film<sup>109</sup> electron microscopy and x-ray diffraction studies were used to support the evidence of the dielectric studies. In a recent review of the electrical properties of glasses, Hench and Schaeke<sup>110</sup> conclude that the use of a heterogeneous dielectric model to explain dielectric losses in glass must be justified by independent methods of structure analysis in order to insure that the observed losses are due to a heterogeneous mechanism and not an atomistic one.

The electrical conductivities of two-phase systems in which the high-conductivity phase is dispersed when present in low volume fractions, but becomes multiply connected at high volume fractions, have been investigated by Blakely and White<sup>111</sup> and Gurland.<sup>28</sup> The electrical conductivities of sintered silver-alumina bodies showed a marked increase for silver contents in excess of  $\sim 25$  percent,<sup>111</sup> presumably because the silver phase became interconnected for long distances through the structure as the volume fraction exceeded a critical value. A sharp transition in electrical conductivity was observed by Gurland<sup>28</sup> for specimens consisting of spheres of silver embedded in a bakelite matrix. In the latter study, the critical volume fraction was  $\sim 0.37$ . Results of this nature are usually explained in terms of percolation probability theory,<sup>28,112,113</sup> which predicts that long-range interconnection of a particulate phase will occur if the average number of contacts between particles of the second phase exceeds a critical value. The variation in different systems of the volume fraction at which the second phase becomes interconnected is apparently due to the variation in particle shape and size distribution.

## The Electrical Properties of Porous Materials

Because residual porosity is usually present in articles fabricated from powders, much attention has been focused on porosity as a special kind of second phase. The effect of porosity on conductivity and static dielectric constant can often be described using one of the heterogeneous dielectric theories. Because the pore phase is an insulator, it will not give rise to conduction losses and the attendant dielectric relaxation phenomena. An important exception occurs when a pore network is exposed to a gas which will adsorb to the surface of the pores. In this case, large dielectric losses may result at certain combinations of frequency and temperature.

Before about 1950, many studies of sintering used electrical conductivity measurements as an indicator of the degree to which a pressed or sintered compact had been consolidated into a coherent mass.

The early work in this area is typified by the paper of Streintz.<sup>114</sup> The experimental scatter found in his results may have been caused by density gradients in his samples.<sup>115</sup> Later, Kantorowicz<sup>116</sup> reported the curious result that the electrical conductivity of a tungsten powder pressing decreased if it was pressed repeatedly to a given pressure. This behavior can be explained if the continued reapplications of pressure had the effect of fracturing the powder particles.

It has already been remarked that density or pore volume fraction is a desirable choice as an independent plotting variable. Since many of the earlier works present data in the forms of plots of physical properties against sintering temperature, without giving density values, it is difficult to construct plots of physical properties against pore

volume fraction. The work of Grube and Schlect<sup>117</sup> is an interesting exception. Figure 1-4, taken from their work, presents electrical conductivity values of sintered nickel powder as a function of volume fraction of porosity. At high pore volumes, data points for three pressures of cold compaction lie on three separate curves. These curves converge to form a single trace as densification occurs. Similar behavior has been observed for the fracture strength of  $UO_2$  powder.<sup>118</sup> The latter effect was explained by noting that green density increased and average interparticle distance decreased as the powders were pressed. When sintered to equivalent densities, specimens pressed at lower pressures have more well-developed necks and larger interparticle contact area. The effect of contact area is a likely explanation for the data of Grube and Schlect.<sup>117</sup>

Rhines and Colton<sup>119</sup> used electrical conductivity measurements to study the homogenization of compacts pressed from mixtures of elemental copper and nickel powders. They do not report the density changes which occur during the homogenization treatments but do show that conductivity changes due to densification are far outweighed by the effects of homogenization.

Other factors which affect the electrical conductivity of sintered materials include sintering atmosphere<sup>120</sup> and purity of the powder. Since the observed electrical behavior is the sum of contributions from several sources, care must be exercised in the interpretations of conductivity data of sintered structures. Independent confirmation of the mechanisms responsible for electrical conductivity must be sought, just as in the case of dielectric relaxation effects in heterogeneous systems.

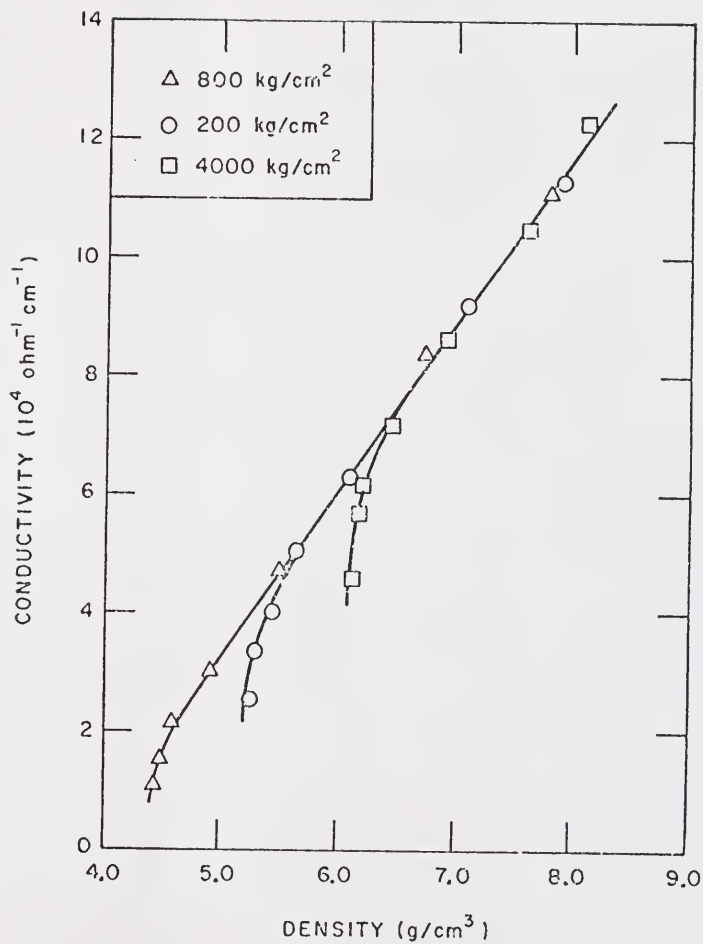


Figure 1-4. Electrical conductivity versus density for sintered nickel. This graph was constructed from the data of Grube and Schlect.<sup>117</sup>

A large body of literature exists on the dielectric relaxation effects of gases adsorbed to the surfaces of porous adsorbents.<sup>121</sup> In most cases, the aim of these studies has been to analyze the dielectric properties of the adsorbate. Often, however, the results contain information about the structure of the adsorbent surface, the degree of surface coverage by adsorbate, or the kinetics of the adsorption process. For example, Ebert and Langhammer<sup>122</sup> and Baldwin and Morrow<sup>123</sup> report frequency and temperature dependent maxima in plots of loss dielectric constant against the amount of water vapor adsorbed on the surface of  $\gamma$ -alumina. Hench<sup>124</sup> reported the change in A.C. conductivity and loss tangent of reactive MgO powders exposed to air of 85 percent relative humidity. Equilibration of the water vapor adsorption process had not occurred after 140 hours of exposure.

### The Electrical Properties of UO<sub>2</sub>

Electrical Conductivity. In common with several other oxide ceramics, the electrical conductivity of UO<sub>2</sub> may be due to either ionic transport or extrinsic or intrinsic semiconduction mechanisms, depending on the temperature of measurement. At room temperature, conductivity values ranging from  $3 \times 10^{-1}$  to  $4 \times 10^{-8}$  ( $\Omega \text{ cm}$ )<sup>-1</sup> have been reported.<sup>125</sup> These values represent extrinsic semiconduction and are markedly influenced by variations in the composition, purity, apparent density, and crystalline perfection of the samples examined.

Hartmann,<sup>126</sup> by using Hall effect measurements, was the first to identify  $UO_2$  as a metal deficit or p-type semiconductor. Meyer<sup>127</sup> reported both p- and n-type behavior. However, subsequent investigations of the U-O phase diagram have failed to confirm the existence of substoichiometric  $UO_2$ ,<sup>128</sup> throwing Meyer's claim into doubt. When n-type semiconduction is observed in " $UO_2$ ," a close examination will reveal either a low purity specimen or the existence of a substoichiometric phase of higher oxidation state, e.g.,  $U_4O_{9-y}$ .<sup>128</sup>

The effect of metallic impurities on the conductivity of  $UO_2$  is consistent with its description as a p-type semiconductor, i.e., lower valence cationic impurities such as  $Ca^{2+}$  increase the conductivity by making  $UO_2$  more p-type.<sup>128</sup> Higher valence cations such as  $Mo^{6+}$  usually do not decrease the p-type character, however, perhaps because they are reduced to the +4 state, accompanied by the formation of  $U^{5+}$  cations.<sup>128</sup>

A somewhat different analysis of the conductivity mechanism in  $UO_2$  is that provided by Aronson and coworkers,<sup>129-131</sup> who measured the electrical conductivity of high density, large grain size, nonstoichiometric plates of  $UO_2$  at temperatures ranging from 500°C to 1150°C. These temperatures are below the range where ionic transport would be expected to contribute to electrical conduction. The observed dependence of conductivity on temperature and O/U ratio is in agreement with a proposed<sup>129</sup> description of nonstoichiometry in  $UO_2$ . The description assumes the existence of  $U^{4+}$  and  $U^{5+}$  ions on lattice sites, and lattice and interstitial  $O^{2-}$  ions. Conduction occurs by a "hopping" mechanism, in which holes are localized at the  $U^{5+}$  sites, but have some freedom to jump to an adjacent  $U^{4+}$  site, thus transferring charge. In a series of papers by Devreese and coworkers,<sup>132-134</sup> the current carriers are identified

as small polarons, which, in the present case, are holes with an associated polarization of the nearby ions.<sup>135</sup> While experimental evidence cited by Devreese and coworkers<sup>132-134</sup> strongly suggests that small polarons are responsible for electrical conduction in nearly stoichiometric  $UO_2$ , the evidence does not exclude the possibility that  $UO_2$  is a band-type semiconductor.

The effect of microstructure on the electrical properties of  $UO_2$  is not well known, probably because the effects of stoichiometry and purity usually dominate the electrical behavior so that the microstructure plays only a secondary role in determining the electrical properties. As a consequence, only a few published works concerning the microstructural effects on the electrical conductivity of  $UO_2$  can be found, and the results of these are often contradictory.

For high density material most workers observe an increase in conductivity with increasing grain size,<sup>136</sup> although a decrease in conductivity with increasing grain size<sup>137</sup> and no effect of grain size on conductivity<sup>138</sup> have also been reported.

For studies in which the effects of stoichiometry are investigated, it is usual to multiply the measured conductivities of porous specimens by a "correction factor," equal to

$$1 + \frac{V_V^P}{[1 - (V_V^P)^{2/3}]},$$

which gives the conductivity that would be measured if the specimens were fully dense.<sup>125</sup> The accuracy and range of applicability of this correction factor has not been established. Willardson et al.<sup>125</sup> caution that the correction factor is not appropriate if grain size variations accompany the density differences among the specimens which are to be compared.

Dielectric properties. In a series of papers, M. Freymann, R. Freymann, and their coworkers,<sup>139-141</sup> give the results of investigations into the dielectric properties of several of the oxides of uranium. These studies were summarized by Freymann et al.,<sup>139</sup> who report for sintered samples of  $UO_2$ : 1) the existence of a Debye-type relaxation peak at low temperatures (150°K at 16 kHz); 2) large losses at room temperature; and 3) thermal hysteresis of the room temperature  $\epsilon''$  value. The low temperature Debye peak was ascribed to the relaxation of the dipoles associated with crystalline defects, i.e., vacancies or impurity ions. The high  $\epsilon''$  values at room temperature correspond to D.C. conduction losses which become important when the free carriers become thermally activated. The hysteresis effect was probably due to the condensation and evaporation of traces of water vapor.

Wachtman,<sup>142</sup> working with  $ThO_2$ , found that the presence of 1.5 mole percent CaO did produce both mechanical and dielectric relaxation at temperatures in excess of 500°K and frequencies in the kilohertz range. The relaxation peaks were found to be due to the interchange of oxygen ions and oxygen vacancies.

More recently, Tateno and Naito,<sup>143</sup> have measured the dielectric constant of  $\text{UO}_2$  as a function of temperature and frequency. The extremely large values of the dielectric constant ( $10^5$  at 20 kHz and room temperature) reported by these workers are probably a result of the specimen preparation technique or of the presence of adsorbed water.

CHAPTER II  
EXPERIMENTAL PROCEDURE

Material Characterization

The powders used in this investigation were supplied by the U.S. Atomic Energy Commission. The material originated at the Mallinkrodt Chemical Works where it was precipitated from solution as ammonium diruranate, calcined to  $UO_3$ , reduced to  $UO_2$ , arc fused and crushed. A chemical analysis of the powder is presented in Table II-1.

Preliminary attempts to sinter the as-received powder met with limited success, even at temperatures in excess of  $2200^{\circ}C$ . Therefore, a program was undertaken to produce well-characterized powders of reasonable sinterability. Parts of this program have been previously described by Tuohig,<sup>72</sup> but are included in the following summary for the sake of completeness.

About 80 percent of the as-received material passed through a 270-mesh sieve (U.S. Standard Series) but was retained on a 325-mesh sieve. Because of its abundance, this powder, designated powder lot 3, was used as a primary source of material for most of the specimens described in this dissertation. A scanning electron micrograph of this material, Figure 2-1b, shows the characteristic granular equiaxed appearance of the particles. Figure 2-1b also shows a number of particles in the 20 to 40  $\mu m$  size range, and many small (1  $\mu m$  and under) particles

Table II-1

Analysis of Impurities in the  $UO_2$  Powders

Carbon	57 ppm
Aluminum	33
Boron	<0.1
Cadmium	<1.0
Chromium	<5.0
Iron	70
Magnesium	<3.0
Nickel	<3.0
Silicon	33

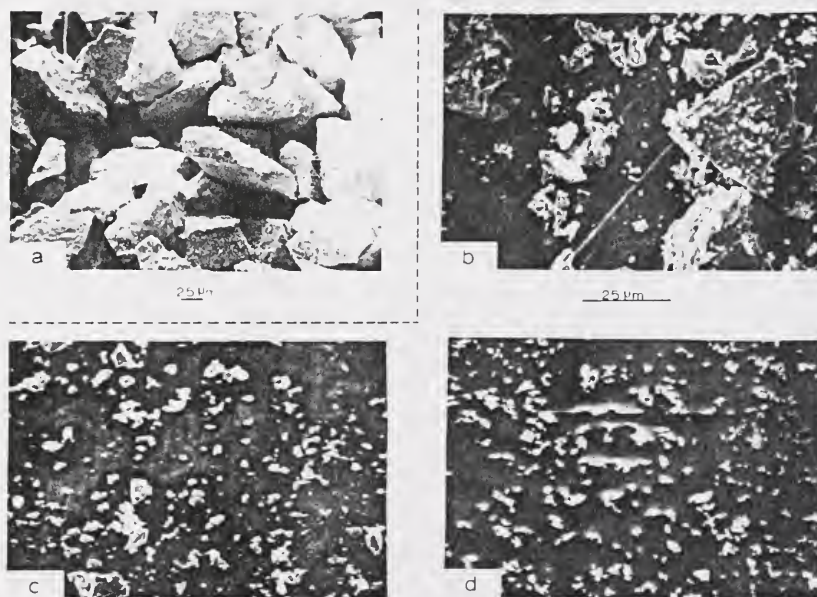


Figure 2-1. Scanning electron micrographs of powders used in this study: (a) lot 6; (b) lot 3; (c) lot 2; and (d) lot 1.

on the surfaces of the larger ones. The presence of these particles, which are small enough to pass through the 45- $\mu\text{m}$  openings in a 325-mesh sieve, is attributed to the tendency of  $\text{UO}_2$  to agglomerate. The adherence of fine particles to larger ones and to each other is a general feature of all powders used in this research.

Powder lot 3 was found to be easily sinterable to densities in excess of 80 percent and was used to make some of the specimens described in the later sections of this dissertation. In addition, this powder was used as the starting material for a ball-milled and a water-settled powder.

Ball milling was performed in a rubber-lined U.S. Stoneware mill with Burundum\* cylinders. The powder was wet milled for 16 hours. The appearance of this powder, called powder lot 2 and shown in Figure 2-1c, differs from that of the source material, in that the average particle size is smaller, and the distribution of particle size is somewhat broader. The estimated average caliper diameter for this material is  $\sim 5 \mu\text{m}$ .

A third powder was obtained by using a sedimentation technique to remove the larger particles from ball milled powder. The ball milled powder was first dispersed in water by adding about 20 ppm of a pigment stabilizer, polyoxyethylene sorbitan monolaurate, to break up the agglomerates. This slurry was mixed in a blender, poured into a 90-cm

---

\*Carborundum Company

column and allowed to stand for 80 minutes. After this time, the supernatant was decanted, and the fine powder recovered from this liquid by evaporation. The settling time and height were calculated from Stokes' Law to yield a maximum equivalent spherical diameter of 5  $\mu\text{m}$ . The resulting settled powder, called powder lot 1, is shown in Figure 2-1d.

In addition to these powders, a number of other powder sizes were used for specialized purposes in the course of this research. Of these, the most important were:

- (1) a (-270 +325) sieve cut which was a nearly monosized fraction. This powder is designated as powder lot 5.
- (2) powder lot 4, a (-325) fraction sieved from the same starting material as powder lot 4.

These powders were part of a special lot from which the electrical properties samples were made. In order to minimize the pickup of impurities, these powders were not milled or settled during preparation. Powder lot 4 was similar to powder lot 3 in particle size and sintering characteristics. Powder lot 5 had a somewhat larger particle size than Powder lot 4. A (-100 +200) sieve fraction, powder lot 6, shown in Figure 2-1a, was used for some experiments. This extremely coarse powder could be successfully hot pressed at temperatures above 1500°C and at a pressure of 5000 psi.

All of these powders were stored in closed containers prior to use.

Since, as discussed in Chapter I, the electrical properties of  $\text{UO}_2$  are extremely sensitive to the O/U ratio, both the powder and fired specimens were further characterized by a stoichiometry determination.

To do this, the results of precision lattice parameter measurements were compared with data of Schaner<sup>144</sup>, who measured the lattice constants of samples of known O/U ratio.

The x-ray diffraction technique employed either a Norelco diffractometer scanned at 0.5 degrees  $2\theta$  per minute or a G.E. diffractometer at 0.2 degrees  $2\theta$  per minute. The  $2\theta$  range from  $70^\circ$  to  $145^\circ$  was examined with filtered copper  $K\alpha$  radiation from a fine-focus tube operated at 35 KV and 15 mA. Annealed 99.999 percent gold fillings were used as an internal standard. Mechanical backlash was eliminated by averaging the peak positions obtained on two runs, increasing  $2\theta$  on one run and decreasing it on the other. These data were fitted by Cohen's method of least squares;<sup>145</sup> the analysis was performed with a computer program supplied by Gvildys of Argonne National Laboratory.<sup>146</sup>

Vacuum hot pressing is reported to have a negligible effect on the O/U ratio, while heating in hydrogen is an effective way of reducing  $UO_{2+x}$  to a composition which is usually termed "nearly stoichiometric."<sup>147</sup> Lattice constant measurements performed as part of the present study indicated that the O/U ratio for the as-received powders and for vacuum-hot-pressed specimens was 2.06. The O/U ratio was reduced to  $<2.005$  by sintering in  $H_2$  at temperatures of 1600 to 1700°C for times of one hour or more. Annealing times at 1600°C in  $H_2$  of up to 20 hours were required to obtain an equivalent reduction of vacuum-hot-pressed specimens.

Low-temperature gas-adsorption surface-area determinations<sup>148</sup> were used to further characterize the  $UO_2$  powders. Results of these experiments are presented in Table II-2.

Table II-2  
Gas-adsorption Surface-area Determinations  
of Three  $\text{UO}_2$  Powder Lots

Powder Lot	Surface Area
1	$1.54 \text{ m}^2/\text{g}$
2	0.87
3	0.1-0.3

## Sample Preparation

### Conventional Sintering

Throughout this dissertation the term "conventional sintering" is used to denote the sintering of loose stacks of powder or of powder compacts. Conventional sintering is distinguished from hot pressing or pressure sintering in which a load is applied to the specimen at temperature.

Because of the slow rate of sintering at experimentally accessible sintering temperatures, loose-stack sintering produced only a limited range of microstructures. As a result, almost all of the conventionally sintered specimens were produced by compacting the powder into pellets prior to sintering.

Powders were mixed with approximately 2 weight percent polyethylene glycol\* as a binder and lubricant prior to pressing into pellets in a specially designed die mounted in a double acting Haller die table. The die had a nominal diameter of 0.689 inches and a taper of 8 minutes per inch. This equipment was capable of producing 0.75 inch tall pellets which were free of density gradients. The useful operating pressure range was from 10,000 psi to 80,000 psi. Lower pressures produced fragile specimens, which usually crumbled when ejected from the die. Higher pressures often yielded samples with laminar separations, caused by excessive die wall friction during ejection.

---

\*Union Carbide, Carbowax 4000.

A resistance-heated alumina muffle furnace\* was used for sintering. The pellets were heated to approximately 200°C for one hour in a flowing carbon dioxide atmosphere to volatilize the binder. The muffle was then vacuum purged and filled with hydrogen before raising the furnace to the sintering temperature at  $\sim 10^\circ\text{C}/\text{minute}$ . A flowing hydrogen atmosphere was used for all sintering runs. Sintering temperature was limited to approximately 1800°C by the alumina muffle. The reported sintering times include only the time at the sintering temperature; the heating and cooling periods are not included.

### Hot Pressing

Hot pressing was used to expand the attainable range of microstructures for these powders and to evaluate the effect on the path of microstructural change of applying pressure at high temperature.

Hot pressing was conducted in an induction heated vacuum hot press. The powder was loaded into a die assembly shown schematically in Figure 2-2. The main die cavity served as a susceptor and was made from graphite. The liner was either boron nitride or graphite lined with boron-nitride-sprayed molybdenum sheet. The graphite punches were capped with either boron nitride disks or with boron-nitride-sprayed molybdenum.

Once in the die the powder was compacted to the pressure (1000, 3000, or 5000 psi) that would later be applied at the hot pressing temperature. This precompaction step was introduced to minimize the galling of the die wall caused by large ram travels at high temperature, and to

---

\*Astro Industries, Model 1000B.

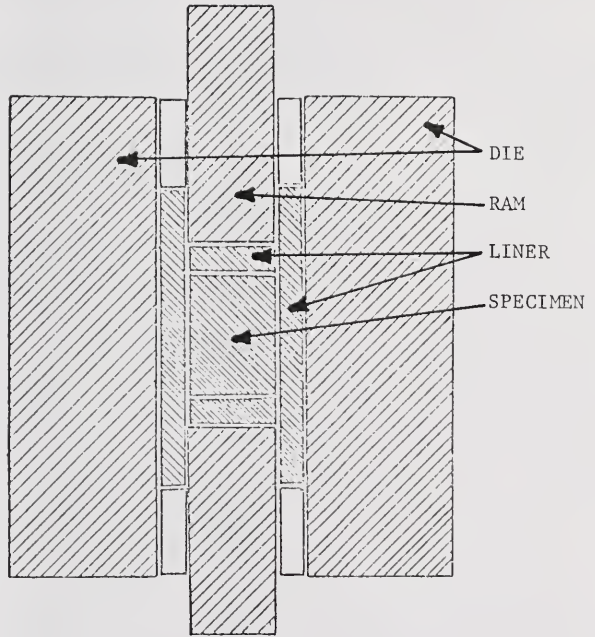


Figure 2-2. Schematic cross section of the die used for hot pressing.

permit a check of the alignment of the components in the load train. Since quantitative microstructural analysis was performed on unfired pellets in the course of this research, the precompacted pellets had well-characterized microstructures which served as the starting point for microstructural evolution during hot pressing.

After the preload was released, the chamber was evacuated to a pressure of approximately  $1 \times 10^{-5}$  Torr, and the die assembly was heated to the desired temperature, where the load on the sample was reapplied. Temperatures between  $1150^{\circ}\text{C}$  and  $2000^{\circ}\text{C}$  were used for times ranging from 15 minutes to 2 hours. The load was then released and the assembly allowed to cool under vacuum.

The load on the sample was kept constant to within  $\pm 10$  psi by a modification of the hydraulic system of the hot press. A fluid-filled reservoir connected, through an isolation valve, to the main hydraulic cylinder, was pressurized with a two-stage-regulated gas supply. The regulated pressure was equal to the pressure on the hydraulic ram, and could be carefully controlled. The pressure was monitored with a gauge with scale divisions of 1 psi.

### Quantitative Metallography

Specimens for metallographic examination were cut in the planned plane of observation, vacuum impregnated with Buehler epoxy resin, and mounted in the same material. The mounts were ground on silicon carbide metallographic papers through 600 grit. Fine polishing on a rotating bronze lap was performed with Linde 0.3- and  $0.05\text{-}\mu\text{m}$  aluminum-oxide abrasives. The lap was covered with a nylon cloth for the  $0.3\text{-}\mu\text{m}$

abrasive and with Buehler microcloth for the 0.05- $\mu\text{m}$  abrasive. The polishing media were suspended in a 2 percent chromic acid solution. This procedure gave a minimum of edge rounding. Grain "pullout" problems were minimized by the epoxy impregnation technique. If substantial pullout occurred even with impregnation, the mount was reimpregnated and repolished. Pullout was most commonly observed for very low density samples.

A solution of 90 percent hydrogen peroxide (stabilized 30 percent) and 10 percent sulfuric acid was used as a grain boundary etchant. Best results were obtained by swabbing the specimen for about 45 seconds, followed by immersion for one to two minutes. In all cases, the quantitative measurements on the pore-solid interface were performed prior to etching.

The metallographic preparation was checked by performing a point count on the pore phase with the Quantimet 720 Image Analyzing Computer. If the density calculated from the point count was within 2.5 percent of the density as determined by the Archimedes immersion principle, the polish was accepted and the other stereological measurements were performed. If the density determined by the point count was outside the 2.5 percent limit, the specimen was reimpregnated with epoxy and repolished.

The Quantimet, interfaced with a metallograph,\* provided one of the two major methods of structure characterization used in this research. This instrument was used for the point count, the line intercept count on the pore-solid interface, and the area tangent count.

---

\*Bausch and Lomb, Inc., Research Metallograph.

Manual counting, the other major characterization method, was used for the grain boundary intercept, grain triple junction and inflection point counts. Grain boundary intercepts were measured with a ruled reticule in the eyepiece of the metallograph; triple junctions and inflection points were counted on large photographic prints of the microstructure.

### Electrical Measurements

The powder preparation and stoichiometry determination methods used for the electrical properties samples have already been discussed. After sintering, these samples were centerless ground and sliced. A disk about 5 mm thick and 15 mm in diameter taken from the center of the specimen was used for electrical measurements. An adjacent slice was mounted and prepared for metallographic examination. Electrodes were attached by lightly clamping each sample in an aluminum holder which masked all but a  $1\text{-cm}^2$  area of each sample face. A thin (approximately  $500 \text{ \AA}$ ) layer of gold was then vapor deposited on the exposed areas. The samples were stored in a vacuum dessicator until used.

The specimen measuring chamber,\* shown in Figure 2-3, held the samples in place by pressing spring-loaded gold-palladium buttons against the sample electrodes. The specimen chamber incorporated coaxially shielded platinum conductors and high resistivity ( $10^{14}$  ohm-cm) insulation. The chamber could be sealed, and evacuated or filled with various atmospheres. In the present study, dry, high-purity helium and air saturated with water vapor were used in the specimen chamber.

---

\*Designed by D. Kinser and D. Jenkins.

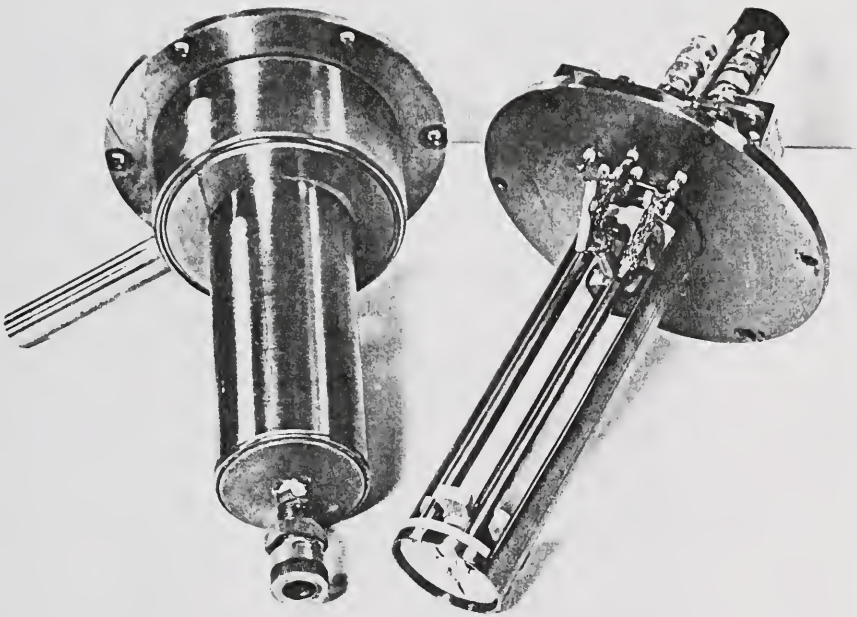


Figure 2-3. Specimen holder used for the electrical measurements.

After the specimens had been transferred to the chamber, and before measurement, helium was introduced and the temperature was raised to 200°C for 30 minutes. The heat served to drive adsorbed water vapor from the specimen surfaces and to promote adherence of the gold electrodes to the specimen. The extended 300°C heat treatment used by Kinser<sup>149</sup> to anneal vapor deposited electrodes was not used for the UO<sub>2</sub> specimens because of the danger of their reacting with trace amounts of oxygen and thus altering the stoichiometry.

The quality of the gold electrodes was checked by measuring the electrical response of several samples at three test voltages with peak amplitudes of 30, 3, and 0.3 volts. Since the measured capacities and conductances were identical for all three voltage levels, the electrode-specimen interface was judged to be ohmic.

The measurement circuit, shown schematically in Figure 2-4, consists of two parallel systems, one for the audio frequency range (100 Hz to 20 KHz) and one for radio frequencies (20 KHz to 1 MHz).

For audio frequencies, a Hewlett-Packard 651A oscillator supplies a signal to the bridge circuit, which consists of the specimen, a Wayne-Kerr B221 transformer-ratio-arm bridge, and a General Radio GR1232-A null detector. At balance, the bridge reports the equivalent parallel conductance and capacity of the sample.

For frequencies between 20 KHz and 100 KHz the measuring circuit is the same except that a Wayne-Kerr B601 bridge is used. Because the null detector is limited to a maximum frequency of 100 KHz, additional equipment is necessary for higher frequencies. In the present system, a General Radio 1232-P1 crystal mixer is used to mix the bridge output with a signal from a Wayne-Kerr 022D video oscillator. The video

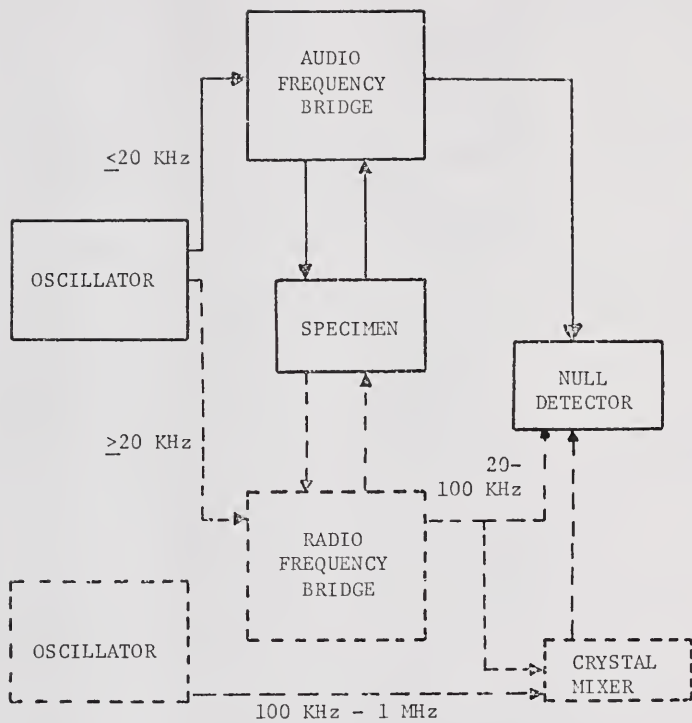


Figure 2-4. Block diagram of the apparatus used for the electrical measurements.

oscillator is set for a frequency 100 KHz higher than the test signal. The output of the crystal mixer contains a 100 KHz beat frequency as one of its components. The null detector receives the beat component when set for 100 KHz. When the bridge is balanced, the intermediate frequency will show a null signal strength, which is indicated on the null detector.

When balanced, the bridge readouts gave the conductance and capacity of a hypothetical circuit, consisting of a resistor and capacitor in parallel, that would have the same response to the applied sinusoidal signal as did the specimen. The equivalent parallel conductance and capacity were frequency-independent for tests performed with high-purity helium in the specimen chamber but were frequency-dependent if the atmosphere was air saturated with water vapor. The electrical conductivities and dielectric properties of the specimens were calculated from the equivalent parallel conductances and capacities with the following formulae.

Let the conductance, capacity, and measurement frequency be denoted by  $G$ ,  $C$ , and  $f$ , respectively. Assume that the specimen is a circular disk with diameter  $d$  and thickness  $t$ . Let  $A$  represent the area of one end of the disk, i.e.,  $A = \pi d^2/4$ . Then the electrical conductivity,  $\sigma$ , is given by

$$\sigma = G \frac{t}{A} \quad (2-1)$$

The units of  $\sigma$  are  $\text{ohm}^{-1} \text{cm}^{-1}$  if  $G$  is measured in  $\text{ohm}^{-1}$ ,  $t$  in  $\text{cm}$ , and  $A$  in  $\text{cm}^2$ . The real component of the complex dielectric constant is denoted by  $\epsilon'$ , and is calculated from

$$\epsilon' = \frac{C}{\epsilon_0} \frac{t}{A} \quad (2-2)$$

The unit of capacity is the farad (F). The constant  $\epsilon_0$ , the permittivity of free space, is equal to  $8.854 \times 10^{-14}$  F/cm. The parameter  $\epsilon'$  is dimensionless. Dielectric losses are expressed by the tangent of the angle in the complex plane between the complex voltage vector,  $V^*$ , and the complex charge vector,  $Q^*$ . The loss tangent is denoted by  $\tan\delta$ , and is calculated by

$$\tan\delta = \frac{G}{2\pi fC} \quad (2-3)$$

The angle between the complex dielectric constant and the real axis is also equal to  $\delta$ . Therefore, the imaginary component of the dielectric constant,  $\epsilon''$ , is given by

$$\epsilon'' = \epsilon' \tan\delta \quad (2-4)$$

For experiments in which large D.C. conductivities are obtained, the A.C. dielectric-loss parameters are usually calculated by replacing the total conductance in Equation (2-3) with the alternating current component of conductance, i.e.,

$$\tan\delta_{AC} = \frac{(G - G_{DC})}{2\pi fC} \quad (2-5)$$

and

$$\epsilon''_{AC} = \epsilon' \tan\delta_{AC} \quad (2-6)$$

where  $G_{DC}$  is the D.C. conductance. For the  $UO_2$  specimens examined in this study, the total conductance was a constant for frequencies between 100 and 1000 Hz. This constant value was used as the direct-current conductance in Equation (2-5).

## CHAPTER III

### THE METRIC PROPERTIES OF SINTERED AND HOT PRESSED $UO_2$

The paths of microstructural change for cold compaction, conventional sintering, and hot pressing are described in this chapter. The variations of the metric properties, average properties derived from the metric properties, and shape parameters are reported as functions of the pore volume fraction and the grain contiguity. New relationships among several of the metric properties were developed by analyzing the relationships among the metric properties and contiguity parameters.

#### The Path of Microstructural Change

The paths of microstructural change for cold compaction, conventional sintering, and hot pressing are described in this section by projecting the n-dimensional paths onto planes containing the  $V_V^P$  axis and the axis of the metric properties of interest. The metric properties considered are  $S_V^{\alpha P}$ ,  $M_V^{\alpha P}$ ,  $S_V^{\alpha\alpha}$ ,  $L_V^{\alpha\alpha P}$ , and  $L_V^{\alpha\alpha\alpha}$ . Results of the inflection-point count for the pore-solid interface of a series of hot-pressed specimens are reported. The metric properties, average properties, and the  $\overline{H}^{\alpha P-P}$  shape index of the pore-solid interface are listed in Tables III-1 and III-2 for conventionally sintered and hot-pressed specimens, respectively. Inflection point measurements for a series of hot-pressed specimens are listed in Table III-3. The metric properties, contiguity parameters, and shape indices of the grain structure are listed in Tables III-4 and III-5.

Table III-1  
Metric Properties of the Pore-solid Interface  
of Conventionally Sintered Specimens

Sample No.	Part. Size	Comp. Press. (ksi)	Time (hr)	Temp. (°C)	$V^P$ $V$	$S_V^{cP}$ ( $10^3 \text{ cm}^{-1}$ )	$M_V^{cP}$ ( $10^6 \text{ cm}^{-3}$ )	$\pi_{TAG}^{cP}$ ( $10^6 \text{ cm}^{-2}$ )	$\bar{\lambda}^P$ ( $10^{-4} \text{ cm}$ )	$\frac{\bar{\lambda}^{cP}}{H}$ ( $10^3 \text{ cm}^{-1}$ )	$\frac{\bar{\lambda}^{cP}}{H}$
1	1	10	5	1760	0.10	2.02	-20.4	21.4	1.98	-10.1	-2.00
2	1	10	1	1600	0.17	6.60	-38.7	76.5	1.03	-5.86	-0.604
3	1	10	3	1760	0.128	2.08	-19.9	21.7	2.47	-9.57	-2.35
4	1	75	3	1760	0.140	3.58	-24.5	27.7	1.57	-6.84	-1.07
5 <sup>a</sup>	2	3	-	-	0.48	9.25	-	-	2.08	-	-
6 <sup>a</sup>	2	30	-	-	0.37	10.9	-	-	1.35	-	-
7 <sup>a</sup>	2	80	-	-	0.34	10.9	-	-	1.24	-	-
8	2	80	0.5	1630	0.201	5.01	-32.8	67.4	1.60	-6.44	-1.05
9	2	3	0.5	1630	0.318	5.22	-10.7	42.4	2.44	-2.05	-0.499
10	2	1	4	1700	0.207	2.76	-8.35	14.4	2.99	-3.02	-0.908
11	2	8	4	1700	0.227	2.54	-9.21	14.3	3.57	-3.63	-1.30

<sup>a</sup>Unfired compacts.

Table III-1 - continued

Sample No.	Part. Size	Comp. Press. (ksi)	Time (hr)	Temp. (°C)	$V_V^P$	$S_V^{\alpha P}$ ( $10^3 \text{ cm}^{-1}$ )	$n_V^{\alpha P}$ ( $10^6 \text{ cm}^{-3}$ )	$\pi_{\Gamma Ag}^{\alpha P}$ ( $10^6 \text{ cm}^{-2}$ )	$\bar{\lambda}^P$ ( $10^{-4} \text{ cm}$ )	$\bar{H}^{\alpha P}$ ( $10^3 \text{ cm}^{-1}$ )	$\frac{\pi^{\alpha P} P}{H}$
12	2	15	1	1600	0.26	4.61	-10.1	33.5	2.26	-2.20	-0.494
13	2	35	1	1700	0.187	3.01	-13.9	28.0	2.48	-4.62	-1.15
14	2	1	1.5	1650	0.32	5.26	-4.92	37.9	2.43	-0.935	-0.227
15	2	15	2.5	1600	0.24	4.67	-9.71	45.3	2.06	-2.08	-0.427
16	2	0	1.5	1650	0.37	4.98	-8.81	45.0	2.97	-1.77	-0.526
17	2	35	2.5	1700	0.194	3.01	-11.5	17.4	2.58	-3.82	-0.985
18	2	80	10	1700	0.199	4.81	-31.0	63.7	1.65	-6.44	-1.06
19	2	30	0.5	1630	0.262	6.73	-23.2	96.4	1.56	-3.45	-0.537
20	2	10	2.5	1700	0.212	3.54	-11.2	20.0	2.40	-3.17	-0.758
21	2	90	1.5	1700	0.146	2.38	-20.5	28.2	2.45	-8.58	-2.11
22	2	3	0.5	1630	0.320	5.25	-12.6	47.5	2.44	-2.40	-0.585
23	2	90	1	1700	0.165	3.03	-22.8	25.9	2.18	-7.55	-1.64
24	2	90	7	1720	0.112	2.04	-14.3	16.5	2.20	-7.01	-1.54
25	2	3	1	1700	0.27	4.58	-7.89	52.7	2.36	-1.72	-0.406

Table III-1 - continued

Sample No.	Part. Size	Comp. Press. (ksi)	Time (hr)	Temp. (°C)	$V_V^P$	$S_V^{\alpha P}$ ( $10^3 \text{ cm}^{-1}$ )	$M_V^{\alpha P}$ ( $10^6 \text{ cm}^{-3}$ )	$\pi_{TAG}^{\alpha P}$ ( $10^6 \text{ cm}^{-2}$ )	$\frac{P}{\lambda^2}$ ( $10^{-4} \text{ cm}$ )	$\frac{H^{\alpha P}}{H}$ ( $10^3 \text{ cm}^{-1}$ )	$\frac{H^{\alpha P}}{\lambda}$
26	3	80	2	1700	0.21	2.79	-9.73	17.7	3.01	-3.48	-1.05
27	3	10	2	1700	0.27	3.04	-6.43	26.8	3.55	-2.12	-0.751
28	3	90	1	1700	0.23	4.04	-10.5	37.1	2.28	-2.60	-0.592
29	3	40	2	1700	0.23	3.34	-12.0	21.4	2.76	-3.59	-0.990
30	3	1	1	1700	0.35	2.96	-0.598	21.0	4.73	-2.02	-0.096
31	3	3	1	1700	0.30	2.81	-4.47	25.4	4.27	-1.59	-0.679
32	3	80	1	1700	0.22	4.12	-18.3	47.3	2.14	-4.45	-0.949
33	3	8	1	1700	0.35	2.88	-2.69	21.2	4.87	-0.937	-0.454
34	3	3	2.5	1680	0.42	4.13	+6.70	40.5	4.07	+1.62	+0.660
35	3	80	2	1700	0.19	2.39	-7.94	14.9	3.18	-3.32	-1.06
36	3	90	2	1700	0.13	1.10	-3.18	3.97	4.73	-2.89	-1.36
37	3	8	1	1720	0.322	2.91	-1.79	13.2	4.43	-0.615	-0.272
38	3	75	1	1720	0.205	2.69	-9.25	17.4	3.05	-3.44	-1.05
39	4	10	21	1680	0.366	2.85	-3.77	12.5	5.13	-1.32	-0.680

Table III-1 - continued

Sample No.	Part. Size	Comp. Press. (ksi)	Time (hr)	Temp. (°C)	$\frac{V^P}{V}$	$\frac{S_V^{\alpha P}}{(10^3 \text{ cm}^{-1})}$	$\frac{M_V^{\alpha P}}{(10^6 \text{ cm}^{-2})}$	$\frac{\pi T_{Ag}^{\alpha P}}{(10^6 \text{ cm}^{-2})}$	$\frac{\bar{\lambda}^P}{10^{-4} \text{ cm}}$	$\frac{H^{\alpha P}}{10^3 \text{ cm}^{-1}}$	$\frac{H^{\alpha P-P}}{H^{\alpha P-\lambda}}$
40	4	80	18	1680	0.191	2.82	-8.76	14.4	2.71	-3.11	-0.842
41	4	30	24	1680	0.238	3.01	-6.36	13.5	3.16	-2.11	-0.668
42	4	10	18	1680	0.272	2.85	-3.64	11.9	3.82	-1.28	-0.488
43	4	10	21	1680	0.273	2.67	-5.03	11.2	4.09	-1.89	-0.770
44	4	10	2	1700	0.279	2.82	-3.81	12.9	3.96	-1.35	-0.535
45	4	30	6	1680	0.280	3.75	-4.45	23.3	2.98	-1.19	-0.354
46	4	30	6	1600	0.381	3.66	+0.996	21.2	4.17	+2.72	+0.113
47	4	10	39	1680	0.275	2.17	-4.54	8.01	5.06	-2.09	-1.06
48	4	80	39	1680	0.173	1.94	-6.25	8.29	3.57	-3.22	-1.15
49	5	30	19	1700	0.301	2.15	-0.014	7.02	5.60	-0.0066	-0.0036
50	5	80	24	1700	0.286	2.28	-2.98	10.3	5.02	-1.31	-0.656
51	5	30	19	1700	0.279	2.91	-	-	3.84	-	-
52	5	80	48	1700	0.219	1.91	-3.19	6.90	4.58	-1.67	-0.766
53	5	80	2	1700	0.401	2.20	-	-	7.29	-	-
54	5	30	2	1700	0.413	2.59	-	-	6.38	-	-

Table III-2

Metric Properties of the Pore-solid Interface  
of Hot-pressed Specimens

Sample No.	Part. Size	Comp. Press. (ksi)	Time (min.)	Temp. (°C)	$V_V^P$	$S_V^{\alpha P}$ ( $10^3 \text{ cm}^{-1}$ )	$M_V^{\alpha P}$ ( $10^6 \text{ cm}^{-2}$ )	$\pi_{TAG}^{\alpha P}$ ( $10^6 \text{ cm}^{-2}$ )	$\bar{\lambda}^P$ ( $10^{-4} \text{ cm}$ )	$H^{\alpha P}$ ( $10^3 \text{ cm}^{-1}$ )	$\frac{H^{\alpha P}}{\bar{\lambda}^P}$
55	1	3	30	1200	0.23	21.1	-75.1	282.	0.430	-3.56	-0.153
56	1	3	30	1650	0.07	1.20	-11.8	12.1	2.33	-9.83	-2.29
57	1	3	30	1350	0.18	9.81	-83.5	235.	0.734	-8.51	-0.625
58	1	3	30	1500	0.13	6.25	-82.1	180.	0.832	-13.1	-1.09
59	1	3	30	1800	0.03	0.378	-0.862	0.952	3.18	-2.29	-0.724
60	2	3	30	1300	0.21	4.92	-37.5	57.9	1.70	-7.62	-1.30
61	2	3	30	1350	0.18	4.50	-36.3	59.9	1.60	-8.06	-1.29
62	2	3	30	1400	0.15	3.49	-31.9	42.9	1.72	-9.15	-1.57
63	2	3	30	1450	0.14	3.07	-22.6	28.4	1.82	-7.35	-1.34
64	2	3	30	1600	0.08	1.10	-6.11	6.97	2.89	-3.81	-1.11
65	2	3	3	1400	0.22	5.75	-38.3	86.7	1.53	-6.67	-1.02
66	2	3	3	1500	0.195	4.45	-39.2	53.5	1.82	-9.16	-1.67

Table III-2 - continued

Sample No.	Part. Size	Comp. Press. (ksi)	Time (min.)	Temp. (°C)	$V_V^P$	$S_V^{\alpha P}$ ( $10^3 \text{ cm}^{-1}$ )	$M_V^{\alpha P}$ ( $10^6 \text{ cm}^{-2}$ )	$\pi T_{AG}^{\alpha P}$ ( $10^6 \text{ cm}^{-2}$ )	$\bar{\lambda}^P$ ( $10^{-4} \text{ cm}$ )	$\bar{H}^{\alpha P}$ ( $10^3 \text{ cm}^{-1}$ )	$\bar{H}^{\alpha P} \bar{\lambda}^P$
67	2	3	10	1500	0.16	3.01	-18.8	22.3	2.13	-6.27	-1.33
68	2	3	30	1500	0.13	2.34	-16.3	24.9	2.23	-6.97	-1.55
69	2	3	90	1500	0.08	0.892	-3.40	5.18	3.59	-3.81	-1.37
70	2	3	1	1500	0.24	6.21	-21.4	72.7	1.55	-3.45	-0.533
71	2	3	10	1250	0.23	6.05	-32.1	68.9	1.52	-5.31	-0.808
72	2	3	90	1250	0.18	3.45	-18.5	28.8	2.08	-5.39	-1.13
73	2	3	10	1700	0.08	0.947	-3.73	4.12	3.38	-3.94	-1.33
74	2	3	30	1700	0.06	0.980	-3.27	3.47	2.45	-3.34	-0.817
75	2	3	45	1550	0.12	2.13	-11.7	12.3	2.25	-5.49	-1.24
76	2	3	30	2000	0.03	0.193	-0.375	0.439	6.21	-1.94	-1.21
77	2	3	30	1200	0.24	9.02	-33.1	132.	1.19	-3.67	-0.439
78	2	5	30	1400	0.149	5.18	-54.1	82.3	1.15	-10.4	-1.20

Table III-2 - continued

Sample No.	Part. Size	Comp. Press. (ksi)	Time (min)	Temp. (°C)	$V_V^P$	$S_V^{\alpha P}$ ( $10^3 \text{ cm}^{-1}$ )	$M_V^{\alpha P}$ ( $10^6 \text{ cm}^{-2}$ )	$\pi_{Ag}^{\alpha P}$ ( $10^6 \text{ cm}^{-2}$ )	$\lambda^P$ ( $10^{-4} \text{ cm}$ )	$\frac{H^{\alpha P}}{H}$ ( $10^3 \text{ cm}^{-1}$ )	$\frac{H^{\alpha P} P}{\lambda}$
79	2	5	30	1500	0.123	4.74	-51.0	67.8	1.04	-10.8	-1.12
80	2	5	30	1300	0.225	7.55	-53.0	111.	1.19	-7.02	-0.837
81	2	5	30	1600	0.065	2.08	-22.2	24.9	1.25	-10.7	-1.33
82	2	1	30	1500	0.208	4.26	-32.1	48.5	1.95	-7.53	-1.47
83	2	1	30	1600	0.179	3.37	-20.5	30.3	2.12	-6.08	-1.29
84	2	1	30	1400	0.326	6.34	-36.6	79.5	2.06	-5.77	-1.19
85	2	1	30	1700	0.143	1.97	-9.36	16.9	2.90	-4.75	-1.38
86	2	1	30	1200	0.341	6.71	-5.31	112.	2.03	-0.791	-0.161
87	3	3	30	1150	0.29	5.38	-4.10	69.8	2.16	-0.763	-0.164
88	3	3	30	1300	0.23	4.10	-13.2	24.9	2.24	-3.22	-0.722
89	3	3	30	1550	0.15	1.78	-8.74	14.6	3.36	-4.90	-1.66
90	3	3	30	1700	0.12	1.05	-4.29	4.87	4.56	-4.08	-1.87
91	3	3	30	1850	0.09	0.733	-2.35	2.73	4.91	-3.21	-1.57

Table III-3  
 Area Inflection-point Count of  
 Hot-pressed Specimens

Sample No.	Part. Size	Press. (ksi)	$V_V^P$	$I_A$ ( $10^7 \text{ cm}^{-2}$ )
66	2	3	0.195	3.80
67	2	3	0.16	1.82
68	2	3	0.13	1.61
69	2	3	0.08	0.145
70	2	3	0.24	7.37

Table III-4

Quantitative Stereology Measurements of the  
Grain Structure of Conventionally Sintered  $UO_2$

Sample No.	Part. Size	Comp. Press. (ksi)	$V_V^P$	$S_V^{\alpha P}$ ( $10^3 \text{ cm}^{-1}$ )	$S_V^{\alpha\alpha}$ ( $10^3 \text{ cm}^{-1}$ )	$L_V^{\alpha P}$ ( $10^7 \text{ cm}^{-2}$ )	$L_V^{\alpha\alpha}$ ( $10^6 \text{ cm}^{-1}$ )	$C^\alpha$	$C^{\alpha\alpha}$
10	2	1	0.207	2.76	0.951	1.14	1.43	0.408	0.274
13	2	35	0.187	3.01	0.958	1.29	2.26	0.389	0.345
14	2	1	0.32	5.26	-	1.03	0.260	-	0.070
15	2	15	0.24	4.67	0.843	2.04	1.36	0.265	0.167
16	2	0	0.37	4.98	0.187	0.897	0.120	0.070	0.039
17	2	35	0.194	3.01	0.650	1.24	1.50	0.302	0.266
18	2	80	0.199	4.81	0.392	-	-	0.140	-
20	2	10	0.212	3.54	0.951	1.34	1.16	0.350	0.206
21	2	90	0.146	2.38	1.08	1.14	1.65	0.475	0.303
22	2	3	0.32	5.25	0.217	0.976	0.225	0.076	0.065
39	4	10	0.366	2.85	0.376	0.611	0.452	0.208	0.182

Table III-4 - continued

Sample No.	Part. Size	Comp. Press. (ksi)	$V_V^P$	$S_V^{\alpha P}$ ( $10^3 \text{ cm}^{-1}$ )	$S_V^{\alpha \alpha}$ ( $10^3 \text{ cm}^{-1}$ )	$L_V^{\alpha P}$ ( $10^7 \text{ cm}^{-2}$ )	$L_V^{\alpha \alpha}$ ( $10^6 \text{ cm}^{-1}$ )	$C^\alpha$	$C^{\alpha \alpha}$
40	4	80	0.191	2.82	0.426	0.836	0.842	0.232	0.232
41	4	30	0.238	3.01	0.375	0.752	0.492	0.205	0.164
42	4	10	0.272	2.85	0.456	-	-	0.243	-
43	4	10	0.273	2.67	0.331	0.640	0.500	0.199	0.190
44	4	10	0.279	2.82	0.405	-	-	0.223	-
45	4	30	0.280	3.75	0.297	0.494	0.180	0.137	0.098
46	4	30	0.381	3.66	0.187	0.387	0.192	0.093	0.130
47	4	10	0.275	2.17	0.441	0.511	0.496	0.289	0.225
48	4	80	0.173	1.94	0.648	0.518	0.836	0.401	0.326
49	5	30	0.301	2.15	0.083	-	-	0.072	-
50	5	80	0.286	2.28	0.142	-	-	0.111	-
52	5	80	0.219	1.91	0.305	-	-	0.242	-

Table III-4 - continued

Sample No.	V <sub>V</sub>	F <sub>1</sub>	F <sub>2</sub>	F <sub>3</sub>	F <sub>4</sub>
10	0.207	1.25	2.99	8.67	6.30
13	0.187	1.34	2.85	10.7	7.03
14	0.32	-	0.932	-	-
15	0.24	1.11	1.87	17.2	14.3
16	0.37	0.638	0.720	133	128
17	0.194	1.58	2.74	20.0	14.7
18	0.199	-	-	-	-
20	0.212	1.02	2.14	9.33	7.41
21	0.146	1.35	4.02	7.01	4.89
22	0.32	0.625	0.708	111	104
39	0.366	1.05	1.50	26.4	21.6
40	0.191	1.43	2.12	30.0	23.0
41	0.238	1.16	1.66	32.0	26.7
42	0.272	-	-	-	-

Table III-5

Quantitative Stereology Measurements of the  
Grain Structure of Hot-pressed Specimens

Sample No.	Part. Size	Comp. Press. (ksi)	$V_V^P$	$S_V^{\alpha P}$ ( $10^3 \text{ cm}^{-1}$ )	$S_V^{\alpha\alpha}$ ( $10^3 \text{ cm}^{-1}$ )	$L_V^{\alpha P}$ ( $10^7 \text{ cm}^{-2}$ )	$L_V^{\alpha\alpha}$ ( $10^6 \text{ cm}^{-2}$ )	$C^\alpha$	$C^{\alpha\alpha}$
64	2	3	0.08	1.10	0.811	-	-	0.596	-
66	2	3	0.195	4.45	1.35	2.61	2.58	0.378	0.229
67	2	3	0.16	3.01	1.52	1.89	3.01	0.502	0.323
68	2	3	0.13	2.34	1.62	1.83	2.68	0.582	0.306
69	2	3	0.08	0.892	0.819	0.193	0.458	0.647	0.416
70	2	3	0.24	6.21	0.280	0.874	0.140	0.083	0.046
71	2	3	0.23	6.05	0.379	-	-	0.111	-
74	2	3	0.06	0.980	0.750	-	-	0.605	-
76	2	3	0.03	0.193	0.261	-	-	0.730	-

Table III-5 - continued

Sample No.	V	F <sub>1</sub>	F <sub>2</sub>	F <sub>3</sub>	F <sub>4</sub>
64	0.08	-	-	-	-
66	0.195	1.17	2.63	9,28	7.16
67	0.16	1.28	4.17	6.04	4.09
68	0.13	1.69	6.68	5.02	3.49
69	0.08	0.818	4.85	2.46	1.43
70	0.24	0.391	0.453	58.4	55.7
71	0.23	-	-	-	-
74	0.06	-	-	-	-
76	0.03	-	-	-	-

### Cold Compaction

The effect of cold compaction pressure on the pore volume fraction of unfired compacts made from powder lot 2 is shown in Figure 3-1. A linear relationship between the logarithm of the compaction pressure and the pore volume fraction was obtained for samples pressed with and without the addition of a 2 weight percent polyethylene glycol as a binder-lubricant. The equations of least-squares regression lines through the data are

$$V_V' = 0.77 - 0.056 \log p \quad (3-1)$$

for samples pressed without a binder, and

$$V_V' = 0.59 - 0.067 \log p, \quad (3-2)$$

for samples pressed with a binder, where  $p$  is the compaction pressure in psi, and  $V_V'$  is the pore volume fraction of the unfired compact. The linearity of the  $V_V'$  versus  $\log p$  curve was first reported by Bal'shin.<sup>150</sup>

Polished sections through low-density unfired pellets indicated the presence of density gradients in the specimens pressed without a binder, but not in specimens pressed with a binder addition. This result, along with the high densities of pellets pressed with binder, indicates that the lubricating quality of the polyethylene glycol helped the particles to slide past one another, and promoted the breakup of multiple particle "bridges" or "arches."

Examples of polished sections through two unfired pellets, pressed without a binder addition, are shown in Figure 3-2. Quantitative stereology measurements performed on the unfired compacts were used to determine the path of pore-solid surface area change shown in Figure 3-3.

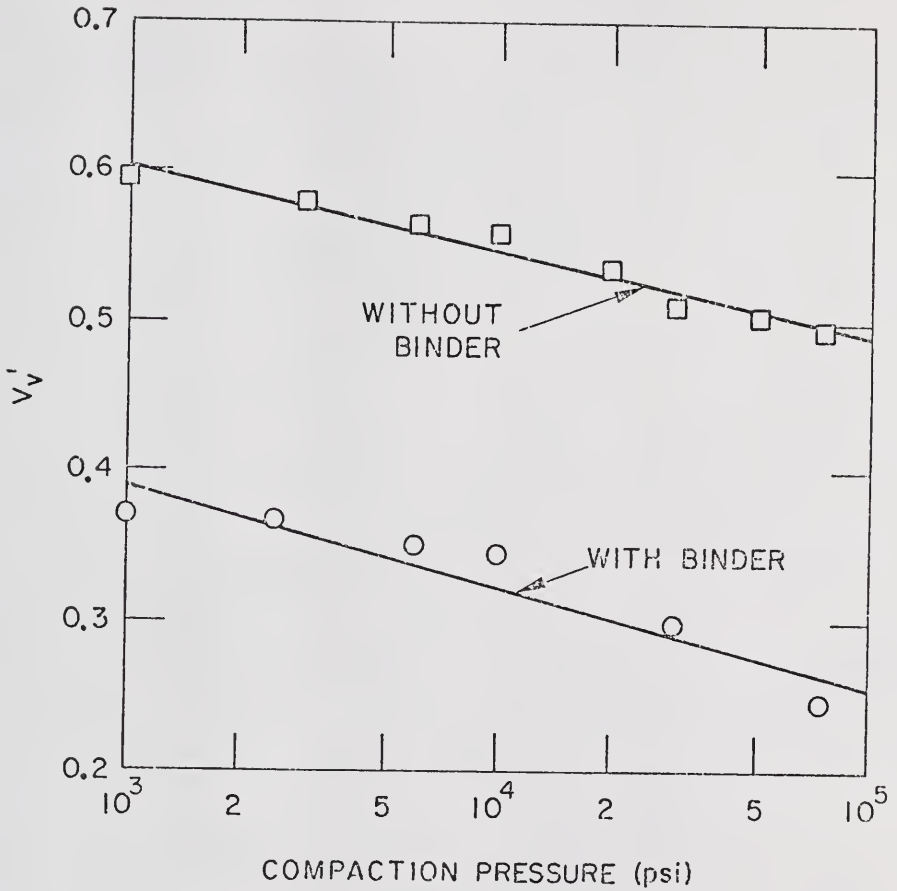
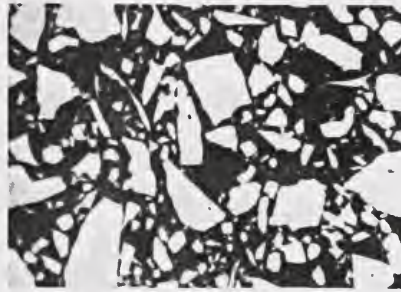
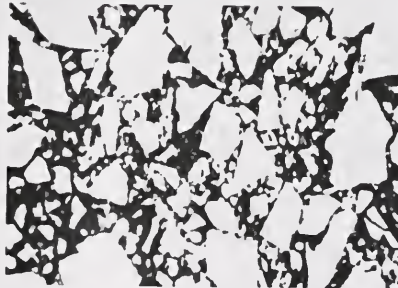


Figure 3-1. Pore volume fraction versus log compaction pressure for cold compaction of powder lot 2.



3 ksi

10  $\mu$ m  
|-----| $V_V = 0.48$ 

75 ksi

 $V_V = 0.34$ 

Figure 3-2. Polished-section micrographs of unfired compacts of powder lot 2 pressed at 3,000 and 75,000 psi.

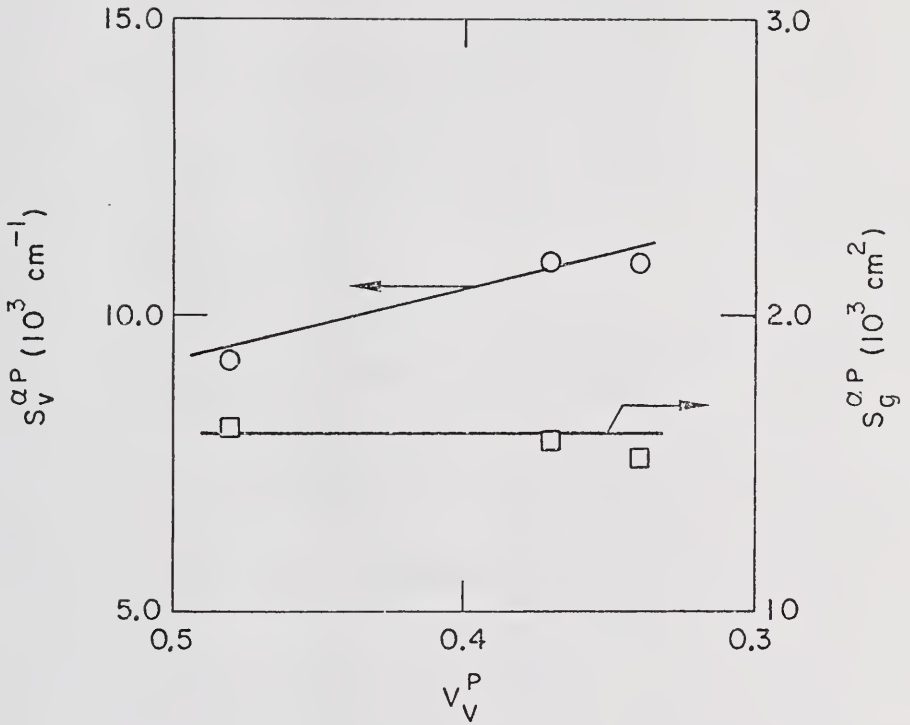


Figure 3-3. The variation of  $S_V^{\alpha P}$  and  $S_g^{\alpha P}$  with pore volume fraction during compaction of powder lot 2 specimens.

The amount of surface area per unit volume of structure,  $S_V^{\alpha P}$ , increased during cold compaction; however, surface area per unit mass,  $S_g^{\alpha P}$ , remained nearly constant. This behavior, first observed by Tuohig,<sup>72</sup> suggested that the dominant geometrical process during cold compaction was a rearrangement of the powder particles that moved more particles, and hence more surface area, into a unit volume of structure. The latter interpretation of the results was confirmed by the examination of the microstructures, Figure 3-2, which showed no evidence of particle fragmentation or cracking, processes that increase  $S_g^{\alpha P}$ . (A third process that can alter surface area during compaction, plastic deformation, does not occur in  $UO_2$  at room temperature.) The apparent drop in  $S_g^{\alpha P}$  at high pressures observed for the present data is the result of extremely close packing of the smaller particles. These particles are packed so close together that the gaps between them cannot be resolved in the optical microscope.

If  $S_g^{\alpha P}$  is a constant,  $S_V^{\alpha P}$  is a linear function of  $V_V^P$ , since

$$(S_V^{\alpha P})' = S_g^{\alpha P} \delta_o (1 - V_V^P), \quad (3-3)$$

where  $\delta_o$  is the density of  $UO_2$ ,  $10.96 \text{ g/cm}^3$ , and  $(S_V^{\alpha P})'$  is the surface area per unit volume in an unfired compact. The slope of the upper curve in Figure 3-3 is  $-\delta_o S_g^{\alpha P}$ . The upper line shows the behavior of  $S_V^{\alpha P}$  for an idealized case in which only particle rearrangement occurs, and all particles are resolved. The data point for an 80,000 psi compaction pressure lies below the line as a result of the inability to resolve all of the interparticle gaps.

Because of the difficulty in resolving the small particles, no attempt was made to determine the total curvature of unfired compacts. However, when the compacts were heated, the fine particles quickly sintered to the surfaces of the larger ones, as shown in Figure 3-4. Therefore, resolution problems were only encountered for a few specimens.

### Conventional Sintering

The effects of average particle size and compaction pressure of the unfired specimens on the paths of microstructural change for sintering are described in this section. Other fabrication parameters that might have affected the path, such as sintering atmosphere and stoichiometry, were held constant. Based on the results of an earlier study,<sup>45</sup> the sintering temperature was not expected to affect the paths of microstructural change. Although a systematic study of the potential effects of temperature was not conducted in this investigation, the data in Tables III-1 and III-4 do not show temperature effects. Note that the range of temperatures used was limited (1600-1720°C, or homologous temperatures of 0.60-0.64) to reduce the probability that the paths of microstructural change were affected by sintering temperature.

Pore-solid surface area. The paths of pore-solid surface area change for two UO<sub>2</sub> powders are shown in Figures 3-5 and 3-6. The microstructural state produced during cold compaction of a pellet is the starting point for microstructural change during sintering. The cold compaction curve for powder lot 2 specimens is indicated in Figure 3-5.

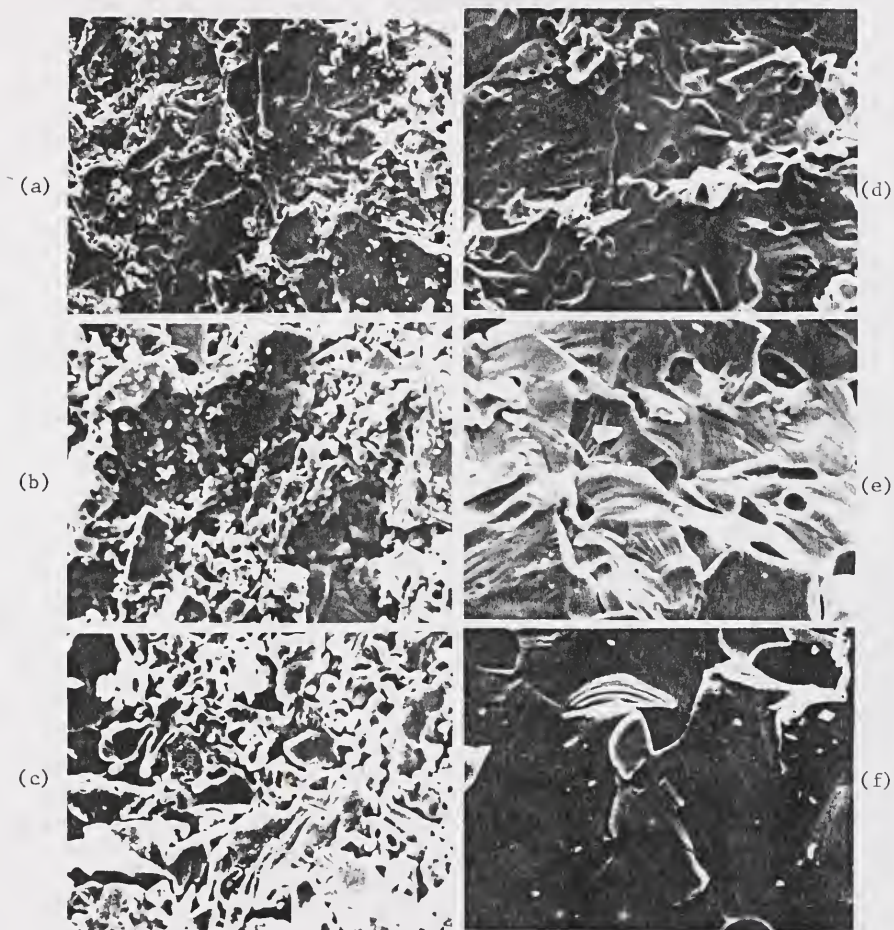


Figure 3-4. Scanning electron micrographs of fracture surfaces through hot-pressed specimens.

(a)  $V_V^P = 0.30$

(b)  $V_V^P = 0.27$

(c)  $V_V^P = 0.21$

(d)  $V_V^P = 0.14$

(e)  $V_V^P = 0.12$

(f)  $V_V^P = 0.05$

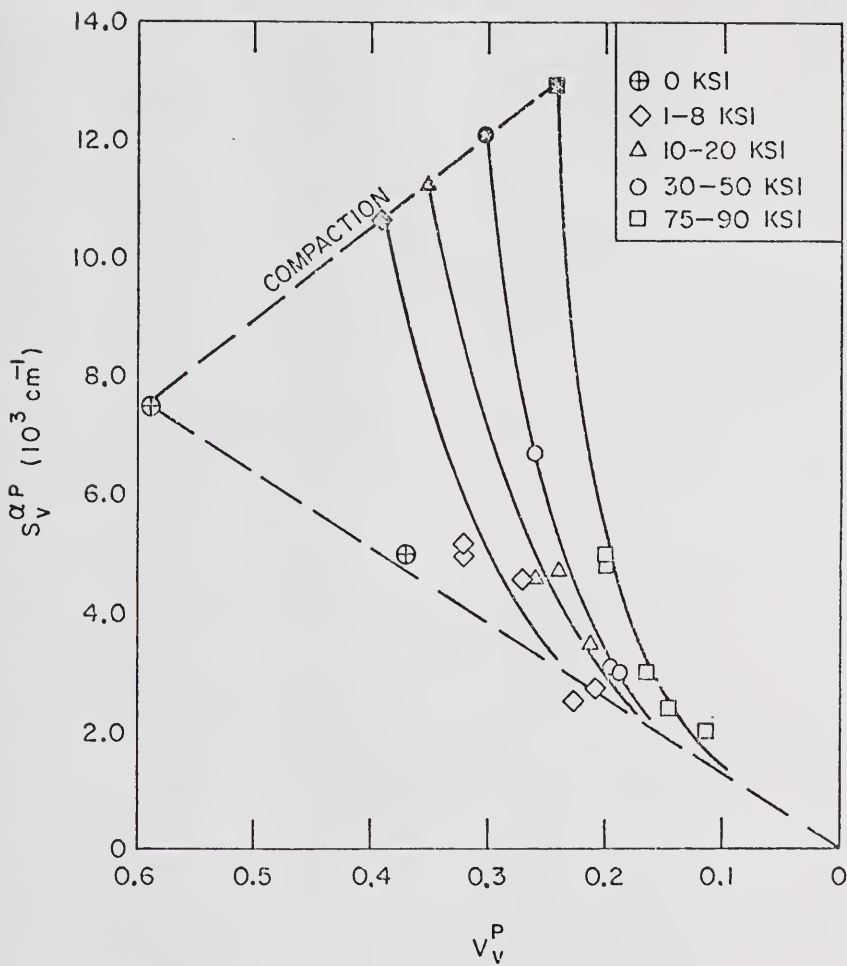


Figure 3-5. Pore-solid surface area versus pore volume fraction for conventionally sintered specimens prepared from powder lot 2.

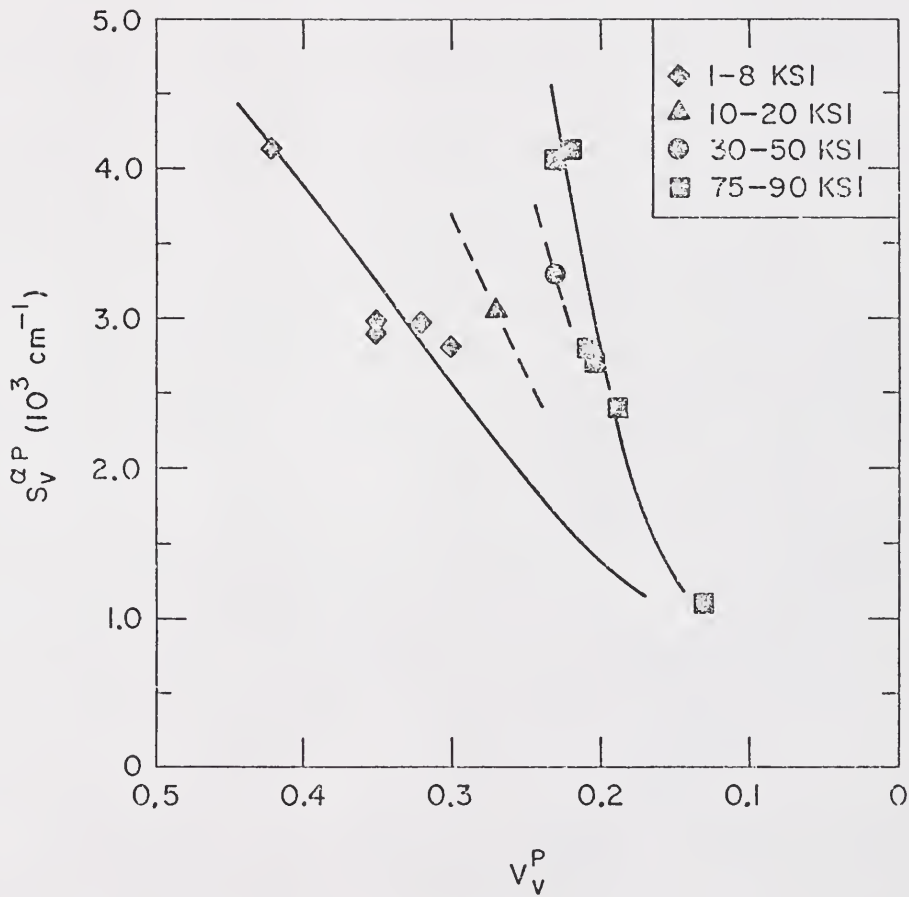


Figure 3-6. Pore-solid surface area versus pore volume fraction for conventionally sintered specimens prepared from powder lot 3.

The initiating points for the sintering curves of specimens pressed with a binder were calculated from Equation (3-3) using the pore-volume fraction data in Figure 3-1. Recall that surface area measurements of unfired compacts, shown in Figures 3-3 and 3-5, were obtained for specimens pressed without a binder. Surface area and volume fraction decrease from their initial values as the pellet is sintered. The path of surface area change for the entire densification process was influenced by the cold compaction pressure. Increasing the pressure shifts the  $S_V^{\alpha P} - V_V^P$  curves to higher densities and surface areas. As a result, the paths of surface area change form an envelope of curves in  $S_V^{\alpha P} - V_V^P$  space. For a given value of  $V_V^P$  in the range 0.10-2.25, the  $S_V^{\alpha P}$  value of the sintered specimen can be varied by a factor of 2 by selection of the compaction pressure.

The envelope of curves collapses at high densities and approaches the straight line drawn from the origin to the points that represent the sintering of uncompact powder. The slopes of the individual curves decrease and approach the slope of the straight line. Envelopes of curves with similar characteristics have been used to describe the paths of surface area change for sintered  $\text{Cu}$ <sup>71</sup> and  $\text{UO}_2$ <sup>72</sup> in earlier studies.

Total curvature. The evolution of total curvature during conventional sintering is shown for powder lots 2 and 3 in Figures 3-7 and 3-8, respectively. Most of the curves depict only a portion of the path of curvature change for a particular set of fabrication conditions. However enough information is present to allow the following description.

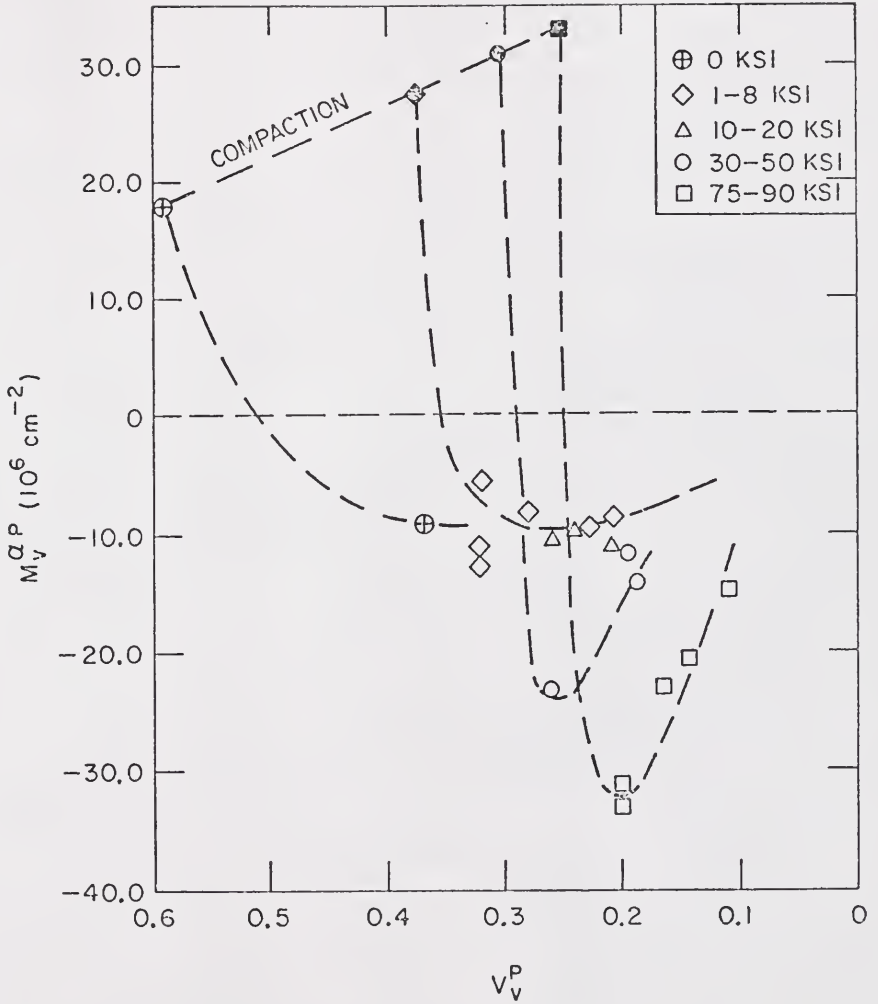


Figure 3-7. Total curvature of the pore-solid interface versus pore volume fraction for conventionally sintered specimens prepared from powder lot 2.

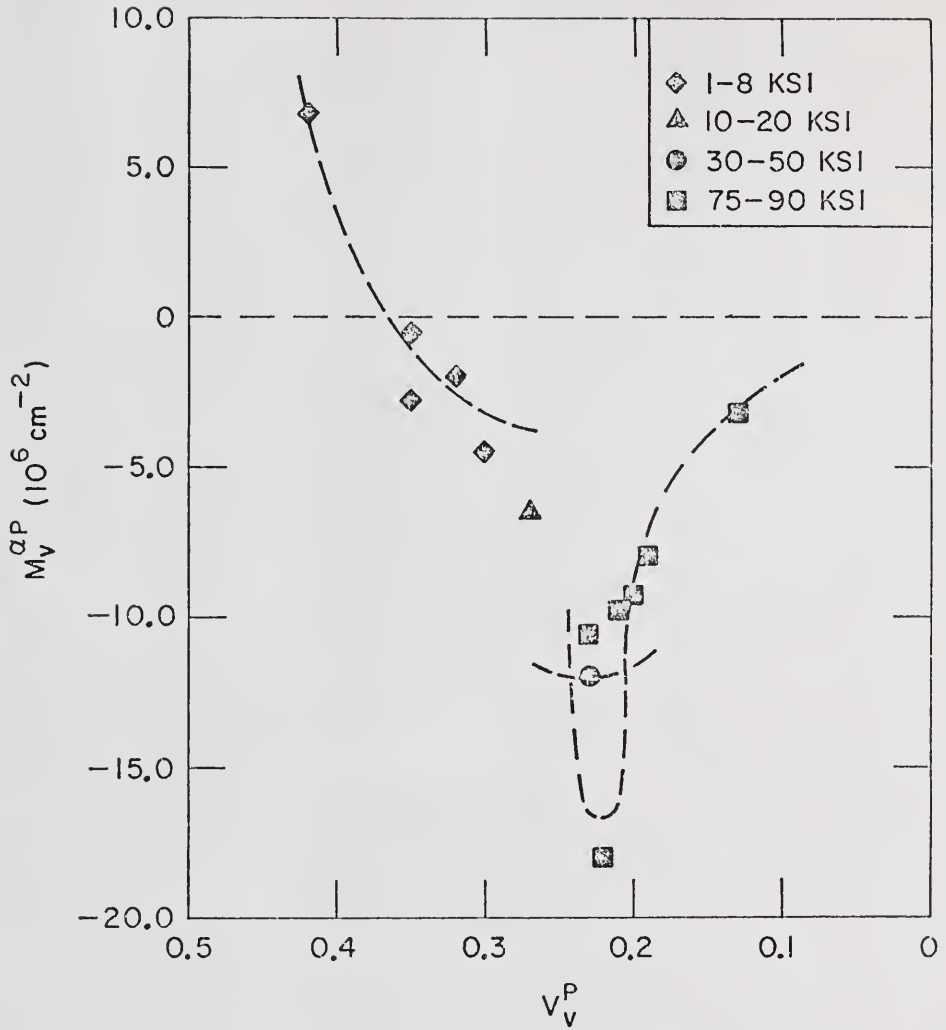


Figure 3-8. Total curvature of the pore-solid interface versus pore volume fraction for conventionally sintered specimens prepared from powder lot 3.

The total curvature of an unfired compact is positive. During sintering, the total curvature decreases, goes through zero, attains a minimum value and then increases toward zero at full density. Although positive  $M_V^{\alpha P}$  values are not present in the data shown in Figures 3-7 and 3-8, the initial positive portions of the  $M_V^{\alpha P}$  paths are sketched in. The estimation procedure used to obtain the initial portions of the paths is described in the following paragraphs.

If particle shape does not change during cold compaction, total curvature will vary in the same manner as pore-solid surface area:

$$(M_V^{\alpha P})' = M_g^{\alpha P} \delta_o (1 - V_V^P), \quad (3-4)$$

where  $(M_V^{\alpha P})'$  is the total curvature of an unfired compact and  $M_g^{\alpha P}$  is the (constant) total curvature of the powder normalized to a unit mass. Although direct measurements were not performed, the total curvature of unfired compacts can be estimated from the SEM photograph, Figure 2-1. For powder lot 2, the average particle "diameter" is estimated to be  $\sim 5\mu\text{m}$ . This value was obtained from measurements on 10 fields of view, including the one shown in Figure 2-1c, but must be regarded as approximate because of the irregular shape of the particles, and the resulting tendency for the particles to lie on a substrate so that the apparent average dimensions are larger than the true average. If the average particle diameter is assumed to be equal to the average caliper diameter, i.e., the distance, averaged over orientation, between parallel tangent planes, the average total curvature of a particle is

$$\bar{M} = 2\pi\bar{D}_V, \quad (3-5)$$

where  $\bar{M}$  is the average total curvature per particle, and  $\bar{D}_V$  is the average caliper diameter.<sup>151</sup> Under the assumption that the average particle volume is given by  $\bar{V} = \pi(\bar{D}_V)^3/6$ , the total curvature per unit mass can be written

$$M_g^{\alpha P} \approx \frac{\bar{M}}{\delta_o \bar{V}} = \frac{12}{\delta_o (\bar{D}_V)^2} . \quad (3-6)$$

Thus, a rough estimate of  $M_g^{\alpha P}$  can be obtained from Equation (3-6). For powder lot 2,  $\bar{D}_V \approx 5 \times 10^{-4}$  cm,  $\delta_o = 10.96$  g/cm<sup>3</sup>, and  $M_g^{\alpha P} \approx 4 \times 10^6$  cm/g.

The estimated value of  $M_g^{\alpha P}$  was used to construct the dashed line marked "compaction" in Figure 3-7. The points on this line give the initial conditions for the paths of  $M_V^{\alpha P}$  change during sintering. The positive portions of the paths were sketched in between the estimated values for unfired compacts and the data points for sintered structures.

The path of total curvature change is a function of the pressure used for cold compaction of the specimen. As in the case of pore-solid surface area, varying the compaction pressure leads to an envelope of  $M_V^{\alpha P}$  paths. However, the paths of curvature change exhibit more complex behavior than was observed for surface area. In addition to shifting the individual curves to lower pore volume fractions, increasing the compaction pressure decreases (makes more negative) the minimum in the  $M_V^{\alpha P}$  path. The minimum  $M_V^{\alpha P}$  value varied linearly with the logarithm of compaction pressure for specimens sintered from three powder lots, as shown in Figure 3-9.

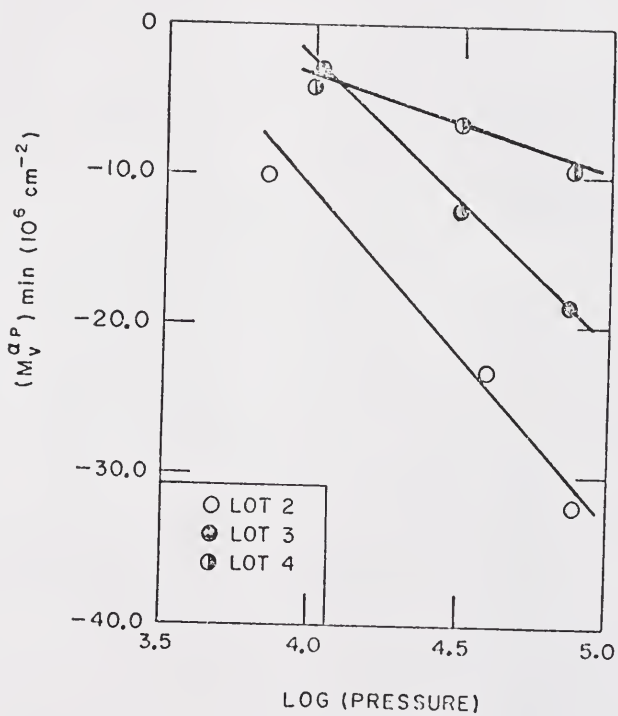


Figure 3-9. Variation of the minimum total curvature value with log compaction pressure for three powder lots.

Average mean curvature. The paths of average mean curvature change for conventional sintering of two powder lots are shown in Figures 3-10 and 3-11. The dashed horizontal line in Figure 3-10 illustrates that  $\bar{H}^{\alpha P}$  is constant during cold compaction, a result which can be deduced from the earlier conclusion that no change in particle size or shape occurred during compaction. From Equations (3-1), (3-2), (3-4), and the definition of  $\bar{H}^{\alpha P}$ , the  $\bar{H}^{\alpha P}$  value of unfired compacts made from powder lot 2 is estimated to be  $\sim 2 \times 10^3 \text{ cm}^{-1}$ .

As the specimens sintered,  $\bar{H}^{\alpha P}$  decreased from the initial positive value and attained negative minima that were functions of the cold compaction pressure. The minimum  $\bar{H}^{\alpha P}$  values occurred at pore volume fractions of 0.21, 0.19, and 0.15 for specimens compacted at 10,000, 35,000, and 80,000 psi, respectively, i.e., at slightly lower volume fractions than the corresponding minima in  $M_V^{\alpha P}$ .

Gross tangent count. As described in Chapter I, the gross tangent count is obtained by summing the concave and convex tangents that a sweeping test line makes with arc elements of the trace of an interface on a polished section. Values of  $T_{Ag}^{\alpha P}$ , multiplied by the normalizing factor  $\pi$ , are plotted against  $V_V^P$  in Figures 3-12 and 3-13. The paths of  $\pi T_{Ag}^{\alpha P}$  change shown in Figure 3-12 are estimates based on the appearance of polished sections through unfired compacts, e.g., Figure 3-2, as well as the measurements on polished sections through sintered structures. The dashed line for cold compaction shows a linear increase in  $\pi T_{Ag}^{\alpha P}$  with decreasing pore volume fraction. This line was constructed by arbitrarily assuming that  $\pi T_{Ag}^{\alpha P} = 2 M_V^{\alpha P}$  during cold compaction.

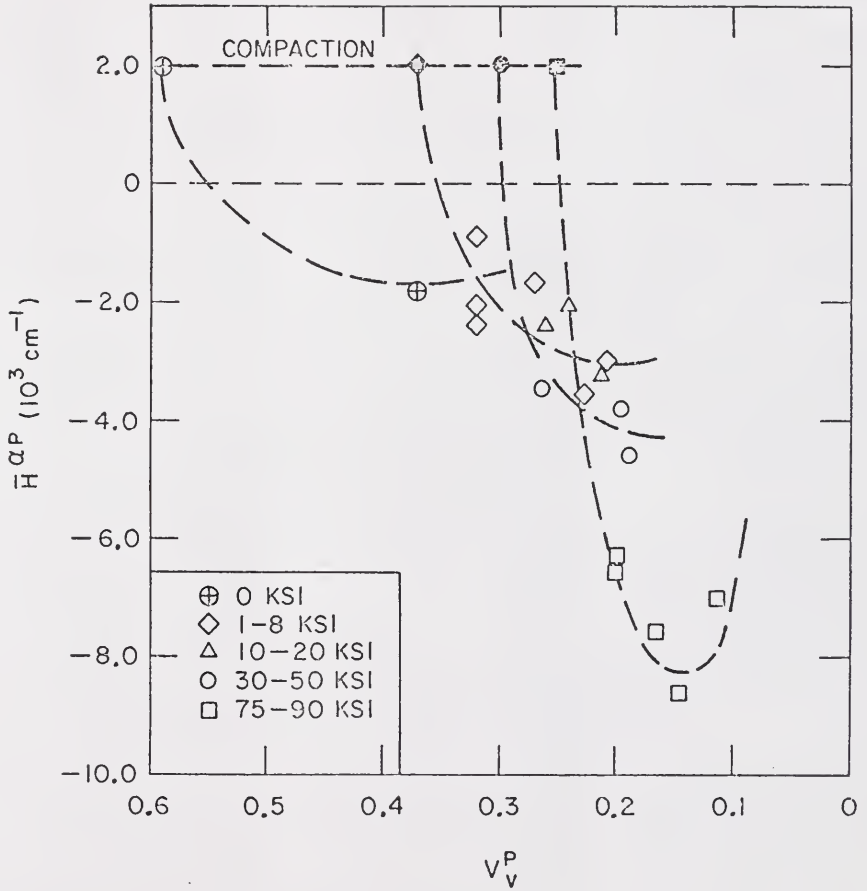


Figure 3-10. Average mean curvature of the pore-solid interface versus pore volume fraction for conventionally sintered specimens prepared from powder lot 2.

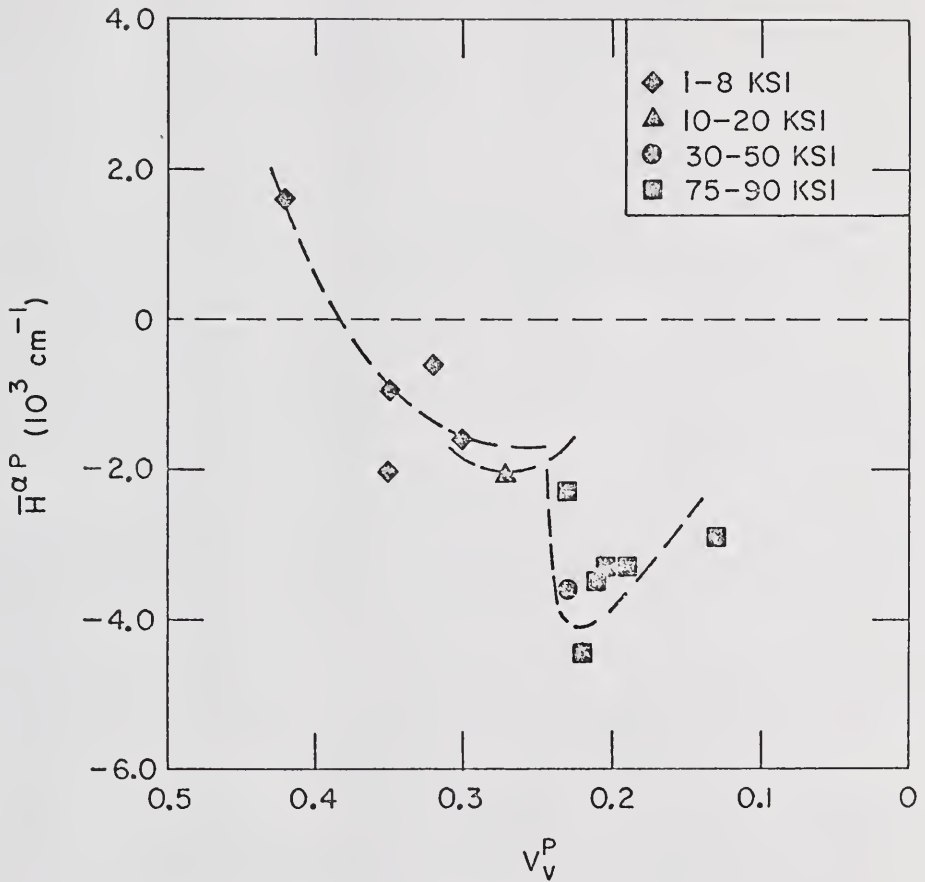


Figure 3-11. Average mean curvature of the pore-solid interface versus pore volume fraction for conventionally sintered specimen prepared from powder lot 3.

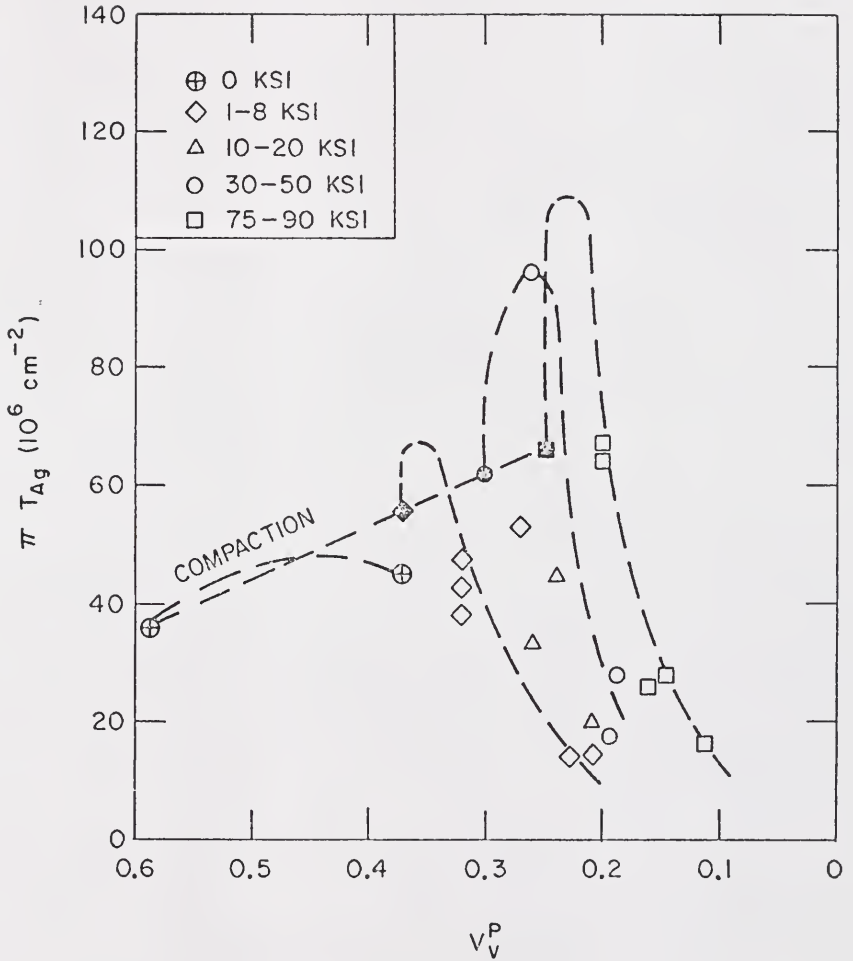


Figure 3-12. Variation of the gross tangent count of the pore-solid interface with pore volume fraction for conventionally sintered specimens prepared from powder lot 2.

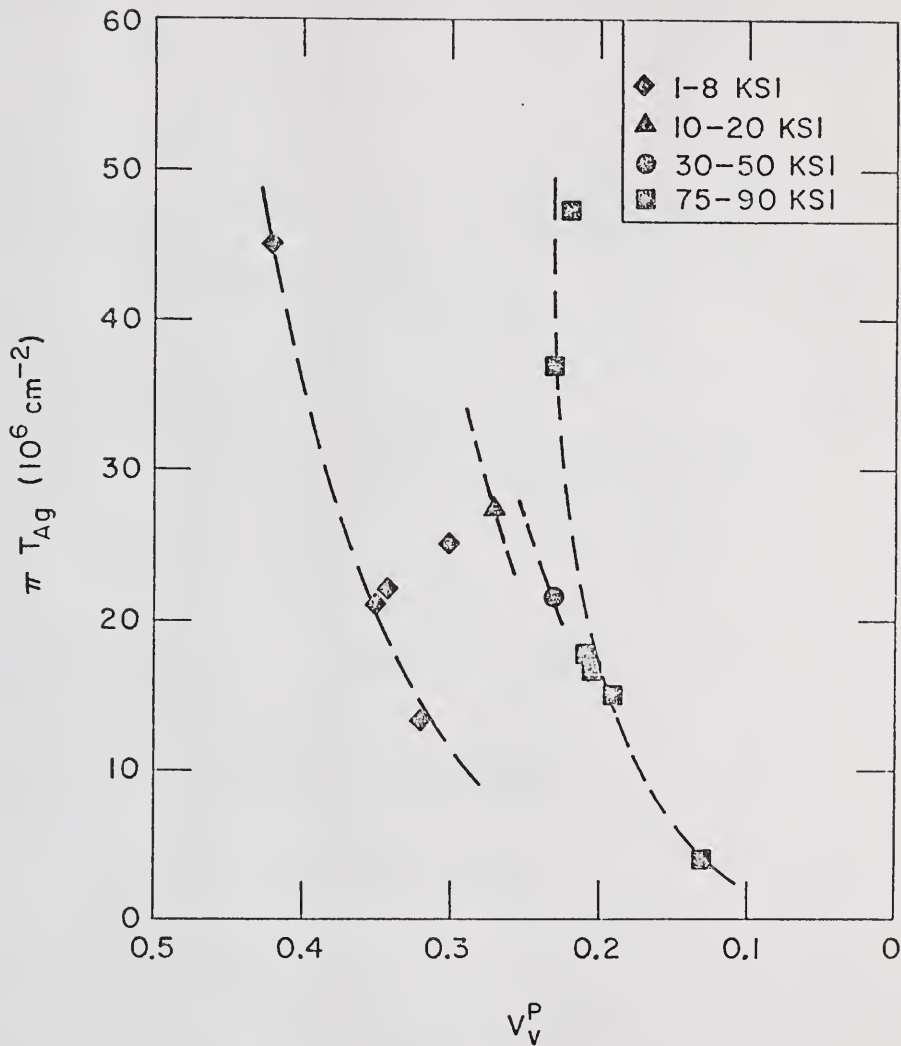


Figure 3-13. Variation of the gross tangent count of the pore-solid interface with pore volume fraction for conventionally sintered specimens prepared from powder lot 3.

Reference to Figure 3-2 shows that the powder particle outlines are not convex and therefore that  $\pi T_{Ag}^{\alpha P}$  will always exceed  $M_V^{\alpha P}$  for unfired specimens. However, since the nonconvex regions consist of relatively slight irregularities in the particle outlines, the contribution of negative tangents does not dominate the gross tangent count. Figure 3-2 suggests that  $\pi T_{Ag}^{\alpha P}$  cannot exceed  $M_V^{\alpha P}$  by more than a factor of 2.

The interparticle weld necks that form and grow during the initial stages of sintering make a large contribution to the negative tangent count during a period in which the positive tangent count remains constant or decreases slightly. As a result, the gross tangent count is expected to show an initial increase, as indicated in Figure 3-12. (Additional evidence for the increase in  $\pi T_{Ag}^{\alpha P}$  was obtained from the hot-pressing studies described in a following section.)

After the initial increase,  $\pi T_{Ag}^{\alpha P}$  goes through a maximum value and decreases toward zero with further densification. It is not known whether the maximum value is a function of compaction pressure. The final decrease in  $\pi T_{Ag}^{\alpha P}$  consists of an envelope of curves produced by using a range of pressures for cold compaction. The envelope of curves is similar in form to that observed for the paths of  $S_V^{\alpha P}$  change.

Grain-boundary surface area. The grain-boundary surface area is expected to have a small positive value for an unfired compact, increase and go through a maximum during sintering, and then decrease as grain growth occurs during third stage sintering. The available data for conventional sintering of powder lots 2 and 4, Figures 3-14 and 3-15, show only the initial portion of the expected behavior, because  $V_V^P$  did not drop to a value that would have allowed grain growth for these specimens.

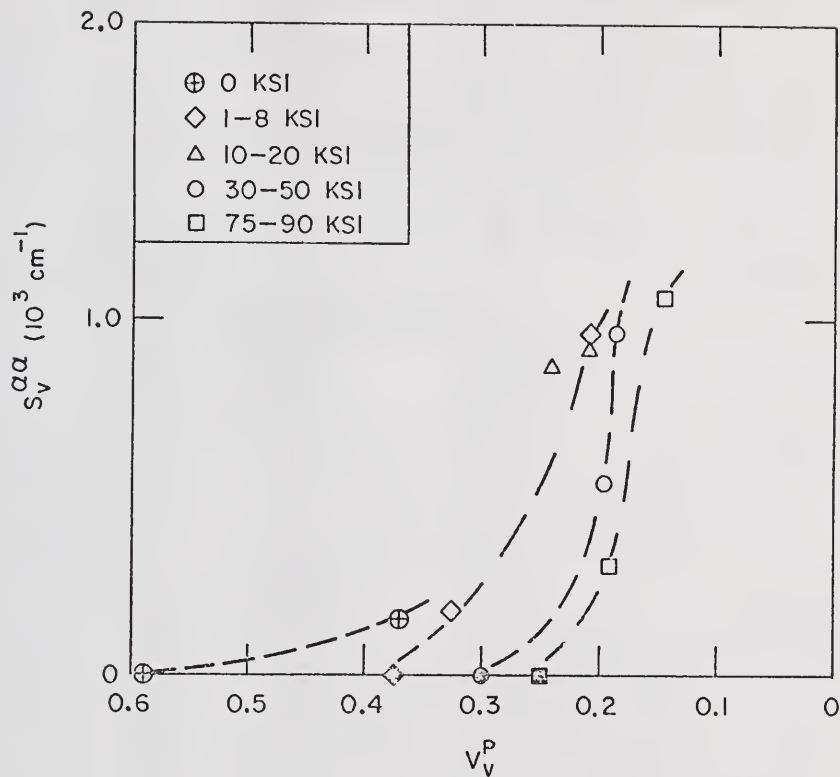


Figure 3-14. Grain-boundary surface area versus pore volume fraction for conventionally sintered specimens prepared from powder lot 2.

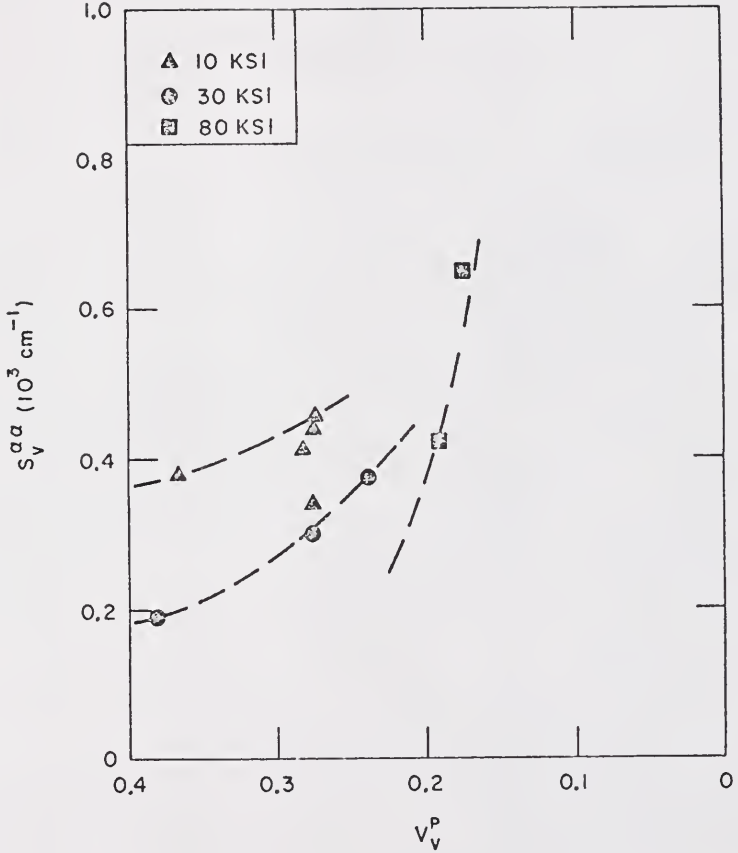


Figure 3-15. Grain-boundary surface area versus pore volume fraction for conventionally sintered specimens prepared from powder lot 3.

The full range of microstructural states was observed for hot pressing, however, and is discussed in a following section of this chapter. The portions of the  $S_V^{\alpha\alpha}$  paths for conventional sintering shown in Figures 3-14 and 3-15 are functions of the pressure used for cold compaction. Increasing the cold compaction pressure has the effect of decreasing the pore volume fraction at which a given  $S_V^{\alpha\alpha}$  value is attained.

Grain-boundary triple-line length. Both  $L_V^{\alpha\alpha P}$  and  $L_V^{\alpha\alpha\alpha}$  equal zero for a compact of monocrystalline particles. As interparticle necks grow, the length of  $\alpha\alpha P$  triple lines increases. The increase in  $L_V^{\alpha\alpha P}$  for conventional sintering of powder lots 2 and 4 is shown in Figures 3-16a and 3-17a, respectively. The path of  $L_V^{\alpha\alpha P}$  change is a function of cold compaction pressure.

As the interparticle necks continue to grow during sintering, they intersect to form  $\alpha\alpha P$  triple lines. The length of these features increases during sintering as shown by the curves in Figures 3-16b and 3-17b. For all paths of microstructural change, the rise in  $L_V^{\alpha\alpha\alpha}$  occurs at a higher density than the  $L_V^{\alpha\alpha P}$  increase. This result is due to the requirement that growth of the  $\alpha\alpha$  grain contacts and of their boundaries, the  $\alpha\alpha P$  triple lines, must occur before the  $\alpha\alpha\alpha$  triple lines can form.

The behavior of the triple line lengths during the final stage of sintering was not observed for the conventionally sintered powders. A discussion of the expected behavior is included in the section on the path of microstructural change of hot pressing.

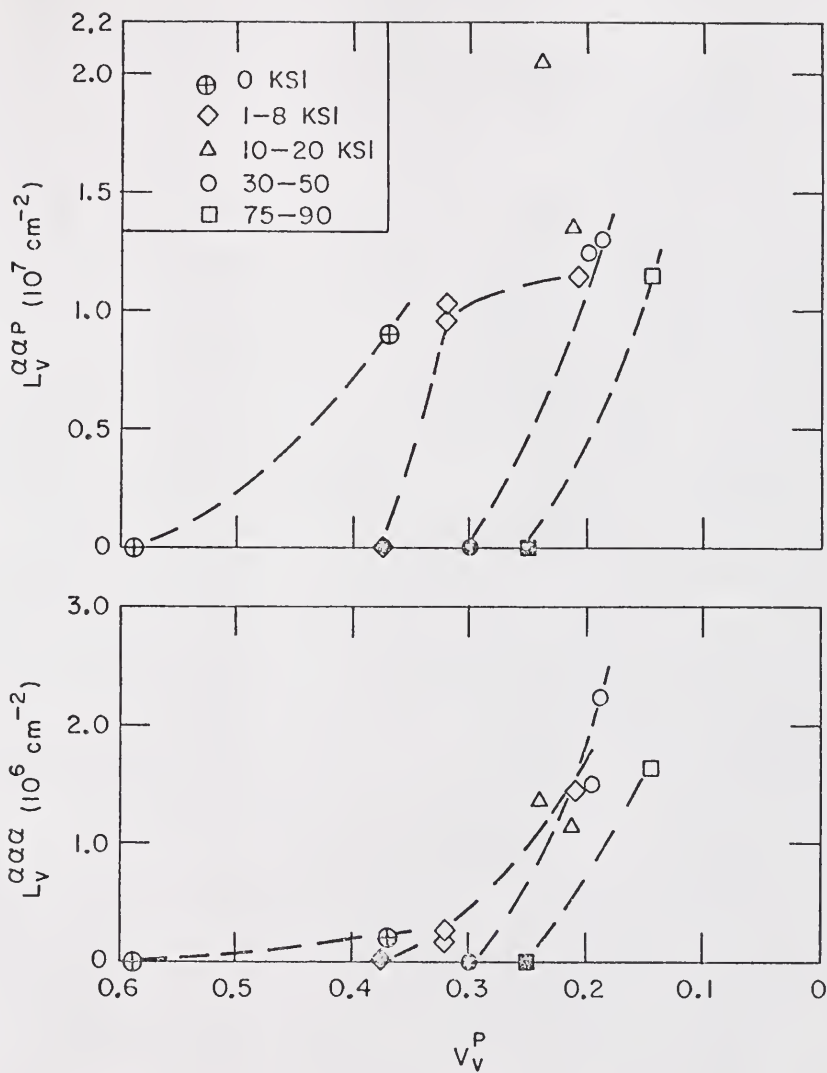


Figure 3-16. The variation of  $\alpha\alpha P$  and  $\alpha\alpha\alpha$  triple-line lengths with pore volume fraction for conventionally sintered specimens prepared from powder lot 2.

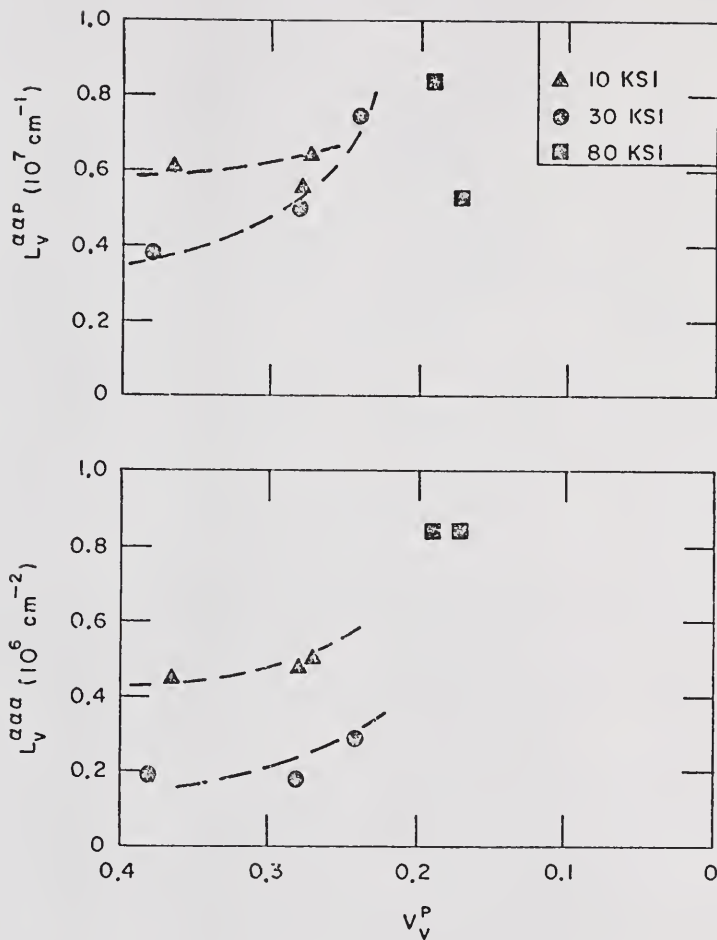


Figure 3-17. The variation of  $\alpha\alpha P$  and  $\alpha\alpha\alpha$  triple-line lengths with pore volume fraction for conventionally sintered specimens prepared from powder lot 4.

### Hot Pressing

The investigation of the path of microstructural change for hot pressing paralleled the study of conventional sintering. The fabrication variables studied were the pressure applied to the sample, the particle size of powder, and the temperature of hot pressing. The effect of temperature on the microstructure of hot pressed samples was studied because of the large range of temperatures used ( $1150^{\circ}\text{C}$  to  $2000^{\circ}\text{C}$  or  $0.46$  to  $0.74 T_m$ ).

Surface area. The path of surface area change for specimens from powder lot 2 hot pressed at 3000 psi is shown in Figure 3-18. The plotting symbols indicate the temperature used. While some scatter is evident, there does not appear to be any systematic effect of temperature on the path of surface area change.

The path originates at  $V_V^P = 0.48$ ,  $S_V^{\alpha P} = 9.25 \times 10^3 \text{ cm}^{-1}$ , i.e., the surface area and volume fraction of a sample cold pressed to 3000 psi without a binder addition. When pressure is reapplied at high temperatures (see Chapter II for a description of hot pressing schedules), substantial densification occurs almost immediately. Since it was not possible to interrupt this initial densification, no samples are available to characterize the first stage of hot pressing. The portion of the curve that was analyzed is similar in shape to the surface area path for conventional sintering, and is probably indicative of a surface-excess condition. In the context of this discussion, a "surface-excess condition" is one in which  $S_V^{\alpha P}$  is larger than the value of a loose-stack-sintered specimen with the same pore volume fraction.

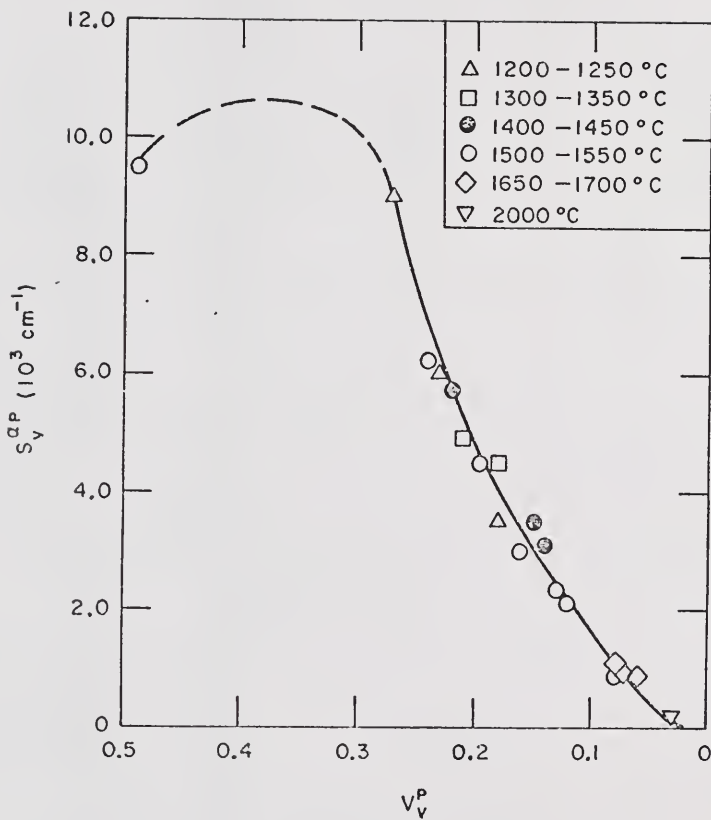


Figure 3-18. The effect of temperature on the path of pore-solid surface area change for specimens of powder lot 2 hot pressed at 3,000 psi.

The effect of pressure on the path of surface area change during hot pressing, shown in Figure 3-19, is qualitatively the same as was described for conventional sintering. The curve for samples pressed at 1000 psi lies below the 3000 psi data at low densities but becomes indistinguishable from the latter curve for  $V_V^P$  less than about 0.25.  $S_V^{\alpha P}$  values for samples hot pressed at 5000 psi lie well above the 3000 psi curve.

The application of a given pressure at temperature is more effective in altering the path of surface area change than the use of the same pressure for the cold compaction of specimens in conventional sintering experiments. Comparison of Figures 3-19 and 3-5 shows that a sample hot pressed at 5000 psi has more surface area in unit volume than a pellet cold pressed at 80,000 psi and sintered to the same pore volume fraction.

The path of surface area change for hot pressing several other particle sizes of  $UO_2$  powder is shown in Figure 3-20. Decreasing the particle size has the expected effect of increasing the magnitude of  $S_V^{\alpha P}$  at a given value of  $V_V^P$ .

Total curvature. The path of total curvature change for specimens pressed at 3000 psi and various temperatures is shown in Figure 3-21. The initial portion of the path, in which  $M_V^{\alpha P}$  is positive, is indicated schematically in the figure, but was not observed because of the rapid initial microstructural changes during hot pressing.  $M_V^{\alpha P}$  attains a minimum value of  $\sim -35 \times 10^6 \text{ cm}^{-2}$  at  $V_V^P \approx 0.22$  and increases toward zero with further densification. The slope of the curve increases (i.e., becomes less negative) as  $V_V^P$  decreases below 0.1.

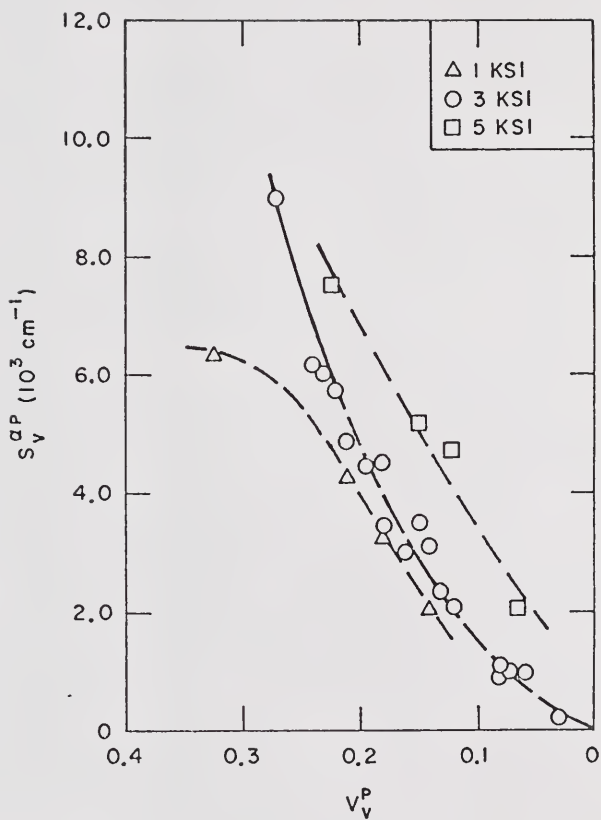


Figure 3-19. The effect of pressure on the path of pore-solid surface area change for hot-pressed specimens of powder lot 2.

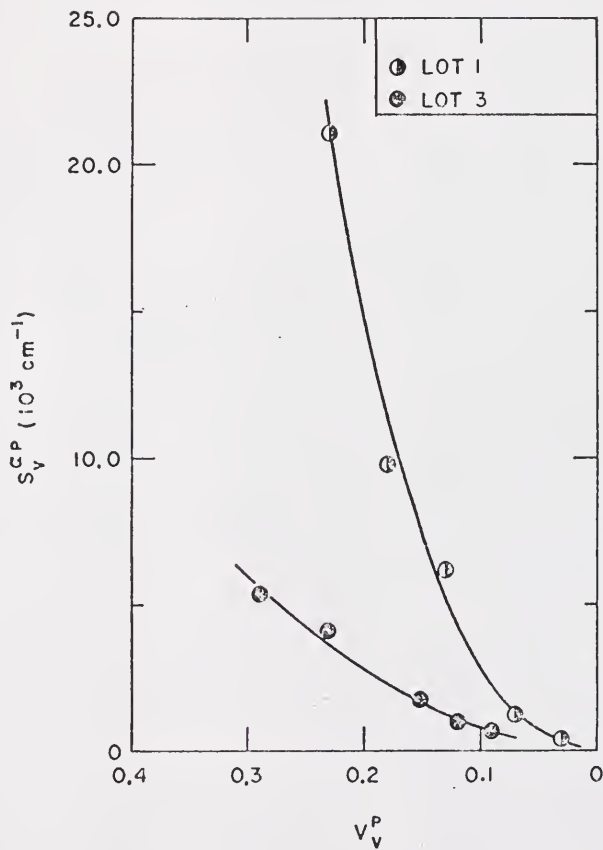


Figure 3-20. The effect of the scale of the system on the path of pore-solid surface area change for hot-pressed specimens.

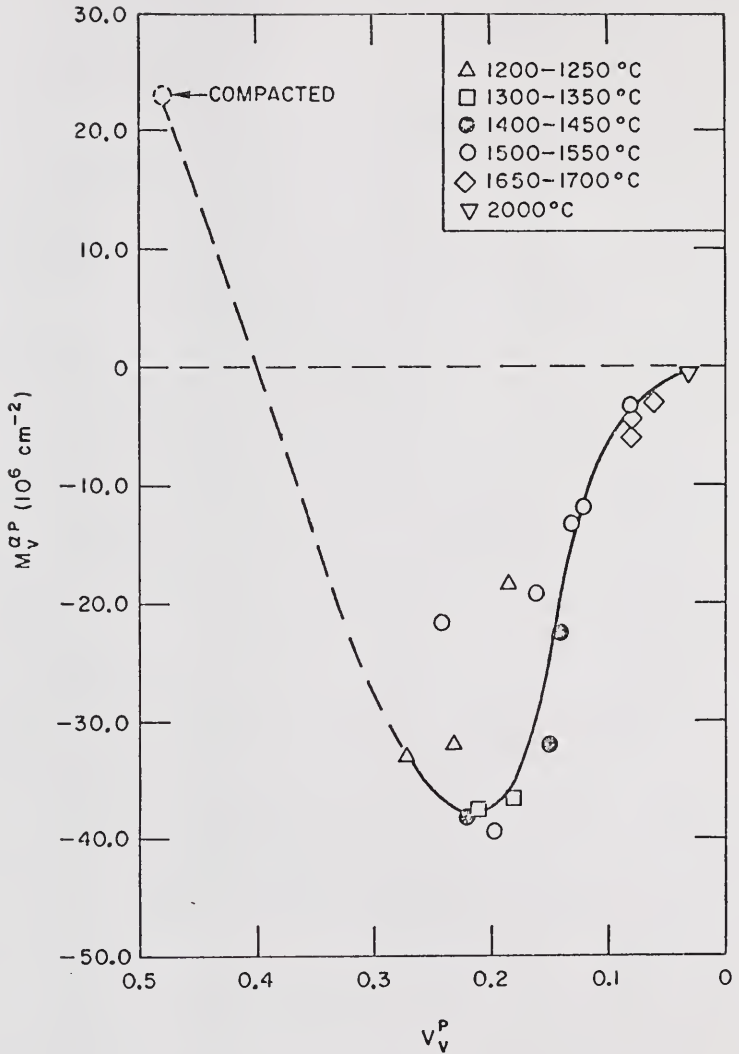


Figure 3-21. The effect of temperature on the path of total curvature change for specimens of powder lot 2 hot pressed at 3,000 psi.

The systematic effects of pressure on the path of total curvature change are shown in Figure 3-22. Increasing the pressure of hot pressing to 5,000 psi decreased the minimum in the curve to  $\sim 54 \times 10^6 \text{ cm}^{-2}$  and shifts the position of the minimum to  $V_V^P = 0.15$ . For a pressure of 1,000 psi the minimum  $M_V^{\alpha P}$  value is essentially the same as for 3,000 psi, but the volume fraction at which the minimum occurs is shifted to a value in the range 0.25-0.30.

As shown in Figure 3-23, the minimum  $M_V^{\alpha P}$  value is a function of the powder lot used to make the specimens. In addition, the volume fraction at which the minimum occurred decreased as the average particle size decreased.

Average mean curvature. The paths of  $\bar{H}^{\alpha P}$  change attain negative minima at intermediate values of  $V_V^P$  and approach zero as  $V_V^P$  approaches zero. Figure 3-24 shows that hot pressing temperature did not have an appreciable effect on the path of  $\bar{H}^{\alpha P}$  change. Figures 3-25 and 3-26 show that increasing the pressure or using a powder lot with a smaller average particle size decreased (i.e., made more negative) the minimum  $\bar{H}^{\alpha P}$  value and decreased the value of  $V_V^P$  at which the minimum occurred. A comparison of Figures 3-24 and 3-10 indicates that the minimum in the  $\bar{H}^{\alpha P}$  path for hot pressing at 3,000 psi is approximately the same as the lowest value attained for specimens cold compacted at 80,000 psi and sintered.

Negative minima in paths of  $\bar{H}^{\alpha P}$  change were also observed in a study of sintering in copper.<sup>45</sup>

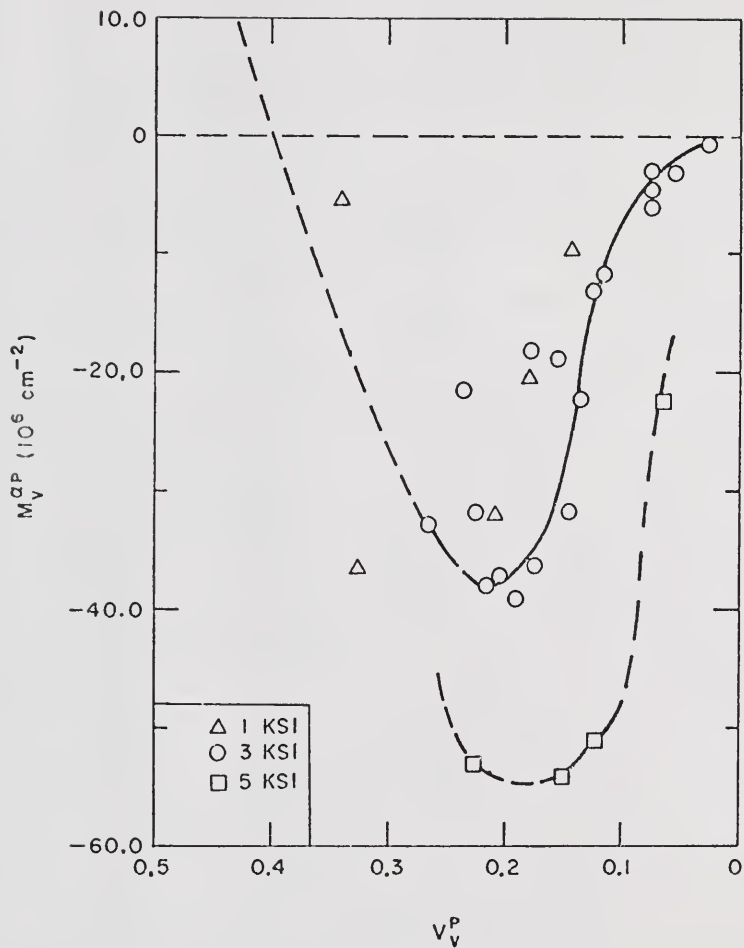


Figure 3-22. The effect of pressure on the path of total curvature change for hot-pressed specimens of powder lot 2.

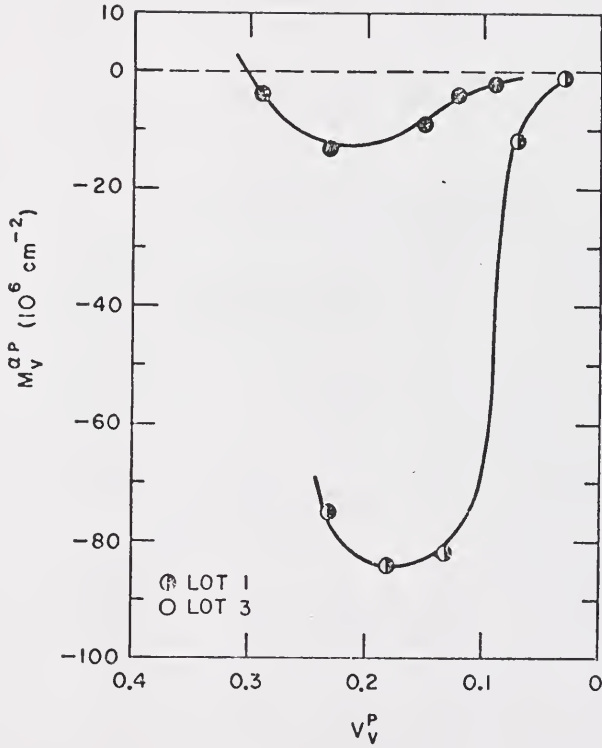


Figure 3-23. The effect of the scale of the system on the path of total curvature change for hot-pressed specimens.

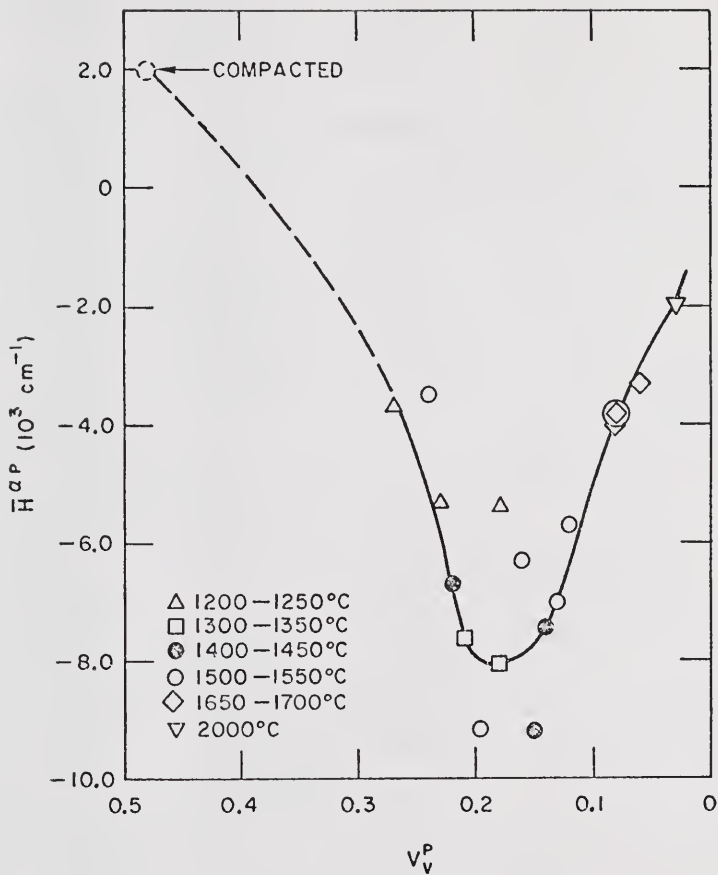


Figure 3-24. The effect of temperature on the path of average mean curvature change for specimens hot pressed from powder lot 2 at 3,000 psi.

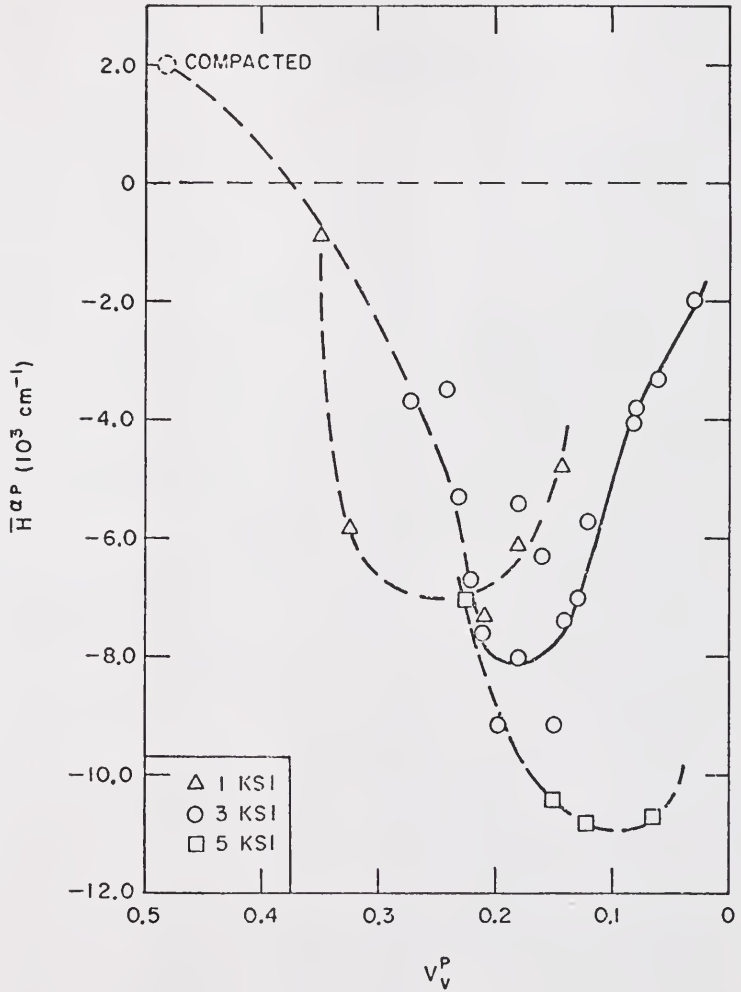


Figure 3-25. The effect of pressure on the path of average mean curvature change for hot-pressed specimens of powder lot 2.

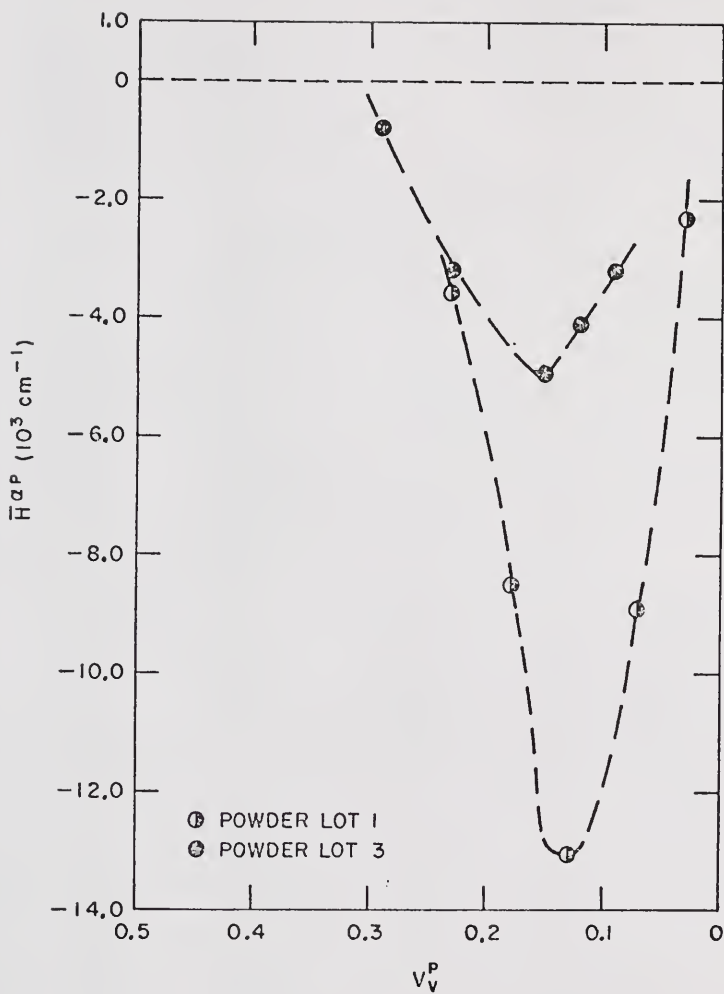


Figure 3-26. The effect of the scale of the system on the path of average mean curvature change for hot-pressed specimens.

Gross tangent count. The evolution of the gross tangent count is shown in Figure 3-27 for specimens hot pressed from powder lot 2 at 3,000 psi and temperatures in the range 1200-2000°C. The  $\pi T_{Ag}^{\alpha P}$  value for an unfired specimen compacted at 3,000 psi is assumed to be  $\sim 46 \times 10^6 \times 10^6 \text{ cm}^{-2}$ , i.e., twice the estimated value of  $M_V^{\alpha P}$ . This assumption is consistent with the appearance of polished sections through unfired compacts, e.g., Figure 3-2. The rise in  $\pi T_{Ag}^{\alpha P}$  from its initial value is indicated in Figure 3-27, although no data points were obtained in this portion of the path. However, since the specimen with the lowest density had a  $\pi T_{Ag}^{\alpha P}$  value of  $132 \times 10^6 \text{ cm}^{-2}$ , it is clear that an initial increase in  $\pi T_{Ag}^{\alpha P}$  must have occurred. A smooth decrease in  $\pi T_{Ag}^{\alpha P}$  was observed for  $V_V^P$  less than 0.25. Figure 3-27 shows that the path of  $T_{Ag}^{\alpha P}$  change was temperature-independent.

The effect of the pressure of hot pressing on the gross-tangent-count paths is shown in Figure 3-28. Increasing the pressure leads to higher  $\pi T_{Ag}^{\alpha P}$  values at a given pore volume fraction. The envelope of curves shown in Figure 3-28 is similar to that observed for the gross tangent count of conventionally sintered specimens, Figure 3-12, and the pore-solid surface area of hot-pressed specimens, Figure 3-18.

The effect of the scale of the system on the gross tangent count of specimens hot pressed at 3,000 psi is shown in Figure 3-29.

Area inflection-point count. At an inflection point on a plane curve, the curvature changes sign, and hence is locally zero. A special class of inflection points is formed by the intersection of a plane with a nonconvex surface for certain orientations and positions of the sectioning plane. Typical sections through convex and nonconvex closed

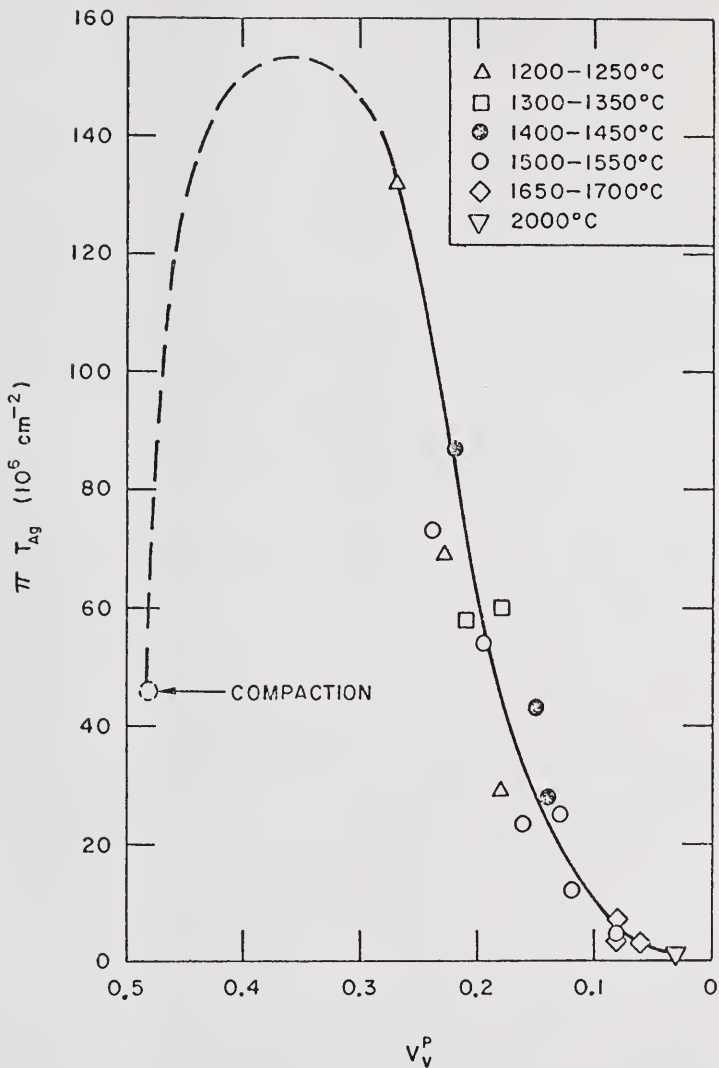


Figure 3-27. The effect of temperature on the path of gross tangent count change for specimens hot pressed from powder lot 2 at 3,000 psi.

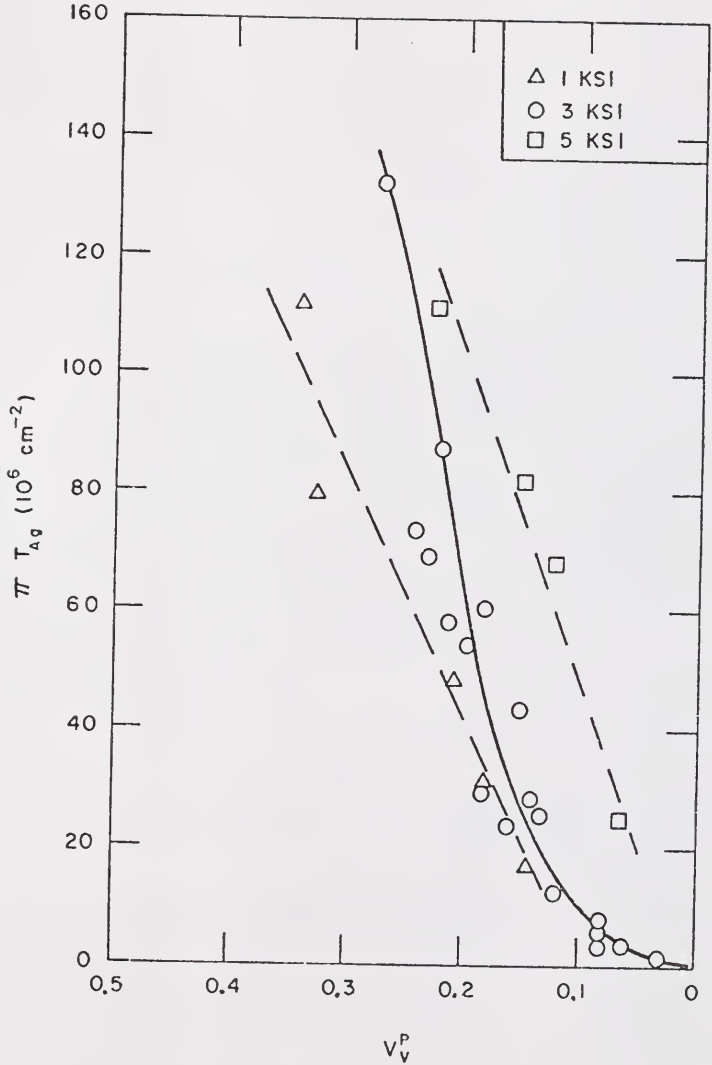


Figure 3-28. The effect of pressure on the path of gross tangent count change for hot-pressed specimens of powder lot 2.

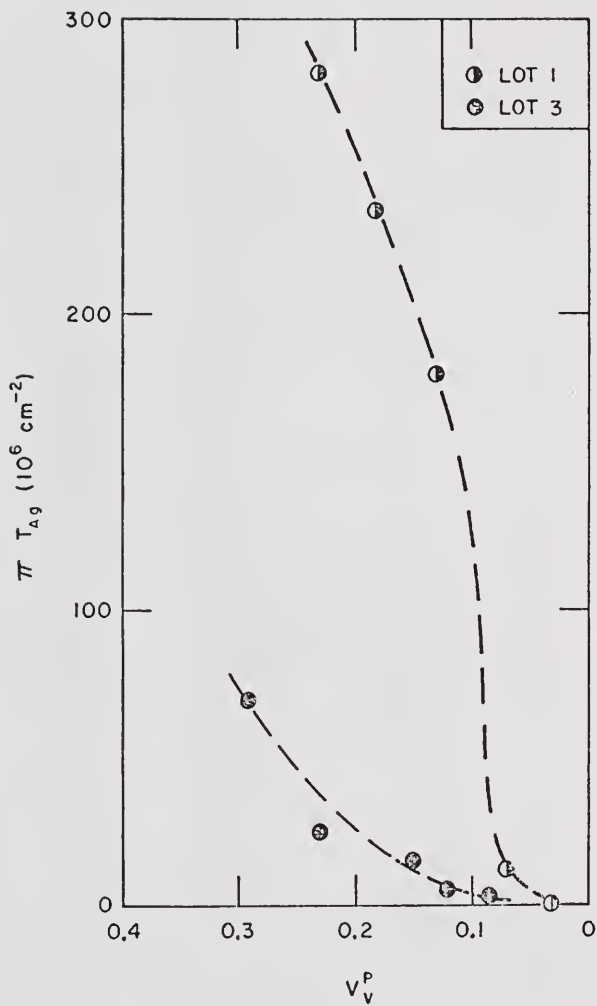


Figure 3-29. The effect of the scale of the system on the path of gross tangent count change for hot-pressed specimens.

surfaces are shown in Figure 3-30. The inflection points on the latter section are indicated. Two important results concerning this class of inflection points are stated here and proved in Appendix B:

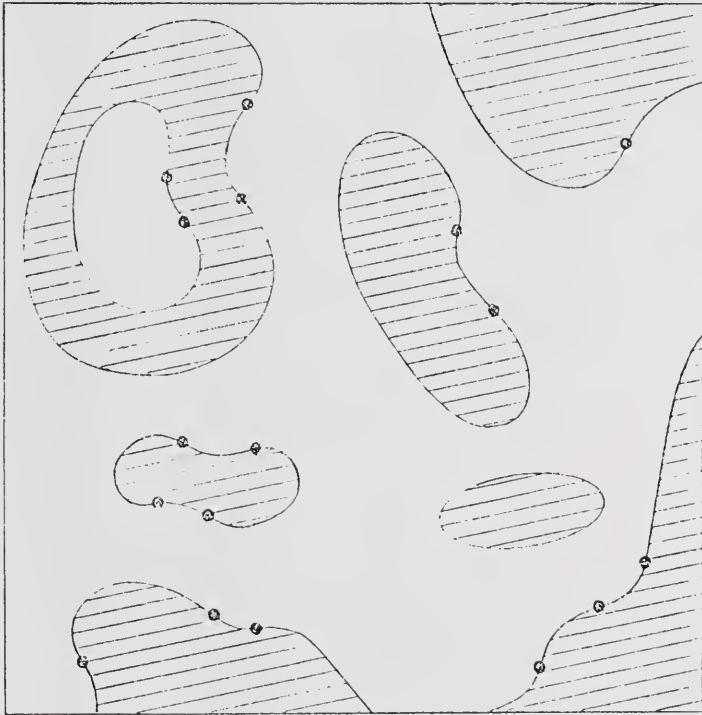
1. Inflection points can only be formed by sections through saddle surface;
2. 
$$I_A = \frac{1}{2} \iint_{S^+} k_{as} dS_V^+, \quad (1-7)$$

where  $I_A$  is the area inflection-point count,  $k_{as}$  is the curvature of asymptotic lines,<sup>152</sup> and the integration is carried out for saddle surface only.

The area inflection point was performed for the pore-solid interface of specimens hot pressed from powder lot 2 at 1500°C and 3000 psi. The variation of  $I_A^{\alpha P}$  with  $V_V^P$  for these specimens is shown in Figure 3-31.

Grain-boundary surface area. The evolution of grain-boundary surface area is shown for specimens from powder lot 2 hot pressed at 3000 psi in Figure 3-32. The curve attains a maximum value of  $\sim 1.6 \times 10^3 \text{ cm}^{-1}$  at  $V_V^P \sim 0.13$  and decreases as  $V_V^P$  drops below 0.1. The decrease is the result of grain growth in the third stage of densification.

Triple-line length. The lengths of  $\alpha\alpha P$  and  $\alpha\alpha\alpha$  triple lines are zero at the start of hot pressing, increase and reach maximum values at intermediate densities and decrease in the final portion of the densification process, as shown in Figure 3-38. The maximum  $L_V^{\alpha\alpha P}$  value was  $\sim 2.6 \times 10^7 \text{ cm}^{-2}$  and occurred at a pore volume fraction of  $\sim 0.20$ . The maximum  $L_V^{\alpha\alpha\alpha}$  value,  $\sim 0.30 \times 10^7 \text{ cm}^{-2}$ , occurred at  $V_V^P \sim 0.16$ , i.e., at a higher density than the  $L_V^{\alpha\alpha P}$  maximum. Both of these maxima occur at higher pore volume fractions than the  $S_V^{\alpha\alpha}$  maximum, Figure 3-32.



① = INFLECTION POINT

Figure 3-30. Illustration of inflection points on a plane section through a microstructure.

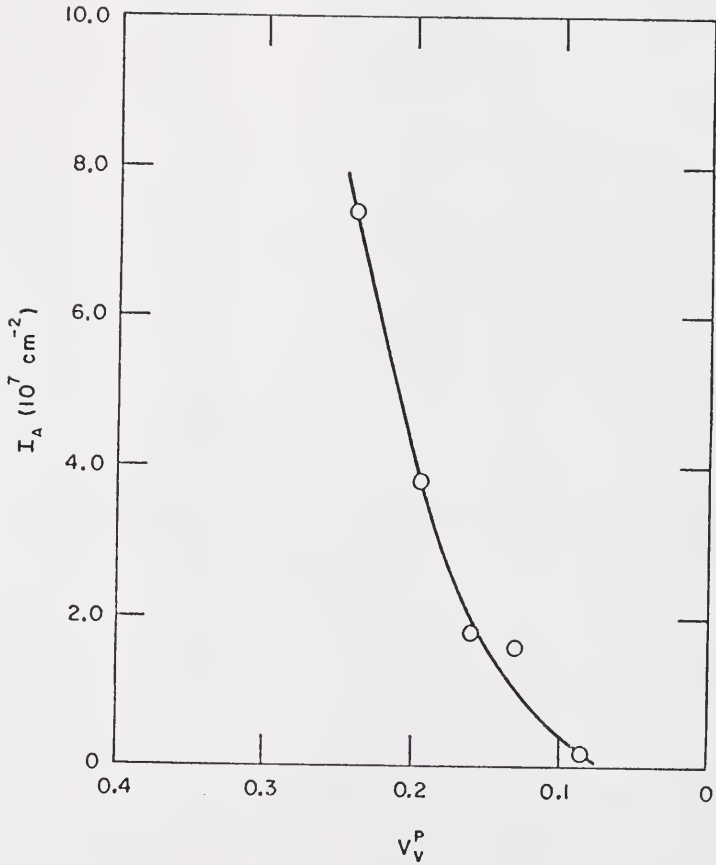


Figure 3-31. Inflection point count versus pore volume fraction for specimens of powder lot 2 hot pressed at 3,000 psi.

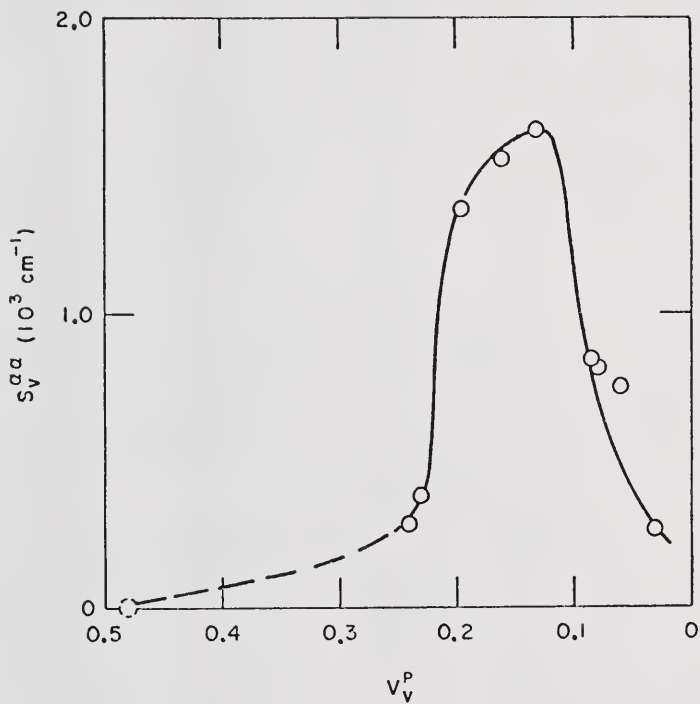


Figure 3-32. Grain-boundary surface area versus pore volume fraction for specimens of powder lot 2 hot pressed at 3,000 psi.

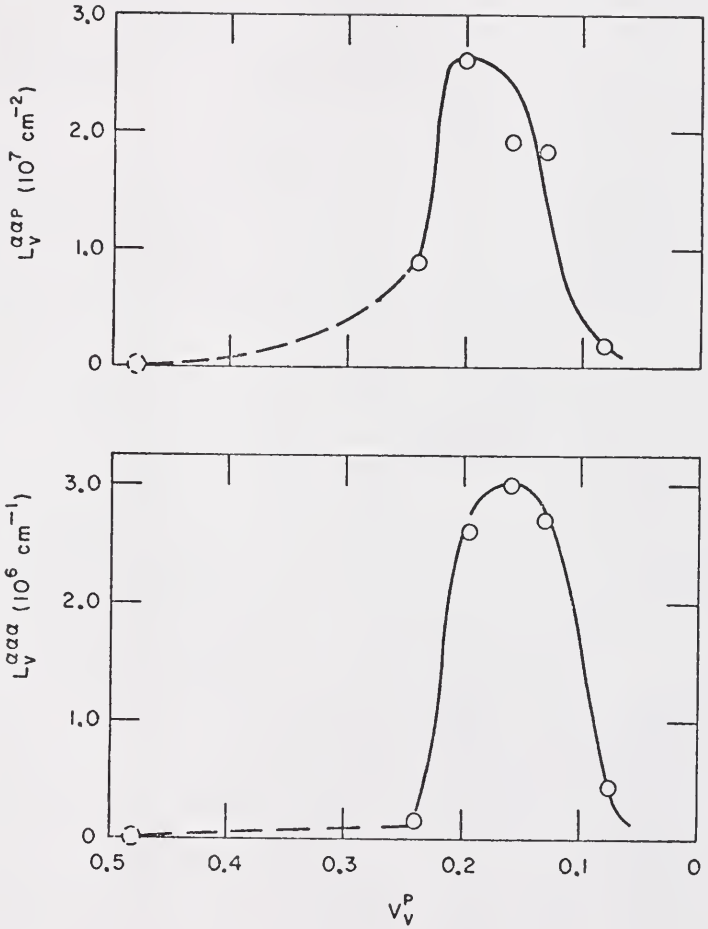


Figure 3-33. The variation of  $\alpha\alpha P$  and  $\alpha\alpha\alpha$  triple-line length with pore volume fraction for powder lot 2 specimens hot pressed at 3,000 psi.

### Contiguity

In the preceding paragraphs, portions of the paths of microstructural change for conventional sintering and hot pressing have been presented as a series of projections onto planes defined by two of the stereology parameters. One of the parameters was pore volume fraction, and it was used as the independent variable in all of the graphical representations of the data. Alternate methods of showing the relationships among the various parameters may be used. In this section one such alternate method, in which the concept of the contiguity parameter<sup>16</sup> is applied to sintered structures, is used to present some new relationships among several of the metric properties.

#### The Variation of Grain Contiguity during Sintering and Hot Pressing

The grain contiguity,  $C^\alpha$ , was defined in Equation (1-12). The relationship between grain contiguity and the mean solid and grain intercepts,  $\bar{\lambda}^\alpha$  and  $\bar{\lambda}^g$ , was given as Equation (1-13). The variation of  $C^\alpha$  with pore volume fraction for powder lot 2 specimens hot pressed at 3,000 psi is shown in Figure 3-34. The grain contiguity increases monotonically with decreasing  $V_V^P$  for these specimens. Also included in this figure are contiguity values calculated from the metric properties of loose-stack-sintered spherical and dendritic copper powder reported by Aigeltinger.<sup>42</sup> The contiguity of structures made from spherical copper powder increases for  $0.4 > V_V^P > 0.15$ , and attains a local maximum at  $V_V^P \approx 0.14$  and a local minimum at  $V_V^P \approx 0.08$ . The sintered dendritic copper powder exhibits higher contiguity values at

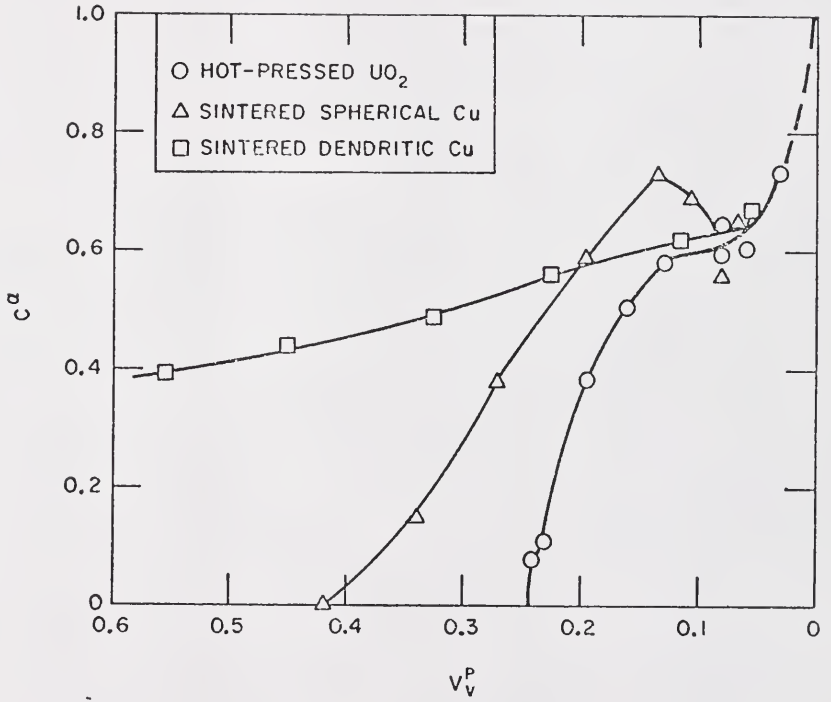


Figure 3-34. The variation of grain contiguity with pore volume fraction for loose-stack-sintered copper and hot-pressed  $UO_2$ .

lower densities than the other materials, probably because the individual powder particles were polycrystalline. All three curves merge at high density so that the paths of contiguity change are nearly identical for widely differing starting materials during late third stage sintering. Note that, by definition,  $C^\alpha$  is identically zero for a fully dense structure, in which  $S_V^{\alpha P} = 0$ .

For the available range of conventionally sintered  $UO_2$  structures,  $C^\alpha$  increases monotonically as densification occurs, Figure 3-35. The path of contiguity change was a function of cold compaction pressure for conventionally sintered specimens.

#### Contiguity and Pore-solid Surface Area

Pore-solid surface area is plotted as a function of grain contiguity for conventional sintering of powder lots 2 and 4 and for hot pressing of powder lot 2 in Figure 3-36. In the hot-pressed specimens,  $S_V^{\alpha P}$  decreased linearly with increasing  $C^\alpha$ , for  $C^\alpha \leq 0.6$ . For conventionally sintered material,  $S_V^{\alpha P}$  decreased linearly with increasing  $C^\alpha$  for all  $C^\alpha$  values obtained. (Recall that third stage sintering was not reached for the conventionally sintered structures.) The lines drawn through the points represent least-squares fits of the data. The equations of the least-squares lines are listed in Table III-6.

The linear relationships are not a result of the definition of contiguity. The equations of the lines are of the form  $S_V^{\alpha P} = mC^\alpha + b$  where  $m$  and  $b$  are the slope and ordinate intercept of the line, respectively. By substituting the definition of  $C^\alpha$  and rearranging terms, the preceding equation becomes

$$S_V^{\alpha\alpha} = \frac{S_V^{\alpha P} (S_V^{\alpha P} - b)}{2(m + b - S_V^{\alpha P})} \quad (3-7)$$

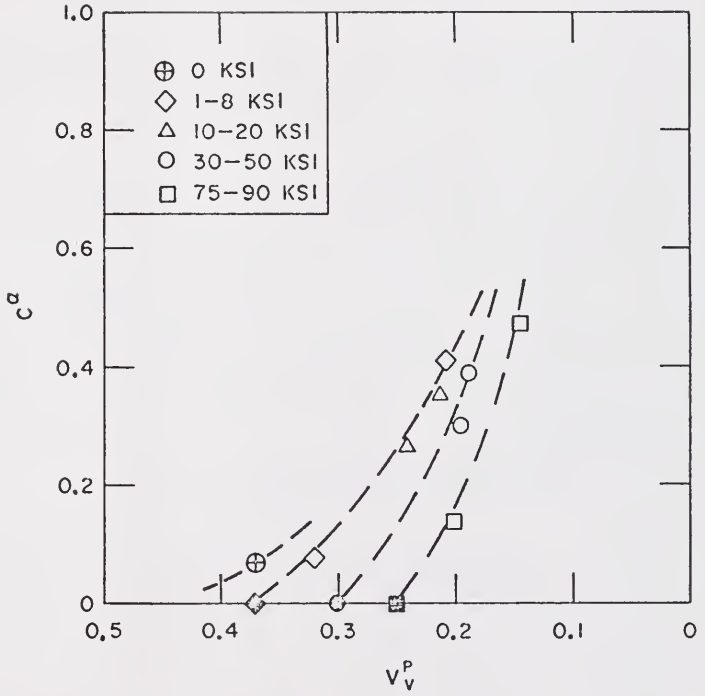


Figure 3-35. The variation of grain contiguity with pore volume fraction for conventionally sintered  $UO_2$ .

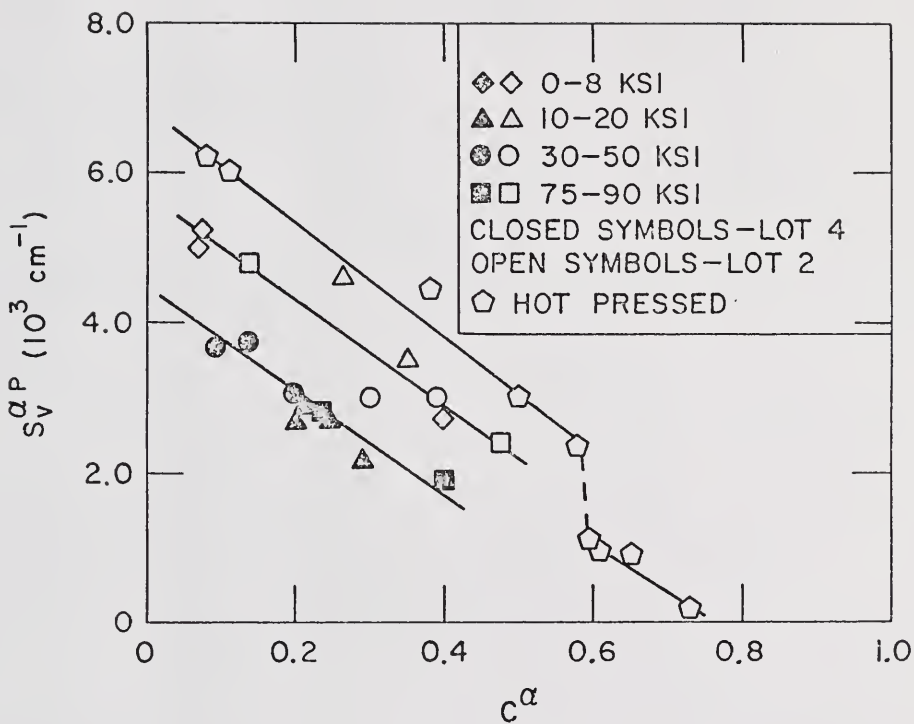


Figure 3-36. Pore-solid surface area versus grain contiguity for conventionally sintered and hot-pressed specimens.

Table III-6

Linear Regression Analyses of the  
 $S_V^{\alpha P}$  -  $C^\alpha$  Correlations

	Slope, m	Intercept, b	Correlation Coefficient, r
Lot 2 - hot-pressed	$-7.65 \times 10^3$	$6.95 \times 10^3$	0.99
Lot 2 - conventionally sintered	$-6.94 \times 10^3$	$5.73 \times 10^3$	0.94
Lot 4 - conventionally sintered	$-6.27 \times 10^3$	$4.25 \times 10^3$	0.93

That is, the observed relationships between  $S_V^{\alpha P}$  and  $C^\alpha$  define a functional dependence of  $S_V^{\alpha\alpha}$  on  $S_V^{\alpha P}$ . The latter equation is clearly not implied by the definition of  $C^\alpha$ , which treats  $S_V^{\alpha\alpha}$  and  $S_V^{\alpha P}$  as independent parameters.

The data in Figure 3-36 show that there is no effect of cold compaction pressure on the relationship of pore-solid surface area to grain contiguity for the conventional sintering. This result is in marked contrast to the description of the paths of microstructural change, which were observed to be strong functions of the cold compaction pressure. In the present case the observed relationships between  $S_V^{\alpha P}$  and  $C^\alpha$  are independent of the path of microstructural change for specimens made from a single powder lot. An alternate way of formulating this result is the statement that specimens with equal pore-solid surface areas had equal grain-boundary areas, even though the cold compaction pressure and the other metric properties were quite different. This result is limited to the pore volume fraction range examined for conventional sintering, i.e., for  $V_V^P \geq 0.1$ .

Figure 3-36 also illustrates that higher values of  $S_V^{\alpha P}$  at a constant  $C^\alpha$  can be obtained by using a powder lot with a smaller average particle size, or by hot pressing.

There is a sharp drop in  $S_V^{\alpha P}$  as  $C^\alpha$  for hot-pressed specimen exceeds 0.59. A comparison of Figure 3-36 with Figure 3-34, the graph of  $C^\alpha$  versus  $V_V^P$ , indicates that the sharp drop in  $S_V^{\alpha P}$  occurs concurrently with a decrease in slope of the  $C^\alpha$  versus  $V_V^P$  curve.

### Contiguity and Triple-line Length

The length of the  $\alpha\alpha P$  and  $\alpha\alpha\alpha$  triple lines are plotted as functions of grain contiguity  $C^\alpha$  in Figures 3-37 and 3-38, respectively. These data show that  $L_V^{\alpha\alpha P}$  and  $L_V^{\alpha\alpha\alpha}$  attain maxima at intermediate values of  $C^\alpha$ . For a given particle size, the  $L_V^{\alpha\alpha\alpha}$  maximum occurs at a higher  $C^\alpha$  value than the  $L_V^{\alpha\alpha P}$  maximum. A similar offset occurred for the variation of the triple-line lengths with pore volume fraction.

For conventional sintering, the data points for all compaction pressures and a single particle size, i.e., for several paths of microstructural change, can be described by a single curve.

The initial rise in  $L_V^{\alpha\alpha P}$  from the near zero value of unfired compacts to a nearly constant value in the second stage of conventional sintering apparently occurs at very low contiguity values and is not shown in Figure 3-36. Micrographs of the early stages of sintering, e.g., Figure 3-39, show that the rapid rise in  $L_V^{\alpha\alpha P}$  is the result of two phenomena. The first of these is the formation of multiple contacts between pairs of particles, a process made possible by the irregular topography of the particle surfaces. The second phenomenon is the sintering of large numbers of small particles to the surfaces of large particles. Both of these effects are most pronounced at the start of the sintering process. Both processes produce high perimeter-to-area ratios of the interparticle contacts, and hence lead to high  $L_V^{\alpha\alpha P}$  values at low values of  $C^\alpha$ .

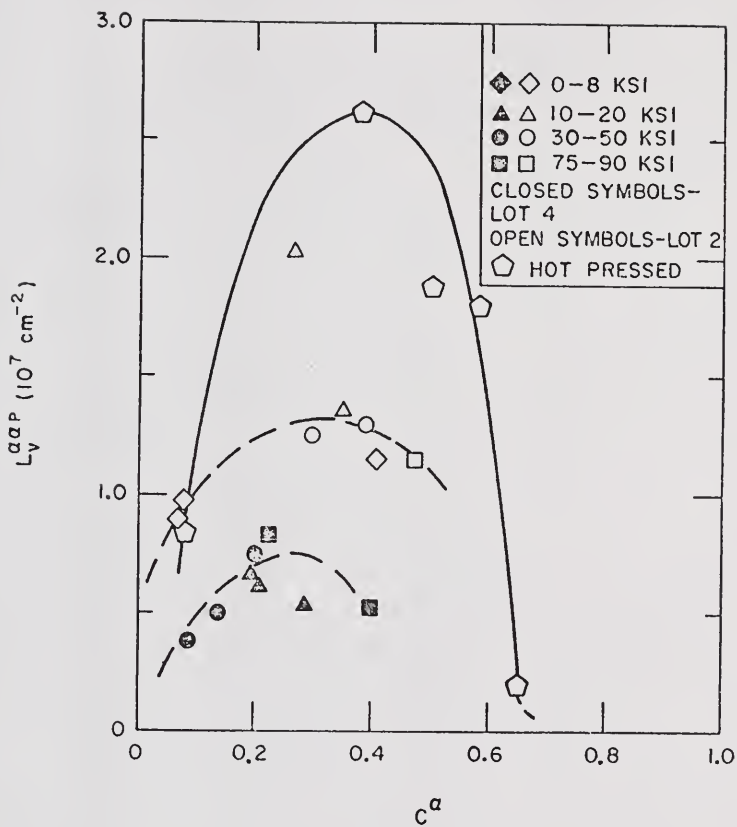


Figure 3-37. Length of  $\alpha\alpha P$  triple lines versus grain contiguity for conventionally sintered and hot-pressed specimens.

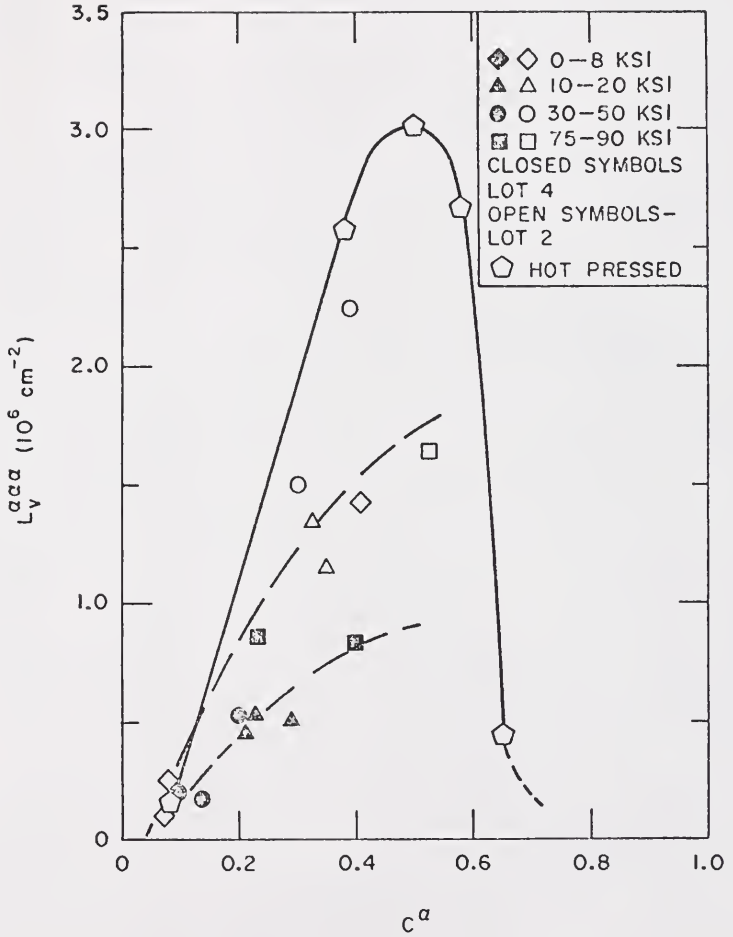


Figure 3-38. Length of  $\alpha\alpha$  triple lines versus grain contiguity for conventionally sintered and hot pressed specimens.

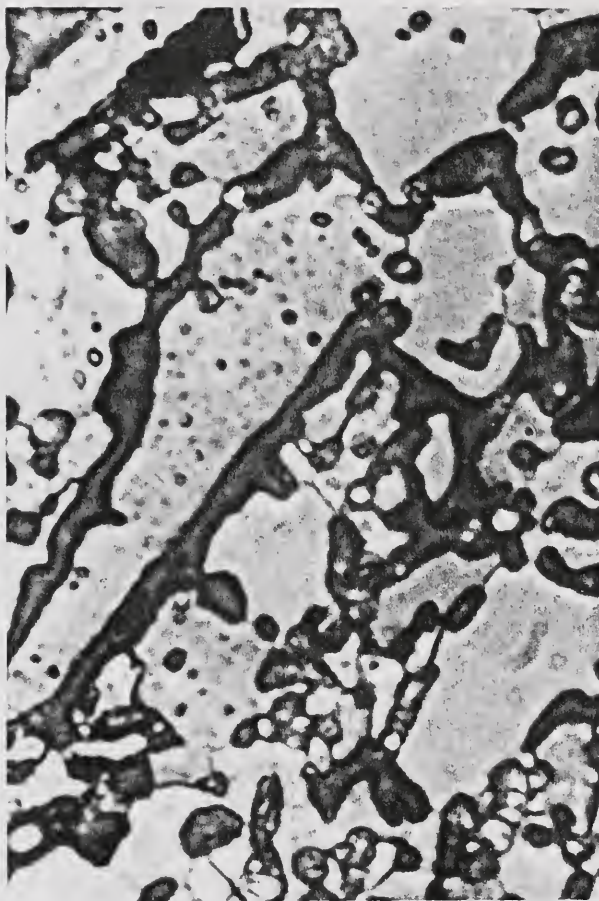


Figure 3-39. Optical micrograph of a lightly sintered specimen showing interparticle weld necks. 2000X

### Grain-face Contiguity

The grain contiguity parameter of Gurland<sup>16</sup> is defined as the ratio of the  $\alpha\alpha$  surface area to the total surface area on  $\alpha$  grains. Thus,  $C^\alpha$  represents the fraction of the  $\alpha$  grain surface that contacts other grains. In an analogous manner, it is possible to define a parameter that measures the fraction of the total boundary of  $\alpha\alpha$  grain faces that is shared with other  $\alpha\alpha$  grain faces. This parameter is a ratio of triple-line lengths, i.e.,

$$C^{\alpha\alpha} = \frac{3L_V^{\alpha\alpha\alpha}}{3L_V^{\alpha\alpha\alpha} + L_V^{\alpha\alpha P}} \quad (3-8)$$

The parameter  $C^{\alpha\alpha}$  will be called the grain-face contiguity.

The definitions of  $C^\alpha$  and  $C^{\alpha\alpha}$  are illustrated in Figure 3-40, which shows schematically two grains extracted from a sintered structure. The  $C^\alpha$  parameter is the ratio of the  $\alpha\alpha$  contact area (shaded regions) to the total surface area of the individual grains. The factor of 2 which precedes the  $S_V^{\alpha\alpha}$  terms in the  $C^\alpha$  definition, Equation (1-12), is used because each  $\alpha\alpha$  contact is shared by two grains. The  $C^{\alpha\alpha}$  parameter is defined in a similar manner. Each  $\alpha\alpha$  contact is bounded by triple lines of the type  $\alpha\alpha\alpha$  or  $\alpha\alpha P$  as indicated in Figure 3-40. The factor of 3 on the  $L_V^{\alpha\alpha\alpha}$  terms arises because each  $\alpha\alpha\alpha$  triple line is shared by three grain contacts. The parameters  $C^\alpha$  and  $C^{\alpha\alpha}$  are, in principle, independent, as illustrated in Figure 3-41. In the microstructure at the top of Figure 3-41,  $C^\alpha$  has a nonzero value, while  $C^{\alpha\alpha}$  is zero since no  $\alpha\alpha\alpha$  triple lines are present. The second microstructure shows that if all the pores are moved to the interior of the grains,  $C^{\alpha\alpha}$  can be

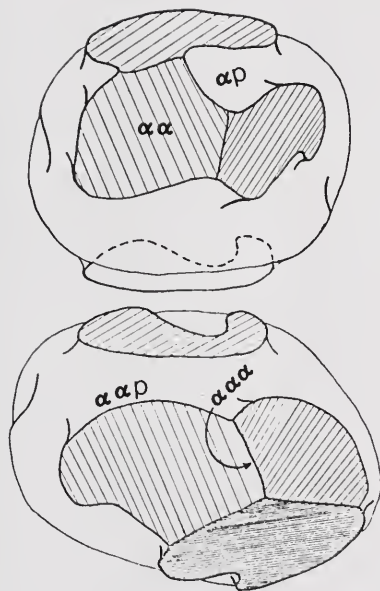


Figure 3-40. Schematic view of the structural features on grain surfaces.

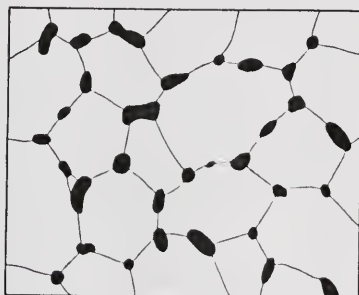
increased to its maximum value of one with little change in  $C^\alpha$ . Figure 3-41 indicates that the ratio of  $C^{\alpha\alpha}$  to  $C^\alpha$  is an index of the tendency for pores to lie within grains, and to avoid the triple junctions.\*

The relationship between  $C^{\alpha\alpha}$  and  $C^\alpha$  for sintered and hot pressed  $UO_2$  powders is shown in Figure 3-42. The points for specimens made from powder lot 4 tend to be above those for powder lot 2, but considerable overlap of the two data sets is evident. Hot pressing of specimens from powder lot 2 had a negligible effect on the relationship between  $C^{\alpha\alpha}$  and  $C^\alpha$ . Data for each particle size fall on a straight line which extrapolate to a point near the origin. The equations of the lines drawn through the data, as determined by linear regression analyses performed for powder lots 2 and 4 separately, and on the combined data, are shown in Table III-7.

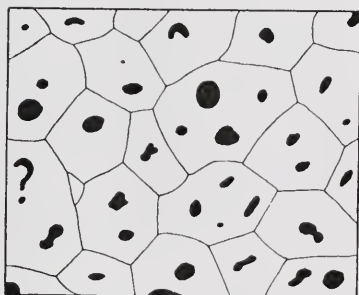
In Appendix C it will be shown that if the grain boundaries are randomly distributed through the structure, so that porosity is not preferentially associated with either the grain boundaries or the grain interiors, then  $C^{\alpha\alpha} = C^\alpha$ . Similarly, if the grain boundaries preferentially intersect the  $\alpha P$  interface and avoid the other  $\alpha\alpha$  surfaces, then  $C^{\alpha\alpha} < C^\alpha$ . The data for sintered and hot pressed  $UO_2$  powders represent examples of the latter case.

---

\*It is recognized that the proposed index fails to account for structures in which the pores lie along the grain boundaries but avoid the grain edges. The existence of this type of structure is improbable in real sintered structures, however.



$$C^a < 1$$
$$C^{aa} = 0$$



$$C^a < 1$$
$$C^{aa} = 1$$

Figure 3-41. Illustration of the independence of the grain-face contiguity and the grain contiguity.

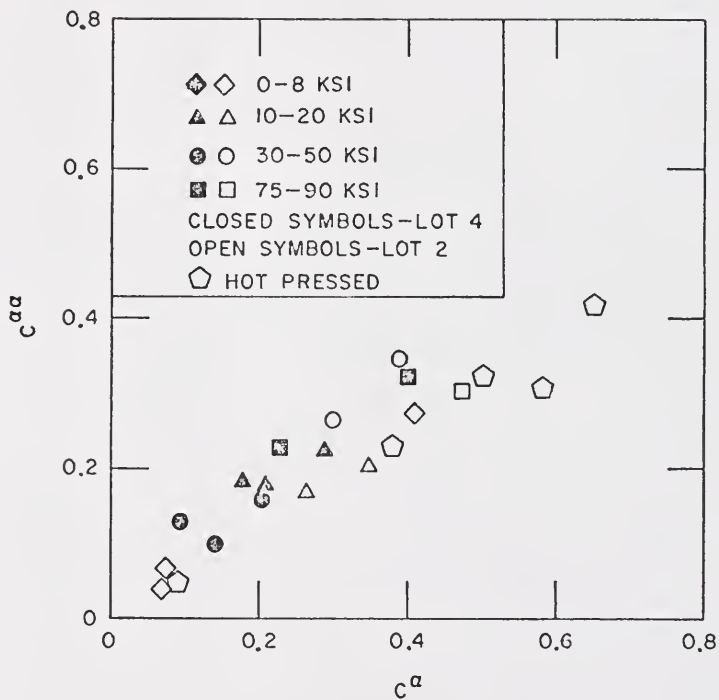


Figure 3-42. Grain-face contiguity versus grain contiguity for conventionally sintered and hot-pressed specimens.

Table III-7  
Linear Regression Analyses of  $C^{\alpha\alpha}$  on  $C^{\alpha}$

	Slope, <u>m</u>	Intercept, <u>b</u>	Correlation Coefficient, <u>r</u>
Lot 2	0.605	0.019	0.94
Lot 4	0.704	0.038	0.94
Combined Data	0.570	0.045	0.93

## Shape

### The Pore-solid Interface

The variation of the geometric shape of the pore-solid interface during conventional sintering, as reported by the  $\overline{H}^{\alpha P-\beta P}$  product, is shown in Figure 3-43. The dashed line, which indicates the decrease in  $\overline{H}^{\alpha P-\beta P}$  that occurs during cold compaction of powder lot 2 specimens, was calculated from the estimated value of  $\overline{H}^{\alpha P}$  and the observed  $S_V^{\alpha P} - V_V^P$  data, Figure 3-3. The  $\overline{H}^{\alpha P-\beta P}$  values decreased continually during sintering for  $V_V^P \geq 0.1$ . The behavior of the shape parameter during conventional sintering was not explored for  $V_V^P < 0.1$ . The data in Figure 3-43 show striation with respect to compaction pressure, indicating that the path of shape change is influenced by the microstructural state at the start of sintering. The overlap in the  $\overline{H}^{\alpha P-\beta P}$  values for different compaction pressures is due to the combined effect of two phenomena. First, the  $\overline{H}^{\alpha P-\beta P}$  has a relatively high statistical variance, which includes contributions from the variances of  $V_V^P$ ,  $S_V^{\alpha P}$ , and  $M_V^{\alpha P}$ . Second, the paths of shape change are influenced by the choice of powder lot. The powder lot effect arises because of the different densities of unfired compacts prepared by pressing different powders at the same pressure, and because the difference in particle size distributions for the various powder lots can influence  $\overline{H}^{\alpha P-\beta P}$ , even for specimens at the same density. Since  $\overline{H}^{\alpha P-\beta P}$  is a dimensionless parameter, it is not affected solely by the changes in the scale of the system caused by varying the powder lot.

The variation of  $\overline{H}^{\alpha P-\beta P}$  during conventional sintering of  $UO_2$  powders is similar to the behavior observed by Rhines et al., for the loose-stack sintering of equiaxed powders.

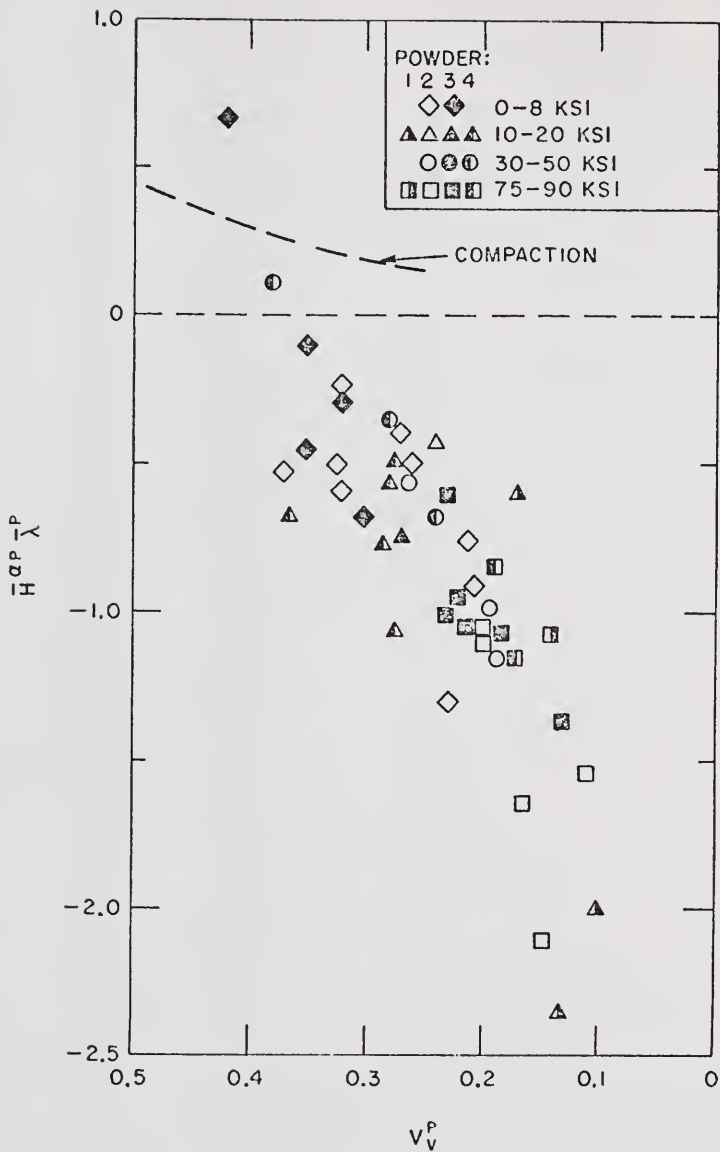


Figure 3-43. Variation of the shape parameter  $H^{\alpha P} \bar{\lambda}^P$  with pore volume fraction for conventionally sintered specimens.

The  $\overline{H}^{\alpha P-P}_{\lambda}$  values of hot-pressed specimens showed a different variation with  $V_V^P$ , Figure 3-44. This behavior is best illustrated by the data for powder lot 2 specimens hot pressed at 3,000 psi. For these conditions,  $\overline{H}^{\alpha P-P}_{\lambda}$  decreases initially, attains a minimum value at  $V_V^P \cong 0.15$ , and increases with continued densification. The data exhibit scatter, particularly after the minimum  $\overline{H}^{\alpha P-P}_{\lambda}$  value is attained. The dashed lines in Figure 3-44 indicate the minimum value and the scatter band.

The effects of varying pressure and average particle size are also shown in Figure 3-44. The initial decrease in  $\overline{H}^{\alpha P-P}_{\lambda}$  for specimens hot pressed from powder lot 2 at 1,000 psi occurs at higher pore volume fractions than the corresponding portion of the curve for 3,000 psi hot pressing. At  $V_V^P \cong 0.2$ , the two curves merge. The  $\overline{H}^{\alpha P-P}_{\lambda}$  path for hot pressing at 5,000 psi is not significantly different from the 3,000 psi data. Increasing the average particle size, by using powder lot 3, has a negligible effect on the path of shape change. However, for powder lot 1 (smallest average particle size) specimens hot pressed at 3,000 psi, the initial decrease in  $\overline{H}^{\alpha P-P}_{\lambda}$  occurs at smaller pore volume fractions than for the specimens made from powder lot 2. The minimum  $\overline{H}^{\alpha P-P}_{\lambda}$  value is smaller and occurs at a lower pore volume fraction than for the powder lot 2 specimens. Minima in the  $\overline{H}^{\alpha P-P}_{\lambda}$  path were observed for all hot-pressing conditions.

### Grain Shape

As discussed in Chapter I, the geometric shape of grains may be evaluated using terms with the general form  $L_V/(S_V)^2$ , where  $L_V$  is the length of grain edge in unit volume, and  $S_V$  is the area of grain surface in unit volume. For many of the structures examined in this study the

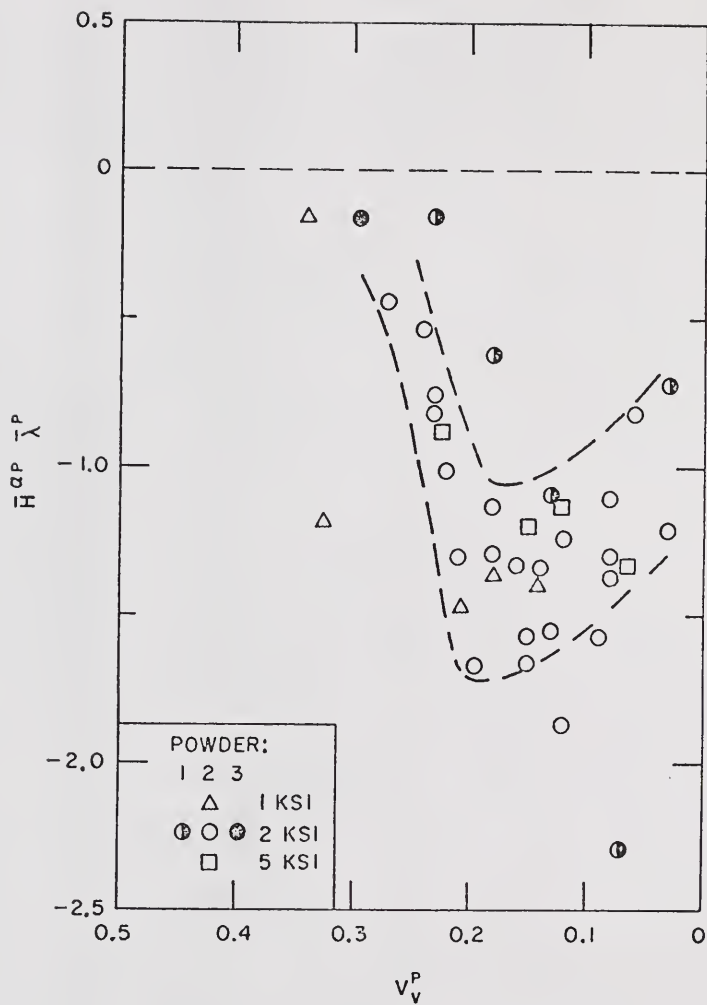


Figure 3-44. Variation of the shape parameter  $\bar{H}^{\alpha P} \bar{\lambda}^P$  with pore volume fraction for hot-pressed specimens.

lengths of both  $\alpha\alpha P$  and  $\alpha\alpha\alpha$  triple lines, and the areas of  $\alpha P$  and  $\alpha\alpha$  surfaces, were determined. These terms can be combined in several ways to generate parameters of the form shown above. The parameters used in this section are not the only ones that may be defined, nor are they necessarily the simplest. The definitions are consistent with those of the contiguity parameters in the ways that the areas and lengths are summed.

Reference to the schematic view of grains from a sintered structure, Figure 3-20, shows that the surface of each grain is covered by both  $\alpha\alpha$  and  $\alpha P$  interfaces. The  $\alpha\alpha$  contacts are bounded by  $\alpha\alpha\alpha$  and/or  $\alpha\alpha P$  triple lines, while the  $\alpha P$  interfaces are bounded by  $\alpha\alpha P$  contacts only. The geometric grain shape parameters are formed by considering the possible combinations of the two types of grain surface, and the triple-line boundaries appropriate for each combination.

It is difficult to relate specific values of the parameter to an intuitive idea of the shape of a grain. Therefore, a brief discussion of the variation of this type of shape parameter in several sample cases will be presented as an aid to the interpretation of the data obtained for sintered structures. For circular disks of a constant size,

$$\frac{L_V}{S_V^2} = \frac{1}{8\pi N_V R^3}, \quad (3-9)$$

where  $N_V$  is the number of disks in unit volume, and  $R$  is the disk radius. By inspection of the right-hand side of this equation, the shape parameter decreases if the total disk area in unit volume increases by increasing either  $N_V$  or  $R$ . From the left-hand side of the equation, it is apparent that the shape parameter will also decrease if the area of

the disks increases by ballooning or rumpling the surfaces out of the original disk planes while the perimeters are held constant. The shape parameter is increased if the outlines of the features are distorted from circular while the areas are held constant.

For the first grain shape parameter, the total edge length and interfacial area in the system are considered. Imagine that the structure is separated into individual grains, Figure 3-40. The total edge length of the broken-up structure (per unit volume of the original structure) is  $2L_V^{\alpha\alpha P} + 3L_V^{\alpha\alpha\alpha}$ . Similarly, the interfacial area of the broken-up structure is  $S_V^{\alpha P} + 2S_V^{\alpha\alpha}$  (again normalized to a unit volume of the original structure). The shape parameter that describes the relationship of total edge length to total surface area, when summed in this way, is

$$F_1 = \frac{(2L_V^{\alpha\alpha P} + 3L_V^{\alpha\alpha\alpha})}{(S_V^{\alpha P} + 2S_V^{\alpha\alpha})^2} . \quad (3-10)$$

For the case of a fully dense structure, i.e.,  $L_V^{\alpha\alpha P} = S_V^{\alpha P} = 0$ ,  $F_1$  reduces to

$$\frac{3}{2} \frac{L_V^{\alpha\alpha\alpha}}{(S_V^{\alpha P})^2}$$

which, except for the coefficient, is the same parameter used by Craig,<sup>40</sup> to describe grain shape in single-phase grain structures.

As shown in Figure 3-45, a general trend, with a broad scatter band, of increasing values of  $F_1$  with decreasing  $V_V^P$  was observed for both conventional sintering and hot pressing. There is no systematic

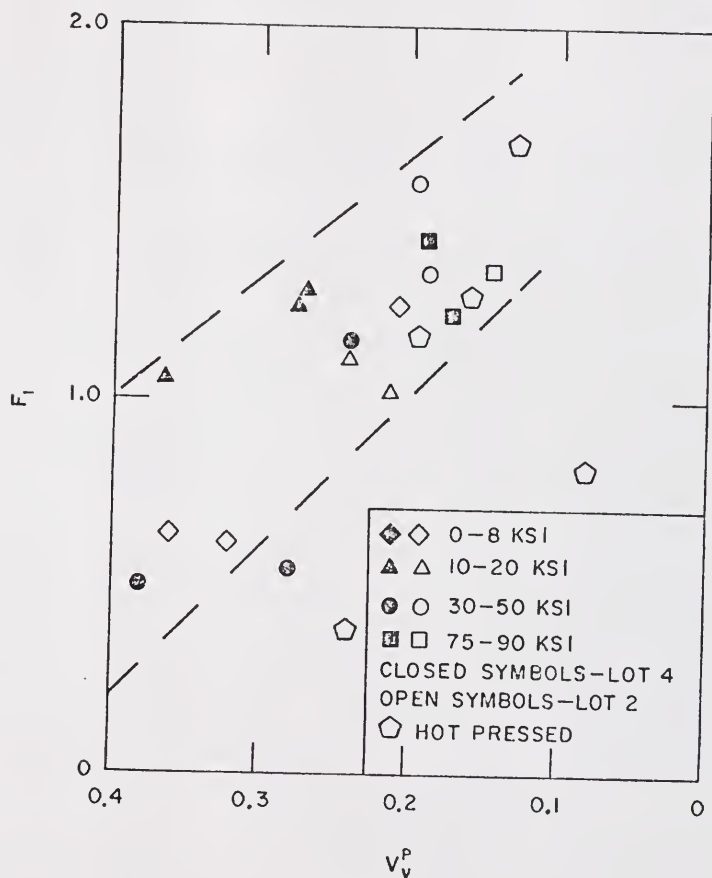


Figure 3-45. Variation of the grain shape parameter  $F_1$  with pore volume fraction for conventionally sintered and hot-pressed specimens.

effect of either cold compaction pressure, particle size, or hot pressing on  $F_1$ . The scatter in the data is essentially unaltered if  $F_1$  is plotted as a function of  $C^\alpha$ , Figure 3-46. These graphs illustrate that  $F_1$  is weakly correlated with  $V_V^P$  and  $C^\alpha$ .

Reference to Figure 3-40 shows that the  $\alpha P$  surfaces, with an area of  $S_V^{\alpha P}$ , are bounded by  $\alpha\alpha P$  triple lines, and that the length of the boundaries in the exploded structure is  $2L_V^{\alpha\alpha P}$ . The corresponding shape parameter is

$$F_2 = \frac{2L_V^{\alpha\alpha P}}{(S_V^{\alpha P})^2} \quad (3-11)$$

Graphs of  $F_2$  versus  $V_V^P$  and  $C^\alpha$  show somewhat stronger relationships, shown in Figures 3-47 and 3-48, than were obtained for the parameter  $F_1$ . The data points for conventional sintering show a systematic striation with respect to compaction pressure when  $F_2$  is plotted as a function of  $V_V^P$ , particularly for low-density specimens. When  $F_2$  is plotted versus  $C^\alpha$ , Figure 3-46, the data points collapse to a single straight line passing through the origin. The line describes the variation of the shape parameter for hot pressing, and for conventional sintering of two powder lots. By definition, Equation (3-11),  $F_2$  describes the relationship between the  $\alpha P$  interfaces and their boundaries, the  $\alpha\alpha P$  triple lines. The steady increase in  $F_2$  during sintering is a result of the concurrent increase in  $L_V^{\alpha\alpha P}$  and decrease in  $S_V^{\alpha P}$  during the first and second stage sintering. When  $L_V^{\alpha\alpha P}$  begins to decrease, as shown in Figure 3-33, the parameter  $F_2$  is probably subject to rapid fluctuations. The apparent increase in scatter at high  $C^\alpha$  values in Figure 3-47 may be due to fluctuations of this type.

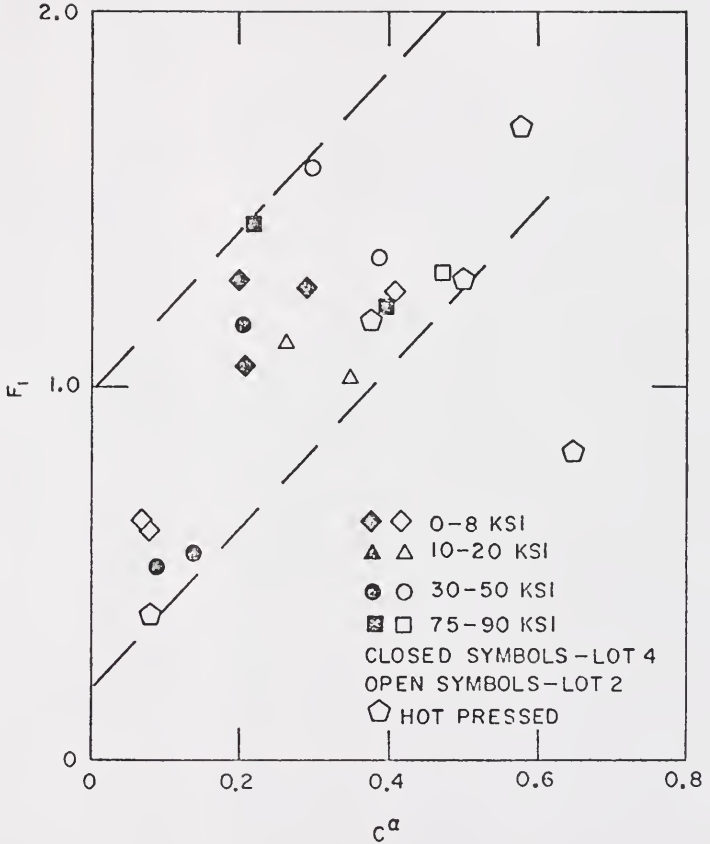


Figure 3-46. Variation of the grain shape parameter  $F_1$  with grain contiguity for conventionally sintered and hot-pressed specimens.

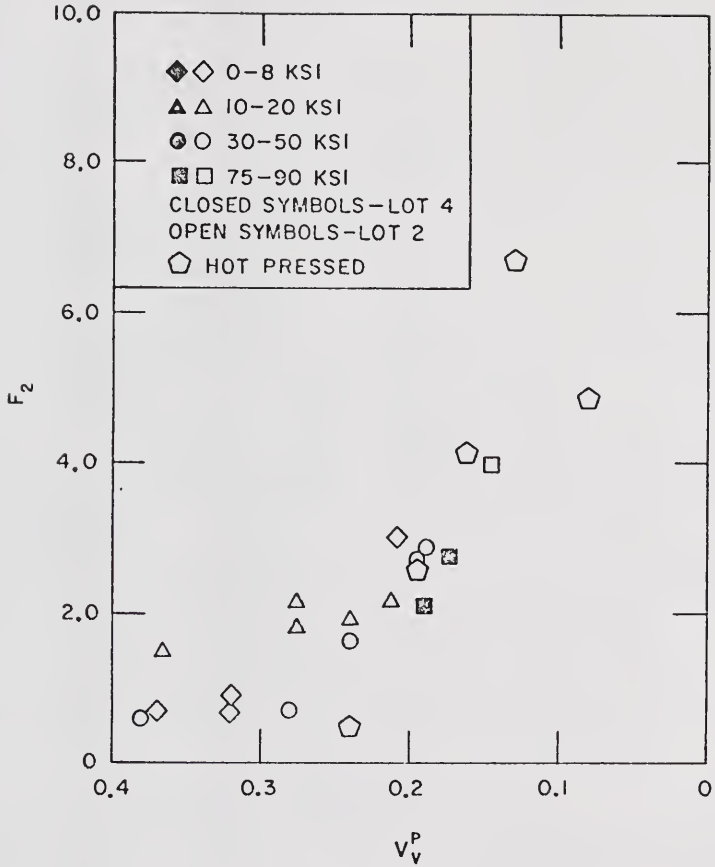


Figure 3-47. Variation of the grain shape parameter  $F_2$  with pore volume fraction for conventionally sintered and hot-pressed specimens.

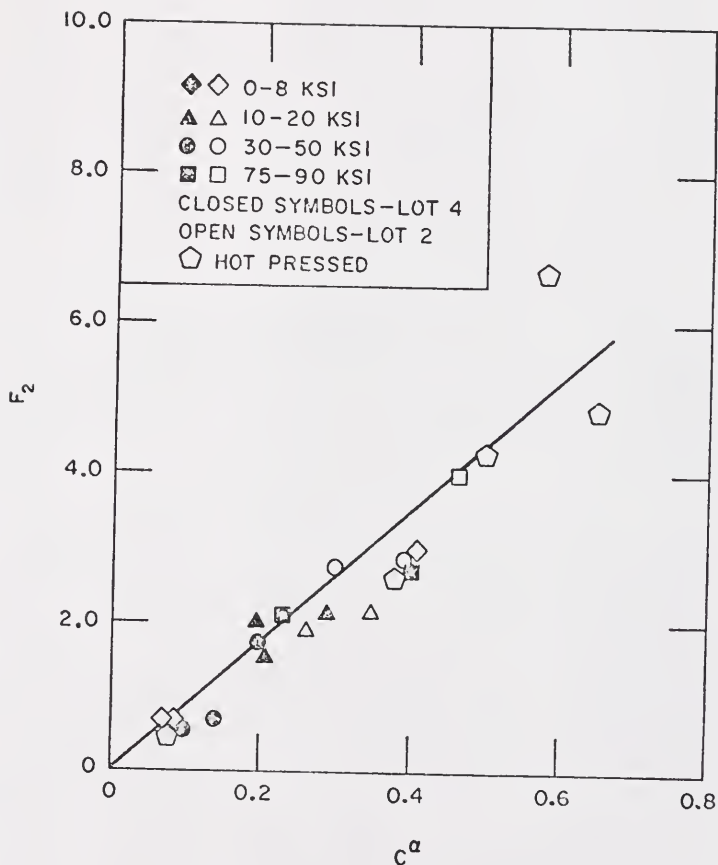


Figure 3-48. Variation of the grain shape parameter  $F_2$  with grain contiguity for conventionally sintered and hot-pressed specimens.

The linear relationship between  $F_2$  and  $C^\alpha$  can be written

$$F_2 = 0.85 C^\alpha, \quad (3-12)$$

which, after substituting the definitions of  $F_2$  and  $C^\alpha$ , and rearranging, becomes

$$L_V^{\alpha\alpha P} = 0.85 \frac{S_V^{\alpha\alpha} (S_V^{\alpha P})^2}{2S_V^{\alpha\alpha} + S_V^{\alpha P}}. \quad (3-13)$$

This relationship between  $\alpha\alpha P$  triple-line length and  $\alpha P$  and  $\alpha\alpha$  interfacial areas will probably not hold if the grain boundaries become unpinned from the porosity during third stage sintering.

A third shape parameter can be constructed by considering the individual  $\alpha\alpha$  grain contacts. The total area and perimeter of these features are  $2S_C^{\alpha\alpha}$  and  $2L_V^{\alpha\alpha P} + 6L_V^{\alpha\alpha\alpha}$ , respectively. The shape parameter is

$$F_3 = \frac{L_V^{\alpha\alpha P} + 3L_V^{\alpha\alpha\alpha}}{2(S_V^{\alpha\alpha})^2}. \quad (3-14)$$

For a fully-dense, single-phase grain structure,  $F_3$  reduces to a constant factor times the shape parameter used by Craig.<sup>40</sup>

Because of its wide range of variation, the shape parameter  $F_3$  is plotted on a logarithmic scale in Figures 3-49 and 3-50. When plotted against  $V_V^P$ ,  $F_3$  shows striation with respect to compaction pressure, particularly at high pore volume fractions. The data collapse to a single curve when  $F_3$  is plotted against  $C^\alpha$ , as shown in Figure 3-49. The increase in  $S_V^{\alpha\alpha}$  during sintering is the primary cause of the rapid decrease in  $F_3$ , which varies with the inverse square of  $S_V^{\alpha\alpha}$ .

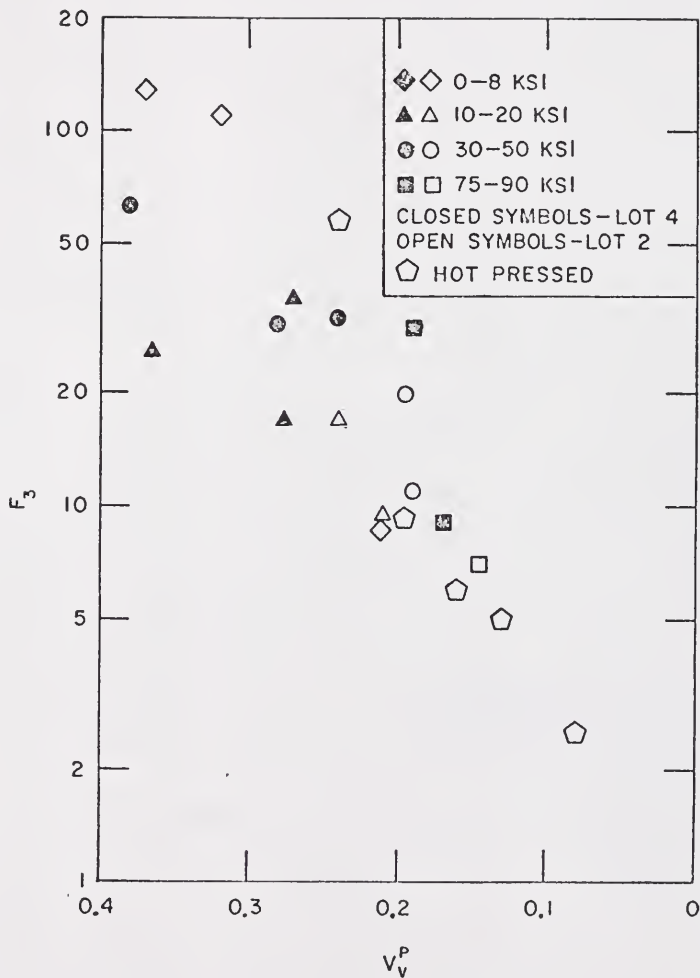


Figure 3-49. Variation of the grain shape parameter  $F_3$  with pore volume fraction for conventionally sintered and hot-pressed specimens.

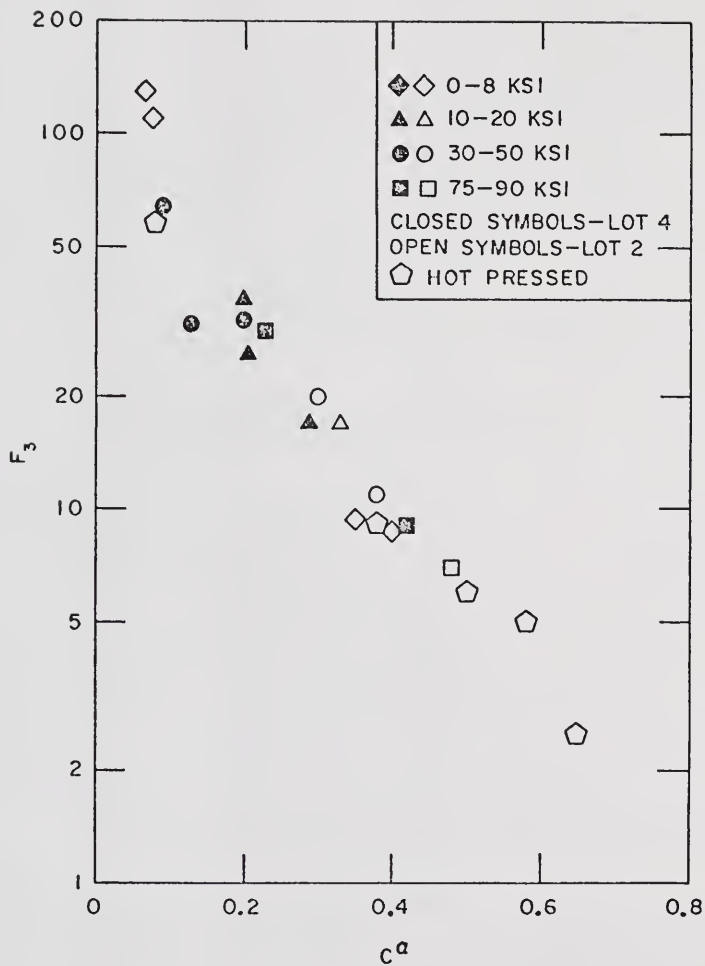


Figure 3-50. Variation of the grain shape parameter  $F_3$  with grain contiguity for conventionally sintered and hot-pressed specimens.

Finally, it is possible to group the  $\alpha\alpha$  interfaces collectively, without separating them into individual contacts. For this situation the area is unchanged from that used for  $F_3$ , but the perimeter is formed only by the  $\alpha\alpha P$  grain edges. The shape parameter is

$$F_4 = \frac{L_V^{\alpha\alpha P}}{2(S_V^{\alpha\alpha})^2} \cdot \quad (3-15)$$

The graphs of  $F_4$  versus  $V_V^P$  and  $C^\alpha$ , Figures 3-51 and 3-52, show that the behavior of this parameter during sintering is similar to that of  $F_3$ . This result is expected because  $F_4$  differs from  $F_3$  by the absence of the term  $3L_V^{\alpha\alpha\alpha}$  from the numerator. The variation of both  $F_3$  and  $F_4$  is controlled by the  $(S_V^{\alpha\alpha})^2$  term in the denominator.

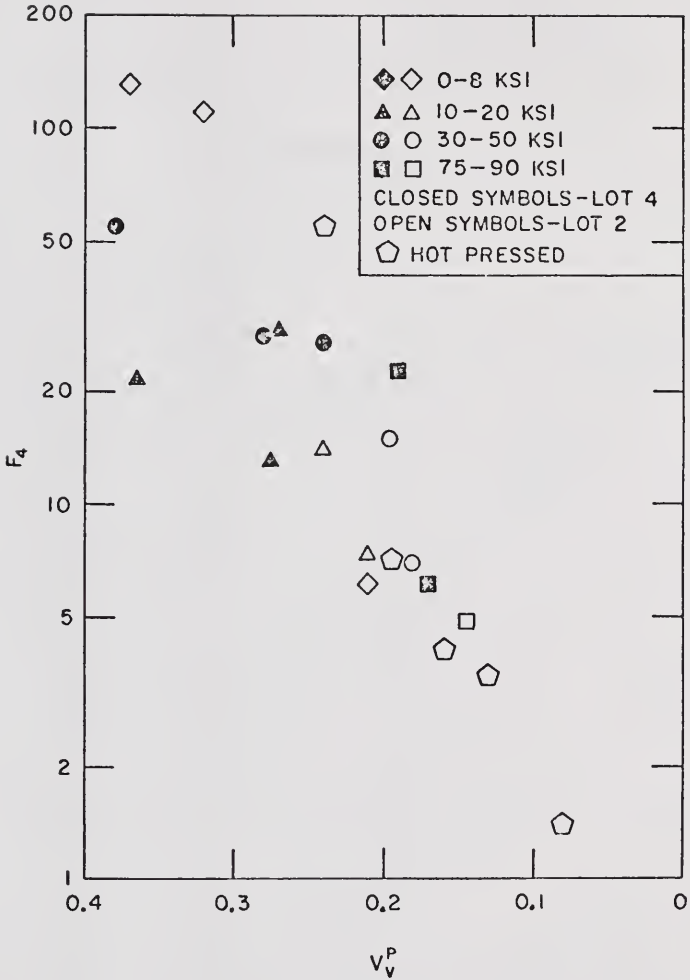


Figure 3-51. Variation of the grain shape parameter  $F_4$  with pore volume fraction for conventionally sintered and hot-pressed specimens.

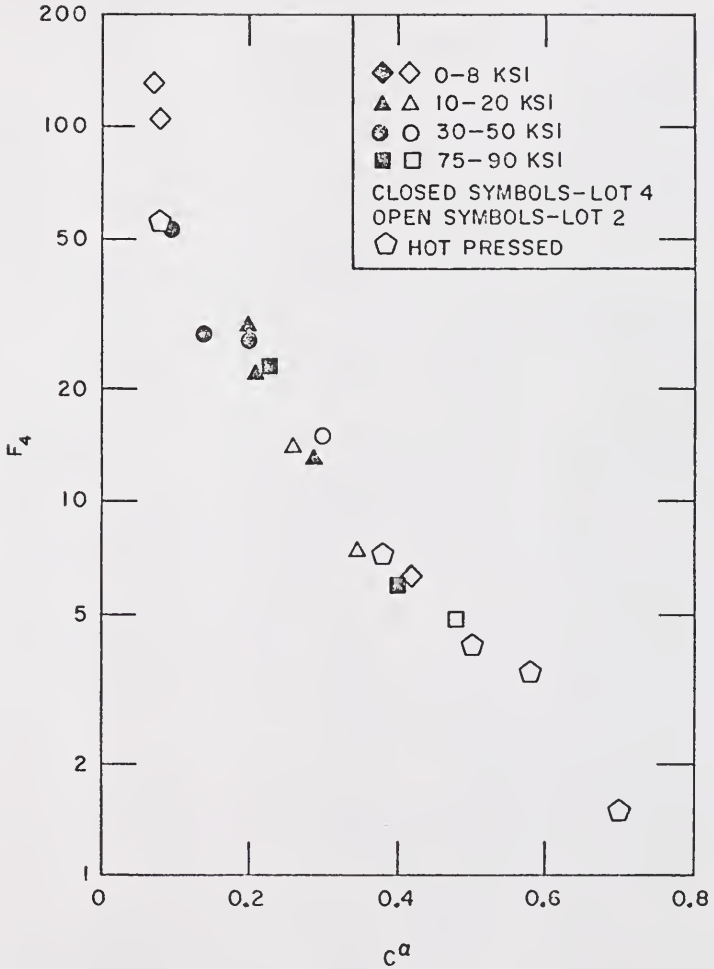


Figure 3-52. Variation of the grain shape parameter  $F_4$  with grain contiguity for conventionally sintered and hot-pressed specimens.

## CHAPTER IV

### THE ELECTRICAL PROPERTIES OF SINTERED URANIUM DIOXIDE

The room-temperature electrical conductivities, dielectric constants, and dielectric-loss tangents were evaluated for a selected set of specimens prepared from powder lots 4 and 5. The fabrication procedures and electrical measurement techniques used for these specimens were described in Chapter II.

A preliminary experiment was performed to determine the extent to which adsorbed water vapor affected the electrical measurements. A sintered specimen, which had been stored for 1 week in humid air (relative humidity =  $\sim 85$  percent), was measured in the test apparatus and found to have a capacity of  $\sim 1200$  pF at 100 Hz. Both the conductance and the capacity were functions of the test frequency for these conditions. The specimen was then heated to  $200^{\circ}\text{C}$  for 3 hours in flowing high-purity argon to remove most of the adsorbed water vapor. After cooling to room temperature, the conductance and capacity were remeasured in the argon atmosphere. Under these conditions, the conductance was independent of frequency over the range 100 Hz to 1.0 MHz. At 100 Hz, the capacity was below the detection limit of the bridge on the range used, i.e., less than 10 pF. The strong influence of adsorbed water vapor on the dielectric properties shown by this experiment indicated the necessity for close control of humidity during the electrical measurements.

### Electrical Conductivity under "Dry" Conditions

The "dry" conditions referred to in this section were obtained by heating the specimens at 200°C for 30 minutes, cooling to room temperature, and measuring the electrical properties in dry, flowing, high-purity helium. For these conditions the capacity was below the detection limit of the measuring bridge, and the conductance was independent of the test frequency.

The electrical conductivities measured under dry conditions are summarized in Table IV-1, along with selected quantitative stereology measurements, for a group of specimens fabricated from powder lots 4 and 5. The electrical conductivities are in the ranges  $8.5 \times 10^{-4}$  to  $17.2 \times 10^{-4} \text{ ohm}^{-1} \text{ cm}^{-1}$  for lot 4 specimens, and  $0.09 \times 10^{-4}$  to  $9.2 \times 10^{-4} \text{ ohm}^{-1} \text{ cm}^{-1}$  for lot 5 specimens. The order of magnitude of these values indicates that conduction occurred by defect-controlled semi-conduction mechanisms.

The electrical conductivities of the sintered  $\text{UO}_2$  specimens can be used to illustrate the technique for developing empirical relationships between physical properties and the quantitative stereology measurements. The theoretical and experimental studies of the electrical properties of heterogeneous systems, which were discussed in Chapter I, showed that the electrical conductivity of a dispersed two-phase system is a function of the volume fraction of the dispersed phase. Therefore, it is reasonable to search for a relationship between the electrical conductivity,  $\sigma_o$ , and  $V_V^P$  for the multiply connected two-phase structures produced in this study. The result of this attempted correlation is

Table IV-1

Electrical Conductivities and Selected Quantitative  
Stereology Results for UO<sub>2</sub> Specimens

Sample No.	Powder Lot	Comp. Press. (ksi)	V <sub>V</sub> <sup>P</sup>	S <sub>V</sub> <sup>αP</sup> (10 <sup>3</sup> cm <sup>-1</sup> )	S <sub>V</sub> <sup>αα</sup> (10 <sup>3</sup> cm <sup>-1</sup> )	C <sup>α</sup>	σ (10 <sup>-4</sup> ohm <sup>-1</sup> cm <sup>-1</sup> )	
							0% R.H. <sup>a</sup>	100% R.H. <sup>a</sup>
39	4	10	0.366	2.85	0.376	0.208	16.3	14.8
40	4	80	0.191	2.82	0.426	0.232	15.6	14.6
41	4	30	0.238	3.01	0.375	0.205	13.4	12.0
43	4	10	0.273	2.67	0.331	0.199	12.5	10.7
44	4	10	0.279	2.82	0.405	0.223	16.6	15.1
45	4	30	0.280	3.75	0.297	0.137	8.70	8.57
46	4	30	0.381	3.66	0.187	0.093	8.75	8.69
47	4	10	0.275	2.17	0.441	0.289	16.8	15.2
48	4	80	0.173	1.94	0.648	0.401	17.2	16.0
49	5	30	0.301	2.15	0.083	0.072	0.095	0.081
50	5	80	0.286	2.28	0.142	0.111	6.60	6.05
52	5	80	0.219	1.91	0.305	0.242	9.20	8.30

<sup>a</sup>R.H. = relative humidity.

shown in Figure 4-1. This figure shows a general trend of increasing electrical conductivity with decreasing pore volume fraction. However, the scatter of the data points indicates that  $V_V^P$  is not the only parameter that controls the electrical conductivity in this system.

Varying degrees of correlation are also observed when  $\sigma_o$  is plotted as a function of the other metric properties. An example of an intermediate amount of correlation is exhibited by the  $\sigma_o$  versus  $S_V^{\alpha P}$  graph in Figure 4-2. For specimens prepared from powder lot 4,  $\sigma_o$  decreased with increasing  $S_V^{\alpha P}$ . This relationship illustrates one of the ways in which information is obtained from comparisons of the physical properties with microstructure for a series of specimens. Note that if electrical conduction occurred along the pore-solid surface, e.g., through a conductive film adsorbed on the surface, an increase in  $\sigma_o$  with increasing  $S_V^{\alpha P}$  would be expected. Since the observed correlation was of the opposite sense, it is possible to conclude that conduction along the pore-solid interface did not make an important contribution to the electrical conduction process.

The strongest correlation obtained by comparing the electrical conductivity with the quantitative stereology parameters is shown in Figure 4-3, in which  $\sigma_o$  is plotted as a function of the grain-boundary surface area,  $S_V^{\alpha\alpha}$ . A linear increase in conductivity occurred as  $S_V^{\alpha\alpha}$  increased from  $\sim 0.05 \times 10^3$  to  $\sim 0.45 \times 10^3 \text{ cm}^{-1}$ . A single data point at  $\sigma_o = 17.2 \times 10^{-4} \text{ ohm}^{-1} \text{ cm}^{-1}$ ,  $S_V^{\alpha\alpha} = 0.648 \times 10^3 \text{ cm}^{-1}$ , suggests that grain-boundary surface area has a relatively minor effect on electrical conductivity for  $S_V^{\alpha\alpha}$  values in excess of  $0.5 \times 10^3 \text{ cm}^{-1}$ . The strength of

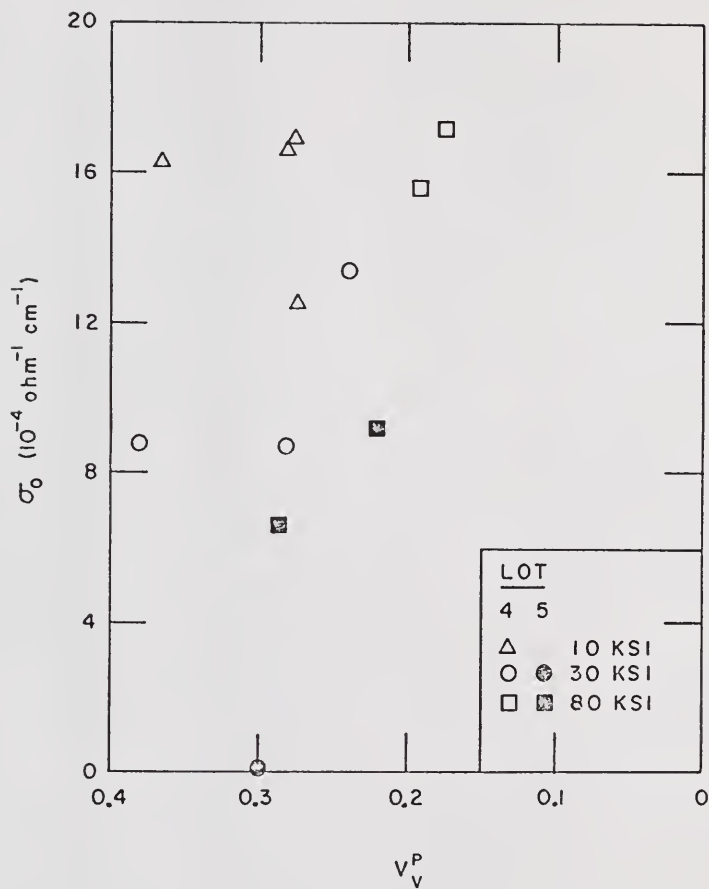


Figure 4-1. Electrical conductivity under dry conditions versus pore volume fraction.

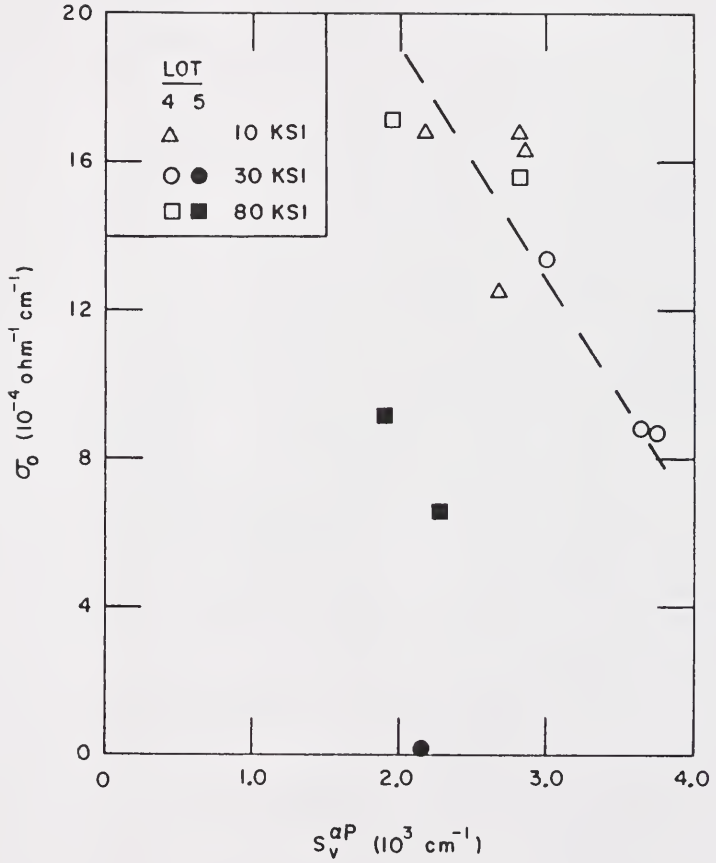


Figure 4-2. Electrical conductivity under dry conditions versus pore-solid surface area.

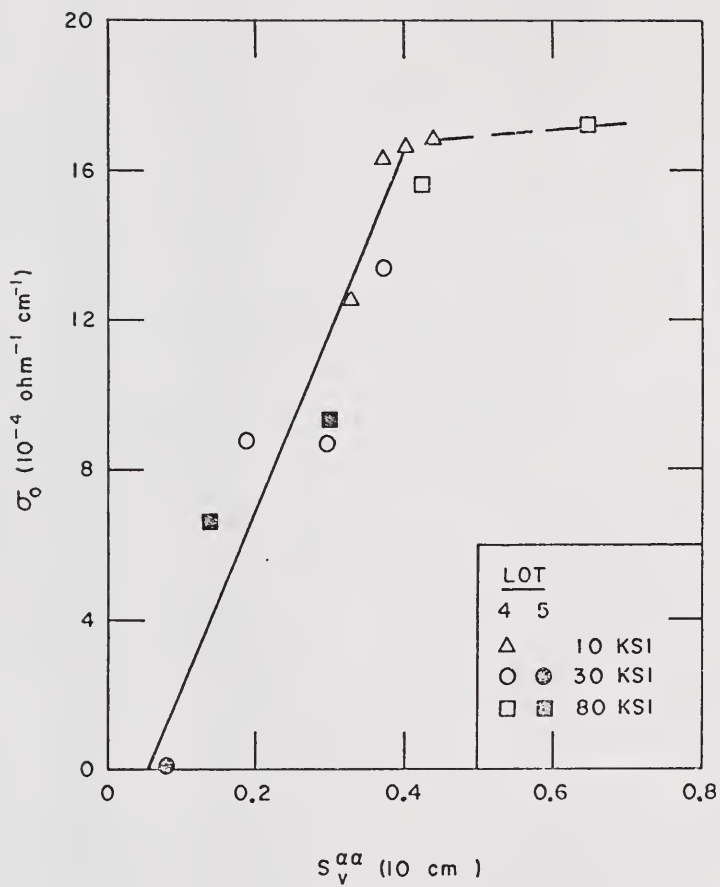


Figure 4-3. Electrical conductivity under dry conditions versus grain-boundary surface area.

this correlation relative to the other attempts at describing the electrical conductivity in terms of the quantitative stereology parameters, e.g., Figures 4-1 and 4-2, suggests that the grain-boundary surface area played a direct role in controlling the electrical conductivity of these specimens.

Two mechanisms can be postulated to explain the observed relationship between  $\sigma_o$  and  $S_V^{\alpha\alpha}$ . The first of these is based on grain-boundary conduction and may be important if the electrical conductivity of the grain boundaries is significantly higher than that of the bulk. In this case, the system can be modeled as a three-phase structure in which the constituent with the highest conductivity, i.e., the grain boundaries, is embedded in a matrix consisting of two lower-conductivity constituents, i.e., the  $\alpha$  grains and the pores. In the early stages of sintering, when the individual grain contacts are isolated, their contribution to the overall conductivity can, in principle, be described with formulae similar to those developed in the theories of the electrical properties of heterogeneous systems described in Chapter I. Such a mathematical treatment is made difficult by the need to know the grain-boundary and bulk conductivities, and the "thickness" of the region adjacent to the boundaries that is responsible for the enhanced electrical conduction.

Unfortunately, the postulate of higher electrical conductivity along the grain boundaries is difficult to verify. However, the mechanism of enhanced grain-boundary conduction is consistent with the observed relationship between  $\sigma_o$  and  $S_V^{\alpha\alpha}$ , and must be considered in a discussion of electrical conduction in sintered  $UO_2$ .

The second mechanism that can be used to explain the effect of the grain-boundary surface area on the electrical conductivity is based on conduction through the bulk, rather than along the grain boundaries. However, for bulk conduction to occur, electrical charge must cross the grain boundaries in order to pass from grain to grain. During the neck-formation and -growth stages of sintering the grain contacts define the minimum areas through which current must flow, and therefore are the circuit elements with highest resistance. For electrical conduction through the bulk, the high resistance associated with the constriction at the grain contacts can substantially reduce the overall electrical conductivity of the structure, particularly at the start of sintering. The increase in  $S_V^{\alpha\alpha}$  that occurs with continued sintering reduces the grain-contact constrictions and thus allows an increase in the electrical conductivity.

At some point in the sintering process, the grain contacts no longer form a constriction in the current path. As sintering continues past this point, further increases in  $S_V^{\alpha\alpha}$  would not be expected to directly result in increases in the bulk electrical conductivity. However, the formation of additional grain-grain surface area can continue to influence the contribution of grain-boundary conduction mechanisms to the total electrical conductivity.

A further discussion of the effects of microstructural variables on electrical conduction by bulk and grain-boundary mechanisms is contained in Chapter 5.

Electrical Conductivity and Dielectric Properties  
under Humid Conditions

The same specimens used for conductivity measurements under dry conditions were remeasured after being allowed to equilibrate with air saturated with water vapor at  $23 \pm 2^{\circ}\text{C}$ . The electrical conductivity values measured at 100 Hz under these conditions are summarized in Table IV-1. Note that these values are from  $\sim 1$  to  $\sim 17$  percent less than the corresponding conductivities measured under dry conditions. This result is in direct contradiction with studies of the electrical conductivities of systems in which water vapor is adsorbed on the internal surfaces of powder compacts,<sup>153</sup> as well as theoretical treatments,<sup>154</sup> in which the electrical conductivity of the specimen increases when water vapor is adsorbed on the surfaces. The anomalous results of the present study are believed to be due to a degradation of the electrode contacts. The electrode effects, which were variable from specimen to specimen, could not be separated from the effects due to the adsorbed water vapor. As a result, correlation could not be obtained between the stereology parameters and the electrical properties of the specimens with adsorbed water vapor. For completeness, a summary of the electrical measurements performed for the specimens with water vapor adsorbed is included in Appendix D.

CHAPTER V  
DISCUSSION

The Path of Microstructural Change

The Effect of Compaction Pressure

In Chapter III, the paths of change of all of the metric properties examined were found to be functions of cold compaction pressure for conventionally sintered specimens and of the pressure used during the fabrication of hot-pressed specimens. For the case of conventionally sintered specimens, the effect of compaction pressure was particularly striking, since the only geometric change that occurred during cold pressing was a rearrangement of the powder particles. The effects of this particle rearrangement on microstructural evolution during a subsequent sintering treatment can be demonstrated by a detailed analysis of some of the data collected during this research.

Pore-solid surface area. The most obvious result of compaction-induced particle rearrangement is the motion of additional pore-solid surface area into a unit volume of the structure. A portion of this excess surface area persists well into the sintering process and gives rise to the envelope of surface area paths. An inspection of the curves in Figure 3-5 suggests that the rate at which surface area decreases from an initial precompact condition increases as the excess surface area (above that expected for a loose-stack sintered specimen with the same pore volume fraction) increases. Here the term "rate" is used to

denote the change in a metric property for a unit change in  $V_V^P$ . The simplest assumption about the form of the  $S_V^{\alpha P} - V_V^P$  curves is that the difference between the instantaneous rate of change of a curve for sintering with precompaction, and the slope of the straight line that describes loose-stack sintering, is proportional to the excess surface area. That is,

$$\frac{dS_V}{dV_V} - \frac{S_V^O}{V_V^O} = g(S_V - V_V \frac{S_V^O}{V_V^O}) , \quad (5-1)$$

where  $V_V^O$  and  $S_V^O$  are the pore volume fraction and specific surface area for a loose stack of powder,  $\frac{S_V^O}{V_V^O}$  is an approximation of the slope of the  $S_V$  versus  $V_V$  plot for loose-stack sintering,  $V_V$  and  $S_V$  are the instantaneous values of volume fraction and surface area,  $g$  is a constant.\* The term  $(S_V - V_V S_V^O/V_V^O)$  is the excess surface area of a structure that is sintered after precompaction. This differential equation has the general solution

$$S_V = V_V \frac{S_V^O}{V_V^O} + h \exp(gV_V) \quad (5-2)$$

where  $h$  is an integration constant that can be evaluated by specifying the initial condition on (5-2). The initial condition is that the surface area of a compacted, unsintered specimen is given by the relationship used to describe the path of surface area change for cold compaction:

---

\*The superscript  $\alpha P$  is omitted from  $V_V$  and  $S_V$  in this discussion for sake of clarity.

$$S_V' = S_g \delta_o (1 - V_V') \quad (3-3)$$

or

$$S_V' = S_V^o \frac{(1 - V_V')}{(1 - V_V^o)} \quad (5-3)$$

where the primes refer to the metric properties of unfined compacts and, by definition,  $S_V^o = S_g \delta_o (1 - V_V^o)$ . If  $S_V$  and  $V_V$  in (5-2) are set equal to  $S_V'$  and  $V_V'$ , respectively, and (5-3) is substituted for  $S_V'$ , the resulting expression can be solved for  $h$  to obtain

$$h = \frac{S_V^o (V_V^o - V_V')}{V_V^o (1 - V_V^o)} \exp(-gV_V') . \quad (5-4)$$

This expression for  $h$  is then substituted into (5-2), to obtain

$$S_V = \frac{S_V^o}{V_V^o} \left[ V_V + \frac{(V_V^o - V_V')}{(1 - V_V')} \exp g(V_V - V_V') \right] . \quad (5-5)$$

$V_V'$  is a function of compaction pressure, as shown in Figure 3-1 and Equation (3-2) for unfined compacts from powder lot 2. The term  $S_V^o/V_V^o$  is the ratio of surface area to pore volume fraction for loose-stack sintering, and is estimated to be  $1.35 \times 10^4$  from the data in Table III-1. The pore volume fraction of a loose stack of powder lot 2,  $V_V^o$ , is taken to be 0.59, the constant term in Equation (3-2). This value is close to 0.61, the measured value of the loose-stack volume fraction of this powder. The constant  $g$  was determined to be 34.8 by a linear regression analysis of the data for powder lot 2.

Values of  $S_V$  calculated from (5-5) are compared with experimental data in Figure 5-1. The agreement is quite good for all four ranges of compaction pressure, and thus provides strong evidence that the rate at which a surface area path for a cold-compacted specimen approaches the path for loose stack sintering is proportional to the instantaneous excess surface area. These relationships hold for pore volume fractions between 0.10 and 0.37 and compaction pressures between 1,000 and 90,000 psi.

An equation of the same form as (5-5) was used to describe the hot-pressing behavior of powder lot 2. A test of the equation with  $b = 8.89$  against experimentally determined  $S_V$  values is shown in Figure 5-2. The smaller value of  $b$ , as compared with the case of conventional sintering, indicates that the rate at which excess surface area is removed is smaller, probably because the applied stress favors densification over surface rounding processes.

Curvature. The effect of compaction pressure on the paths of total and average mean curvature change is more difficult to describe in a quantitative manner. The fact that the curvature paths cross each other, so that at a particular volume fraction two specimens compacted at different pressures will have equal  $\bar{H}^{\alpha P}$  values, seems to rule out the existence of a simple relationship between compaction pressure and path of curvature change. For any pair of compaction pressures, it is difficult to specify with precision the volume fraction at which crossover occurs. This problem arises because the crossover occurs at small values of  $|\bar{H}^{\alpha P}|$ , and small  $T_A$  net, for which the statistical variance is usually quite large. There is consequently considerable uncertainty of the exact position of the paths in the crossover region.

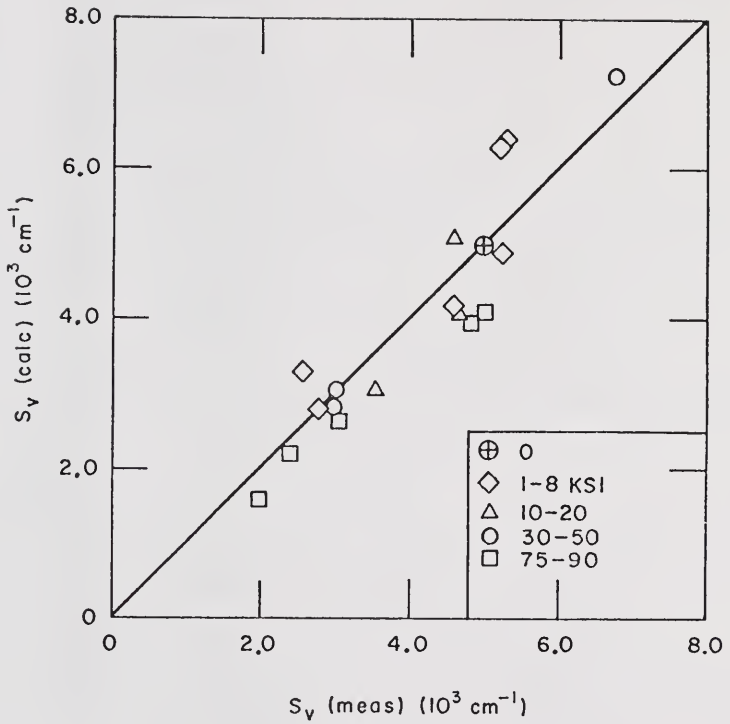


Figure 5-1. Calculated versus measured values of pore-solid surface area for specimens conventionally sintered from powder lot 2.

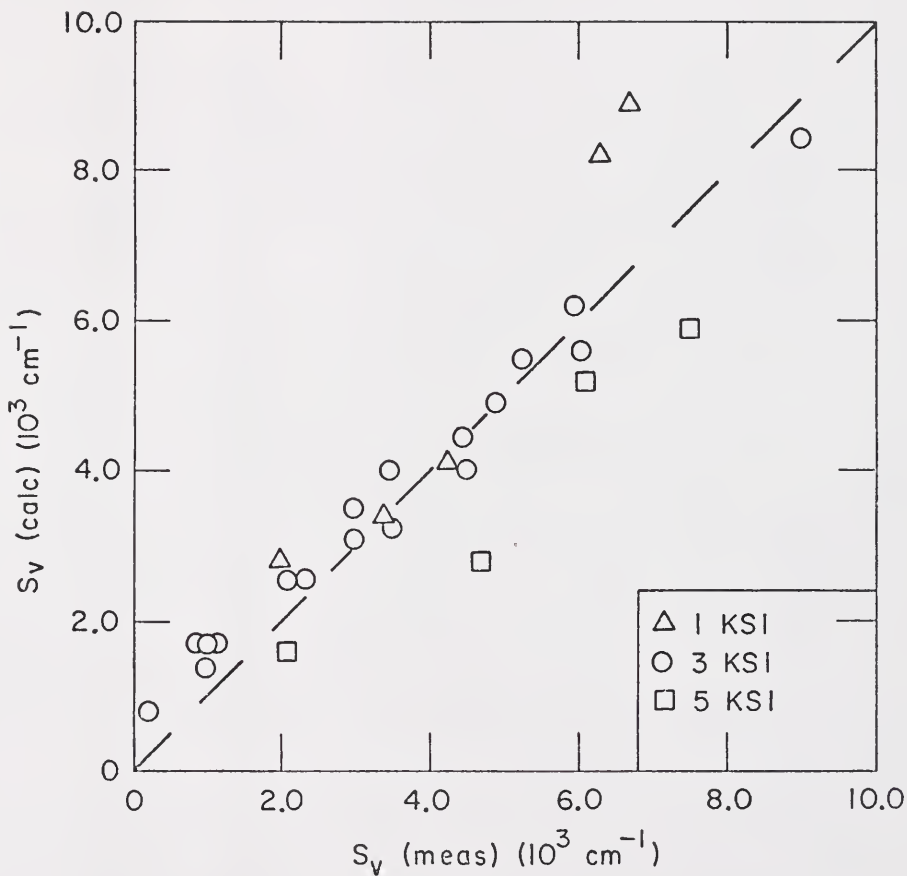


Figure 5-2. Calculated versus measured values of pore-solid surface area for specimens hot pressed from powder lot 2.

However, a linear relationship between a characteristic feature of the  $M_V$  path, the minimum value, and the logarithm of compaction pressure has been observed and was presented in Chapter III. For a single particle size this correlation has the form

$$M_{V\min} = M_o + q \log p \quad (5-6)$$

where  $M_{V\min}$  is the minimum total curvature for each path,  $p$  is the compaction pressure and  $M_o$  and  $q$  are constants. Compaction pressure was shown in Chapter III to determine the density of an unfired compact by

$$V_V' = V_V^o + a \log p, \quad (3-2)$$

or

$$\log p = \frac{V_V' - V_V^o}{a}. \quad (5-7)$$

The preceding expression can be substituted into (5-6) to obtain

$$M_{V\min} = M_o + \frac{q}{a} (V_V' - V_V^o). \quad (5-8)$$

Equation (5-3) can be solved for  $V_V'$  and the resulting expression substituted into (5-8), i.e.,

$$M_{V\min} = M_o + \frac{c}{a} \frac{(1 - V_V^o)(S_V^o - S_V')}{S_V^o}, \quad (5-9)$$

to show that the magnitude of the minimum total curvature increases linearly with  $S_V'$ , the specific surface area of the green compact.

The preceding results illustrate the dependence of the path of curvature change on the microstructural state of the unfired compact. The mechanisms by which compaction pressure affects the curvature of partially sintered specimens appear to be related to the relative rotation and translation of surface elements of adjacent particles that occur during rearrangement. Specifically, these relative displacements

promote the formation of additional interparticle contacts during sintering. In addition, adjacent particles will tend to become aligned with their flat surfaces close and nearly parallel to each other. Necks that form between such surfaces will have higher net spherical images than other types of particle contacts. Both of these mechanisms will affect the curvature well into the sintering process. The formation of multiple contacts leads to more channels at the start of second stage sintering. Even after they are pinched off, the channels contribute negative curvature to the total. The high spherical image of contacts between parallel particle surfaces is likewise persistent, since a small amount of particle rotation occurs during sintering.

The average number of contacts per particle in a loose stack or compact also has an effect on the rate at which  $M_V^{\alpha P}$  changes from the initial positive value to a negative value in the early stages of sintering. To see this relationship, recall that positive values of  $M_V^{\alpha P}$  indicate that the number of closed loops of particle outline on random sectioning planes exceeds the number of closed loops of pore outline, see Equation (1-4). This requirement can be met for lightly sintered structures if the sectioning planes intersect a large number of particles and relatively few interparticle weld necks. (The preceding statement is true as long as the individual particles have neither large numbers of internal holes nor an extensively reentrant topography.)

Consider a group of particles in a loose stack or compact. Let  $\bar{n}_p$  be the average net number of closed loops of particle outline observed on imaginary, randomly oriented sections through the unfired structure.

Allow weld necks to form and grow at the interparticle contact points and repeat the sectioning process. Whenever a sectioning plane passes through a weld neck, the number of particle outline loops is reduced by one from the value that would have been observed if the necks were not present. Therefore, if  $\bar{n}_w$  weld necks are sectioned by randomly oriented sectioning planes, the net number of closed loops of particle outline is

$$N_{\text{net}} = \bar{n}_p - \bar{n}_w, \quad (5-10a)$$

or

$$N_{\text{Anet}} = \frac{\bar{n}_p}{A} - \frac{\bar{n}_w}{A}. \quad (5-10b)$$

where  $A$  is the area of the sectioning plane. The relationships between the number of features in a three-dimensional structure and the number observed on sections through the features,<sup>151</sup> allow the terms on the right-hand side of (5-10b) to be rewritten

$$\frac{\bar{n}_p}{A} = N_{Vp} \bar{D}_{Vp}, \quad (5-11a)$$

and

$$\frac{\bar{n}_w}{A} = N_{Vw} \bar{D}_{Vw}, \quad (5-11b)$$

where  $N_{Vp}$  and  $N_{Vw}$  are the numbers of particles and welds, respectively, and  $\bar{D}_{Vp}$  and  $\bar{D}_{Vw}$  are the average caliper diameters of particles and welds, respectively. The expressions (5-11a) and (5-11b) can be substituted into (5-10b) to obtain

$$N_{\text{Anet}} = N_{Vp} \bar{D}_{Vp} - N_{Vw} \bar{D}_{Vw}, \quad (5-12)$$

or

$$M_V = 2\pi N_{Vp} (\bar{D}_{Vp} - W_p \bar{D}_{Vw}), \quad (5-13)$$

where  $W_p = N_{Vw}/N_{Vp}$ , the average number of welds per particle. Equation (5-13) illustrates how several parameters influence  $M_V$  during the initial stages of sintering. Changing  $N_{Vp}$ , e.g., by varying compaction pressure, affects the magnitude, but not the algebraic sign, of  $M_V$ . Weld neck growth increases  $\bar{D}_{Vw}$  and tends to drive  $M_V$  negative. An increase in the number of welds per particle,  $W_p$ , also tends to change the signs of  $M_V$ . The particle rearrangement processes of cold compaction produce additional particle contacts and thus increase  $W_p$  as necks form during sintering. Therefore, specimens compacted at high pressures can attain negative  $M_V$  values with a smaller amount of neck growth than specimens compacted at low pressures. The presence of a size distribution of particles, as in powder lots 1, 2, 3, and 4, can also increase the number of contacts per particle in unfired specimens, and hence increase  $W_p$  for lightly sintered specimens.

#### Additional Relationships

Additional relationships among the metric properties can be derived by combining the results of the empirical relationships developed in Chapter III. From the graph of the grain shape parameter,  $F_2$ , versus  $C^\alpha$ , the expression

$$L_V^{\alpha P} = \frac{k S_V^{\alpha\alpha} (S_V^{\alpha P})^2}{2 S_V^{\alpha\alpha} + S_V^{\alpha P}}, \quad (3-13)$$

where  $k \approx 0.85$  was developed. This equation is valid for two powder sizes, for all compaction pressures in conventional sintering experiments, and for hot pressing. From the linear relationship of  $S_V^{\alpha P}$  and  $C^\alpha$ ,

Figure 3-35, the following equation relating  $S_V^{\alpha\alpha}$  to  $S_V^{\alpha P}$  was derived:

$$S_V^{\alpha\alpha} = \frac{S_V^{\alpha P} (S_V^{\alpha P} - b)}{2(m + b - S_V^{\alpha P})} . \quad (3-7)$$

Separate equations of this form, with different values for the constants  $m$  and  $b$ , were obtained for conventional sintering of powder sizes 2 and 4, and for hot pressing of powder size 2. The values of  $m$  and  $b$  are listed in Table III-5. If (3-7) is substituted into (3-13), many of the terms in the resulting expression cancel to yield

$$L_V^{\alpha\alpha P} = \frac{k}{2m} (S_V^{\alpha P} - b) (S_V^{\alpha P})^2 . \quad (5-14)$$

That is, for a given powder lot,  $L_V^{\alpha\alpha P}$  is a cubic function of  $S_V^{\alpha P}$ . A single equation, i.e., a single pair of  $m$  and  $b$  values, describes the relationship between  $L_V^{\alpha\alpha P}$  and  $S_V^{\alpha P}$  for the range of paths of microstructural change attainable by varying compaction pressure for conventional sintering of one powder lot. For conventional sintering of a second powder lot, or for hot pressing, a second set of constants is necessary.

Note that the relationship between  $S_V^{\alpha P}$  and  $V_V^P$ , i.e., Equation (5-5), can be substituted into (5-14) to obtain an expression that directly relates  $L_V^{\alpha\alpha P}$  and  $V_V^P$ . However, the relationship between  $L_V^{\alpha\alpha P}$  and  $S_V^{\alpha P}$  presented as Equation (5-14) is preferred because of its simpler form.

The linear relationship between  $C^{\alpha\alpha}$  and  $C^\alpha$ , Figure 3-42, can be written

$$C^{\alpha\alpha} = dC^\alpha \quad (5-15)$$

where the constant  $d$  depends on powder lot. By substituting the definition for  $C^{\alpha\alpha}$  and  $C^{\alpha}$ , (5-13) becomes

$$\frac{3L_V^{\alpha\alpha\alpha}}{3L_V^{\alpha\alpha\alpha} + L_V^{\alpha\alpha P}} = d \frac{2S_V^{\alpha\alpha}}{2S_V^{\alpha\alpha} + S_V^{\alpha P}}, \quad (5-16)$$

which can be solved for  $L_V^{\alpha\alpha\alpha}$  to obtain

$$L_V^{\alpha\alpha\alpha} = \frac{d}{3} \frac{L_V^{\alpha\alpha P}}{1 - d + S_V^{\alpha P}/2S_V^{\alpha\alpha}} \quad (5-17)$$

If Equations (5-14) and (3-7) are substituted for  $L_V^{\alpha\alpha P}$  and  $S_V^{\alpha\alpha}$ , respectively, in (5-17), the following expression is obtained:

$$L_V^{\alpha\alpha\alpha} = \frac{k/6m(S_V^{\alpha P} - b)^2 (S_V^{\alpha P})^2}{S_V^{\alpha P} - b + m/d}. \quad (5-18)$$

For a given set of  $m$  and  $b$  values, this expression, like Equation (5-14), is valid for all conventionally sintered specimens made from a single powder size, regardless of compaction pressure, and for hot pressing. Equation (5-18) shows that  $L_V^{\alpha\alpha\alpha}$  is a quartic function of  $S_V^{\alpha P}$ .

#### Extensions of the Path of Microstructural Change to Other Systems

In the preceding sections, the path of microstructural change was determined in seven dimensions to show the concurrent variation of  $V_V^P$ ,  $S_V^{\alpha P}$ ,  $M_V^{\alpha P}$ ,  $\pi T_{Ag}^{\alpha P}$ ,  $S_V^{\alpha\alpha}$ ,  $L_V^{\alpha\alpha P}$ , and  $L_V^{\alpha\alpha\alpha}$  during conventional sintering and hot pressing of a group of  $UO_2$  powders. Empirical expressions were developed to describe the relationship of  $S_V^{\alpha P}$  and  $V_V^P$ , and the relationships of  $S_V^{\alpha\alpha}$ ,  $L_V^{\alpha\alpha P}$ , and  $L_V^{\alpha\alpha\alpha}$  to  $S_V^{\alpha P}$ . A partial description of the path of  $M_V^{\alpha P}$  change was provided by the relationship between  $M_{Vmin}^{\alpha P}$  and  $(S_V' - S_V^0)$ , the excess surface area in an unfired compact. The paths

of microstructural change were found to be functions of the applied pressure for hot-pressed specimens, and of the cold-compaction pressure for conventional sintering. The effect of pressure was quantitatively described in the correlations between  $S_V^{\alpha P}$  and  $V_V^P$ . Therefore, the pressure effects are implicit in the relationships of the other metric properties to  $S_V^{\alpha P}$ . The results obtained in this study allow the construction of an envelope of paths in seven dimensions, analogous to the three-dimensional representation of the path, shown in Figure 1-1, for a simple sintering experiment.

The paths of microstructural change for sintering in other systems will, in general, differ from the paths developed in this study. However, several of the features of the paths observed in the present case can be expected to apply to other sintering studies. As an example, consider the linear dependence of  $S_V^{\alpha P}$  on  $V_V^P$  during cold compaction. This relationship is clearly due to the fact that particle rearrangement is the only geometric change that took place during compaction. Similar relationships will be observed in any system in which compaction causes particle rearrangement, but not deformation or fracture.

The expression that relates  $S_V^{\alpha P}$  to  $V_V^P$  during conventional sintering and hot pressing, i.e., Equation (5-5), was derived by assuming that the instantaneous rate of surface area change,  $dS_V/dV_V$ , was proportional to the excess surface area in the structure, but otherwise independent of pressure. However, close inspection of Figures 5-1 and 5-2 indicates that the assumption of pressure-independent behavior is only approximately correct for the sintered and hot-pressed specimens examined in this study. The calculated surface areas tend to be lower than the measured values at the highest pressures and higher than the measured

values at the lowest pressures, particularly for the case of hot pressing. (A similar, but much less pronounced, tendency occurred for conventional sintering.) The higher-than-calculated surface areas for high applied hot-pressing pressures can be qualitatively explained by noting that the new surface area forced into a reference volume by the applied pressure partially offsets the effects of the surface-rounding processes and diminishes the rate at which surface area is reduced. This explanation suggests a criterion for determining the applicability of Equation (5-5) to sintering and hot pressing in other systems. The criterion is that Equation (5-5) gives a valid description of the  $S_V^{\alpha P} - V_V^P$  relationship as long as other effects are not allowed to interfere with the normally dominant surface-tension-driven processes. The way in which Equation (5-5) becomes approximate during hot pressing has already been discussed. Other situations in which deviations from Equation (5-5) are possible include:

1. "inhibition" sintering, in which vapor transport is accentuated by the formation of highly volatile species;
2. systems in which gas evolution causes bubble formation and growth during sintering;
3. liquid phase sintering, in which the relationship between the surface area and volume fraction of porosity may be controlled by reaction rates at the solid-liquid interface.

The linear correlation of  $M_{Vmin}^{\alpha P}$  with  $(S_V' - S_V^0)$  observed for conventional sintering could not be verified for hot pressing, because of the limited data base in the latter case. However, the available data for hot pressing do show that the magnitude of  $M_{Vmin}^{\alpha P}$  increases with increasing  $(S_V' - S_V^0)$ . The effect of particle contact formation during compaction on the negative curvature contribution during sintering has already been described. This result suggests that a positive

correlation between  $M_{Vmin}^{\alpha P}$  and  $(S_V' - S_V^0)$  will also be observed for sintering in other systems. The form of such correlations is likely to vary with the details of the specific sintering experiment.

The correlations between  $S_V^{\alpha\alpha}$ ,  $L_V^{\alpha\alpha P}$ ,  $L_V^{\alpha\alpha\alpha}$ , and  $S_V^{\alpha P}$  describe the relationships of the grain structure to the pore-solid interface. These relationships, which were given in Equations (3-7), (5-14), and (5-18), were independent of compaction pressure. With appropriate constants, the expressions described the evolution of grain structure for conventional sintering of two powder lots and for hot pressing. Each of these equations expressed a property of the grain structure as a function of  $S_V^{\alpha P}$  alone. Since the equations were demonstrated to be applicable to a wide range of sintering and hot-pressing conditions in this study, it is likely that the metric properties of the grain structure can also be written as functions of the pore-solid surface area for other systems. Relationships of this type will not be valid if the pore and grain structures can develop independently, e.g., if there is a large difference between pore and grain size. Such situations can arise if the grain boundaries become unpinned from the porosity, leading to exaggerated grain growth during third-stage sintering, or for inhibition sintering and "bloating" (i.e., extreme bubble growth due to gas evolution) in which the pore size greatly exceeds the grain size.

Relationships between Electrical Conductivity  
and the Quantitative Stereology Parameters

In Chapter IV, two hypotheses were advanced to explain the observed correlation of  $\sigma_o$  with  $S_V^{\alpha\alpha}$ , shown in Figure 4-3. The first hypothesis was based on the assumption that the electrical conductivity was higher in the vicinity of grain boundaries. Under this assumption, the increase in  $S_V$  that occurs during sintering is equivalent to an increase in the "volume" of the high-conductivity material, which in turn leads to an increase in the total conductivity of the specimen. This hypothesis does not describe the physical phenomena responsible for the higher grain-boundary conductivity, although the sensitivity to impurities of the electrical conductivity of  $UO_2$ , and the tendency for impurities to collect at the grain boundaries of  $UO_2$ , make plausible the underlying assumption of the first hypothesis.

One experimental result that argues against this hypothesis is the absence of dielectric relaxation phenomena in the  $UO_2$  specimens measured under dry conditions. High dielectric constants and dielectric relaxation are commonly observed when a high-conductivity constituent is dispersed in a lower-conductivity matrix, because of the buildup of charge at the interfaces between the two materials. The absence of a measurable dielectric constant and of dielectric relaxation in the present case indicates that charge buildup did not occur, and therefore that the conductivity difference between the bulk and the region near the grain boundaries was not very great.

The second hypothesis is based on the assumption that electrical conduction occurs through the bulk. The dependence of  $\sigma_o$  on  $S_V^{\alpha\alpha}$  arises because the grain contacts define the minimum cross area through which current must pass. Bulk conduction will be governed by a minimum-area effect for all sintered structure, regardless of density or the extent to which the grain structure has developed. The grain-contact area is equivalent with the minimum cross-section area during the initial stages of sintering, i.e., when the grain contacts form constrictions between adjacent grains.

As sintering continues, the grain contacts meet to form three-grain edges, and  $S_V^{\alpha\alpha}$  begins to increase more rapidly for a given change in  $V_V^P$ , e.g., Figures 3-14, 3-15, and 3-32. During this period  $S_V^{\alpha\alpha}$  increases more rapidly than the minimum cross-section area, and the dependence of  $\sigma_o$  on  $S_V^{\alpha\alpha}$  will no longer be observed.

For wide variations in the scale of the system, direct comparisons of  $\sigma_o$  and  $S_V^{\alpha\alpha}$  can be misleading because the microstructural parameter that determines the minimum cross-section area is actually the fractional coverage of  $\alpha\alpha$  area on the grain surfaces and not the absolute value of  $S_V^{\alpha\alpha}$ . The fractional coverage of the grain surfaces is the grain contiguity parameter,  $C^\alpha$ . A graph of  $\sigma_o$  versus  $C^\alpha$ , Figure 5-3, shows a relationship that is similar in form to the  $\sigma_o$  versus  $S_V^{\alpha\alpha}$  plot, Figure 4-3. A single specimen, with  $\sigma_o = 9.20 \times 10^{-4} \text{ ohm}^{-1} \text{ cm}^{-1}$ ,  $C^\alpha = 0.242$ , shows a significant deviation from the linear increase in  $\sigma_o$  observed during the initial stage of sintering.

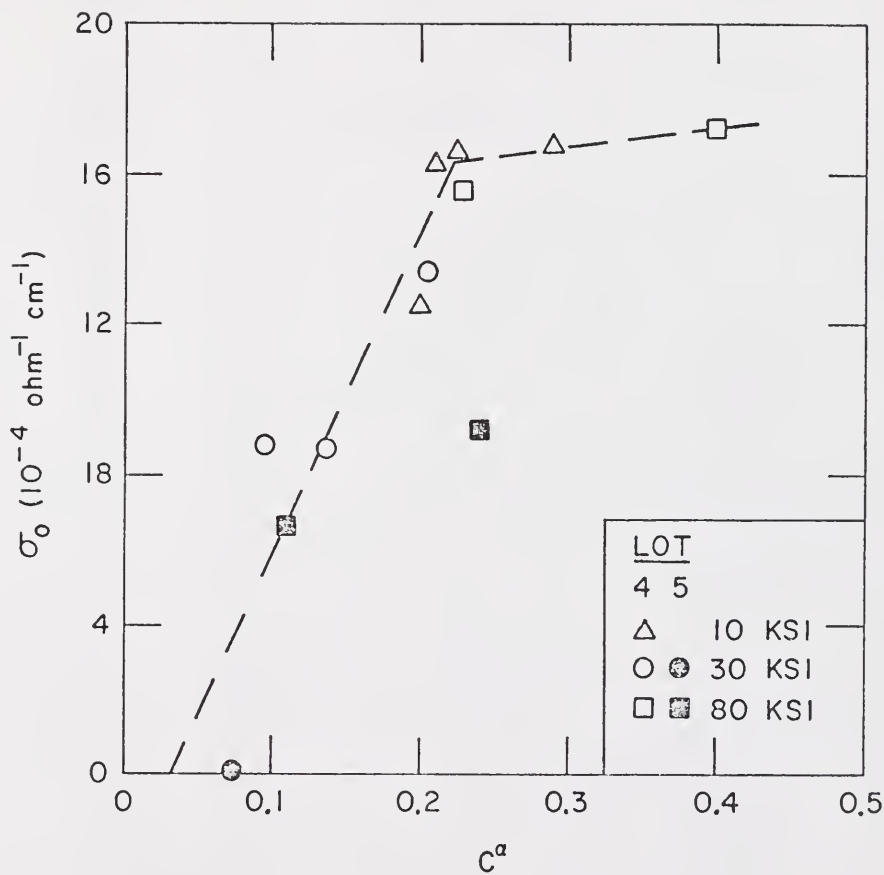


Figure 5-3. Electrical conductivity under dry conditions versus grain contiguity.

The data in Figure 5-3 suggest that the minimum cross-section area is determined by the growth of grain contacts until  $C^\alpha$  equalled  $\sim 0.22$ . Little increase in  $\sigma_0$  was observed as  $C^\alpha$  increased from  $\sim 0.22$  to 0.405, the highest value attained for this series of specimens. This behavior is consistent with the description of the behavior of the minimum cross-section area given earlier. That is, the small change in  $\sigma_0$  as  $C^\alpha$  increased above 0.22 indicates that in this regime the minimum area is no longer controlled by the growth of the grain contacts. Minimum-area effects have also been used to describe the tensile strength of porous, sintered copper,<sup>155</sup> and  $UO_2$ .<sup>118</sup> The effect of cold compaction pressure on electrical conductivity of sintered nickel, i.e., Figure 1-4 taken from the work of Grube and Schlect,<sup>117</sup> is believed to be the result of small values of the grain-contact area at the start of sintering. With continued growth, the grain contacts reach a state at which they no longer control the minimum cross-section area. This condition is marked by the points at which the conductivity values for specimens compacted at high pressures join the curve for specimens compacted at lower pressures.

## CHAPTER VI

### SUMMARY AND CONCLUSIONS

1. The paths of microstructural change were evaluated in seven dimensions for conventional sintering and hot pressing by determining the variation of  $S_V^{\alpha P}$ ,  $M_V^{\alpha P}$ ,  $\pi T_{Ag}^{\alpha P}$ ,  $S_V^{\alpha\alpha}$ ,  $L_V^{\alpha\alpha P}$ , and  $L_V^{\alpha\alpha\alpha}$  with  $V_V^P$ . The paths were found to be functions of the scale of the system and of the cold compaction pressure used prior to conventional sintering, and the applied pressure during hot pressing. The path of microstructural change was independent of pressure for hot pressing.

2. For a given powder lot, the path of  $S_V^{\alpha P}$  change was described with a relationship from the assumption that the excess surface area controlled the rate of approach of the  $S_V^{\alpha P}$  path to the "balance line" of loose-stack sintering. Constant values of excess surface area produced approximately constant values of  $(dS_V/dV_V^P)$ , which were nearly independent of compaction pressure and pore volume fraction.

3. Empirical relationships were also developed between  $S_V^{\alpha P}$ ,  $S_V^{\alpha\alpha}$ ,  $L_V^{\alpha\alpha P}$ , and  $L_V^{\alpha\alpha\alpha}$ . For a given powder lot and fabrication technique, these relationships were independent of compaction pressure and pore volume fraction.

4. These relationships were developed from the observed variation of the metric properties and grain-shape parameters with the grain contiguity. The relationships demonstrate the applicability of the grain contiguity parameter as an index of the development of sintered

structures. Grain contiguity is particularly useful for the description of systems in which monocrystalline particles are compacted by various amounts prior to sintering. Under these conditions, a wide range of structures may have the same pore volume fraction. However, as in this study, the grain contiguity values can be expected to uniquely define  $S_V^{\alpha P}$ ,  $L_V^{\alpha\alpha P}$ , and  $L_V^{\alpha\alpha\alpha}$ . Pore volume fraction, which is ordinarily used as an index of the extent of sintering, can be combined with grain contiguity to give a more complete picture of the development of structure during sintering.

5. The grain-face contiguity parameter was defined in this study and evaluated for conventionally sintered and hot-pressed specimens. The grain-face contiguity of a specimen was found to be linearly related to grain contiguity by a factor less than unity. This circumstance was demonstrated to be a result of the tendency for the  $\alpha\alpha$  grain boundaries to preferentially intersect  $\alpha P$  interfaces and avoid other  $\alpha\alpha$  interfaces.

6. The area inflection-point count of the pore-solid interface decreased by a factor of  $\sim 50$  as pore volume fraction decreased from 0.24 to 0.08 during hot pressing. The area inflection-point count was shown to be proportional to the integral of the asymptotic-line curvature over the domain of saddle surface in unit volume.

7. The gross tangent count increased rapidly during the first part of sintering and hot pressing as a result of the highly curved surfaces that result from neck formation and growth, reached a maximum value and then decreased toward zero with continued densification. The gross tangent count was shown to provide an upper bound for the total absolute curvature. Differences between the total and net tangent counts

were ascribed to the presence of saddle surface. Both exact and approximate expressions were developed for the gross tangent count on sections through saddle surface. The exact expression was a function of the ratios, sums, and products of the principal normal curvatures. The approximate expression showed that the gross tangent count gives an approximate measure of the integral of the root mean square curvature over the domain of saddle surface.

8. The electrical conductivity showed strong correlations with  $S_V^{\alpha\alpha}$  and  $C^\alpha$  during the early stages of sintering. This behavior is consistent with a mechanism in which the bulk conductivity is controlled by the minimum cross-section area through which current must pass. The minimum area is determined by the size of the grain contacts until  $\sim 20$  percent of the grain surface is occupied by grain boundaries (i.e.,  $C^\alpha \approx 0.2$ ). For higher values of coverage the minimum cross-section area is believed to increase more slowly than grain contiguity.

## CHAPTER VII

### SUGGESTIONS FOR FUTURE RESEARCH

The results presented in the preceding chapters raise several important questions that should be addressed in future investigations.

One class of such studies consists of determinations of the paths of microstructural change for other types of sintering processes. The information obtained in these studies could be used to delineate the ranges of validity of the empirical relationships among the metric properties that were developed in the present study. Several examples of areas in which this type of investigation should be particularly informative include:

1. extensions of the present data base to encompass the third stage of conventional sintering and further define the third stage of hot pressing;
2. evaluations of the paths of microstructural change for sintering of nonequiaxed powders and powders in which the initial particles are polycrystalline;
3. studies of the effects of other fabrication variables, e.g., preslugging techniques, the use of pore formers, and the use of sintering aids, on the paths of microstructural change.

The first of these proposed studies should be designed to provide information on the variation of total curvature and the  $\overline{H}^{\alpha P-\lambda P}$  shape parameter, and the relationship of  $C^\alpha$  to  $C^{\alpha\alpha}$ . The variations of the contiguity parameters at the start of the third-stage sintering should provide a sensitive indication of the point at which the grain boundaries become unpinned from the pore network.

The second and third proposed investigations could be combined, with emphasis placed on the fabrication variables that are of greatest commercial interest, to survey a wide variety of paths of microstructural change, and thus determine the degree of generality of the various relationships among the metric properties. The effect of sintering aids, which retard the motion of grain boundaries during third-stage sintering, could be studied by comparing the variation of the contiguity parameters for the cases of sintering with and without sintering aids.

The techniques employed in the present study can also be used to determine the stability of sintered structures under service conditions. As an example, the formation and growth of fission-gas-filled bubbles during the thermal cycling and irradiation of nuclear fuels could be investigated by evaluating the paths of microstructural change for the processes. The interaction of the bubbles with the grain surfaces and triple junctions could be described with the grain and grain-face contiguities.

Studies should also be undertaken to improve the understanding of microstructural effects on the electrical properties of sintered structures. The effect of the minimum cross-section area in determining electrical conductivity should be verified by experiments on other materials, preferably metallic systems in which wide variations in the initial particle size can be produced without accompanying variations in purity. Ductile metals also afford the opportunity for an independent determination of the minimum area by measurements on fractured tensile specimens.<sup>155</sup> Similar attempts at determining the

minimum area for materials that fail by brittle fracture will be less conclusive because of the tendency for crack propagation to occur without the changes in direction necessary for failure along the minimum area.

The effect of microstructure on the dielectric properties of systems in which surface layers, i.e., adsorbed gases or oxide films, coat the pore-solid interface can most effectively be evaluated if the D.C. conductivity is low. That is, if adsorbed gases are present, the bulk conductivity of the material should be low. If oxide films have formed on a metallic substrate, the film should be highly insulating. Studies in which the concurrent variation of the dielectric and metric properties would allow the fabrication conditions to be optimized for the production of a given set of operating characteristics. Because of the potential effect of small structural features on the dielectric properties, high-resolution microscopy techniques may be necessary for the required quantitative stereology characterizations.

APPENDIX A  
THE GROSS TANGENT COUNT

When the total curvature is measured by tangent counting, two independent quantities are determined: the number of positive tangents,  $T_A^+$ , and the number of negative tangents,  $T_A^-$ . However, when the total curvature is calculated, only one independent parameter,  $T_{Anet} = T_A^+ - T_A^-$ , is used. In other words, the total curvature uses only a portion of the structural information contained in the area tangent count. The additional information may be included by separately tabulating  $T_A^+$  and  $T_A^-$  values or, as in this dissertation, by reporting the gross tangent count,  $T_{Ag} = T_A^+ + T_A^-$ , as well as the net tangent count. A simple example of the extra structural definition which results when two independent parameters are used to describe the tangent count results is illustrated in Figure A-1, which shows two structures with identical  $T_{Anet}$  values but different  $T_{Ag}$  values.

The gross tangent count measured on a sectioning plane may be related to a property of the three-dimensional structure in the following way.

The trace of an interface on a sectioning plane will have a local curvature given by<sup>152</sup>

$$k = \frac{\kappa_1 \cos^2 \theta + \kappa_2 \sin^2 \theta}{\sin \phi} \quad (A-1)$$

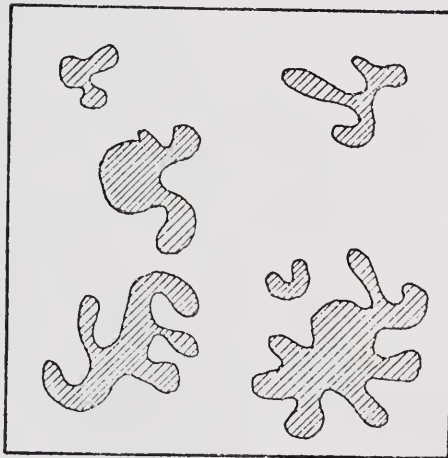
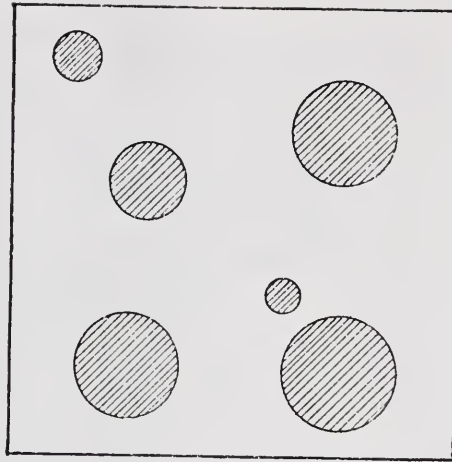


Figure A-1. Schematic plane sections through structures with equal  $T_{Anet}$  values and differing  $T_{Ag}$  values.

where  $\phi$  and  $\theta$  specify the orientation of the sectioning plane relative to the surface normal, Figure A-2, and  $\kappa_1$  and  $\kappa_2$  are the principal normal curvatures of the surface at the point sectioned. Note that if  $\kappa_1$  and  $\kappa_2$  are of opposite sign, i.e., for sections through saddle surface,  $k$  may be either positive or negative, depending on the value of  $\theta$ .

The tangent count consists of sweeping a test line over an area  $A$  of the sectioning plane and counting the number of times the test line makes a tangent with the trace of an interface. The probability of forming a tangent with an arc element,  $d\lambda$ , is equal to<sup>151</sup>

$$dT_A = \frac{d\psi}{A\pi} = \frac{1}{A\pi} \frac{d\psi}{d\lambda} d\lambda = \frac{k d\lambda}{A\pi} \quad (\text{A-2})$$

where  $d\psi$  is the angle subtended by  $d\lambda$ ,  $d\psi/d\lambda$  is by definition the curvature of a two-dimensional curve,<sup>152</sup> and  $A$  is the area sectioned. For a finite length of arc, the number of tangents per unit area may be obtained by integrating the preceding expression. If the net tangent count is desired, convex ( $k > 0$ ) and concave ( $k < 0$ ) tangents are summed separately and added algebraically. If, as in the present case, the gross number of tangents is desired, convex and concave tangents are summed without regard to sign and the integral becomes

$$\pi T_{Ag} = \frac{1}{A} \int |k| d\lambda \quad (\text{A-3})$$

In order to evaluate the right-hand side of (A-3) it is necessary to perform the integration over all of the interfacial area in a unit volume. The appropriate change of variable is<sup>151</sup>

$$d\lambda = \frac{\sin^2 \phi}{4\pi L} d\theta d\phi du dv \quad (\text{A-4})$$

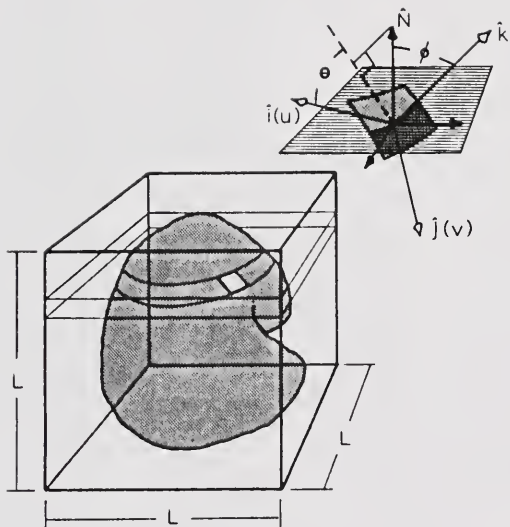


Figure A-2. Angular relationships between a sectioning-plane normal and a small surface element.<sup>151</sup>

where  $u$  and  $v$  define a coordinate net on the surface  $S$  and  $L$  is the edge length of the cube of structure being sampled. Performing the indicated substitutions yields

$$\pi T_{Ag} = \frac{1}{4\pi V} \int_v \int_u \left[ \int_0^\pi \int_0^\pi |\kappa_1 \cos^2 \theta + \kappa_2 \sin^2 \theta| \sin \phi \, d\theta \, d\phi \right] du \, dv, \quad (A-5)$$

where  $V = AL$  is the specimen volume.

Integrating over  $\phi$  and substituting

$$dS_V = (du \, dv)/V \text{ gives}$$

$$\pi T_{Ag} = \frac{1}{2\pi} \iint_{S_V} \left[ \int_0^{2\pi} |\kappa_1 \cos^2 \theta + \kappa_2 \sin^2 \theta| \, d\theta \right] dS_V. \quad (A-6)$$

Because of the absolute value signs, the integration over  $\theta$  is difficult to evaluate. Instead, the Schwartz inequality may be used to give

$$\begin{aligned} \pi T_{Ag} &\geq \frac{1}{2\pi} \iint_{S_V} \left| \int_0^{2\pi} (\kappa_1 \cos^2 \theta + \kappa_2 \sin^2 \theta) \, d\theta \right| dS_V \\ &= \frac{1}{2} \iint_{S_V} |\kappa_1 + \kappa_2| \, dS_V. \end{aligned} \quad (A-7)$$

Thus, the gross tangent count serves as an upper bound for the integral of the absolute value of the local mean curvature. This integral, called the total absolute curvature, may be divided by  $S_V$  to yield an average of the absolute value of mean curvature

$$\overline{|\mathbb{H}|} = \frac{\frac{1}{2} \iint |\kappa_1 + \kappa_2| \, dS_V}{S_V}. \quad (A-8)$$

The Schwartz inequality is now applied to the total absolute curvature to obtain

$$\frac{1}{2} \iint |\kappa_1 + \kappa_2| dS_V \geq \frac{1}{2} \left| \iint (\kappa_1 + \kappa_2) dS_V \right| = |M_V| . \quad (\text{A-9})$$

Equations (A-7) and (A-9) can be combined to yield

$$\pi T_{Ag} \geq \frac{1}{2} \iint |\kappa_1 + \kappa_2| dS_V \geq |M_V| . \quad (\text{A-10})$$

That is,  $\pi T_{Ag}$  and  $|M_V|$  are upper and lower bounds, respectively, for the total absolute curvature.

Since the inequalities in (A-9) hold only for saddle surface, i.e., when  $\kappa_1$  and  $\kappa_2$  have opposite signs, the difference between  $|M_V|$  and  $\pi T_{Ag}$  is due solely to the presence of saddle surface. A typical plot of  $|M_V|$  and  $\pi T_{Ag}$  for a sintering experiment is shown in Figure A-3. The plot of the total absolute curvature lies somewhere between these two bounding curves.

A closer analysis of the gross tangent count can be performed to relate it to properties of the three-dimensional structure with an equality, and not an inequality. To do this, it is necessary to evaluate the integral enclosed in brackets in (A-6). For sections through elements of concave or convex surface, the absolute value signs may be immediately moved outside the integral to give

$$\begin{aligned} \iint_{S_V} \int_0^{2\pi} |\kappa_1 \sin^2\theta + \kappa_2 \sin^2\theta| d\theta dS_V &= \pi \iint_{S_V} |\kappa_1 + \kappa_2| dS_V \\ &= 2\pi M_V^{++} \text{ for convex surface} \\ &= 2\pi M_V^{--} \text{ for concave surface.} \end{aligned} \quad (\text{A-11})$$

It remains to evaluate this integral for saddle elements.

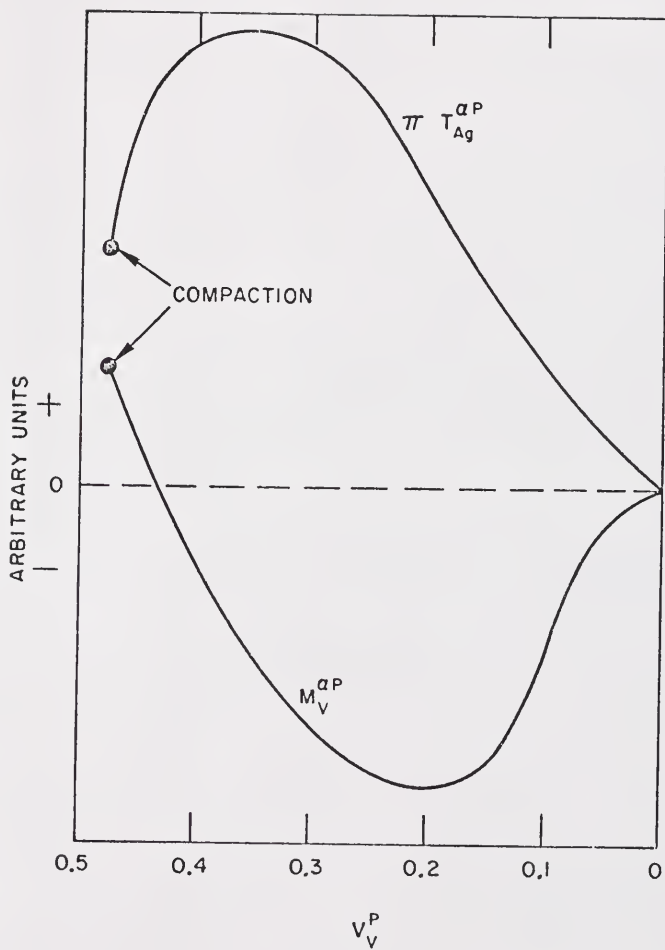


Figure A-3. Schematic variation of  $M_V^{\alpha P}$  and  $\pi T_{Ag}^{\alpha P}$  during a sintering experiment.

The quantity  $(\kappa_1 \cos^2 \theta + \kappa_2 \sin^2 \theta)$  is sketched as function of  $\theta$  in Figure A-4, for a typical section through a saddle element in which  $\kappa_1$  is assumed to be positive, and  $\kappa_1 = -2\kappa_2$ . One full cycle of this function, which repeats with a period of  $\pi$ , is presented.

The integral of the absolute value of this function can be evaluated by integrating separately over the  $\theta$  ranges where the function is positive and negative, and preceding the negative contributions by a minus sign, i.e.,

$$\int_0^{2\pi} |\kappa_1 \cos^2 \theta + \kappa_2 \sin^2 \theta| d\theta = 4 \left[ \int_0^\alpha (\kappa_1 \cos^2 \theta + \kappa_2 \sin^2 \theta) d\theta - \int_\alpha^\pi (\kappa_1 \cos^2 \theta + \kappa_2 \sin^2 \theta) d\theta \right] \quad (\text{A-12})$$

where  $\alpha$ , the angle defined by  $(\kappa_1 \cos^2 \alpha + \kappa_2 \sin^2 \alpha) = 0$ , is given by

$$\alpha = \arctan(-\kappa_1/\kappa_2)^{1/2} \quad (\text{A-13})$$

The right-hand side of (A-12) can be evaluated and rearranged to yield

$$\text{RHS} = (4\alpha - \pi)(\kappa_1 + \kappa_2) + 2 \sin 2\alpha(\kappa_1 - \kappa_2) \quad (\text{A-14})$$

If the definition of  $\alpha$  is substituted into (A-14), and  $\kappa_1 \kappa_2$  is identified as the Gaussian curvature,  $K^{152}$  the following expression is obtained

$$\text{RHS} = 4 \left[ \left[ \arctan(-\kappa_1/\kappa_2)^{1/2} - \frac{\pi}{4} \right] (\kappa_1 + \kappa_2) + (-K)^{1/2} \right]. \quad (\text{A-15})$$

This expression, which is valid for saddle surface only, and the results for concave and convex surfaces, Equation (A-11), are substituted into (A-6), to obtain

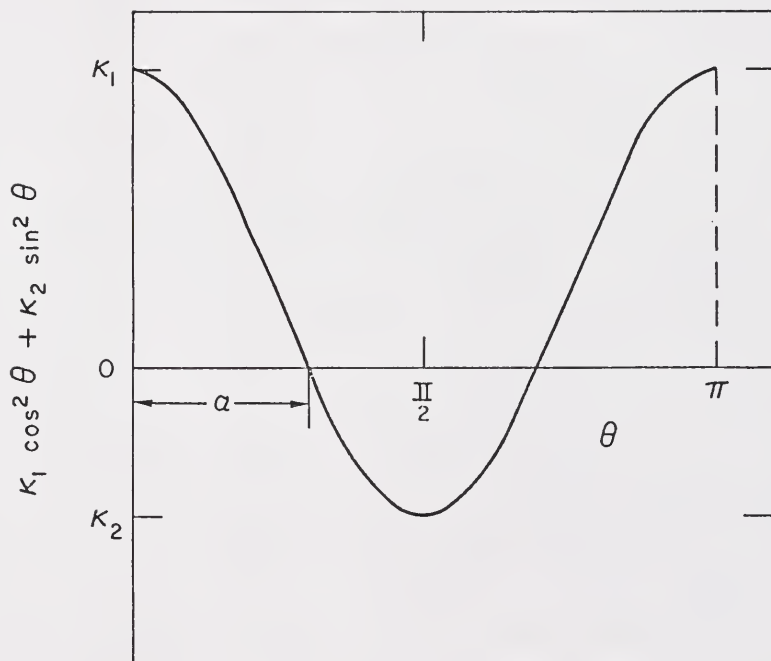


Figure A-4. Schematic variation of the normal curvature with  $\theta$  for sections through saddle surface.

$$\pi T_{Ag} = M_V^{++} - M_V^{--} + \frac{2}{\pi} \iint_{S_V} \left[ \arctan(\kappa_1/\kappa_2)^{1/2} - \frac{\pi}{4} \right] (\kappa_1 + \kappa_2) dS_V^{+-} + \frac{2}{\pi} \iint_{S_V} (-\kappa)^{1/2} dS_V^{+-}. \quad (A-16)$$

None of the terms on the right-hand side of (A-16) can be evaluated, except by serial sectioning techniques, because elements of convex, concave, and saddle surface cannot be unambiguously identified by their traces on a sectioning plane. In addition, the complex mathematical form of the last two terms in (A-16) makes difficult an intuitive grasp of how variations in the principal normal curvatures affect the gross tangent count. The latter problem can be remedied by developing an approximate expression for  $\pi T_{Ag}$ .

To develop the approximation, (A-13) will first be rewritten as

$$\pi T_{Ag} = M_V^{++} - M_V^{--} + \frac{2}{\pi} \iint_{S_V} Z dS_V^{+-} \quad (A-17)$$

where

$$Z = \left[ \arctan(\kappa_1/\kappa_2)^{1/2} - \frac{\pi}{4} \right] (\kappa_1 + \kappa_2) + (-\kappa_1 \kappa_2)^{1/2} \quad (A-18)$$

The functional dependence of  $Z$  on  $\kappa_1$  and  $\kappa_2$  defines the surface shown in Figure A-5. The intersections of the surface with the planes  $\kappa_1 = 0$  and  $\kappa_2 = 0$  are straight lines that pass through the origin with slope  $\pi/4$ . Moreover, the intersection of the surface with any plane that contains the  $Z$  axis (i.e., one with an equation of the form  $\kappa_1 = -\beta \kappa_2$ ,  $\beta \geq 0$ ) is the straight line

$$Z = \kappa_2 \left[ \left( \arctan \beta^{1/2} - \frac{\pi}{4} \right) (1 - \beta) - \beta^{1/2} \right]. \quad (A-19)$$

That is, the surface defined by (A-18) is a ruled surface whose generating lines all pass through the origin. In addition, this surface has mirror symmetry about the plane  $\kappa_1 = -\kappa_2$ ; the symmetry may be demonstrated by noting that the right-hand side of (A-18) is not altered by the substitution of  $-\kappa_1$  for  $\kappa_2$  and  $-\kappa_2$  for  $\kappa_1$ .

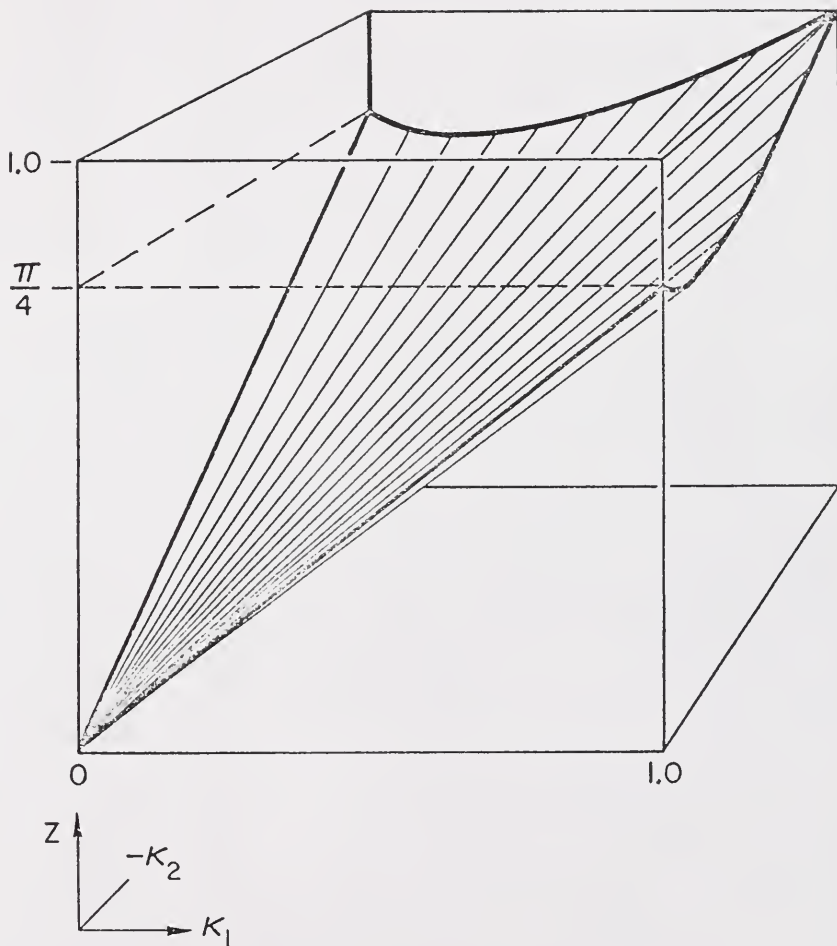


Figure A-5. Variation of the function  $Z$  with  $\kappa_1$  and  $\kappa_2$ .

The function Z may be approximated by the function

$$Z' = \left[ \frac{\kappa_1^2 + \kappa_2^2}{2} \right]^{1/2} \quad (\text{A-20})$$

Like Z, Z' is a ruled surface with generating lines passing through the origin and is mirror symmetrical about the plane  $\kappa_1 = -\kappa_2$ . For  $\kappa_1 = -\kappa_2$ ,  $Z' = Z = \kappa_1$ . For  $\kappa_1 = -\beta\kappa_2$  ( $\beta \geq 0$ ,  $\beta \neq 1$ ) Z' is slightly less than Z. As shown in Figure A-6, the maximum difference between Z and Z' is less than 10 percent, and occurs for  $\kappa_1 = 0$  (and for  $\kappa_2 = 0$ ). For  $-\kappa_1/\kappa_2 > 0.25$  the difference between the two functions is less than 1.7 percent. Z' is thus a close approximation to the more complex function Z.

If Z' is substituted for Z in (A-16) the expression

$$\pi T_{Ag} \approx M_V^{++} - M_V^{--} + \frac{2}{\pi} \iint_{S_V^{+-}} \left[ \frac{\kappa_1^2 + \kappa_2^2}{2} \right]^{1/2} dS_V^{+-} \quad (\text{A-21})$$

is obtained. An alternate method of writing (A-21) is

$$\pi T_{Ag} \approx M_V^{++} - M_V^{--} + \frac{2}{\pi} \iint_{S_V^{+-}} H_{rms} dS_V^{+-} \quad (\text{A-22})$$

where Z' has been identified as the root mean square local curvature,  $H_{rms}$ . The preceding expression, while simpler in form than (A-16), is of limited utility because of the difficulty of evaluating  $M_V^{++}$ ,  $M_V^{--}$ , and  $S_V^{+-}$ .

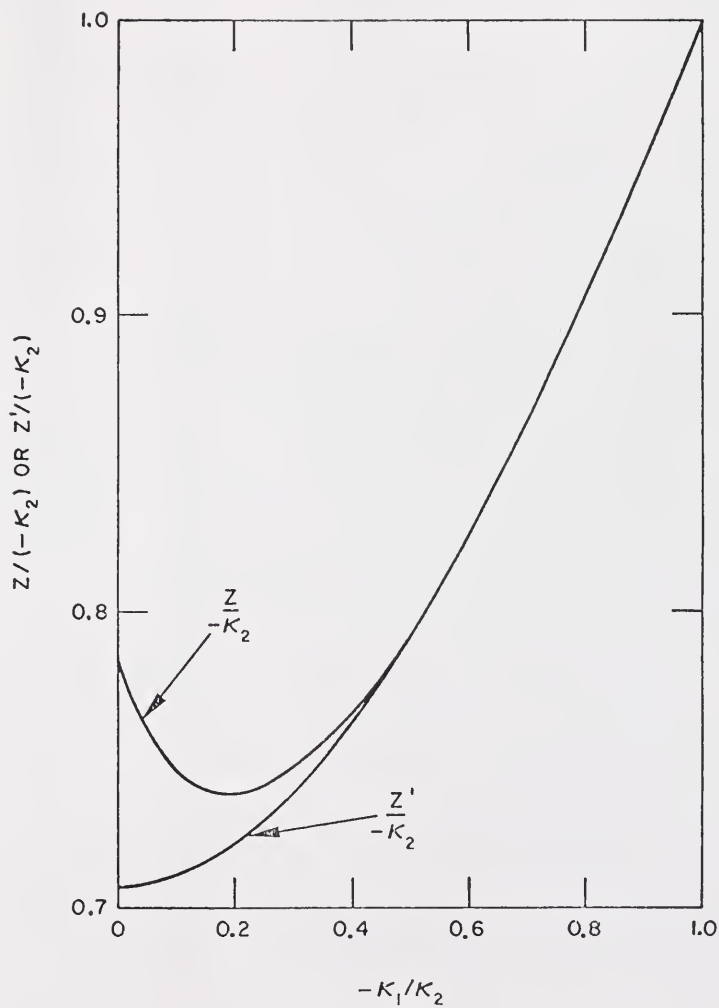


Figure A-6. Variation of the functions  $Z'$  and  $Z$  with  $-\kappa_1/\kappa_2$ .

To summarize, three relationships involving the gross tangent count have been developed

$$\pi T_{Ag} \geq \frac{1}{2} \iint_{S_V} |\kappa_1 + \kappa_2| dS_V \geq |M_V| \quad , \quad (A-10)$$

$$\begin{aligned} \pi T_{Ag} = M_V^{++} - M_V^{--} + \frac{2}{\pi} \iint_{S_V}^{+-} [\arctan(\kappa_1/\kappa_2)^{1/2} - \frac{\pi}{4}] \\ (\kappa_1 + \kappa_2) dS_V^{+-} + \frac{2}{\pi} \iint_{S_V}^{+-} (-K)^{1/2} dS_V^{+-} \end{aligned} \quad (A-16)$$

and

$$\pi T_{Ag} \approx M_V^{++} - M_V^{--} + \frac{2}{\pi} \iint_{S_V}^{+-} H_{rms} dS_V^{+-} \quad . \quad (A-22)$$

APPENDIX B  
THE AREA INFLECTION POINT COUNT

Inflection points are points on plane curves where the curvature changes sign, and thus is locally zero. In this appendix, a relationship is developed between the properties of a surface in three dimensions and the density of inflection points on the intersection of the surface with randomly oriented planes.

The curvature of the curve of intersection is

$$k = \frac{\kappa_1 \cos^2 \theta + \kappa_2 \sin^2 \theta}{\sin \phi} \quad (A-1)$$

where  $\kappa_1$  and  $\kappa_2$  are the local principal normal curvatures,  $\phi$  is the angle between the surface and sectioning plane normals, and  $\theta$  is the angle between the " $\hat{i}$ " principal direction in the surface and the projection of the sectioning plane normal on the  $\hat{i}\text{-}\hat{j}$  plane. The geometry of the intersection between the test plane and the surface is shown in Figure A-2. The angle  $\phi$  takes on values between zero and  $\pi$ . Since  $\sin \phi$ ,  $\cos^2 \theta$ , and  $\sin^2 \theta$  are always greater than or equal to zero,  $k$  can only be zero if  $\kappa_1$  and  $\kappa_2$  have opposite algebraic signs.\* Therefore, inflection points will only be observed on sections through saddle surface.

---

\*If one or both of the  $\kappa$ 's are equal to zero,  $k$  may also be zero. Such situations often, but do not necessarily, lead to intersections that consist of line segments and not inflection points. In this discussion  $\kappa_1$  and  $\kappa_2$  are restricted to nonzero values.

The normal curvature,  $k_n$ , at a point on a surface is the curvature which is observed when the surface is intersected by a plane oriented at right angles to the surface. For such a plane  $\phi$  in Figure A-2 is equal to  $\frac{\pi}{2}$  and

$$k_n = \kappa_1 \cos^2 \theta + \kappa_2 \sin^2 \theta . \quad (\text{B-1})$$

Note that if  $k_n = 0$ , then  $k = 0$ . Directions in the surface along which  $k_n = 0$  are called asymptotic directions.<sup>152</sup> There are two intersecting asymptotic directions, defined by

$$\theta = \pm \arctan(-\kappa_1/\kappa_2)^{1/2} , \quad (\text{B-2})$$

at every point in a saddle surface. For a finite area of saddle surface, the asymptotic directions form a net consisting of two sets of intersecting lines. These are called the asymptotic lines.<sup>152</sup>

From the definition of the asymptotic direction, it can be concluded that the appearance of an inflection point on a sectioning plane (i.e.,  $k = k_n = 0$ ) indicates that the plane contains the asymptotic direction at that point. In order to establish a one-to-one correspondence between inflection points and section plane tangencies with asymptotic directions, it is necessary to prove the converse of the preceding statement, i.e., that if a sectioning plane is locally tangent to an asymptotic direction, an inflection point will be observed. This proof is presented as a separate lemma at the end of Appendix B. For the following derivation, the assumption is made that tangencies of the sectioning plane with the asymptotic directions produce inflection points on the section.

The following development of a relationship between the area inflection point count and a property of the sectioned surface is based on the Figure B-1, which shows an element of saddle surface. The coordinate system  $\hat{i}-\hat{j}-\hat{k}$  is fixed to the surface element with  $\hat{k}$  normal to the surface, and  $\hat{i}$  and  $\hat{j}$  tangent to the surface and aligned with the principal directions. The dimensions of the surface element are  $du$  and  $dv$  in the  $\hat{i}$  and  $\hat{j}$  directions, respectively. The principal normal curvatures are  $\kappa_1$  ( $\kappa_1 > 0$ ) measured in the  $\hat{j}-\hat{k}$  plane, and  $\kappa_2$  ( $\kappa_2 < 0$ ) measured in the  $\hat{i}-\hat{k}$  plane. The dimensions  $du$  and  $dv$  are chosen so that the vectors  $d\vec{l} = du\hat{i} + dv\hat{j}$  and  $d\vec{l}' = du\hat{i} - dv\hat{j}$  point in the asymptotic directions. This requirement is equivalent to choosing  $(du/dv) = \tan\theta_0$ , where  $\theta_0$  is the angle between the  $\hat{i}$  axis and the line PQ, which is perpendicular to  $d\vec{l}'$  and lies in the  $\hat{i}-\hat{j}$  plane. Note that  $\theta_0$  is also the acute angle between the  $\hat{j}$  axis and  $d\vec{l}$ .

The probability of forming an inflection point with the area element is equal to the probability of intersecting the element with a randomly oriented sectioning plane multiplied by the probability that the curvature of the section trace equals zero. The probability that an area element is intersected by a sectioning plane was used in the derivation in Appendix A. For the present case, a more general formula is used because the coordinate axes are defined differently. The probability is

$$\text{Pr} = \frac{1}{L} \int_{\sigma} dp d\sigma \quad (\text{B-3})$$

where  $d\sigma = \sin\phi \, d\phi d\theta / 4\pi$  is the area element on the unit sphere,  $L$  is the specimen dimension measured parallel to the section plane normal, and  $dp$  is the projection of the longest dimension of the area element on the normal to the sectioning plane. That is,  $dp = d\vec{l} \cdot \hat{N}$ , where  $\hat{N}$ , a unit

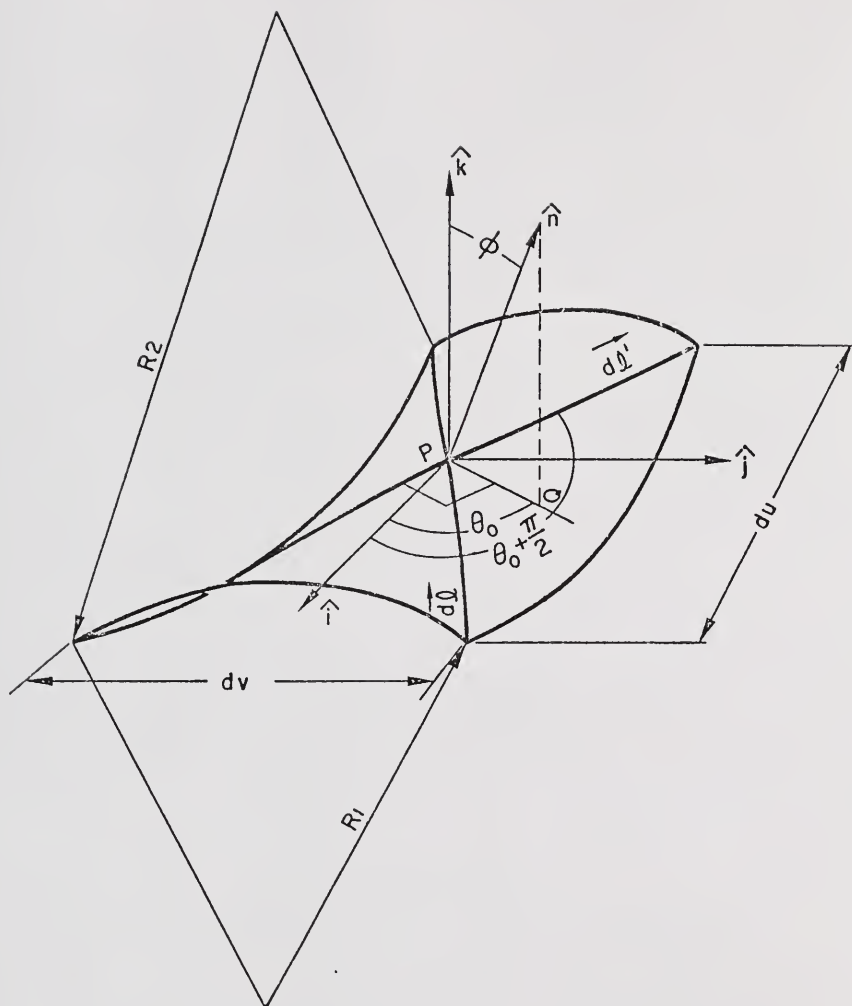


Figure B-1. Angular and vector relationships for a plane intersecting an element of saddle surface.

vector, is the sectioning plane normal shown in Figure B-1. The differential  $dp$  is evaluated by writing the  $\hat{i}$ ,  $\hat{j}$ , and  $\hat{k}$  components of  $d\vec{l}$  and  $\hat{N}$ , and performing the indicated operations:

$$\begin{aligned} dp &= d\vec{l} \cdot \hat{N} \\ &= (du\hat{i} + dv\hat{j}) \cdot (\cos\theta \sin\phi \hat{i} + \sin\theta \sin\phi \hat{j} + \cos\phi \hat{k}) \\ &= (\cos\theta du + \sin\theta dv) \sin\phi . \end{aligned} \tag{B-4}$$

The expressions for  $dp$  and  $d\sigma$  are then substituted into (4-3) to obtain

$$Pr = \frac{1}{4\pi L} \int_{\sigma} (\cos\theta du + \sin\theta dv) \sin^2\phi d\theta d\phi , \tag{B-5}$$

which, after integrating over  $\phi$ , becomes

$$Pr = \frac{1}{8L} \int_0^{\pi} (\cos\theta du + \sin\theta dv) d\theta . \tag{B-6}$$

Equation (B-6) gives the probability that the area element is intersected by a randomly oriented sectioning plane. If an inflection point is formed on the section, the additional condition that  $\theta = \theta_0$  must be met. To express this condition, the function  $\delta(\theta_0)$  is introduced, where  $\delta(\theta_0) = 1$  if  $\theta = \theta_0$  and  $\delta(\theta_0) = 0$  if  $\theta \neq \theta_0$ . By using the  $\delta$  function, the probability that an inflection point is formed by the intersection of a randomly oriented plane with the area element can be written

$$Pr' = \frac{1}{8L} \int_0^{\pi} \delta(\theta_0) (\cos\theta du + \sin\theta dv) d\theta , \tag{B-7}$$

or

$$Pr' = \frac{1}{8L} (\cos\theta_0 du + \sin\theta_0 dv) d\theta_0 . \tag{B-8}$$

The parameter  $\theta_0$  is a function of position on the saddle surface,

i.e.,  $\theta_o = \theta_o(u,v)$ . We state without proof that  $\theta_o(u,v)$  is a scalar field, and therefore

$$d\theta_o = \frac{\partial \theta_o}{\partial u} du + \frac{\partial \theta_o}{\partial v} dv . \quad (\text{B-9})$$

Reference to Figure B-1 shows that

$$\cos \theta_o = \frac{dv}{dl} \quad (\text{B-10a})$$

and

$$\sin \theta_o = \frac{du}{dl} . \quad (\text{B-10b})$$

In addition,

$$du = \frac{du}{dv} dv \quad (\text{B-11a})$$

and

$$dv = \frac{dv}{du} du . \quad (\text{B-11b})$$

The substitutions (B-9), (B-10), and (B-11) are made in (B-8), to obtain

$$Pr' = \frac{1}{8L} \left[ \frac{\partial \theta_o}{\partial u} \frac{du}{dv} \frac{dv}{dl} + \frac{\partial \theta_o}{\partial u} \frac{du}{dl} + \frac{\partial \theta_o}{\partial v} \frac{dv}{dl} + \frac{\partial \theta_o}{\partial v} \frac{dv}{du} \frac{dv}{dl} \right] du dv , \quad (\text{B-12})$$

which, after applying the chain rule to the first and fourth terms in the parentheses, becomes

$$Pr' = \frac{1}{4L} \left[ \frac{\partial \theta_o}{\partial u} \frac{du}{dl} + \frac{\partial \theta_o}{\partial v} \frac{dv}{dl} \right] du dv$$

The parameter in brackets is the directional derivative of  $\theta_o$  in the  $l$ , i.e., asymptotic, direction, and is by definition the curvature of the asymptotic line. Therefore, the probability of forming an inflection point with an area element of saddle surface is

$$Pr' = \frac{1}{4L} k_{as} du dv , \quad (\text{B-14})$$

where  $k_{as}$  is the asymptotic line curvature. The total number of inflection points per unit area of sectioning plane is obtained by integrating  $Pr'$  over the saddle surface area in the structure and dividing by  $\bar{A}$ , the average area of a sectioning plane.

$$I_A = \frac{1}{2L\bar{A}} \iint k_{as}^{+-} dS^{+-}, \quad (B-15)$$

where the superscript  $+-$  indicates saddle surface, and a factor of 2 is included to indicate that both sets of asymptotic lines can contribute to the inflection point count. Finally, since  $L\bar{A} = V$ , the specimen volume, (B-15) can be rewritten

$$I_A = \frac{1}{2} \iint k_{as}^{+-} dS_V^{+-} \quad (B-16)$$

#### Lemma

The preceding derivation is based on the existence of a one-to-one correspondence between inflection points on sections through saddle surface and tangencies of the sectioning plane with an asymptotic direction. To complete this proof, it is necessary to show that if the sectioning plane is tangent to an asymptotic direction, then an inflection point will be observed on the section.

Assume that the plane with a normal vector  $\hat{N}$  is tangent to the asymptotic direction  $d\vec{l}'$  in Figure B-1. Then  $\theta = \theta_0$  and

$$k = k_n = 0 = \kappa_1 \cos^2 \theta_0 + \kappa_2 \sin^2 \theta_0 \quad (B-17)$$

We wish to examine  $k$  at locations on the section close to the point  $P$  at which  $k = 0$ . At the nearby points the local values of  $\kappa_1$ ,  $\kappa_2$ , and  $\theta_0$  will, in general, differ from the values at  $P$ , and the coordinate system

fixed to the surface will have a slightly different orientation. Let P' be a point on the surface separated from P by  $d\vec{l}'$ . Then P' is intersected by the sectioning plane. The coordinate system at P' has axes  $(\hat{i} + \delta\hat{i})$ ,  $(\hat{j} + \delta\hat{j})$ , and  $(\hat{k} + \delta\hat{k})$  where

$$\begin{aligned}\delta\hat{i} &= -\kappa_2 du \hat{k} \\ \delta\hat{j} &= +\kappa_1 dv \hat{k} \\ \delta\hat{k} &= +\kappa_2 du \hat{i} - \kappa_1 dv \hat{j} .\end{aligned}\tag{B-18}$$

The normal to the sectioning plane can be written with reference to the new coordinate system as follows:

$$\begin{aligned}\hat{N} &= [\hat{N} \cdot (\hat{i} + \delta\hat{i})](\hat{i} + \delta\hat{i}) + [\hat{N} \cdot (\hat{j} + \delta\hat{j})](\hat{j} + \delta\hat{j}) \\ &\quad + [\hat{N} \cdot (\hat{k} + \delta\hat{k})](\hat{k} + \delta\hat{k})\end{aligned}\tag{B-19}$$

$$\begin{aligned}&= [\hat{N} \cdot \hat{i} - \kappa_2 du \hat{N} \cdot \hat{k}](\hat{i} + \delta\hat{i}) + [\hat{N} \cdot \hat{j} + \kappa_1 dv \hat{N} \cdot \hat{k}](\hat{j} + \delta\hat{j}) \\ &\quad + [\hat{N} \cdot \hat{k} + \kappa_2 du \hat{N} \cdot \hat{i} - \kappa_1 dv \hat{N} \cdot \hat{j}](\hat{k} + \delta\hat{k}) .\end{aligned}\tag{B-20}$$

Let  $\theta'$  be the angle between the  $(\hat{i} + \delta\hat{i})$  axis and the projection of  $\hat{N}$  on the  $(\hat{i} + \delta\hat{i}) - (\hat{j} + \delta\hat{j})$  plane. Then

$$\tan\theta' = \frac{\hat{N} \cdot \hat{j} - \kappa_1 dv \hat{N} \cdot \hat{k}}{\hat{N} \cdot \hat{i} + \kappa_2 du \hat{N} \cdot \hat{k}}\tag{B-21}$$

The dot products in (B-21) can be evaluated by inspection of Figure B-1, to obtain

$$\tan\theta' = \frac{\sin\theta_o \sin\phi - \kappa_1 dv \cos\phi}{\cos\theta_o \sin\phi + \kappa_2 du \cos\phi}\tag{B-22}$$

Equation (B-17) can be rearranged to give

$$\kappa_1 = -\kappa_2 \tan^2\theta_o .\tag{B-23}$$

Figure B-1 shows that

$$du = dv \tan\theta_o . \quad (B-24)$$

The expressions (B-23) and (B-24) are substituted into (B-22) to obtain

$$\tan\theta' = \frac{\sin\theta_o \sin\phi + \kappa_2 \tan^2\theta_o dv \cos\phi}{\cos\theta_o \sin\phi + \kappa_2 \tan\theta_o dv \cos\phi} , \quad (B-25)$$

which can be rearranged to give

$$\tan\theta' = \frac{\tan\theta_o (\cos\theta_o \sin\phi + \kappa_2 \tan\theta_o dv \cos\phi)}{(\cos\theta_o \sin\phi + \kappa_2 \tan\theta_o dv \cos\phi)} , \quad (B-26)$$

or

$$\tan\theta' = \tan\theta_o . \quad (B-27)$$

That is, if PQ is the projection of  $\hat{N}$  on the  $\hat{i}$ - $\hat{j}$  plane, and P'Q' is the projection of  $\hat{N}$  on the  $(\hat{i} + \delta\hat{i}) - (\hat{j} + \delta\hat{j})$  plane, then the angle between PQ and the  $\hat{i}$  axis equals the angle between P'Q' and the  $(\hat{i} + \delta\hat{i})$  axis.

The normal curvature at the point P' is given by

$$k_n' = \kappa_1' \cos^2\theta_o + \kappa_2' \sin^2\theta_o . \quad (B-28)$$

The asymptotic direction at P' is  $\theta_o' = \theta_o + (d\theta_o/dl)dl$ . Then

$\tan^2[\theta_o + (d\theta_o/dl)dl] = -\kappa_1'/\kappa_2'$  and

$$k_n' = -\kappa_2' \left[ \frac{\sin^2(\theta_o + \frac{d\theta_o}{dl} dl)}{\cos^2(\theta_o + \frac{d\theta_o}{dl} dl)} \cos^2\theta_o - \sin^2\theta_o \right] \quad (B-29)$$

A similar expression can be developed for the point P'' separated by  $-dl'$  from the point P:

$$k_n'' = -\kappa_2'' \left[ \frac{\sin^2(\theta_o - \frac{d\theta_o}{dl} dl)}{\cos^2(\theta_o - \frac{d\theta_o}{dl} dl)} \cos^2\theta_o - \sin^2\theta_o \right] \quad (B-30)$$

Inspection of (B-29) and (B-30) indicates that

1.  $k_n' \neq 0$  and  $k_n'' \neq 0$  except if  $d\theta_o/dl = 0$
2. if  $d\theta_o/dl \neq 0$ , then  $k_n'$  and  $k_n''$  (and hence  $k'$  and  $k''$ ) are of opposite sign
3. if  $d\theta_o/dl$  changes sign at P, an indeterminate situation occurs.

The second result completes the proof that the curvature of a section trace changes sign (i.e., forms an inflection point) at points where  $k = 0$ . The only exceptions consist of surfaces for which  $d\theta_o/dl$ , the asymptotic line curvature, is equal to zero, or instances in which  $d\theta_o/dl$  changes sign at the point P, a case which is expected to constitute a set of points of measure zero.

## APPENDIX C

### NOTES ON THE GRAIN CONTIGUITY AND THE GRAIN FACE CONTIGUITY

Assume that the  $\alpha\alpha$  grain boundaries are distributed uniformly and randomly through the  $\alpha$  phase. Then the set of  $\alpha\alpha$  interfaces satisfy the necessary and sufficient conditions for a random test surface, which can be used to sample the three-dimensional structure. Under this assumption, measures of the intersection of the  $\alpha\alpha$  boundaries (test surfaces) with other microstructural features can be used to give unbiased estimates of the metric properties associated with those features. In particular, the  $\alpha\alpha\alpha$  and  $\alpha\alpha P$  triple lines, which are the intersections of the  $\alpha\alpha$  boundaries with the other  $\alpha\alpha$  boundaries and the  $\alpha P$  surfaces, respectively, can be used to estimate  $S_V^{\alpha\alpha}$  and  $S_V^{\alpha P}$ .

The length of the intersection of a test surface with an interface is related to the area in unit volume of that interface by<sup>17,151</sup>

$$S_V = \frac{4}{\pi} L_A \quad (\text{C-1})$$

where  $L_A$  is the length of intersection per unit area of test surface. If the  $\alpha\alpha$  surfaces are used to sample the  $\alpha P$  surfaces, the required  $L_A$  is given by

$$L_A = \frac{L_V^{\alpha\alpha P}}{S_V^{\alpha\alpha}}, \quad (\text{C-2})$$

and the pore-solid surface area is

$$S_V^{\alpha P'} = \frac{4}{\pi} \frac{L_V^{\alpha\alpha P}}{S_V^{\alpha\alpha}} \quad (C-3)$$

The prime (') is used to indicate that this estimate of  $S_V^{\alpha P}$  was made under the assumption that the  $\alpha\alpha$  boundaries are distributed randomly and uniformly.

When the  $\alpha\alpha$  boundaries are used as test surfaces to sample themselves, an additional factor must be considered. Each  $\alpha\alpha\alpha$  triple line represents the intersection of three  $\alpha\alpha$  surfaces; one of these is taken as the test surface. Therefore only two-thirds of the  $\alpha\alpha$  grain contacts are represented in a measurement of the  $\alpha\alpha\alpha$  triple line length. Since the three grain surfaces that meet at a triple line are indistinguishable, any one of them can be used as the test surface; thus two-thirds of the  $\alpha\alpha$  area is counted in a measurement of the  $\alpha\alpha\alpha$  triple line length. The latter property is normalized to a unit area of test surface by dividing by  $S_V^{\alpha\alpha}$ , so that

$$\frac{2}{3} S_V^{\alpha\alpha'} = \frac{4}{\pi} \frac{L_V^{\alpha\alpha\alpha}}{S_V^{\alpha\alpha}} \quad (C-4)$$

Equations (C-3) and (C-4) can be substituted into the definition of gram contiguity,

$$C^{\alpha'} = \frac{2S_V^{\alpha\alpha'}}{2S_V^{\alpha\alpha'} + S_V^{\alpha P'}} \quad (C-5)$$

to obtain

$$C^{\alpha'} = \frac{3L_V^{\alpha\alpha\alpha}}{3L_V^{\alpha\alpha\alpha} + L_V^{\alpha\alpha P}} \quad (C-6)$$

The right-hand side of this expression is identically equal to the grain face contiguity,  $C^{\alpha\alpha}$ . Thus

$$C^{\alpha'} = C^{\alpha\alpha}. \quad (C-7)$$

The nature of the departure of real structures from the model of randomly distributed  $\alpha\alpha$  surfaces may be inferred by comparison of  $C^{\alpha}$ , the grain contiguity for the real structure, with  $C^{\alpha'} = C^{\alpha\alpha}$ , the grain contiguity calculated under the assumptions of the model. For a structure in which  $\alpha\alpha$  surfaces avoid intersections with each other and preferentially intersect the  $\alpha P$  interface,  $S_V^{\alpha P'}$  is larger than  $S_V^{\alpha P}$ , and  $S_V^{\alpha\alpha'}$  is smaller than  $S_V^{\alpha\alpha}$ . Then, by comparison of (C-5) and (1-12), it is possible to conclude that

$$C^{\alpha} > C^{\alpha'} = C^{\alpha\alpha}. \quad (C-8)$$

An example of this kind of structure is a lightly sintered structure in which monocrystalline particles are joined at weld necks but formation of  $\alpha\alpha\alpha$  triple lines has not occurred.

For a structure in which the  $\alpha\alpha$  surfaces preferentially intersect themselves and avoid the  $\alpha P$  interfaces,  $S_V^{\alpha P'}$  is smaller than  $S_V^{\alpha P}$ , and  $S_V^{\alpha\alpha'}$  is larger than  $S_V^{\alpha\alpha}$ . In this case

$$C^{\alpha} < C^{\alpha'} = C^{\alpha\alpha}. \quad (C-9)$$

APPENDIX D  
ELECTRICAL MEASUREMENTS FOR SPECIMENS  
WITH WATER VAPOR ADSORBED

Table D-1

## Dielectric Properties of Specimen 39

f (Hz)	$G^{-1}$ (ohm <sup>-1</sup> )	C (F)	$(\text{ohm}^{-1} \sigma \text{cm}^{-1})$	$\tan \delta$	$\epsilon'$	$\epsilon''$	$\tan \delta_{AC}$	$\epsilon''_{AC}$
1.000E2	5.4000E-3	1.0000E-8	1.4813E-3	8.5944E2	3.0933E4	2.6628E7	5.3052E-1	1.6437E4
2.000E2	5.3900E-3	1.0300E-8	1.4786E-3	4.1643E2	3.1912E4	1.3289E7	0.0000E0	0.0000E0
5.000E2	5.4000E-3	1.0000E-8	1.4813E-3	1.7189E2	3.0983E4	5.3255E6	1.0610E-1	3.2874E3
1.000E3	5.3900E-3	9.8600E-9	1.4786E-3	8.7003E1	3.0549E4	2.6578E6	0.0000E0	0.0000E0
2.000E3	5.3800E-3	9.4300E-9	1.4758E-3	4.5401E1	2.9217E4	1.3264E6	0.0000E0	0.0000E0
5.000E3	5.4000E-3	9.0000E-9	1.4813E-3	1.9099E1	2.7884E4	5.3255E5	1.1789E-2	3.2874E2
1.000E4	5.5900E-3	7.9600E-9	1.5334E-3	1.1177E1	2.4662E4	2.7564E5	3.8656E-1	9.5339E3
2.000E4	5.6000E-3	5.8300E-9	1.5362E-3	7.6438E0	1.8063E4	1.3807E5	2.7754E-1	5.0132E3
5.000E4	6.7568E-3	2.5000E-9	1.8535E-3	8.6030E0	7.7457E3	6.6636E4	1.7317E0	1.3413E4
1.000E5	7.0423E-3	7.8000E-10	1.9318E-3	1.4369E1	2.4166E3	3.4726E4	3.3577E0	8.1144E3
2.000E5	7.1942E-3	1.4000E-10	1.9735E-3	4.0893E1	4.3376E2	1.7738E4	1.0218E1	4.4320E3
5.000E5	7.4074E-3	0.0000E0	2.0320E-3	0.0000E0	0.0000E0	0.0000E0	0.0000E0	0.0000E0
1.000E6	7.4074E-3	0.0000E0	2.0320E-3	0.0000E0	0.0000E0	0.0000E0	0.0000E0	0.0000E0

Table D-2

## Dielectric Properties of Specimen 40

f (Hz)	$G$ (ohm <sup>-1</sup> )	C (F)	(ohm <sup>-1</sup> cm <sup>-1</sup> )	tanδ	ε'	ε''	tanδ <sub>AC</sub>	ε'' <sub>AC</sub>
1.0000E2	5.2200E-3	1.0000E-9	1.4585E-3	8.3079E3	3.1556E3	2.6217E7	0.0000E0	0.0000E0
2.0000E2	5.2200E-3	9.0000E-10	1.4585E-3	4.6155E3	2.8401E3	1.3108E7	0.0000E0	0.0000E0
5.0000E2	5.2200E-3	8.9000E-10	1.4585E-3	1.8669E3	2.8085E3	5.2433E6	0.0000E0	0.0000E0
1.0000E3	5.2200E-3	9.0000E-10	1.4585E-3	9.2310E2	2.8401E3	2.6217E6	0.0000E0	0.0000E0
2.0000E3	5.2200E-3	9.4000E-10	1.4585E-3	4.4191E2	2.9663E3	1.3108E6	0.0000E0	0.0000E0
5.0000E3	5.2200E-3	9.0000E-10	1.4585E-3	1.8462E2	2.8401E3	5.2433E5	0.0000E0	0.0000E0
1.0000E4	5.2400E-3	8.6000E-10	1.4641E-3	9.6973E1	2.7138E3	2.6317E5	3.7013E-1	1.0045E3
2.0000E4	5.2900E-3	6.8000E-10	1.4780E-3	6.1907E1	2.1458E3	1.3284E5	8.1918E-1	1.7578E3
5.0000E4	5.3476E-3	5.5000E-10	1.4941E-3	3.0949E1	1.7356E3	5.3715E4	7.3844E-1	1.2816E3
1.0000E5	5.5556E-3	2.7000E-10	1.5522E-3	3.2748E1	8.5202E2	2.7902E4	1.9780E0	1.6853E3
2.0000E5	5.6497E-3	7.3000E-11	1.5785E-3	6.1588E1	2.3036E2	1.4187E4	4.6844E0	1.0791E3
5.0000E5	5.7143E-3	0.0000E0	1.5966E-3	0.0000E0	0.0000E0	0.0000E0	0.0000E0	0.0000E0
1.0000E6	5.7143E-3	0.0000E0	1.5966E-3	0.0000E0	0.0000E0	0.0000E0	0.0000E0	0.0000E0

Table D-3

## Dielectric Properties of Specimen 41

f (Hz)	$\frac{G}{\text{ohm}^{-1}}$	C (F)	$\frac{\sigma}{\text{ohm}^{-1} \text{cm}^{-1}}$	tan $\delta$	$\epsilon'$	$\epsilon''$	tan $\delta_{AC}$	$\epsilon''_{AC}$
1.000E2	4.8200E-3	3.0000E-9	1.1998E-3	2.5571E3	8.4342E3	2.1567E7	0.0000E0	0.0000E0
2.000E2	4.8200E-3	2.9000E-9	1.1998E-3	1.3226E3	8.1530E3	1.0783E7	0.0000E0	0.0000E0
5.000E2	4.8200E-3	2.8000E-9	1.1998E-3	5.4795E2	7.8719E3	4.3134E6	0.0000E0	0.0000E0
1.000E3	4.8200E-3	2.8000E-9	1.1998E-3	2.7397E2	7.8719E3	2.1567E6	0.0000E0	0.0000E0
2.000E3	4.8300E-3	2.7800E-9	1.2023E-3	1.3826E2	7.8156E3	1.0806E6	2.8625E-1	2.2372E3
5.000E3	4.8400E-3	2.6200E-9	1.2048E-3	5.8802E1	7.3658E3	4.3313E5	2.4298E-1	1.7898E3
1.000E4	4.8800E-3	2.3800E-9	1.2147E-3	3.2633E1	6.6911E3	2.1835E5	4.0123E-1	2.6847E3
2.000E4	5.0200E-3	1.8800E-9	1.2496E-3	2.1249E1	5.2854E3	1.1231E5	8.4657E-1	4.4745E3
5.000E4	5.2083E-3	1.0200E-9	1.2965E-3	1.6254E1	2.8676E3	4.6609E4	1.2119E0	3.4752E3
1.000E5	5.4645E-3	4.3000E-10	1.3602E-3	2.0226E1	1.2089E3	2.4451E4	2.3854E0	2.8837E3
2.000E5	5.5556E-3	1.1000E-10	1.3829E-3	4.0191E1	3.0925E2	1.2429E4	5.3212E0	1.6456E3
5.000E5	5.6180E-3	0.0000E0	1.3984E-3	0.0000E0	0.0000E0	0.0000E0	0.0000E0	0.0000E0
1.000E6	5.6180E-3	0.0000E0	1.3984E-3	0.0000E0	0.0000E0	0.0000E0	0.0000E0	0.0000E0

Table D-4

## Dielectric Properties of Specimen 43

$f$ (Hz)	$G$ (ohm $^{-1}$ )	$C$ (F)	$(\text{ohm}^{-1}\sigma \text{ cm}^{-1})$	$\tan\delta$	$\epsilon'$	$\epsilon''$	$\tan\delta_{AC}$	$\epsilon''_{AC}$
1.0000E2	4.4500E-3	1.4000E-8	1.0738E-3	5.0589E2	3.8155E4	1.9302E7	0.0000E0	0.0000E0
2.0000E2	4.4500E-3	1.3000E-8	1.0738E-3	2.7240E2	3.5429E4	9.6509E6	0.0000E0	0.0000E0
5.0000E2	4.4600E-3	1.2960E-8	1.0762E-3	1.0954E2	3.5320E4	3.8690E6	1.6374E-1	5.7833E3
1.0000E3	4.4500E-3	1.2500E-8	1.0738E-3	5.6659E1	3.4067E4	1.9302E6	0.0000E0	0.0000E0
2.0000E3	4.4900E-3	1.1800E-8	1.0834E-3	3.0280E1	3.2159E4	9.7377E5	2.4727E-1	7.9521E3
5.0000E3	4.6100E-3	9.5400E-9	1.1124E-3	1.5382E1	2.6000E4	3.9992E5	5.2273E-1	1.3591E4
1.0000E4	4.8200E-3	6.4000E-9	1.1631E-3	1.1986E1	1.7442E4	2.0907E5	9.1183E-1	1.5904E4
2.0000E4	5.0600E-3	3.2600E-9	1.2210E-3	1.2352E1	8.8845E3	1.0974E5	1.4809E0	1.3157E4
5.0000E4	5.4054E-3	8.9000E-10	1.3043E-3	1.9333E1	2.4255E3	4.6892E4	3.4051E0	8.2592E3
1.0000E5	5.4645E-3	2.2000E-10	1.3186E-3	3.9532E1	5.9957E2	2.3702E4	7.3150E0	4.3858E3
2.0000E5	5.4945E-3	1.8000E-11	1.3258E-3	2.4291E2	4.9056E1	1.1916E4	4.6030E1	2.2580E3
5.0000E5	5.4945E-3	0.0000E0	1.3258E-3	0.0000E0	0.0000E0	0.0000E0	0.0000E0	0.0000E0
1.0000E6	5.4945E-3	0.0000E0	1.3258E-3	0.0000E0	0.0000E0	0.0000E0	0.0000E0	0.0000E0

Table D-5  
Dielectric Properties of Specimen 44

f (Hz)	$G$ (ohm <sup>-1</sup> )	C (F)	$\frac{C}{f}$ (ohm <sup>-1</sup> cm <sup>-1</sup> )	tan $\delta$	$\epsilon'$	$\epsilon''$	tan $\delta_{AC}$	$\epsilon''_{AC}$
1.0000E2	6.2500E-3	1.0000E-8	1.5081E-3	9.9472E2	2.7253E4	2.7109E7	0.0000E0	0.0000E0
2.0000E2	6.2500E-3	9.4000E-9	1.5081E-3	5.2911E2	2.5618E4	1.3555E7	0.0000E0	0.0000E0
5.0000E2	6.2500E-3	9.2800E-9	1.5081E-3	2.1438E2	2.5291E4	5.4219E6	0.0000E0	0.0000E0
1.0000E3	6.2500E-3	9.1000E-9	1.5081E-3	1.0931E2	2.4800E4	2.7109E6	0.0000E0	0.0000E0
2.0000E3	6.2600E-3	8.8200E-9	1.5103E-3	5.6480E1	2.4037E4	1.3576E6	9.0224E-2	2.1687E3
5.0000E3	6.3200E-3	8.1600E-9	1.5250E-3	2.4653E1	2.2239E4	5.4826E5	2.7306E-1	6.0725E3
1.0000E4	6.4600E-3	6.9000E-9	1.5588E-3	1.4901E1	1.8805E4	2.8020E5	4.8438E-1	9.1087E3
2.0000E4	6.8400E-3	4.6600E-9	1.6503E-3	1.1680E1	1.2700E4	1.4834E5	1.0075E0	1.2796E4
5.0000E4	7.2993E-3	1.6200E-9	1.7613E-3	1.4342E1	4.4150E3	6.3321E4	2.0617E0	9.1024E3
1.0000E5	7.6923E-3	4.0000E-10	1.8562E-3	3.0607E1	1.0901E3	3.3365E4	5.7388E0	6.2560E3
2.0000E5	7.6923E-3	4.0000E-11	1.8562E-3	1.5203E2	1.0901E2	1.6683E4	2.8694E1	3.1280E3
5.0000E5	7.6923E-3	0.0000E0	1.8562E-3	0.0000E0	0.0000E0	0.0000E0	0.0000E0	0.0000E0
1.0000E6	7.6923E-3	0.0000E0	1.8562E-3	0.0000E0	0.0000E0	0.0000E0	0.0000E0	0.0000E0

Table D-6

## Dielectric Properties of Specimen 45

f (Hz)	$G$ (ohm <sup>-1</sup> )	$C$ (F)	$\sigma$ (ohm <sup>-1</sup> cm <sup>-1</sup> )	tan $\delta$	$\epsilon'$	$\epsilon''$	tan $\delta$ AC	$\epsilon''$ AC
1.0000E2	3.7500E-3	4.0000E-9	8.5725E-4	1.4921E3	1.0328E4	1.5409E7	6.4709E-14	6.6828E-10
2.0000E2	3.7500E-3	3.6000E-9	8.5725E-4	8.2893E2	9.2948E3	7.7047E6	3.5949E-14	3.3414E-10
5.0000E2	3.7500E-3	4.0200E-9	8.5725E-4	2.9693E2	1.0379E4	3.0819E6	1.2877E-14	1.3366E-10
1.0000E3	3.7600E-3	3.7000E-9	8.5954E-4	1.6174E2	9.5530E3	1.5451E6	4.3015E-1	4.1092E3
2.0000E3	3.7600E-3	3.3600E-9	8.5954E-4	8.9051E1	8.6751E3	7.7253E5	2.3684E-1	2.0546E3
5.0000E3	3.7900E-3	2.8000E-9	8.6639E-4	4.3086E1	7.2293E3	3.1148E5	4.5473E-1	3.2874E3
1.0000E4	3.8500E-3	2.1800E-9	8.8011E-4	2.8108E1	5.6285E3	1.5820E5	7.3007E-1	4.1092E3
2.0000E4	3.9800-3	1.3800E-9	9.0983E-4	2.2951E1	3.5630E3	8.1773E4	1.3263E0	4.7256E3
5.0000E4	4.032E-3	5.3000E-10	9.2177E-4	2.4217E1	1.3684E3	3.3139E4	1.6952E0	2.3197E3
1.0000E5	4.1494E-3	1.7000E-10	9.4855E-4	3.8847E1	4.3892E2	1.7051E4	3.7390E0	1.6411E3
2.0000E5	4.2017E-3	3.2000E-11	9.6050E-4	1.0449E2	8.2620E1	8.6328E3	1.1232E1	9.2802E2
5.0000E5	4.2017E-3	0.0000E0	9.6050E-4	0.0000E0	0.0000E0	0.0000E0	0.0000E0	0.0000E0
1.0000E6	4.2017E-3	0.0000E0	9.6050E-4	0.0000E0	0.0000E0	0.0000E0	0.0000E0	0.0000E0

Table D-7  
Dielectric Properties of Specimen 46

f (Hz)	G (ohm <sup>-1</sup> )	C (F)	$\frac{\sigma}{\text{ohm}^{-1} \text{cm}^{-1}}$	tan $\delta$	$\epsilon'$	$\epsilon''$	tan $\delta_{AC}$	$\epsilon''_{AC}$
1.0000E2	3.4900E-3	2.0000E-9	8.6873E-4	2.7773E3	5.6228E3	1.5616E7	4.3139E-13	2.4256E-9
2.0000E2	3.4900E-3	1.6000E-9	8.6873E-4	1.7358E3	4.4982E3	7.8079E6	2.6962E-13	1.2128E-9
5.0000E2	3.4900E-3	1.7000E-9	8.6873E-4	6.5347E2	4.7794E3	3.1232E6	1.0150E-13	4.8512E-10
1.0000E3	3.4900E-3	1.6000E-9	8.6873E-4	3.4716E2	4.4982E3	1.5616E6	5.3924E-14	2.4256E-10
2.0000E3	3.4900E-3	1.6000E-9	8.6873E-4	1.7358E2	4.4982E3	7.8079E5	2.6962E-14	1.2128E-10
5.0000E3	3.5000E-3	1.4200E-9	8.7122E-4	7.8457E1	3.9922E3	3.1321E5	2.2416E-1	8.9489E2
1.0000E4	3.5300E-3	1.2000E-9	8.7869E-4	4.6818E1	3.3737E3	1.5795E5	5.3052E-1	1.7898E3
2.0000E4	3.6100E-3	7.6000E-10	8.9860E-4	3.7799E1	2.1367E3	8.0764E4	1.2565E0	2.6847E3
5.0000E4	3.6496E	3.0000E-10	9.0847E-4	3.8724E1	8.4342E2	3.2660E4	1.6938E0	1.4286E3
1.0000E5	3.7037E-3	8.0000E-11	9.2193E-4	7.3683E1	2.2491E2	1.6572E4	4.2515E0	9.5621E2
2.0000E5	3.7037E-3	5.0000E-12	9.2193E-4	5.8946E2	1.4057E1	8.2860E3	3.4012E1	4.7810E2
5.0000E5	3.7037E-3	0.0000E0	9.2193E-4	0.0000E0	0.0000E0	0.0000E0	0.0000E0	0.0000E0
1.0000E6	3.7037E-3	0.0000E0	9.2193E-4	0.0000E0	0.0000E0	0.0000E0	0.0000E0	0.0000E0

Table D-8  
Dielectric Properties of Specimen 47

f (Hz)	G (ohm <sup>-1</sup> L)	C (F)	$\sigma$ (ohm <sup>-1</sup> cm <sup>-1</sup> )	tan $\delta$	$\epsilon'$	$\epsilon''$	tan $\delta$ <sub>AC</sub>	$\epsilon''$ <sub>AC</sub>
1.0000E2	6.3600E-3	3.0000E-10	1.5185E-3	3.3741E4	8.0899E2	2.7296E7	0.0000E0	0.0000E0
2.0000E2	6.3900E-3	3.0000E-10	1.5257E-3	1.6950E4	8.0899E2	1.3712E7	3.5368E1	2.8612E4
5.0000E2	6.3800E-3	3.0000E-10	1.5233E-3	6.7694E3	8.0899E2	5.4764E6	3.5368E0	2.8612E3
1.0000E3	5.3700E-3	3.2000E-10	1.2821E-3	2.6708E3	8.6292E2	2.3047E6	0.0000E0	0.0000E0
2.0000E3	6.3800E-3	3.0000E-10	1.5233E-3	1.6923E3	8.0899E2	1.3691E6	8.8419E-1	7.1530E2
5.0000E3	6.4000E-3	3.2000E-10	1.5281E-3	6.3662E2	8.6292E2	5.4935E5	2.3210E0	2.0029E3
1.0000E4	6.3900E-3	2.8000E-10	1.5237E-3	3.6321E2	7.5506E2	2.7425E5	7.5788E-1	5.7224E2
2.0000E4	6.4400E-3	2.0000E-10	1.5376E-3	2.5624E2	5.3933E2	1.3820E5	2.5200E0	1.3591E3
5.0000E4	6.4935E-3	2.0800E-10	1.5504E-3	9.9372E1	5.6090E2	5.5738E4	1.7880E0	1.0029E3
1.0000E5	6.4935E-3	8.2000E-11	1.5504E-3	1.2603E2	2.2112E2	2.7869E4	2.2678E0	5.0146E2
2.0000E5	6.6667E-3	0.0000E0	1.5917E-3	0.0000E0	0.0000E0	0.0000E0	0.0000E0	0.0000E0
5.0000E5	6.6667E-3	0.0000E0	1.5917E-3	0.0000E0	0.0000E0	0.0000E0	0.0000E0	0.0000E0
1.0000E6	6.6667E-3	0.0000E0	1.5917E-3	0.0000E0	0.0000E0	0.0000E0	0.0000E0	0.0000E0

Table D-9  
Dielectric Properties of Specimen 48

f (Hz)	$G$ (ohm <sup>-1</sup> )	$C$ (F)	$\sigma$ (ohm <sup>-1</sup> cm <sup>-1</sup> )	tan $\delta$	$\epsilon'$	$\epsilon''$	tan $\delta_{AC}$	$\epsilon''_{AC}$
1.0000E2	6.9200E-3	2.0000E-9	1.5819E-3	5.5068E3	5.1638E3	2.8436E7	0.0000E0	0.0000E0
2.0000E2	7.0000E-3	2.0000E-9	1.6002E-3	2.7852E3	5.1638E3	1.4382E7	1.1937E1	6.1638E4
5.0000E2	6.9900E-3	1.9600E-9	1.5979E-3	1.1352E3	5.0605E3	5.7447E6	3.2481E0	1.6437E4
1.0000E3	6.9600E-3	1.8800E-9	1.5911E-3	5.8921E2	4.8539E3	2.8600E6	0.0000E0	0.0000E0
2.0000E3	6.9900E-3	1.7600E-9	1.5979E-3	3.1605E2	4.5441E3	1.4362E6	9.0429E-1	4.1092E3
5.0000E3	6.9900E-3	1.5200E-9	1.5979E-3	1.4638E2	3.9245E3	5.7447E5	4.1883E-1	1.6437E3
1.0000E4	6.9800E-3	1.2000E-9	1.5956E-3	9.1038E1	3.1499E3	2.8682E5	1.3045E-1	4.1092E2
2.0000E4	7.0500E-3	8.3000E-3	1.6116E-3	6.7593E1	2.1430E3	1.4485E5	7.6701E-1	1.6437E3
5.0000E4	7.2993E-3	3.7000E-3	1.6686E-3	6.2795E1	9.5530E2	5.9988E4	2.8327E0	2.7061E3
1.0000E5	7.4074E-3	8.0000E-3	1.6933E-3	1.4737E3	2.0655E1	3.0438E4	8.7019E1	1.7974E3
2.0000E5	7.4074E-3	0.0000E0	1.6933E-3	0.0000E0	0.0000E0	0.0000E0	0.0000E0	0.0000E0
5.0000E5	7.4074E-3	0.0000E0	1.6933E-3	0.0000E0	0.0000E0	0.0000E0	0.0000E0	0.0000E0
1.0000E6	7.4074E-3	0.0000E0	1.6933E-3	0.0000E0	0.0000E0	0.0000E0	0.0000E0	0.0000E0

Table D-10  
Dielectric Properties of Specimen 49

f (Hz)	G (ohm <sup>-1</sup> )	C (F)	(ohm <sup>-1</sup> cm <sup>-1</sup> ) <sup>σ</sup>	tanδ	ε'	ε''	tanδ <sub>AC</sub>	ε'' <sub>AC</sub>
1.0000E2	3.9000E-5	2.0000E-10	8.1229E-6	3.1035E2	4.7048E2	1.4601E5	0.0000E0	0.0000E0
2.0000E2	3.9000E-5	2.2000E-10	8.1229E-6	1.4107E2	5.1752E2	7.3007E4	0.0000E0	0.0000E0
5.0000E2	3.9000E-5	2.2000E-10	8.1229E-6	5.6428E1	5.1752E2	2.9203E4	0.0000E0	0.0000E0
1.0000E3	3.9000E-5	2.2000E-10	8.1229E-6	2.8214E1	5.1752E2	1.4601E4	0.0000E0	0.0000E0
2.0000E3	3.9000E-5	2.0000E-10	8.1229E-6	1.5518E1	4.7048E2	7.3007E3	0.0000E0	0.0000E0
5.0000E3	4.1000E-5	1.8800E-10	8.5395E-6	6.9419E0	4.4225E2	3.0700E3	3.3863E-1	1.4976E2
1.0000E4	4.4000E-5	1.4200E-10	9.1643E-6	4.9318E0	3.3404E2	1.6473E3	5.6040E-1	1.8720E2
2.0000E4	5.1000E-5	9.6000E-11	1.0622E-5	4.2276E0	2.2583E2	9.5470E2	9.9472E-1	2.2464E2
5.0000E4	5.9524E-5	4.0000E-11	1.2393E-5	4.7368E0	9.4095E1	4.4571E2	1.6332E0	1.5368E2
1.0000E5	6.2500E-5	2.1000E-11	1.3018E-5	4.7368E0	4.9400E1	2.3400E2	1.7810E0	8.7982E1
2.0000E5	6.7568E-5	1.1000E-11	1.4073E-5	4.8881E0	2.5876E1	1.2648E2	2.0667E0	5.3478E1
5.0000E5	7.2993E-5	6.0000E-12	1.5203E-5	3.8724E0	1.4114E1	5.4656E1	1.8034E0	2.5453E1
1.0000E6	7.6923E-5	5.0000E-12	1.6022E-5	2.4485E0	1.1762E1	2.8799E1	1.2071E0	1.4198E1

Table D-11  
Dielectric Properties of Specimen 50

f (Hz)	G (ohm <sup>-1</sup> L)	C (F)	$\sigma$ (ohm <sup>-1</sup> cm <sup>-1</sup> L)	tan $\delta$	$\epsilon'$	$\epsilon''$	tan $\delta$ <sub>AC</sub>	$\epsilon''$ <sub>AC</sub>
1.0000E2	2.8700E-3	2.0000E-9	6.0505E-4	2.2839E3	4.7621E3	1.0876E7	3.4511E-13	1.6435E-9
2.0000E2	2.8700E-3	2.8000-9	6.0505E-4	8.1567E2	6.6670E3	5.4381E6	1.2325E-13	8.2174E-10
5.0000E2	2.8700E-3	2.8300E-9	6.0505E-4	3.2281E2	6.7384E3	2.1752E6	4.8779E-14	3.2869E-10
1.0000E3	2.8700E-3	2.7780E-9	6.0505E-4	1.6443E2	6.6146E2	1.0876E6	2.4846E-14	1.6435E-10
2.0000E3	2.8800E-3	2.6300E-9	6.0716E-4	8.7142E1	6.2622E3	5.4570E5	3.0258E-1	1.8948E3
5.0000E3	2.9000E-3	2.2800E-9	6.1138E-4	4.0487E1	5.4288E3	2.1980E5	4.1883E-1	2.2738E3
1.0000E4	2.9600E-3	1.6200E-9	.2403E-4	2.9080E1	3.8573E3	1.1217E5	8.8419E-1	3.4106E3
2.0000E4	3.0700E-3	8.0000E-10	6.4722E-4	3.0538E1	1.9049E3	5.8170E4	1.9894E0	3.7896E3
5.0000E4	3.0769E-3	2.7000E-10	6.4868E-4	3.6275E1	6.4289E2	2.3321E4	2.4395E0	1.5683E3
1.0000E5	3.1250E-3	9.0000E-11	6.5881E-4	5.5262E1	2.1430E2	1.1842E4	4.5094E0	9.6635E2
2.0000E5	3.1746E-3	3.0000E-11	6.6927E-4	7.6554E1	7.8575E1	6.0152E3	7.3453E0	5.7716E2
5.0000E5	3.1746E-3	9.0000E-12	6.6927E-4	1.1228E2	2.1430E1	2.4061E3	1.0773E1	2.3086E2
1.0000E6	3.2787E-3	1.0000E-12	6.912E-4	5.2182E2	2.3811E0	1.2425E3	7.5045E1	1.5488E2

Table D-12  
Dielectric Properties of Specimen 52

f (Hz)	$G$ (ohm <sup>-1</sup> )	$C$ (F)	(ohm <sup>-1</sup> cm <sup>-1</sup> ) $\sigma$	tan $\delta$	$\epsilon'$	$\epsilon''$	tan $\delta_{AC}$	$\epsilon''_{AC}$
1.0000E2	3.4300E-3	6.0000E-9	8.2766E-4	9.0984E2	1.6352E4	1.4878E7	0.0000E0	0.0000E0
2.0000E2	3.4400E-3	6.0000E-9	8.3007E-4	4.5624E2	1.6352E4	7.4605E6	4.4219E-1	7.2291E3
5.0000E2	3.4400E-3	6.2400E-9	8.3007E-4	1.7548E2	1.7006E4	2.9842E6	1.7004E-1	2.8917E3
1.0000E3	3.4500E-3	5.8700E-9	8.3248E-4	9.3541E1	1.5998E4	1.4964E6	3.6151E-1	5.7833E3
2.0000E3	3.4600E-3	5.2000E-9	8.3490E-4	5.2950E1	1.4172E4	7.5038E5	3.5708E-1	5.0604E3
5.0000E3	3.5200E-3	3.6600E-9	8.4938E-4	3.0613E1	9.9747E3	3.0536E5	7.2475E-1	7.2291E3
1.0000E4	3.6000E-3	2.1000E-9	8.6868E-4	2.7284E1	5.7232E3	1.5615E5	1.2379E0	7.0846E3
2.0000E4	3.7100E-3	9.0000E-10	8.9522E-4	3.2804E1	2.4528E3	8.0460E4	2.4168E0	5.9279E3
5.0000E4	3.7594E-3	2.6000E-10	9.0714E-4	4.6025E1	7.0858E2	3.2613E4	3.9511E0	2.7997E3
1.0000E5	3.8168E-3	8.0000E-11	9.2099E-4	7.5933E1	2.1803E2	1.6555E4	7.5624E0	1.6488E3
2.0000E5	3.8168E-3	1.4000E-11	9.2099E-4	2.1695E2	3.8155E1	8.2776E3	2.1607E1	8.2440E2
5.0000E5	3.8462E-3	0.0000E0	9.2808E-4	0.0000E0	0.0000E0	0.0000E0	0.0000E0	0.0000E0
1.0000E6	3.8462E-3	0.0000E0	9.2808E-4	0.0000E0	0.0000E0	0.0000E0	0.0000E0	0.0000E0

#### LIST OF REFERENCES

1. J. Maxwell, A Treatise on Electricity and Magnetism, Vol. 1, Dover Publications, Inc., New York, 452 (1958).
2. K. Wagner, Arch. Elektrotech., 2, 371 (1914).
3. R. Sillars, J. Proc. Instn. Elec. Engrs., 80, 378 (1937).
4. L. Bochkaryova and A. Simashkevish, Thin Solid Films, 20, 329 (1974).
5. G. Bandyopahdyay and R. Fullrath, J. Am. Ceram. Soc., 54, 182 (1974).
6. M. Gensamer, E. Pearsall, W. Pellini, and J. Low, Trans. Am. Soc. Met., 30, 983 (1942).
7. J. Gurland, Trans. AIME, 227, 1146 (1963).
8. R. A. Graham, Master's Thesis, University of Florida (1973).
9. S. Nazaré and G. Ondracek, The Microscope, 22, 39 (1974).
10. S. Carniglia, J. Am. Ceram. Soc., 55, 243 (1972).
11. R. Forlano, A. Allen, and R. Beals, J. Am. Ceram. Soc., 50, 93 (1967).
12. R. Coble and W. Kingery, J. Am. Ceram. Soc., 39, 377 (1956).
13. G. Ondracek and B. Schulz, J. Nuc. Mater., 46, 253 (1973).
14. W. Duckworth, J. Am. Ceram. Soc., 36, 68 (1953).
15. D. Freund and W. Schikarski, KFK-1031, EURFNR-773 (1970).
16. J. Gurland, Trans. AIME, 212, 452 (1958).
17. E. Underwood, Quantitative Stereology, Addison-Wesley, Reading, Mass. (1970).
18. E. Thomson, J. Geol., 38, 193 (1930).

19. C. Smith and L. Guttman, Trans. AIME, 197, 81 (1953).
20. J. Cahn, Trans. AIME, 239, 611 (1967).
21. R. Delloff, Trans. AIME, 239, 617 (1967).
22. F. Rhines, R. DeHoff, and R. Rummel, Annual Report, AEC Contract No. AT-(40-1)-2851 (1962).
23. R. DeHoff and S. Gehl in Proceedings of the Fourth International Congress for Stereology, NBS Special Publication 431, 29 (Jan., 1976).
24. J. Gibbs, The Scientific Papers of J. Willard Gibbs, Vol. 1, Dover Publications, Inc., New York (1961).
25. D. Johnson, J. Am. Ceram. Soc., 53, 574 (1970).
26. R. DeHoff, University of Florida, private communication.
27. G. Dorfler in Proceedings of the Second International Congress for Stereology, ed. by H. Elias, Springer-Verlag, Inc., New York (1967).
28. J. Gurland, Trans. AIME, 236, 642 (1966).
29. H. Fischmeister and H. Exner, Arch. Eisenhuttwes., 37, 499 (1966).
30. J. Cahn and J. Williard, Trans. AIME, 215, 759 (1959).
31. P. Pinheiro, Doctoral Dissertation, University of Florida (1973).
32. R. DeHoff in Proceedings of the Symposium on Statistical and Probabilistic Problems in Metallurgy, ed. by W. Nicholson, special supplement to Advances in Applied Probability (Dec., 1972).
33. H. Coxeter, Ill. J. Math., 2, 746 (1958).
34. E. Sinnott, The Problem of Organic Form, Yale University Press, New Haven, Conn. (1962).
35. E. Matzke, Am. J. Botany, 33, 58 (1946).
36. D. Thompson, On Growth and Form, abridged edition, ed. by J. Bonner, Cambridge University Press, Cambridge, England (1961).
37. C. Smith in Metal Interfaces, American Society for Metals, Cleveland, Ohio (1952).
38. W. Williams and C. Smith, J. Metals, 4, 755 (1952).

39. E. Scheil and H. Wurst, Z. Metallkunde, 28, 40 (1936).
40. K. Craig, Doctoral Dissertation, University of Florida (1972).
41. J. Kronsbein, L. Buteau, and R. DeHoff, Trans. AIME, 233, 1961 (1965).
42. E. Aigeltinger, Doctoral Dissertation, University of Florida (1970).
43. H. Fischmeister in Newsletter '74 in Stereology, ed. by G. Ondracek, Gesellschaft fur Kernforschung M.B.H., Karlsruhe (1974).
44. R. DeHoff, Trans. AIME, 230, 764 (1964).
45. F. Rhines, R. DeHoff, and J. Kronsbein, Final Report, AEC Contract No. AT-(40-1)-2581 (1969).
46. F. Rhines, Trans. AIME, 166, 474 (1946).
47. C. Hardy, Metal Progress, 35, 171 (1939).
48. K. Endell, Metall. u. Erz., 18, 169 (1921).
49. R. Wright and R. Smith, J. Chem. Soc., 119, 1683 (1921).
50. R. Smith, J. Chem. Soc., 123, 2088 (1923).
51. F. Sauerwald, Z. Elektrochem., 29, 79 (1923).
52. F. Sauerwald, Z. Metallkunde, 16, 41 (1924).
53. F. Sauerwald, Z. Metallkunde, 20, 227 (1928).
54. F. Sauerwald and S. Kubik, Z. Elektrochem., 38, 33 (1932).
55. W. Dawihl, Stahl u. Eisen, 61, 907 (1941).
56. W. Jones, Principles of Powder Metallurgy, Arnold, London (1937).
57. C. Desch, J. Chem. Soc., 123, 280 (1923).
58. C. C. Balke, Iron Age, 147, 23 (1941).
59. A. Shaler and J. Wulff, Phys. Rev., 72, 79 (1947).
60. G. Kuczynski, Trans. AIME, 185, 169 (1949).
61. G. Kuczynski, J. Appl. Phys., 20, 1160 (1949).
62. B. Alexander and R. Balluffi, Acta. Met., 5, 666 (1957).
63. W. Kingery and M. Berg, J. Am. Ceram. Soc., 26, 1205 (1955).

64. R. Coble, J. Am. Ceram. Soc., 41, 55 (1958).
65. H. Ichinose and G. Kuczynski, Acta. Met., 10, 209 (1962).
66. R. Coble and T. Guptka in Proceedings of the Second International Conference on Sintering and Related Phenomena, ed. by G. Kuczynski, C. Gibbon, and N. Hooten, Gordon and Breach, New York, 423 (1967).
67. R. Coble in Proceedings of the Third International Conference on Sintering and Related Phenomena, ed. by G. Kuczynski, Plenum Press, New York, 177 (1973).
68. F. Rhines, Plansee Proc., 3rd Seminar, Reutte, Tyrol, 38 (1958).
69. W. Wollaston, Phil. Trans. Roy. Soc. London, 119, 1 (1829).  
Also: Trans. Am. Soc. Met., 60, 597 (1967).
70. F. Rhines, C. Birchenall, and L. Hughes, Trans. AIME, 188, 378 (1950).
71. R. DeHoff, R. Rummel, H. LaBuff, and F. Rhines in Modern Developments in Powder Metallurgy, Vol. 1, ed. by H. Hausner, Plenum Press, New York, 310 (1966).
72. W. Tuohig, Doctoral Dissertation, University of Florida (1972).
73. F. Rhines and R. Gregg, Met. Trans., 4, 1365 (1973).
74. R. Coble, J. Appl. Phys., 32, 787 (1961).
75. J. Burke, J. Am. Ceram. Soc., 40, 80 (1957).
76. T. Guptka, J. Mater. Sci., 6, 25 (1971).
77. A. Mocellin and W. Kingery, J. Am. Ceram. Soc., 56, 309 (1973).
78. J. Burke in Ceramic Microstructures, ed. by R. Fullrath and J. Pask, John Wiley and Sons, New York, 681 (1968).
79. H. Hoekstra in Uranium Dioxide: Properties and Nuclear Applications, ed. by J. Belle, U. S. Govt. Printing Office, Washington, D. C., 229 (1961).
80. J. Williams, E. Barnes, R. Scott, and A. Hiall, J. Nuc. Mater., 1, 28 (1959).
81. R. Wolfe and S. Kaufman, WAPD-TM-587, AEC Contract No. AT(11-1)-Gen-14 (1967).
82. R. Ackermann, P. Gilles, and R. Thorn, J. Chem. Phys., 25, 1089 (1956).

83. B. Schaner in Uranium Dioxide: Properties and Nuclear Applications, ed. by J. Belle, U. S. Govt. Printing Office, Washington, D. C., 126 (1961).
84. F. Kreith, Principles of Heat Transfer, 2nd edition, International Textbook Co., Scranton, 79 (1967).
85. R. Weidner and R. Sells, Elementary Classical Physics, Vol. 2, Allyn and Bacon, Boston, 938 (1965).
86. Lord Rayleigh, Phys. Mag., 34, 481 (1892).
87. H. Fricke, Phys. Rev., 24, 575 (1924).
88. D. Bruggeman, Ann. der Phys., 24, 636 (1935).
89. D. Bruggeman, Ann. der Phys., 25, 645 (1936).
90. H. Fricke, J. Phys. Chem., 57, 934 (1953).
91. T. Digges, Jr. and R. Tauber, Met. Trans., 2, 1683 (1971).
92. R. Meredith and C. Tobias, J. Appl. Phys., 31, 1270 (1960).
93. W. Watson, W. Hahn, Jr., and R. Kraft, Met. Trans., 6A, 151 (1975).
94. W. Brown, J. Chem. Phys., 23, 1514 (1955).
95. C. Herring, J. Appl. Phys., 31, 1939 (1960).
96. Z. Hashin and S. Shtrikman, Phys. Rev., 130, 129 (1963).
97. R. A. Millikan, Wied. Ann., 61, 337 (1897). Cited in Reference 99.
98. J. Dryden and R. Meakins, Proceedings of the Physical Society B, 70, 427 (1957).
99. H. Fricke and S. Morse, Phys. Rev., 25, 361 (1925).
100. H. Fricke, J. General Physiology, 9, 137 (1925).
101. A. Maunsbach, J. Ultrastruct. Res., 15, 242 (1968).
102. K. Cole, Biophysical Journal, 2, 101 (1962).
103. T. Blewitt, R. Coltman, and J. Redman, Report on Conference on Defects in Crystalline Solids, Phys. Soc. London, 309 (1955).
104. L. Clarebrough, M. Hargreaves, and M. Loretto, Phil. Mag., 7, 115 (1962).

105. J. V. Sharp, A. Mitchell, and J. Christian, Acta. Met., 13, 965 (1965).
106. A. Owen, Phys. Chem. Glasses, 2, 152 (1961).
107. R. Charles, J. Am. Ceram. Soc., 46, 235 (1963).
108. D. Kinser and L. Hench, J. Am. Ceram. Soc., 51, 445 (1968).
109. D. Kinser and L. Hench, J. Mater. Sci., 5, 369 (1970).
110. L. Hench and H. Schaake in Introduction to Glass Science, ed. by L. Pye, H. Stevens, and W. LaCourse, Plenum Press, New York, 583 (1972).
111. T. Blakely and A. White in Plansee Proc., 2nd Seminar, Reutte/Tyrol, 1955, ed. by F. Benesovsky, Pergamon Press, London, 335 (1956).
112. F. Forscher, J. Franklin Inst., 259, 107 (1955).
113. K. Maschke, H. Overhof, and P. Thomas, Phys. Stat. Solid. (b), 60, 563 (1973).
114. F. Streintz, Ann. der Phys., 314, 854 (1902).
115. C. Goetzal, Treatise on Powder Metallurgy, Vol. 1, Interscience, New York (1949).
116. O. Kantorowicz, Ann. der Phys., 12, 1 (1932).
117. G. Grube and H. Schlecht, Z. Elektrochem., 44, 367 (1938).
118. F. Rhines, R. DeHoff, and E. Whitney, Final Report, AEC Contract No. AT-(40-1)-4212 (1975).
119. F. Rhines and R. Colton in Powder Metallurgy, ed. by J. Wulff, American Society Metals, Cleveland, 67 (1942).
120. H. Hauser and J. Dedrick in The Physics of Powder Metallurgy, ed. by W. Kingston, McGraw-Hill Book Co., New York, 320 (1951).
121. R. McIntosh, Dielectric Behavior of Adsorbed Gases, Marcel Dekker, New York (1966).
122. G. Ebert and G. Langhammer, Kolloid Z., 174, 5 (1961).
123. M. Baldwin and J. Morrow, J. Chem. Phys., 36, 1574 (1962).
124. L. Hench in Advanced Techniques for Material Investigation and Fabrication, Vol. 14, Western Periodicals, North Hollywood, Calif. (1968). Also: Engr. Prog. U. Fla., 23(2), 1 (1969).

125. R. Willardson, J. Moody, and H. Goering, J. Inorg. Nuc. Chem., 6, 19 (1958).
126. W. Hartmann, Z. Phys., 102, 79 (1936).
127. W. Meyer, Z. Elektrochem., 50, 274 (1944).
128. R. Willardson and J. Moody in Uranium Dioxide: Properties and Nuclear Applications, ed. by J. Belle, U. S. Govt. Printing Office, Washington, D. C., 211 (1961).
129. S. Aronson, J. Rulli, and B. Schaner, J. Chem. Phys., 35, 1382 (1961).
130. S. Aronson and J. Clayton, J. Chem. Phys., 32, 749 (1960).
131. S. Aronson and J. Clayton, J. Chem. Phys., 35, 1055 (1961).
132. R. DeConinck and J. Devreese, Phys. Stat. Sol., 32, 823 (1969).
133. J. Devreese, R. DeConinck, and H. Pollak, Phys. Stat. Sol., 17, 825 (1966).
134. P. Nagels, J. Devreese, and M. Denayer, J. Appl. Phys., 35, 1175 (1964).
135. D. Emin, J. Sol. State Chem., 12, 246 (1975).
136. A. Rubio, Compt. Rend. Acad. Sci. Ser. B, 272, 1435 (1971).
137. W. Schikarski and G. Ondracek, J. Nuc. Mater., 45, 171 (1972/73).
138. J. Bates, BNWL-296, AEC Contract No. AT(40-1)-1830 (1967).
139. M. Freymann, S. Langevin, M. Rolland-Bernard, M. Perio, and R. Kleinberger, J. Phys. et Rad., 15, 82 (1954).
140. M. Freymann and R. Freymann, J. Chem. Phys., 20, 1970 (1952).
141. J. Day, M. Freymann, and R. Freymann, Compt. Rend. Acad. Sci., 229, 1013 (1949).
142. J. Wachtman, Phys. Rev., 131, 517 (1963).
143. J. Tateno and K. Naito, Sol. State Comm., 7, 807 (1969).
144. B. Schaner, J. Nucl. Mater., 2, 110 (1960).

145. B. Cullity, Elements of X-ray Diffraction, Addison-Wesley, New York, 335 (1956).
146. J. Gvildys, Argonne National Laboratory, Program B-150.
147. P. Kofstad, Nonstoichiometry, Diffusion, and Electrical Conductivity in Binary Metal Oxides, Wiley-Interscience, New York, 310 (1972).
148. S. Brunauer, P. Emmett, and E. Teller, J. Am. Chem. Soc., **60**, 309 (1938).
149. D. Kinser, Doctoral Dissertation, U. of Florida (1968).
150. M. Bal'shin, Vestnik Metalloprom., **18**, 124 (1938).
151. R. DeHoff and F. Rhines (eds.), Quantitative Microscopy, McGraw-Hill Book Company, New York (1968).
152. D. Struik, Lectures on Classical Differential Geometry, Addison-Wesley, Cambridge, Mass. (1950).
153. R. McIntosh, Dielectric Behavior of Physically Adsorbed Gases, M. Dekker, New York (1966).
154. V. Daniel, Dielectric Relaxation, Academic Press, London (1967).
155. R. DeHoff and J. Gillard in Modern Developments in Powder Metallurgy, Vol. 4, ed. by H. Hausner, Plenum Press, New York, 281 (1970).

## BIOGRAPHICAL SKETCH

Stephen Mark Gehl was born November 17, 1947, in West Bend, Wisconsin. He attended primary and secondary schools in Ft. Lauderdale, Florida, and graduated from St. Thomas Aquinas High School in 1965. He attended the University of Notre Dame in South Bend, Indiana, and graduated with a degree of Bachelor of Science in Metallurgical Engineering in 1969. He entered the University of Florida in 1969 in pursuit of the degree of Doctor of Philosophy. Since May, 1975, he has been associated with the Materials Science Division of Argonne National Laboratory and has conducted research on the behavior of nuclear fuels during steady-state and transient heating conditions.

The author is married to the former Patricia Ann Knight of Gainesville, Florida, and is the father of seven children. He is a member of Alpha Sigma Mu and the American Ceramic Society.

I certify that I have read this study and that in my opinion it conforms to acceptable standards of scholarly presentation and is fully adequate, in scope and quality, as a dissertation for the degree of Doctor of Philosophy.



---

R. T. DeHoff, Chairman  
Professor of Materials Science and  
Engineering

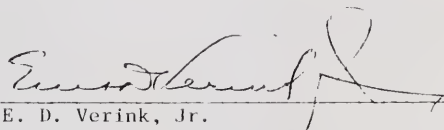
I certify that I have read this study and that in my opinion it conforms to acceptable standards of scholarly presentation and is fully adequate, in scope and quality, as a dissertation for the degree of Doctor of Philosophy.



---

F. N. Rhines  
Professor of Materials Science and  
Engineering

I certify that I have read this study and that in my opinion it conforms to acceptable standards of scholarly presentation and is fully adequate, in scope and quality, as a dissertation for the degree of Doctor of Philosophy.



---

E. D. Verink, Jr.  
Professor of Materials Science and  
Engineering

I certify that I have read this study and that in my opinion it conforms to acceptable standards of scholarly presentation and is fully adequate, in scope and quality, as a dissertation for the degree of Doctor of Philosophy.



---

C. P. Luehr  
Associate Professor of Mathematics

This dissertation was submitted to the Graduate Faculty of the College of Engineering and to the Graduate Council, and was accepted as partial fulfillment of the requirements for the degree of Doctor of Philosophy.

December 1977

  
\_\_\_\_\_  
Dean, College of Engineering

\_\_\_\_\_  
Dean, Graduate School

52  
# 599. See Main B.S.  
F1131-71-0385 (113)